

# Kent Academic Repository

## Full text document (pdf)

### Citation for published version

Rumens, Christina Victoria (2016) The Integration of Stimulus-Responsive Polymers into Passive Ultra-High Frequency Radio Frequency Identification (UHF-RFID) Sensors. Doctor of Philosophy (PhD) thesis, University of Kent,.

### DOI

### Link to record in KAR

<http://kar.kent.ac.uk/62467/>

### Document Version

UNSPECIFIED

#### Copyright & reuse

Content in the Kent Academic Repository is made available for research purposes. Unless otherwise stated all content is protected by copyright and in the absence of an open licence (eg Creative Commons), permissions for further reuse of content should be sought from the publisher, author or other copyright holder.

#### Versions of research

The version in the Kent Academic Repository may differ from the final published version.

Users are advised to check <http://kar.kent.ac.uk> for the status of the paper. **Users should always cite the published version of record.**

#### Enquiries

For any further enquiries regarding the licence status of this document, please contact:

[researchsupport@kent.ac.uk](mailto:researchsupport@kent.ac.uk)

If you believe this document infringes copyright then please contact the KAR admin team with the take-down information provided at <http://kar.kent.ac.uk/contact.html>

# The Integration of Stimulus-Responsive Polymers into Passive Ultra-High Frequency Radio Frequency Identification (UHF-RFID) Sensors

Christina Victoria Rumens

A thesis submitted to the University of Kent in partial fulfilment of the  
requirements for the degree of Doctor of Philosophy

University of Kent

Canterbury

Kent

CT2 7NH

November 2016

## DECLARATION

No part of this thesis has been submitted by me or anyone else in support of an application for any other degree or qualification at the University of Kent or any other University.

Signed: Christina Victoria Rumens

Date: 24.11.2016

## Abstract

Recently there has been much interest in designing passive radio frequency identification (RFID) tags with sensing capabilities. Passive RFID sensor tags are ideal for many applications due to their low cost, wireless monitoring with non-line of sight operation capabilities, small size and pre-existing infrastructure. There are two approaches in designing passive RFID sensor tags: either a functioning passive sensor is integrated into the integrated circuit (IC) of a RFID tag or a sensing component (stimuli-responsive material) is used. In the former approach the sensor readout is digital while in the latter approach the sensor readout is made indirectly by monitoring variances in the analog response of the RFID tag. The advantage of the latter approach over the former is that commercially available IC chips can be utilised - further lowering the cost of the sensor tag. The aim of this research was to fabricate and investigate several stimuli-responsive polymers for use as sensing components in passive UHF-RFID sensor tags.

An epidermal passive strain sensor, composed of a flexible antenna mounted onto a stretchable barium titanate ( $\text{BaTiO}_3$ ) loaded PDMS composite is presented for assisted living applications. Permittivity of the elastomer could be controlled by the weight % loading of  $\text{BaTiO}_3$  and self-adhesion of the antenna was achieved during the elastomers curing process. The epidermal strain sensor presented in this thesis can differentiate between y and x-axis stretching and monitor an increase in x-axis strain up to 10.4 %.

The known characteristic of PDMS swelling in solvent vapours was exploited and utilised as an actuator mechanism in a solvent vapour displacement sensor. The swelling extents of several polysiloxane networks in various solvent vapours, along with the diffusion properties of the solvent vapours into the polysiloxane networks were studied. A prototype solvent vapour sensor with a standard PDMS elastomer actuator is demonstrated. The sensor could differentiate between solvents as the RFID response was related to the extent of polymer swelling at a given exposure time. Ink-jet printing of PDMS was also explored for work towards additive manufacturing of PDMS based sensing components for RFID tags.

A light sensor design is also presented, in which a photosensitive material that becomes highly conductive as a result of light exposure acts as a short circuit resulting in the degradation of the tags performance. Silver nitrate-PVA composite films were explored as possible candidates for the photosensitive material. However, these films were found to be unsuitable for this application as the measured film resistance was not low enough to achieve a short circuit and was not affected by light irradiation.

## Publications and Presentations

### Peer-Reviewed Journal Articles:

*Switchable Disposable Passive RFID vapour Sensors from Inkjet Printed Electronic Components Integrated with PDMS as a Stimulus Responsive Material.* K. E. Belsey, A. V. S. Parry, C. V. Rumens, M. A. Ziai, S. G. Yeates, J. C. Batchelor and S. J. Holder, *Journal Materials Chemistry C*, 2017.

*Swelling of PDMS networks in solvent vapours; applications for passive RFID wireless sensors.* C. V. Rumens, M. A. Ziai, K. Belsey, J. C. Batchelor and S. J. Holder, *Journal of Materials Chemistry C*, 2015, **3**, 10091-10098.

### Peer-Reviewed Letter:

*Epidermal Passive RFID Strain Sensor for Assisted Technologies.* O. O. Rakibet, C. V. Rumens, J. C. Batchelor and S. J. Holder, *IEEE Antennas and Wireless Propagation Letters*, 2014, **13**, 814-817.

### Peer-Reviewed Conferences Papers:

*Accurate RFID Strain gauges for skin mounting.* J. C. Batchelor, O. O. Rakibet, C. V. Rumens and S. J. Holder, *Antennas and Propagation Society International Symposium (APSURSI)*, IEEE, 2014, 836-837.

*Polydimethylsiloxane Substrates for passive UHF RFID Sensors.* C. V. Rumens, O. O. Rakibet, J. C. Batchelor and S. J. Holder, *Antennas and Propagation Conference (LAPC)*, IEEE, 2014.

### Poster Presentations:

*Swellable Polysiloxane Elastomers as Substrates for Passive Radio Frequency Identification (RFID) Gas Sensors.* C. V. Rumens, M. A. Ziai, K. Belsey, J. C. Batchelor and S. J. Holder, 249<sup>th</sup> ACS National Meeting, Denver, Colorado, March 22 – 26, 2015.

## Acknowledgments

I would like to thank the following people for all their support during my PhD studies. Firstly, I wish to express my sincerest gratitude to my primary supervisor Dr. Simon Holder who gave me the opportunity to undertake this PhD. His continuous support, guidance and invaluable advice has been greatly appreciated and without which this research would never have reached completion. I will greatly miss working with him and could not have wished for a better supervisor. I would also like to express my thanks to my co-supervisor Professor John Batchelor who introduced me to the world of RFID, helped guide the RFID aspect of my work and willingness to answer the numerous questions about RFID I had.

My thanks to Dr. Osman Rakibet who performed the waveguide permittivity measurements, CST simulations, designed the strain sensor tag and performed the strain sensor tag measurements. Also, for graciously taking his time to explain many aspects of RFID antenna tag design. Thank you to Dr. Ali Ziai who designed both the solvent vapour sensor tag and light sensor tag, guided and helped me with both the DAK permittivity measurements and using the Voyantic TagperformanceLite UHF RFID characterisation system. Also, his generosity with both his time and his knowledge of RFID technology. My thanks to Dr. Adam Parry for his help and advice in using the Dimatix ink-jet printer. Thank you to Dr. Laura Vera Stimpson for performing the XRD measurements and Dr. Francesco Caddeo for his help with the nitrogen physisorption measurements. Thank you Dr. Kate Belsey who first introduced me to the working ways of the lab and all her help. My sincere thanks also goes to all the technical and administrative staff in both the School of Physical Sciences and School of Engineering and Digital Arts.

Thank you to all my colleagues and friends at the University of Kent especially Laura, Kate, Liv, Chrissie, Christian, Mark, Ollie, Trevor, JJ, Alex, Yarry, and Francesco for their understanding, willingness to be sounding boards and their friendship. I look back at my time at Kent with great fondness.

My best friends Jennie and Helen, thank you for always supporting and believing in me. Also, thank you to my friends at home and family for their constant support. I would also like to offer my gratitude to Robert and Andrea Sinclair who graciously provided me an ideal space to write my thesis.

Finally, thank you to my parents and Jonathan who have supported me throughout my time at University. Their continuous encouragement and belief that I could achieve anything I put my mind to, led to both the undertaking and completion of this PhD thesis. I cannot thank them enough.

**To**  
**My Parents**

# Table of Contents

|                                     |      |
|-------------------------------------|------|
| DECLARATION.....                    | i    |
| Abstract.....                       | ii   |
| Publications and Presentations..... | iii  |
| Peer-Reviewed Journal Article.....  | iii  |
| Peer-Reviewed Letter.....           | iii  |
| Peer-Reviewed Conferences.....      | iii  |
| Poster Presentations.....           | iii  |
| Acknowledgements.....               | iv   |
| Table of Contents.....              | vi   |
| Table of Figures.....               | xiii |
| Abbreviations.....                  | xxi  |

## **Chapter 1: Introduction**

|  |   |
|--|---|
| 1.0 Introduction to Radio Frequency Identification (RFID)..... | 1 |
| 1.0.1 Origins of RFID.....                                     | 1 |
| 1.0.2 Current Applications of RFID technology.....             | 2 |
| 1.1 RFID tags.....   | 4 |
| 1.1 Active & Passive Tags.....                                 | 5 |
| 1.1.2 Frequencies.....   | 5 |
| 1.1.3 Communication method of passive tags.....                | 6 |
| 1.1.3.1 Inductive Coupling.....                                | 6 |
| 1.1.3.2 Backscatter.....                                       | 6 |
| 1.1.4 Standards.....   | 7 |
| 1.1.5 Tag Antenna.....   | 7 |
| 1.1.6 Tag Substrate.....                                       | 8 |
| 1.2 RFID sensor tags.....                                      | 8 |



|   |    |
|---|----|
| 1.2.1 Sensor components in passive RFID sensor tags.....  | 10 |
| 1.2.1.1 Temperature sensor tags.....  | 10 |
| 1.2.1.2 Humidity sensor tags.....   | 11 |
| 1.2.1.3 Chemical sensor tags.....   | 11 |
| 1.2.1.4 Strain sensor tags.....   | 12 |
| 1.2.1.5 Light sensor tags.....  | 12 |
| 1.3 Stimuli-responsive polymers.....  | 12 |
| 1.4 Epidermal UHF-RFID strain sensor tag.....   | 13 |
| 1.5 Elastomeric materials.....  | 14 |
| 1.5.1 Mechanical properties of elastomers.....  | 17 |
| 1.6 Silicone elastomers.....  | 19 |
| 1.6.1 Polysiloxanes.....  | 20 |
| 1.6.2 Cross-linking mechanisms of polysiloxanes.....  | 22 |
| 1.6.3 Compound design to modify dielectric properties of silicone elastomers.....   | 23 |
| 1.7 UHF-RFID solvent vapour displacement sensor tag.....  | 27 |
| 1.8 Swelling phenomenon in elastomeric materials.....   | 27 |
| 1.9 UHF-RFID light sensor tag.....  | 30 |
| 1.10 Light sensitive polymeric materials.....   | 30 |
| 1.11 Polyvinyl alcohol.....   | 35 |
| 1.12 Aims and Objectives.....   | 37 |
| 1.13 References.....  | 39 |
| <br>  |    |
| <b>Chapter 2: Fabrication of BaTiO<sub>3</sub>-PDMS composites as substrates for passive wireless epidermal UHF-RFID strain sensors</b> |    |
| 2.0 Introduction.....   | 45 |
| 2.1 Experimental.....   | 47 |
| 2.1.1 Materials and Apparatus.....  | 47 |

|  |    |
|--|----|
| 2.1.2 Synthesis of TEOS and TESPN cross-linked elastomers.....   | 47 |
| 2.1.3 Synthesis of BaTiO <sub>3</sub> -PDMS composite elastomers.....  | 48 |
| 2.1.4 Synthesis of BaTiO <sub>3</sub> pellet.....  | 48 |
| 2.1.5 Measurements and Instruments.....  | 48 |
| 2.2 Results and Discussion.....  | 50 |
| 2.2.1 Characterisation of TEOS and TESPN cross-linked PDMS elastomers, BaTiO <sub>3</sub> -PDMS<br>elastomers and BaTiO <sub>3</sub> pellet..... | 50 |
| 2.2.1.1 TEOS and TESPN cross-linked PDMS elastomers.....   | 50 |
| 2.2.1.2 BaTiO <sub>3</sub> -PDMS elastomers.....   | 51 |
| 2.2.1.3 BaTiO <sub>3</sub> Pellet.....   | 53 |
| 2.2.2 Effect of chemical modification and inorganic filler on permittivity of PDMS.....  | 54 |
| 2.2.2.1 Permittivity.....  | 54 |
| 2.2.2.2 Effect of TESPN cross-linker on permittivity.....  | 56 |
| 2.2.2.3 Effect of barium titanate filler on permittivity.....  | 56 |
| 2.2.2.4 Comparison between waveguide and DAK measurements.....   | 60 |
| 2.2.3 High molecular weight PDMS composites.....   | 60 |
| 2.2.4 Antenna attachment.....  | 63 |
| 2.2.5 Antenna resistance.....  | 65 |
| 2.2.6 Design and Fabrication of Prototype RFID strain sensor.....  | 67 |
| 2.2.7 Strain sensor RFID measurements.....   | 68 |
| 2.3 Conclusions.....   | 71 |
| 2.4 References.....  | 72 |
| <br>   |    |
| <b>Chapter 3: Swelling of polysiloxane networks in solvent vapours; applications for passive UHF-<br/>RFID wireless sensors</b>                  |    |
| 3.0 Introduction.....  | 75 |
| 3.1 Experimental.....  | 76 |

|   |     |
|---|-----|
| 3.1.1 Materials and Apparatus.....  | 76  |
| 3.1.2 Synthesis of polysiloxane networks: Sn catalysed condensation method..... | 77  |
| 3.1.2.1 Synthesis of standard PDMS elastomers.....                              | 77  |
| 3.1.2.2 Synthesis of TESPN cross-linked PDMS elastomers.....                    | 77  |
| 3.1.2.3 Synthesis of PDMS sponges.....  | 77  |
| 3.1.2.4 Synthesis of 40 wt% BaTiO <sub>3</sub> -PDMS composites.....            | 78  |
| 3.1.2.5 Synthesis of polytrifluoropropylmethylsiloxane (PTFPMS) elastomers..... | 78  |
| 3.1.3 Characterisation of the polysiloxane networks.....                        | 78  |
| 3.1.4 Swelling experiments.....   | 79  |
| 3.1.5 Solvent scrubber experiments.....   | 79  |
| 3.2 Results and Discussion.....   | 79  |
| 3.2.1 Polysiloxane Network Characterisation.....                                | 79  |
| 3.2.1.1 PDMS sponges.....   | 79  |
| 3.2.1.2 PTFPMS elastomers.....  | 84  |
| 3.2.2 Standard PDMS swelling.....   | 86  |
| 3.2.3 Correlation between swelling and solubility parameters.....               | 88  |
| 3.2.4 Effect of polymer morphology on equilibrium swelling.....                 | 96  |
| 3.2.4.1 Fillers.....  | 96  |
| 3.2.4.2 Porosity.....   | 97  |
| 3.2.4.3 Nature of cross-links.....  | 98  |
| 3.2.4.4 Fluoro containing Polysiloxanes.....                                    | 99  |
| 3.2.5 PDMS elastomers as solvent scrubbers.....                                 | 107 |
| 3.3 Conclusions.....  | 108 |
| 3.4 References.....   | 108 |

## **Chapter 4: Diffusion rate of solvent vapours into polysiloxane networks; applications for passive UHF-RFID wireless sensors**

|   |     |
|---|-----|
| 4.0 Introduction.....   | 111 |
| 4.1 Experimental.....   | 111 |
| 4.1.1 Materials and Apparatus.....  | 111 |
| 4.1.2 Synthesis of polysiloxane networks: Sn catalysed condensation method.....       | 111 |
| 4.1.3 Absorption Rate Experiments.....  | 112 |
| 4.2 Results and Discussion.....   | 112 |
| 4.2.1 Absorption Rate / swelling kinetics of polysiloxane networks.....               | 112 |
| 4.2.2 Diffusion Coefficient.....  | 123 |
| 4.2.3 Solvent Vapour Diffusion Rates.....   | 124 |
| 4.2.4 Effect of the polymer morphology on the diffusion rate of a solvent vapour..... | 128 |
| 4.2.4.1 Barium titanate fillers.....  | 128 |
| 4.2.4.2 Porosity.....   | 130 |
| 4.2.4.3 Nature of cross-links.....  | 132 |
| 4.2.4.4 Fluoro-containing Polysiloxanes.....  | 133 |
| 4.3 Conclusions.....  | 134 |
| 4.4 References.....   | 135 |

## **Chapter 5: Passive UHF-RFID displacement solvent vapour sensor tag with a PDMS elastomer actuator**

|  |     |
|--|-----|
| 5.0 Introduction.....                            | 137 |
| 5.1 Experimental.....                            | 138 |
| 5.1.1 Materials and Apparatus.....               | 138 |
| 5.1.2 Synthesis of standard PDMS elastomers..... | 138 |
| 5.1.3 Sensor tag design.....                     | 138 |
| 5.1.4 RFID sensor tag measurements.....          | 140 |

|   |     |
|---|-----|
| 5.2 Results and Discussion.....                         | 140 |
| 5.2.1 RFID response versus PDMS swelling.....           | 140 |
| 5.2.2 RFID response time and analyte concentration..... | 143 |
| 5.3 Conclusions.....                                    | 144 |
| 5.4 References.....                                     | 145 |

**Chapter 6: Ink-jet printing of PDMS; applications for printed passive UHF-RFID wireless sensors**

|  |     |
|--|-----|
| 6.0 Introduction.....  | 146 |
| 6.1 Experimental.....  | 147 |
| 6.1.1 Materials and Apparatus.....   | 147 |
| 6.1.2 Fabrication of Sylgard® 184 ink.....                                     | 147 |
| 6.1.3 Ink-Jet printing parameters.....   | 147 |
| 6.2 Results and Discussion.....  | 148 |
| 6.2.1 Characterisation of pre-cure Sylgard® 184 inks.....                      | 148 |
| 6.2.2 Printing using pre-cure Sylgard® 184 (30 wt %)-xylene (70 wt %) ink..... | 151 |
| 6.2.3 Printing using pre-cure Sylgard® 184 (5 wt %)-xylene (95 wt %) ink.....  | 154 |
| 6.3 Conclusions.....   | 157 |
| 6.4 References.....  | 158 |

**Chapter 7: Fabrication of silver salt-PVA composites as light sensitive components of a UHF-RFID light sensor**

|   |     |
|---|-----|
| 7.0 Introduction.....                                 | 160 |
| 7.1 Experimental.....                                 | 162 |
| 7.1.1 Materials and Apparatus.....                    | 162 |
| 7.1.2 Synthesis of light sensitive PVA materials..... | 162 |
| 7.1.2.1 AgNO <sub>3</sub> -PVA solutions.....         | 162 |
| 7.1.2.2 AgNO <sub>3</sub> -PVA composite films.....   | 162 |

|  |     |
|--|-----|
| 7.1.3 Measurements and Instruments.....                            | 163 |
| 7.2 Results and Discussion.....                                    | 163 |
| 7.2.1 Nature of formation of silver nanoparticles in solution..... | 163 |
| 7.2.2 Nature of formation of silver nanoparticles in films.....    | 170 |
| 7.2.3 Resistance Measurements.....                                 | 177 |
| 7.2.3.1 AgNO <sub>3</sub> -PVA films.....                          | 177 |
| 7.2.3.2 Increased AgNO <sub>3</sub> loading.....                   | 180 |
| 7.2.3.3 Thermal treatment.....                                     | 183 |
| 7.3 Conclusions.....   | 185 |
| 7.3 References.....  | 186 |

## **Chapter 8: Conclusions and further work**

|                                       |     |
|---------------------------------------|-----|
| 8.0 Conclusions and further work..... | 189 |
|---------------------------------------|-----|

## **Appendix**

|  |     |
|--|-----|
| A.1 NMR spectrum of silanol-terminated polydimethylsiloxane (PDMS) (cSt 1000).....                     | 192 |
| A.2 NMR spectrum of silanol-terminated polydimethylsiloxane (PDMS) (cSt 18000).....                    | 193 |
| A.3 NMR spectrum of silanol-terminated polytrifluoropropylmethylsiloxane (PTFPMS) (cSt 150 – 250)..... | 194 |
| A.4 NMR spectrum of xylene.....  | 195 |

# Table of Figures

## Chapter 1:

|   |    |
|---|----|
| Figure 1.0: Basic operation of radio frequency identification (RFID).....   | 1  |
| Figure 1.1: Current applications of RFID technology.....  | 3  |
| Figure 1.2: (a) circular loop antenna (b) square loop antenna with several turns (c) wire dipole antenna (d) wire folded dipole antenna (e) slot antenna and (f) microstrip patch antenna.....  | 8  |
| Figure 1.3: Illustration of Stress-strain plots for typical Hookean and non-Hookean materials.....  | 17 |
| Figure 1.4: Illustration of stress-strain plots for various polymeric materials.....  | 18 |
| Figure 1.5: Illustration of the dielectric polarisation processes. E represents the applied electric field.....   | 24 |
| Figure 1.6: Frequency dependence of dielectric polarisation.....  | 25 |
| Figure 1.7: UHF-RFID solvent vapour displacement sensor tag design. The red arrow indicates the direction in which the feed loop antenna is pushed as a result of elastomer swelling.....   | 27 |
| Figure 1.8: Schematic representation of polymer dissolution; (a) morphology of polymer chains just after being added to a solvent (b) first stage of polymer dissolution: polymer swelling due to the penetration of solvent molecules between the polymer chains and (c) second stage of polymer dissolution: polymer chains are fully solvated and dispersed into a solution..... | 28 |
| Figure 1.9: Light sensor tag design.....  | 30 |

## Chapter 2:

|   |    |
|---|----|
| Figure 2.0: (a) X-axis and (b) Y-axis stretching effect on single slot stretchable antenna design. (c) Simulation results showing the effect of stretch percentage on resonant frequency..... | 46 |
| Figure 2.1: FTIR spectrum of pure PDMS, cross linked PDMS elastomers with varying ratio of TEOS cross linker and pure TEOS.....   | 50 |
| Figure 2.2: FTIR spectrum of pure PDMS, cross-linked PDMS elastomers with varying ratios of the TESPN cross linker and pure TESPN.....  | 51 |
| Figure 2.3: FTIR spectra of BaTiO <sub>3</sub> , PDMS and 27.8 wt% BaTiO <sub>3</sub> PDMS composite.....   | 52 |
| Figure 2.4: XRD of barium titanate powder and 27.8 wt% BaTiO <sub>3</sub> -PDMS composite.....  | 53 |
| Figure 2.5: Distribution of barium titanate (a) 0 wt% (b) 1.0 wt% (c) 1.9 wt% (d) 4.6 wt% (e) 8.8 wt% (f) 16.3 wt% (g) 27.8 wt% and (h) 36.6 wt%.....   | 53 |

|   |    |
|---|----|
| Figure 2.6: XRD of barium titanate powder and barium titanate pellet.....   | 54 |
| Figure 2.7: Illustration of S11 and S22 parameters. S11 refers to the reflected signal where $S11 = b1/a1$ S21 refers to the transmitted signal where $S21 = b2/a1$ .....   | 55 |
| Figure 2.8 Cubic and tetragonal phases of BaTiO <sub>3</sub> .....  | 57 |
| Figure 2.9: Sketch of domains in BaTiO <sub>3</sub> showing 90 and 180 boundaries.....  | 57 |
| Figure 2.10: Relative permittivity of barium titanate pellet.....   | 58 |
| Figure 2.11 Relative permittivity of barium filled PDMS composites (permittivity measurements performed between 3 - 6 GHz).....   | 59 |
| Figure 2.12: (a) FTIR of BaTiO <sub>3</sub> (28.5 wt%)-PDMS <sub>77,000</sub> composite fabricated using method B section 2.2.3 and BaTiO <sub>3</sub> (27.8 wt%)-PDMS <sub>26,000</sub> . SEM micrographs of BaTiO <sub>3</sub> (28.5 wt%)-PDMS <sub>77,000</sub> (a) cross section (b) corner edge of cross-section and upper surface and (c) corner edge of cross-section and lower surface..... | 62 |
| Figure 2.13: SEM micrographs of Silver Lycra® at magnification (a) x 65 and (b) x 474.....  | 63 |
| Figure 2.14: Image of antenna with silicone IC chip attached.....   | 63 |
| Figure 2.15: SEM micrograph (a) cross-section of silver Lycra® adhered to BaTiO <sub>3</sub> - PDMS substrate (b) expanded image of highlighted area in micrograph (a).....   | 65 |
| Figure 2.16: Silver Lycra placed on substrate at varying times (4 minutes apart) during the curing process (far left is 24 minutes into curing, far right is 44 minutes into curing).....   | 66 |
| Figure 2.17: Prototype RFID strain sensor antenna design.....   | 67 |
| Figure 2.18: Image of (a) silver Lycra® antenna BaTiO <sub>3</sub> -PDMS tag prototype (b) copper antenna BaTiO <sub>3</sub> -PDMS tag prototype.....   | 68 |
| Figure 2.19: Prototype tag on PFTE jig for strain measurements (a) no strain (b) 10% strain.....  | 69 |
| Figure 2.20: Transmitted power versus frequency.....  | 70 |
| Figure 2.21: Transmitted Power of the prototype tag as a function of stretch (%).....   | 70 |

### Chapter 3:

|   |    |
|---|----|
| Figure 3.0: SEM micrograph of PDMS sponge prepared using (a) caster sugar template and (b) granulated sugar template. SEM micrograph of (c) caster sugar and (d) granulated sugar. Scale bar is 1 mm in length..... | 80 |
|---|----|



|  |           |
|--|-----------|
| Figure 3.1: SEM micrographs of (a) top surface and (b) bottom surface of PDMS sponge prepared using a caster sugar template and (c) top surface and (d) bottom surface of PDMS sponge prepared using a granulated sugar template. Scale bar is 1 mm in length.....   | <b>81</b> |
| Figure 3.2: Nitrogen physisorption isotherm of PDMS sponges fabricated using a caster sugar template.....  | <b>82</b> |
| Figure 3.3: FTIR spectra of (a) standard PDMS elastomer, (b) PDMS sponge formed using a caster sugar template, (c) PDMS sponge formed using a granulated sugar template and (d) caster sugar.....  | <b>84</b> |
| Figure 3.4: FTIR spectra of (a) TEOS (b) silanol terminated PTFPMS (pure polymer) and (c) cross-linked PTFPMS elastomer.....   | <b>85</b> |
| Figure 3.5: SEM micrographs (a-b) top surface, (c-d) bottom surface and (e) cross-section of PTFPMS elastomer. Scale bar for (a) and (c) is 1 mm and for (b), (d) and (e) is 80 $\mu\text{m}$ in length.....   | <b>86</b> |
| Figure 3.6: Swelling ratio (Q) of PDMS elastomer after 72 hours exposure to a range of solvent vapours.....  | <b>87</b> |
| Figure 3.7: Moles of solvent vapour absorbed into elastomer after 72 hours exposure.....   | <b>88</b> |
| Figure 3.8: Swelling ratio, S of PDMS in various solvents versus the solvent's Hildebrand solubility parameter, $\delta$ .....   | <b>89</b> |
| Figure 3.9: (a) QV (b) QW and (c) moles of absorbed solvent vapour versus $R_a$ for each solvent. The numbers relate to the ranking of the solvents swelling ability.....  | <b>90</b> |
| Figure 3.10: (a) QV versus vapour pressure (b) QW versus vapour pressure and (c) moles of solvent vapour in swollen elastomer versus vapour pressure.....  | <b>91</b> |
| Figure 3.11: (a) QV versus the total Hansen solubility parameter and vapour pressure of each solvent (b) QW versus the total Hansen solubility parameter and vapour pressure of each solvent and (c) moles of solvent in swollen elastomer versus the total Hansen solubility parameter and vapour pressure of each solvent.....   | <b>93</b> |
| Figure 3.12: (a) Measured volume swelling ratio versus predicted swelling ratio calculated using results from linear regression analysis. $R_a$ and vapour pressure variables used (equation 3.10) (b) Measured volume swelling ratio versus predicted swelling ratio calculated using results from linear regression analysis. $\delta_d$ , $\delta_p$ , $\delta_h$ and vapour pressure variables used (equation 3.11)..... | <b>94</b> |
| Figure 3.13: (a) Measured weight swelling ratio versus predicted swelling ratio calculated using results from linear regression analysis. $R_a$ and vapour pressure variables used (equation 3.10) (b)   |           |

|  |            |
|--|------------|
| Measured weight swelling ratio versus predicted swelling ratio calculated using results from linear regression analysis. $\delta d$ , $\delta p$ , $\delta h$ and vapour pressure variables used (equation 3.11).....  | <b>94</b>  |
| Figure 3.14: (a) Measured moles of solvent vapour in swollen elastomer versus predicted moles of vapour calculated using results from linear regression analysis. $R_a$ and vapour pressure variables used (equation 3.10) (b) Measured moles of solvent vapour in swollen elastomer versus predicted moles of vapour calculated using results from linear regression analysis. $\delta d$ , $\delta p$ , $\delta h$ and vapour pressure variables used (equation 3.11)..... | <b>96</b>  |
| Figure 3.15: (a) QV and (b) QW of standard PDMS elastomers and BaTiO <sub>3</sub> -PDMS composites after 72 hours exposure to a range of solvent vapours.....  | <b>94</b>  |
| Figure 3.16: (a) QV and (b) QW of standard PDMS elastomers and PDMS sponges after 72 hours exposure to a range of solvent vapours.....   | <b>97</b>  |
| Figure 3.17: (a) QV and (b) QW of standard PDMS elastomers and TESP <sub>N</sub> cross-linked PDMS elastomers after 72 hours exposure to a range of solvent vapours.....   | <b>99</b>  |
| Figure 3.18: (a) QV and (b) QW of standard PDMS elastomers and PTFPMS elastomers after 72 hours exposure to a range of solvent vapours.....  | <b>99</b>  |
| Figure 3.19: (a) QV versus the total Hansen solubility parameter and vapour pressure of each solvent (b) QW versus the total Hansen solubility parameter and vapour pressure of each solvent.....  | <b>102</b> |
| Figure 3.20: Side on view illustration of (a) double layered elastomer and (b) PTFPMS elastomer with a PDMS tip. Orange represents PDMS and blue represents PTFPMS.....  | <b>103</b> |
| Figure 3.21: Images of 2 cm <sup>2</sup> double layered PTFPMS/PDMS elastomer exposed to diethyl ether vapour for (a) 90 minutes (b) 5 hours (c) 5 hours and (d) 46.5 hours.....   | <b>104</b> |
| Figure 3.22: Images of PTFPMS strip with PDMS tip after (a) 0 minutes (b) 1 hour (c) 5 hours and (d) 72 hours diethyl ether exposure time.....   | <b>104</b> |
| Figure 3.23: (a) SEM micrograph of double layered elastomer. EDX spectra of (b) point 9 and (c) point 10 on SEM micrograph.....  | <b>106</b> |
| <br><b>Chapter 4:</b>  |            |
| Figure 4.0: Area swelling ratio versus solvent vapour exposure time for standard PDMS elastomers.....  | <b>113</b> |
| Figure 4.1: Swelling kinetics of standard PDMS elastomers in acetone, xylene, diethyl ether, DCM, acetonitrile and methanol solvent vapour.....  | <b>115</b> |

|  |            |
|--|------------|
| Figure 4.2: Relationship between PDMS area swelling, QA and solvent vapour exposure time. Inclusion of the solvent vapours toluene and hexane.....   | <b>115</b> |
| Figure 4.3: (a) Swelling kinetics, (b) the first 55 % swelling data versus the square root of time for the standard PDMS elastomers and (c) plot to determine diffusion exponent, n and polymer characteristic constant, k for the swelling of standard PDMS in diethyl ether, DCM, acetone, xylene, toluene and hexane.....                                       | <b>116</b> |
| Figure 4.4: Area swelling ratio versus solvent vapour exposure time for (a) PDMS sponges (b) 40 wt% BaTiO <sub>3</sub> -PDMS elastomers (c) TESP <sub>N</sub> cross-linked PDMS elastomers and (d) PTFPMS elastomers. The data gap observed in (d) for acetone was due to the camera going out of focus which meant the area could not be accurately measured..... | <b>120</b> |
| Figure 4.5: First 55 % swelling data versus the square root of time for (a) PDMS standard elastomers (b) 40 wt% BaTiO <sub>3</sub> -PDMS elastomers (c) TESP <sub>N</sub> cross-linked elastomers (d) PDMS sponges and (e) PTFPMS elastomers.....  | <b>124</b> |
| Figure 4.6: Comparison of the diffusion rate of solvent vapours into standard PDMS elastomers and 40 wt% BaTiO <sub>3</sub> -PDMS elastomers.....  | <b>129</b> |
| Figure 4.7: Comparison of the diffusion rate of solvent vapours into standard PDMS elastomers and PDMS sponges.....  | <b>130</b> |
| Figure 4.8: Comparison of the diffusion rate of solvent vapours into standard PDMS elastomers and TESP <sub>N</sub> cross-linked PDMS elastomers.....  | <b>132</b> |
| Figure 4.9: Comparison of the diffusion rate of the solvent vapours into the standard PDMS elastomers and PTFPMS elastomers.....   | <b>133</b> |

## **Chapter 5:**

|  |            |
|--|------------|
| Figure 5.0: Displacement feed loop RFID tag antenna design. Dimensions in Table 5.0.....   | <b>139</b> |
| Figure 5.1: (a) Transmitted power ratio versus solvent vapour exposure time, (b) Area swelling ratio, QA versus solvent vapour exposure time and (c) image of a standard PDMS elastomer from left to right after 0 minutes, 30 minutes, 150 minutes and 1440 minutes diethyl ether exposure: top - images taken during absorption rate measurements and bottom - images taken during RFD measurements..... | <b>141</b> |
| Figure 5.2: Comparison of RFID response at 1440 minutes solvent exposure time and PDMS swelling volume ratio (QV).....   | <b>142</b> |

## Chapter 6:

|  |     |
|--|-----|
| Figure 6.0: Stages of droplet formation.....   | 149 |
| Figure 6.1: Surface tension of the Sylgard-xylene inks with varying xylene wt %.....   | 151 |
| Figure 6.2: Schematic of the Dimatix materials printer 2800 series used in this chapter.....   | 152 |
| Figure 6.3: (a) Example of a printing waveform and (b) illustrations of the ink cartridge at different stages of the printing waveform. The arrowheads show the direction of the ink flow.....   | 153 |
| Figure 6.4: Printing of Sylgard (30 wt%)-xylene (70 wt %) ink on glass substrate with a 150 micron drop spacing (a) image taken from middle of the printed square and (b) image taken at the edge of the printed square.....   | 154 |
| Figure 6.5: Printing of 5 wt% sylgard ink onto a glass substrate with a 200 micron drop spacing (a) before and (b) after 60 °C curing.....   | 154 |
| Figure 6.6: Printing of 5 wt% pre-cure Sylgard® 184 ink on glass substrate drop spacing of (a) 100 (b) 50 and (c) 30. Note figure 6.7(b) was after 60 °C curing using a heating mantle.....  | 155 |
| Figure 6.7: Printing of 5 wt % pre-cure Sylgard® 184 ink on glass substrate (a) 2 layers with drop spacing 100 apart and (b) 2 layers with drop spacing 150 apart with platen temperature set at 60 °C.....  | 156 |
| Figure 6.8: Printing of 5 wt% pre-cure Sylgard® 184 ink on glass substrate with a drop space of 40 microns with platen temperature set at 60 °C (a) 5 layers using 1 nozzle and (b) 20 layers using 4 nozzles. Note that these are images of the edge of the printed continuous Sylgard® 184 film, the left hand side in both images (smoother side) is the glass substrate, while the right hand side in both images is of the Sylgard® 184 film..... | 157 |

## Chapter 7:

|   |     |
|---|-----|
| Figure 7.0: Prototype RFID light sensor tag design. Tag designed by M.A. Ziai.....  | 161 |
| Figure 7.1: UV-Visible spectra of (a) light irradiated 40 wt% AgNO <sub>3</sub> -PVA solution (b) non-irradiated 40 wt% AgNO <sub>3</sub> -PVA solution (c) light irradiated 60 wt% AgNO <sub>3</sub> -PVA solution (d) non-irradiated 60 wt% AgNO <sub>3</sub> -PVA solution (e) light irradiated acidified 60 wt% AgNO <sub>3</sub> -PVA and (f) non-irradiated 60 wt% AgNO <sub>3</sub> -PVA solution over time..... | 165 |
| Figure 7.2: Images of (a) 40 wt% AgNO <sub>3</sub> -PVA solutions (b) 60 wt% AgNO <sub>3</sub> -PVA solutions after 142 hours and (c) acidified 60 wt% AgNO <sub>3</sub> -PVA solutions after 144 hours. In each image the solution on the left was non-irradiated and the solution on the right was light treated.....   | 166 |

|   |            |
|---|------------|
| Figure 7.3: Plot of lambda max of 40 wt% and acidified 60 wt% AgNO <sub>3</sub> -PVA solutions versus light exposure time.....  | <b>167</b> |
| Figure 7.4: Mean number particle distribution from DLS measurements of light irradiated (144 hours) acidified 60 wt% AgNO <sub>3</sub> -PVA solution.....   | <b>168</b> |
| Figure 7.5: SEM micrographs of (a) 40 wt% AgNO <sub>3</sub> -PVA solution (b) 60 wt% AgNO <sub>3</sub> solution after 142 hours light irradiation and (c) acidified 60 wt% AgNO <sub>3</sub> -PVA solution after 144 hours light irradiation.....   | <b>169</b> |
| Figure 7.6: FTIR of (a) standard PVA and light irradiated 40 wt % AgNO <sub>3</sub> -PVA composites after (b) 0 hrs (c) 24 hrs (d) 48 hrs (e) 142 hrs and (f) 700.5 hrs light irradiation.....  | <b>171</b> |
| Figure 7.7: FTIR of (a) standard PVA and non-irradiated 40 wt % AgNO <sub>3</sub> -PVA composites after (b) 0 hrs (c) 24 hrs (d) 48 hrs (e) 142 hrs and (f) 700.5 hrs dark exposure.....  | <b>171</b> |
| Figure 7.8: FTIR of (a) standard PVA and light irradiated 60 wt% AgNO <sub>3</sub> -PVA composites after (b) 0 hrs (c) 24 hrs (d) 48 hrs (e) 142 hrs and (f) 700.5 hrs light irradiation.....   | <b>171</b> |
| Figure 7.9: FTIR of (a) standard PVA and non-irradiated 60 wt% AgNO <sub>3</sub> -PVA composites after (b) 0 hrs (c) 24 hrs (d) 48 hrs (e) 142 hrs and (f) 700.5 hrs dark exposure.....   | <b>171</b> |
| Figure 7.10: FTIR of (a) standard PVA and light irradiated acidified 60 wt% AgNO <sub>3</sub> -PVA composites after (b) 0 hrs (c) 23 hrs (d) 47 hrs (e) 96 hrs and (f) 144 hrs light irradiation.....   | <b>171</b> |
| Figure 7.11: FTIR of (a) standard PVA and non- irradiated acidified 60 wt% AgNO <sub>3</sub> -PVA composites after (b) 0 hrs (c) 23 hrs (d) 47 hrs (e) 96 hrs and (f) 144 hrs dark exposure.....  | <b>171</b> |
| Figure 7.12: PVA-Ag <sup>+</sup> chelate structure proposed by Zidan.....   | <b>172</b> |
| Figure 7.13: PVA-Ag <sup>+</sup> chelate structure proposed by Yen et al.....   | <b>172</b> |
| Figure 7.14: Images of 40 wt% AgNO <sub>3</sub> -PVA films after a) 0 hrs light exposure (b) 553 hrs non-irradiated and (c) 553 hrs light exposure. Images of 60 wt% AgNO <sub>3</sub> -PVA films after (d) 0 hrs light exposure (e) 553 hrs non-irradiated and (f) 553 hrs light exposure. Images of acidified 60 wt% AgNO <sub>3</sub> -PVA films after (g) 0 hrs light exposure (h) 144 hrs non-irradiated and (i) 144 hrs light exposure..... | <b>174</b> |
| Figure 7.15: SEM micrographs of 40 wt% AgNO <sub>3</sub> -PVA film after (a) 142 hrs light exposure (b) 142 hrs non-irradiated (c) 700.5 hrs light exposure and (d) 700.5 hrs non-irradiated.....   | <b>175</b> |
| Figure 7.16: SEM micrographs of 60 wt% AgNO <sub>3</sub> -PVA film after (a) 142 hrs light exposure (b) 142 hrs non-irradiated (c) 700.5 hrs light exposure and (d) 700.5 hrs non-irradiated.....   | <b>176</b> |
| Figure 7.17: SEM micrographs of acidified 60 wt% AgNO <sub>3</sub> -PVA film after 144 hrs (a) light exposure (b) non-irradiated.....   | <b>176</b> |

Figure 7.18: Average resistance measurements of the top surface of light irradiated and non-irradiated (a) 40 wt% AgNO<sub>3</sub>-PVA films (b) 60 wt% AgNO<sub>3</sub>-PVA films and (c) acidified 60 wt % AgNO<sub>3</sub>-PVA films. In figure 13 (a) resistance measurements were too high to record from 335 to 505 hours exposure time.....**178**

Figure 7.19: Resistance of the top and bottom surface of a 60 wt% AgNO<sub>3</sub>-PVA film (a) light irradiated and (b) non-irradiated.....**178**

Figure 7.20: Images of 90 wt% AgNO<sub>3</sub>-PVA aluminium test bed after (a) 0 hrs dark exposure (b) 0 hrs light irradiation (c) 144 hrs dark exposure (d) 144 hrs light irradiation. Images of 60 wt% AgNO<sub>3</sub>-PVA aluminium test bed after (e) 144 hrs dark exposure and (f) 144 hrs light irradiation.....**181**

Figure 7.21: Resistance of 90 wt% AgNO<sub>3</sub>-PVA test bed over a period of 165.25 light exposure.....**182**

Figure 7.22: Resistance of both 90 wt% and 60 wt% AgNO<sub>3</sub>-PVA silver test beds. The lack of resistance readings between 5 – 151 and 289 – 391 hours light irradiation time for the 60 wt% test bed was due to 0.L values being measured.....**183**

Figure 7.23: Resistance as a function of light exposure time for 90 wt% AgNO<sub>3</sub>-PVA silver test beds dried before and during heat treatment.....**184**

## Abbreviations

|                    |   |
|--------------------|---|
| Abs.               | absorbance                              |
| AgNO <sub>3</sub>  | silver nitrate                          |
| ASIC               | application specific integrated circuit |
| asym               | asymmetric                              |
| BaTiO <sub>3</sub> | barium titanate                         |
| BSE                | back-scattered electrons                |
| DAK                | dielectric assessment kit               |
| DCM                | dichloromethane or methylene dichloride |
| def                | deformation                             |
| DLS                | dynamic light scattering                |
| DMP                | Dimatix materials printer               |
| EDX                | energy-dispersive x-ray spectroscopy    |
| FTIR               | fourier transform infra-red             |
| g                  | grams                                   |
| HNO <sub>3</sub>   | nitric acid                             |
| IC                 | integrated circuit                      |
| M. W.              | molecular weight                        |
| PDI                | polydispersity index                    |
| PDMS               | polydimethylsiloxane                    |
| PTFE               | polytetrafluoroethylene                 |
| PTFPMS             | polytrifluoropropylmethylsiloxane       |
| PVA                | polyvinyl alcohol                       |
| Q <sub>A</sub>     | area swelling ratio                     |
| Q <sub>V</sub>     | volume swelling ratio                   |
| Q <sub>W</sub>     | weight swelling ratio                   |
| rock               | rocking                                 |

|            |   |
|------------|---|
| SEM        | scanning electron microscope                        |
| str        | stretching  |
| sym        | symmetric   |
| $T_g$      | glass transition temperature                        |
| TEOS       | tetraethyl orthosilicate                            |
| TESPN      | 2-cyanotriethoxysilane                              |
| THF        | tetrahydrofuran                                     |
| UHF RFID   | ultra-high frequency radio frequency identification |
| UV-visible | ultraviolet-visible spectroscopy                    |
| wt %       | weight percentage                                   |
| XRD        | x-ray diffraction                                   |



# Chapter 1: Introduction

## 1.0 Introduction to Radio

Radio frequency identification (RFID) is a technology which uses radio waves to identify items or people.<sup>1</sup> A RFID system has three main components: a RFID tag (also called a transponder), a RFID reader and a controller (which is often a P.C.). At its most basic a RFID system operates in the following way: a RFID tag is placed onto the object you want to identify and when the RFID tag is interrogated by a RFID reader it transmits back identifying information which in turn is processed by the controller (Figure 1.0).

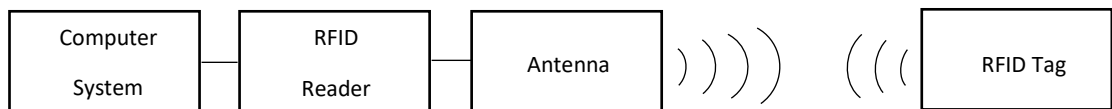


Figure 1.0: Basic operation of radio frequency identification (RFID).

RFID systems can be classified as automatic identification (auto-ID) systems where an identifier is attached to an object that can automatically read. There are many different kinds of RFID systems: they can vary in power source, operating frequencies and functionalities. The characteristics of a RFID system (i.e. power source etc.) are determined by its application and the characteristics of the RFID system and regulatory restrictions will in turn determine the RFID systems cost, physical size and performance. A brief history of RFID will be presented along with the major applications of RFID technology used today followed by a detailed discussion of RFID tags.

### 1.0.1 Origins of RFID

The origins of RFID are found in the 19<sup>th</sup> century when progress into understanding electromagnetic energy was achieved. Most notably, Faraday's discovery of electromagnetic inductance, Maxwell's equations which described the behaviour of the interaction between a magnetic and electric field and Hertz who applied Maxwell's theory of electromagnetism to produce radio waves laid the way to RFID technology.<sup>2</sup> In the early 20<sup>th</sup> century the use of radio waves in detection systems had been realised – RADAR developed by Watson-Watt being the most well-known. During World War II, radar was being used by both sides to warn of approaching aircrafts however as it is only a detection system it could not be used to differentiate between enemy and allied planes. To solve this problem the British developed the Identity Friend or Foe (IFF) system where they placed transponders onto their own and allied aircrafts which could respond to a radio signal transmitted from base stations.<sup>3</sup> For many the IFF system is considered the first use of RFID.

A few years after the war in 1948, Stockman, an engineer introduced the idea of passive RFID systems in his paper *Communication by Means of Reflected Power*. However, it was almost 30 years later after developments into integrated circuits, microprocessors and transistors when Stockman's vision would begin to reach fruition. During the 1950s and 1960s research into RFID technology continued. Most notably the 1950s saw the development of long range IFF transponders and the 1960s saw the first commercial use of RFID technology in electronic article surveillance (EAS) - an anti-theft system. RFID based EAS uses 1-bit passive tags which are either on or off. When the passive tag is on, it will be detected by the RFID readers placed at the exit of shops and sound an alarm. When the tag is turned off or removed (item has been paid for) no radio signal is detected and therefore no alarm is sounded. These systems are still in use today. There was an explosion of RFID development in the 1970s with inventors, companies, academic institutions and government bodies all actively working on RFID systems for an array of applications. A select few have been described here. In 1973, Cardullo received the first patent for a passive RFID tag with rewritable memory.<sup>4</sup> In the same year Walton received a patent for a passive transponder that could unlock a door without a key. When the RFID reader near or on the door interrogated the passive transponder and received valid identification data the door would be unlocked. At the request of the U.S. Department of Agriculture scientists at Los Alamos Scientific Laboratory (University of California) developed a passive identification system for livestock which reported both the cattle's identity and temperature.<sup>5</sup> The tag in this system used modulated backscatter to communicate information to the RFID reader. This research formed the foundation of passive UHF RFID tags today which utilise modulated backscatter. In 1977 Sterzer of RCA (Radio Corporation of America) developed an 'electronic license plate for motor vehicles' for the following purposes: electronic identification of vehicles for traffic control, anti-theft protections and automatic toll billing.

The 1980s saw RFID technology being implemented in various applications but most notably in electronic toll collection systems. By the 1990s and early 21<sup>st</sup> century RFID technology had become widespread and was a part of everyday life. Current applications of RFID technology are briefly discussed in the next section. It was also during this period that industrial standards and government regulations concerning both the power and frequency used in RFID systems were formed.

### 1.0.2 Current Applications of RFID technology

At present RFID technology is being used in a variety of applications including logistics, healthcare, animal tracking and human identification. A non-exhaustive list of current applications of RFID is shown in Figure 1.1.

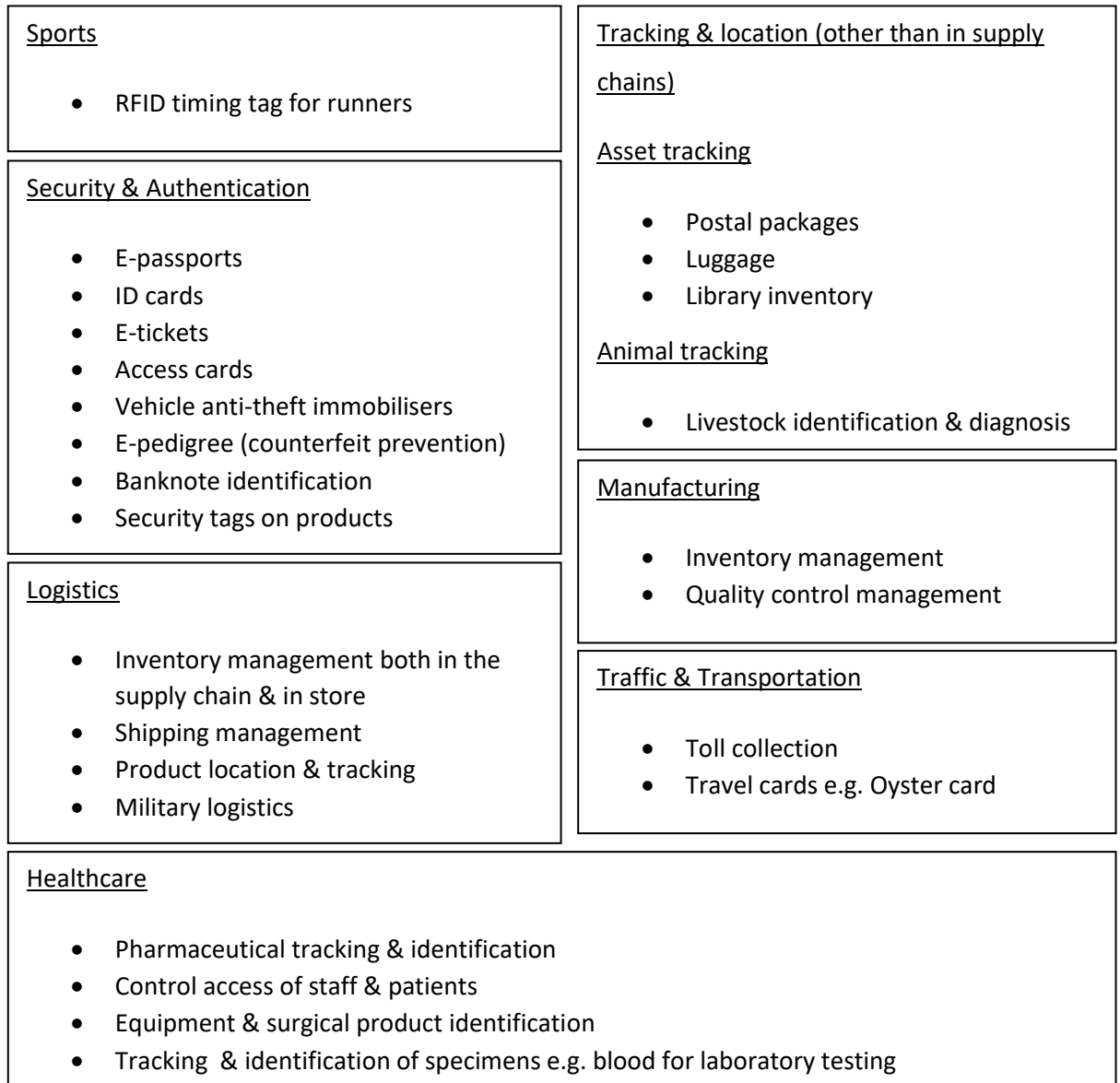


Figure 1.1: Current applications of RFID technology.

As the use of RFID technology is so widespread only a select few applications will be further discussed. One of the most famous applications of RFID is in supply chain management. In 2003 Wal-Mart famously announced that their top 100 suppliers would be required to use RFID tags on cases and pallets of inventory shipped to its Texas distribution centres by January 2005.<sup>6</sup> Other major retailers, such as Tesco and METRO have also implemented RFID in their supply chains. Though in addition to RFID in their supply chains METRO is currently experimenting with item-level RFID in store for smart shelving.<sup>7</sup> Smart shelving indicates to the store personnel when the shelf needs to be replenished. Currently in the Metro Future Store 4 products use item-level RFID (Procter & Gamble Pantene shampoo, Kraft Philadelphia cream cheese, Gillette Mach3 razors and DVD's). This store also contains RFID gates between the inbound landing dock and the store backroom as well as between the store backroom and sales floor allowing for complete tracking of all RFID-tagged merchandise. Several

shipping services such as UPS, DHL and FedEx have utilised RFID tagging in their postal tracking systems.<sup>8</sup> Along with retailers and shipping services, airports and airlines have also begun to replace their bar code tags with RFID tags.<sup>9</sup>

In 2008 Hong Kong International airport became one of the first airports to utilise RFID baggage tags and in the last month Delta airlines announced they will be using RFID for baggage tracking. Delta airlines have installed RFID readers at the belt loaders which will interrogate each bag's RFID tag before the bag is loaded onto the plane. The reader will flash green if the bag is being loaded onto the correct aircraft and go red if the bag is being loaded onto the wrong aircraft. As well as RFID being used in the supply chain, many manufacturers have implemented RFID into their assembly lines as a means to identify the product being assembled along with any parts that need to be fitted to that product. This means that during assembly an instant check can be performed to either verify which parts need to be fitted or to ensure the correct parts have been fitted (quality control). This type of system has been utilised by Ford – the car manufacturer.<sup>10</sup>

Security and authentication is another major application of RFID. RFID tags have been embedded in many ID cards such as student ID cards and e-passports. E-passports are currently issued by 74 countries around the world and contain biometric information of the holder so it can be used to validate the holder's identity. The UK and USA are also incorporating RFID tags into visas to prevent forgeries. RFID tag cards are also used by many different organisations in access control<sup>11</sup> as well as ID. The RFID readers are positioned at building entrances and internal doors and only authorized personnel can gain access. The advantage of RFID tag cards is that they can be programmed to only grant access to certain areas. RFID tags have been embedded in several products such as pharmaceuticals and banknotes to aid in authentication and counterfeit prevention. This is achieved via (i) the presence of a RFID tag, (ii) the specific details encoded onto the RFID tag and (iii) chain of custody i.e. the record of different tag reads throughout the chain supply which will be saved on a supply chain computer system. The RFID chain of custody of a product is also known as an e-pedigree of a product. With the e-pedigree of a product the progress of the product from manufacturer to customer can be determined ensuring the validity of the product.

## 1.1 RFID Tags

The main components of a RFID tag (also called a transponder) are an integrated circuit, an antenna and a substrate. In some cases extra components such as, power sources (in the case of active tags) and sensors are also a part of a RFID tag. The basic function of a RFID tag is to store and transmit data to the RFID reader. The IC is responsible for storing data, processing data and modulating and demodulating received radio signals. The antenna is responsible for receiving transmitting radio

signals. The substrate offers support and protection to the other tag components. RFID tags can be classified based on four main criteria: power source, type of memory, computational power and functionality.<sup>12</sup> However, RFID tags are mostly classified on their power source and can be categorised as either active, semi-passive or passive.

### 1.1.1 Active & Passive Tags

Active RFID tags have an internal power source which is used to power the IC and transmit data to a RFID reader. In most cases the power source is in the form of a battery.<sup>13</sup> There are two types of active tags: beacons and transponders. Beacon type tags transmit a radio signal at pre-set intervals, whereas transponder type tags only transmit a signal once activated by a RFID reader. Major advantages of active tags are their large read range and identification capability. Read ranges of active tags can reach up to 100 meters. The internal power source also allows for greater memory storage up to 128 Kbytes compared to 16 of 64 Kbytes of memory in passive tags<sup>14</sup> and means sensors and GPS can be integrated into the active tag. The disadvantages of active tags are their large size, high cost and poor lifetime. Tag cost and size increases as a result of the power source and additional components such as sensors. The operational life of an active tag is restricted by the lifetime of the power source which in most cases is 2 – 7 years.

Passive RFID tags do not have an internal power source. The IC is powered by the radio signal transmitted from a RFID reader. In passive tags data transfer between the RFID reader and tag is achieved by either inductive coupling or backscatter (these two communication methods are discussed in more detail later). Advantages of passive tags are their small size, low cost and potentially infinite lifetimes. Disadvantages include small read ranges and less memory when compared to active tags.

Semi-passive (also called semi-active) RFID tags have an internal power source which is used to power the IC. Semi-passive tags, like passive tags, utilise either inductive coupling or backscatter to transmit data to a RFID reader. In some cases these tags will be 'asleep' until activated by a radio signal transmitted from a RFID reader. The read range of semi-passive tags are larger than passive tags as all the received energy is used to transmit the data back to the RFID reader. In the case of passive tags a portion of the received energy is required to power the IC. However, due to their power source component semi-passive tags tend to be larger in size and cost more than passive tags.

### 1.1.2 Frequencies

As RFID systems communicate via radio waves they are classified and regulated as radio systems. To avoid signal interference with other radio systems, all radio systems are allocated narrow frequency bands within the frequency range 300 GHz to 3 KHz. The three main frequency ranges in which RFID systems operate in are: low frequency (LF) 30 – 300 KHz, high frequency (HF) 3 – 30 MHz and ultra-high

frequency (UHF) 300 MHz – 3 GHz. More specifically, LF RFID systems operate between 125 – 134.2 KHz, HF systems at 13.56 MHz and UHF systems at either 433 MHz or between 865 – 928 MHz. Frequencies for RFID are subject to regulations and can differ between different geographies. For example, the UHF frequency range for passive tags in Europe is 865.6 – 867.6 MHz whereas the UHF frequency range used in the United States is 902 – 928 MHz. Active tags only operate at UHF (mainly at 433 MHz), while passive tags can be designed to operate at all three frequency ranges. There are advantages and disadvantages associated with each frequency. UHF tags have longer read ranges and faster data transfer rates. An additional advantage of UHF tags is their small size – high frequencies have short wavelengths which means they can operate with small antennas. The main disadvantage of UHF tags is that their performance can be affected by their environment, surrounding conductive metals reflect any radio waves altering the electromagnetic field and water absorbs any radio waves reducing the amount of energy available for the tag to operate. LF tags have the smallest read range and slow data transfer but the long wavelengths can penetrate liquids, live tissue and objects resulting in these tags not being as effected by their surrounding environment. HF tags have a read range between LF and UHF tags and are effected by metal surroundings but not water.

### 1.1.3 Communication method of passive tags

As previously mentioned passive tags use either inductive coupling or backscatter to communicate and transfer data to a RFID reader. Inductive coupling is a near field effect and used by LF and HF tags and backscatter is a far field effect and used by UHF passive tags.

#### 1.1.3.1 Inductive Coupling

Inductive coupling occurs between two wire coils that have the property of mutual inductance. Mutual inductance is when two or more coils are magnetically linked and a change in current flow in one coil will induce a voltage in the others. Tags that use inductive coupling have wire coils as antennas. The magnetic field generated by the RFID reader coil antenna induces a voltage in the tags coil antenna which is used to power the IC. Transfer of data from the tag to the RFID reader is performed by load modulation. The IC varies the load on the tag antenna in accordance with the data to be transmitted, by switching a load resistor on and off. The resistor switching causes the current in the tag coil to vary resulting in fluctuations in the magnetic field. The fluctuations in the magnetic field are detected by the RFID reader as variation in voltage in the reader coil antenna.

#### 1.1.3.2 Backscatter

Backscatter uses the radio signal rather than the magnetic field to communicate and transfer data to the RFID reader. Tags that use backscatter reflect back the radio signal emitted by the RFID reader. The IC is powered by the received radio waves and transfer of data is performed by the IC varying its

input impedance between two different states. The radar cross section of the tag i.e. measure of the tags ability to reflect radar signals in the direction of the RFID reader differs for the two impedance states. Therefore when the IC varies its input impedance, the radio signal reflected back is modulated – this is why the reflected radio waves are called modulated backscatter.

#### 1.1.4 Standards

RFID standards provide specifications about the frequencies at which RFID systems operate, the method of communication, data transfer and applications. International organisations that provide RFID standards include EPCglobal and the joint committee set up between the International Standards Organisation (ISO) and the International Electrotechnical Commission (IEC). A few of the standards for RFID are described here. The standards for contactless smart cards (at 13.56 MHz) are ISO/IEC 10536, 14443 and 15693. The standards for animal identification (at 132.4 KHz) are ISO/IEC 1178-x and 14223-x. The standard ISO/IEC 18000-6 part c / EPC class 1 generation 2 describe both air interface and data protocols of UHF RFID systems used in item management. Air interface protocols include rules for encoding, modulation and reading and writing to a tag. Data protocols specify tag data formatting, size and structure of the tag memory and the way information is stored, accessed and transferred.

#### 1.1.5 Tag Antenna

An antenna can be defined as ‘that part of a transmitting or receiving system that is designed to radiate or to receive electromagnetic waves’. In the case of passive RFID tags the antenna also acts as an energy transformer and impedance matching between the antenna and IC is extremely important for maximum power transfer. It is the tags application that defines the antenna specifications. The tags application determines the read range, surrounding environment, size and cost of the RFID tag. These properties in turn define the type of RFID tag chosen i.e. active or passive LF, HF or UHF. LF and HF tags use inductive coupling as their communication method and mostly utilise loop antennas (Figure 1.2 (a) & (b)). The type of antennas used for UHF RFID tags include microstrip patch, wire or microstrip dipole and slot antennas (Figure 1.2 (c-f)).

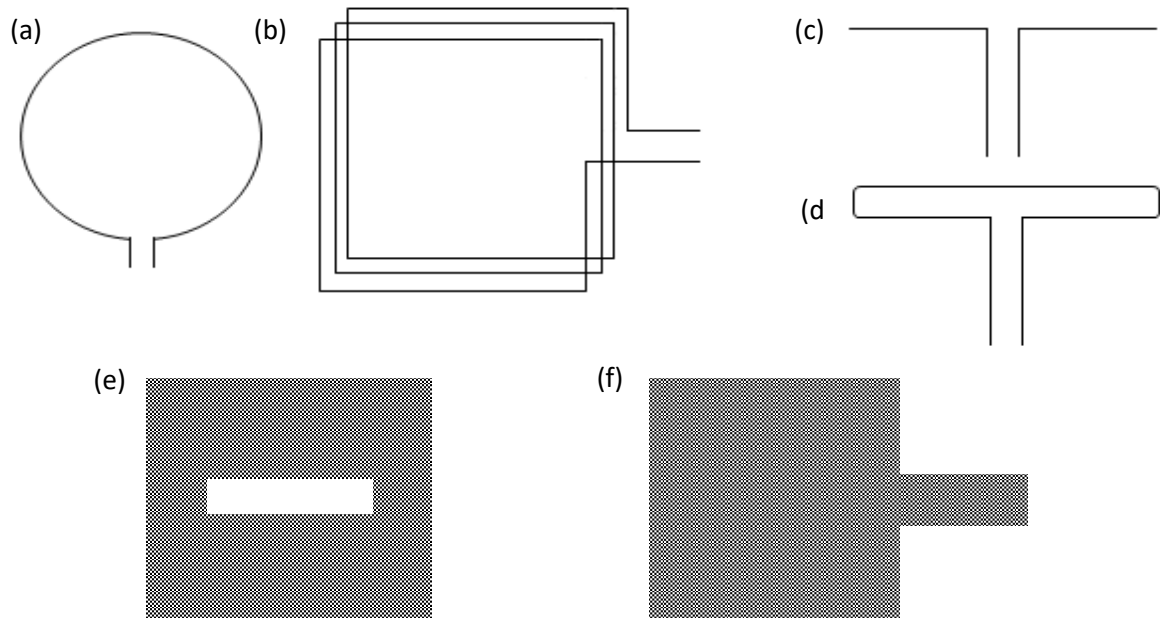


Figure 1.2: (a) circular loop antenna (b) square loop antenna with several turns (c) wire dipole antenna (d) wire folded dipole antenna (e) slot antenna and (f) microstrip patch antenna.

### 1.1.6 Tag substrate

In some cases the tag substrate is simply to act as the support structure for the other components of the tag and used for protection measures. However, substrates can play a vital role in the development of RFID tags for various applications. For example, there has been much interest in developing flexible electronic substrates. Also along with the tag antennas geometry, the physical properties of the substrate have an effect on both the impedance and reflectivity of a passive UHF RFID tag antenna meaning that the type of tag substrate used could have an effect on the tags performance and size. Babar *et al.* found that a high permittivity low dielectric loss substrate allowed for a smaller tag antenna and resulted in an increased read range.<sup>15</sup>

## 1.2 RFID sensor tags

In recent years the use of RFID technology has become widespread and is most notably used in access control and manufacturer tagging. So far many of the RFID tags available only store and transmit static data, however, there has been much interest in RFID tags with sensing capabilities.<sup>16</sup> The ability to both track the position of the tag and gain information of the tags environment such as temperature, pressure and humidity has many possibilities. For example a RFID sensor tag attached to perishable goods could record the temperature during transit. The recipients of the goods can read this information to determine if the perishable goods are still fresh and fit for consumption. There are already several commercial RFID sensor tags on the market – only a select few are discussed here. The CAEN RFID easy2log® A927Z is a semi passive UHF sensor tag which monitors temperature. It is mainly used for monitoring perishable foods and temperature sensitive pharmaceuticals during storage and



transportation. The Savi ST-673 and ST-674 are active sensor tags which monitor temperature and humidity. Acceptable temperature and humidity ranges are set and if the recorded temperatures and humidity values are out of the set ranges an alarm is sent via the internet, phone or email. These Savi tags are used in both military and commercial shipments. The G2 microsystems G2C501 is an UHF active tag which can be combined with a number of different sensors including temperature, shock pressure, motion, light and radiation which makes it extremely versatile. It was found that many of the commercially available RFID sensor tags were either active or semi-passive.

The main competitive technologies of RFID sensor tags are data loggers, indicators and wireless sensor networks (WSNs).<sup>16</sup> The advantages of RFID sensor tags is that the RFID infrastructure is already in place. Many companies already use RFID tags for tagging and as RFID is standardised compatible hardware is available. Data loggers are an electronic devices that records data over time. They are equipped with a microprocessor, memory and sensors and can either be used as a stand-alone device i.e. they can process the collected data or they can interface with a computer. A flight data recorder is an example of a data logger. The advantages of data loggers is that they can collect data continuously, however due to the presence of microprocessors and large memory storage, data loggers can be quite expensive and large in size. Indicators do not store or transmit any data, they display a visual change in response to a stimulus. For example optical CO<sub>2</sub> indicators which utilise a CO<sub>2</sub>-sensitive material that changes colour in response to CO<sub>2</sub> exposure have been demonstrated.<sup>17</sup> Though indicators can only be used to sense one environment they are often inexpensive, are easily analysed by untrained individuals and do not require extra electronic infrastructure for data reading or analysis.

Wireless sensor networks (WSNs) consist of several sensor nodes. Each node consists of a sensor, microcontroller, a transceiver and a power source. The nodes communicate with one another and form an ad-hoc network to send their data back to a monitoring station.<sup>18</sup> As the power source of the nodes cannot be replaced, power consumption in the designed WSN is an important factor. WSNs are able to monitor stimuli in a number of specific places within a large area with only one monitoring station. One of the most notable applications of a WSN is the monitoring of the Leach's storm petrel habitat on Great Duck Island.<sup>19</sup> Recently, there has been an interest in integrating RFID into WSNs to extend the operating area of RFID.<sup>20</sup>

There are two different approaches in designing RFID sensor tags.<sup>21</sup> One method is to design a tag whose analog response i.e. read range, resonance frequency or backscattered power varies as a response to stimuli such as temperature<sup>22</sup>, strain and humidity. These sensor tags utilise external sensor components i.e. stimuli responsive materials. More often than not these tags work on the principle that the sensing material's electrical properties vary as a response to the stimuli being

measured. The change in the electrical properties in turn causes impedance mismatching between the antenna and chip, resulting in the tags analog response to vary. A disadvantage of these type of tags is that it can be difficult to be sure that the variation in the tags analog response is due to the stimuli rather than other factors such as electrical interference and some stimuli-responsive materials can be expensive. The other approach in designing RFID sensor tags is to integrate different working sensors such as light, temperature and moisture<sup>23</sup> sensors into a RFID tag. In the past these sensor tags were often expensive and large in size due to the fact that additional components such as an on board power source and microcontroller were required. However, there has been a move to integrate passive sensors into the RFID IC chip<sup>24</sup> which removes the need of an on board power source. RFID sensor tags are classified according to their power source, operational frequency and function.

### 1.2.1 Sensor components in passive RFID sensor tags

#### 1.2.1.1 Temperature sensor tags

In temperature sensor tags researchers have used water<sup>22</sup>, nano conductive inks<sup>25</sup> and shape memory polymers<sup>26</sup> as the sensor components. Virtanen *et al.* demonstrated a tag design which relied on the fact that water's relative permittivity is a function of temperature. A water pocket – consisting of distilled water encased in a plastic container – was placed onto the impedance matching network part of the tag. As temperature varies, the permittivity of the water varies which has an effect on the impedance matching between the antenna and chip. Impedance mismatching results in a change of the measured power transmitted to the tag along with a change in resonance frequency. The authors found a linear relationship between ambient temperature and frequency point of lowest power on tag. Gao *et al.* presented a temperature sensor tag with a printed silver ink on-off switch.<sup>25</sup> At a certain temperature, sintering of the silver ink would occur resulting in a drop in resistance of the printed silver switch. The change in resistance of the switch resulted in the tag to be essentially unreadable. Bhattacharyya *et al.* utilised both the phase difference of a polymer below and above its glass transition temperature ( $T_g$ ) and that RFID tags performance degrades near metal in their tag design.<sup>26</sup> The tag consists of two RFID tags separated by 25 mm in distance. Underneath these two tags is a metal plate attached to crosslinked *t*BA-co-PEGDMA (*tert*-butyl acrylate co poly(ethylene glycol) dimethacrylate). The metal plate is positioned under one of the tags as a starting point. When the ambient temperature increases above the  $T_g$  of *t*BA-co-PEGDMA, the polymer becomes soft and rubbery and acts as an actuator causing the metal plate to move from its starting position to underneath the other RFID tag. The RFID response is measured as the difference between the tag performance of each tag as the tag with the metal plate underneath it will have a lowered performance when compared to the metal free tag. The advantage of this threshold sensor design is that because the  $T_g$  of the polymer can be altered a range of sensors that trigger at different temperatures can be formulated.

### 1.2.1.2 Humidity sensor tags

In humidity sensor tags polyimide films,<sup>27,28</sup> moisture absorbing materials<sup>29</sup> and PEDOT: PSS (poly(3, 4-ethylenedioxythiophene): poly(styrenesulfonic acid))<sup>30</sup> have been used as the stimuli-responsive materials. Both Chang *et al.* and Virtanen *et al.* used polyimide films whose relative permittivity is dependent on moisture. While Virtanen *et al.* used a commercially available polyimide film – Kapton HN, Chang *et al.* synthesised an aromatic polyimide film from oxydianiline (ODA) and *m*-pyromellitic dianhydride (PMDA). Though both researches used the same sensing component the tag designs differed greatly. Manzari *et al.* utilised the conducting polymer PEDOT: PSS whose conductivity varies with humidity. The authors demonstrated an H shaped slot antenna in which the PDOT: PSS could be deposited within the slot. It was found that as the relative humidity increased the required turn on power for the tag increased as a result of the increased PDOT: PSS conductivity. The authors also showed that different RFID responses for the same relative humidity could be gained by depositing the PDOT: PSS in certain patterns within the H shaped slot. In complete contrast Siden *et al.* presented a method to turn ordinary RFID tags into humidity sensor tags by embedding them in layers of blotting paper. Blotting paper is highly absorbent and in high humidity environments a large amount of water vapour is absorbed by the blotting paper. The RFID tags proximity to the water laden blotting paper results in a degradation of tag performance (more specifically detuning of the tag antenna occurs). The sensor tag set up consisted of two tags in which only one was embedded in layers of blotting paper and the transmitted power difference between the two tags was recorded with increasing relative humidity. It was found the transmitted power difference increased with relative humidity. The authors also investigated the effect of the thickness of blotting paper used and where the blotting paper was placed i.e. only in front of the tag or in front and behind.

### 1.2.1.3 Chemical sensor tags

Polymer composites, and Nafion polymers have found great success as sensing components in RFID chemical sensor tags. Potyrailo and Morris adapted conventional RFID tags for vapour sensing by coating them in a thin layer of Nafion – a copolymer of tetrafluoroethylene and sulfonyl fluoride vinyl ether.<sup>31</sup> The ionic conductivity of Nafion varies with the absorption of polar vapours. The change in the conductivity of Nafion as a response to polar vapours effects the impedance of the antenna resulting in impedance mismatching between the antenna and chip. Fiddes and Yan demonstrated an array of passive volatile chemical sensor tags which utilised carbon black polymer composites as the sensing element.<sup>32</sup> When exposed to volatile vapours the carbon black polymer composites swelled causing the distance between the carbon black particles to increase resulting in the composites conductivity to change. The conductivity change resulted in the RFID tags output frequency to change.

Each tag within the array had a different polymer, therefore producing a unique pattern of signals for each vapour.

#### 1.2.1.4 Strain sensor tags

In the majority of passive strain sensor tag designs found in literature the RFID antenna itself was utilised as the sensing component. Occhiuzzi *et al.* proposed a passive strain sensor design based on a meander-line antenna (MLA).<sup>33</sup> A copper wire MLA with one turn either side of a tuning T-match section was used. When vertical stress is applied the MLA elongates which results in a change in the antenna's input impedance and radiation performance. A RFID folded patch design was demonstrated by Yi *et al.*<sup>34</sup> The patch antenna was fabricated using copper cladding and along with the IC chip was mounted onto a PTFE substrate. The back of the tag was also clad with copper which acted as the electronic ground plane. When the tag is placed on a specimen experiencing strain, the strain transfers to the copper antenna deforming it resulting in a shift in the tag's resonant frequency. The authors found a linear relationship between strain and normalised frequency change. Bhattacharyya *et al.* demonstrated a displacement strain sensor tag which utilises the known RFID performance degradation effects of metal.<sup>35</sup> The sensor system is composed of a conventional RFID tag and a metal backplane which is attached to the specimen being monitored so that any strain experienced will cause the distance between the backplane and tag to decrease. The RFID tag's performance decreases as the metal backplane moves closer to the tag. In contrast Merilampi *et al.* presented a wearable strain sensor design where the tag antenna was screen printed using a conductive polymer thick film (PTF) ink.<sup>36</sup> Two different antenna designs were investigated on two different stretchable substrates – polyvinyl chloride (PVC) and fabric. The conductivity of the antenna (PTF ink) decreased with increasing strain resulting in a change in the tag's backscattered signal power.

#### 1.2.1.5 Light sensor tags

The majority of passive light sensor tags demonstrated in literature have light sensors integrated into the IC chip rather than using an external light sensitive component.<sup>24</sup> However, Amin *et al.* presented a light sensor design where an off the shelf photoresistor was integrated into a multiresonator RFID tag.<sup>37</sup> With light exposure, the resistance of the photoresistor varies causing an impedance change in the resonator it is integrated into. As the resonator impedance varies so does the resonant frequency.

### 1.3 Stimuli-responsive polymers

Stimuli-responsive polymers or 'smart' polymers are polymers which respond with property changes to changes in their environment. It has been shown that stimuli-responsive polymers have been used to great success as the sensing components in passive RFID sensor tags.<sup>26-28,30-32</sup> As well as being utilised in sensors, stimuli-responsive polymer materials have found uses in numerous applications including

drug delivery<sup>38</sup>, tissue engineering, coatings, diagnostics and microelectromechanical systems.<sup>39</sup> They can be classified according to the stimuli they respond to: temperature, pH, light, chemical agents, mechanical deformation, biological agents, electric fields or magnetic fields.<sup>40</sup> It should be noted some stimuli-responsive polymers respond to multiple stimuli.<sup>40</sup> Another method to classify stimuli-responsive polymers is according to their physical form: chains in solutions, chains grafted onto surfaces or cross-linked polymer chains. The response of stimuli-responsive polymers to stimuli can be a change in permeability, shape, conductivity, solubility and hydrophobicity/hydrophilicity of the polymer. In some cases several responses will be observed at the same time for one stimuli. Both the type of stimuli the polymer responds to and the way in which the polymer responds determines the applications of a stimuli-responsive polymer. Polymers have the advantage that they can be easily modified, thus resulting in a lot of research designing polymers to respond in specific ways to specific stimuli. In the case of designing UHF-RFID sensor tags, stimuli-responsive polymers whose electrical properties vary in response to stimuli are often used.<sup>27-28,30-32</sup> This is due to the fact that the performance of UHF-RFID tags are susceptible to electrical variances. For optimum UHF-RFID tag performance the tags antenna impedance must conjugately match the impedance of the IC. To ensure this matching, the tag antenna and other tag components such as the substrate or sensing material are designed with specific electrical properties. If at any point the electrical properties of the antenna varies as a direct result of stimuli or indirectly through variances in electrical properties of components attached to the antenna, impedance mismatching and antenna detuning occurs. Impedance mismatching results in the tags read range to vary and antenna detuning results in the resonant frequency of the tag to vary. Tag antenna and IC chip impedance mismatching and antenna detuning as a response to stimuli is the basis of all passive sensor UHF-RFID tag designs which use sensing components. It is the method in which mismatching and detuning is caused that separates the different sensor tag designs from one another and determines the type of stimuli-responsive polymer required. In some cases it is the design of the tag that inspires the choice of stimuli-responsive polymer, where as in others the type of response shown by a stimuli-responsive polymer inspires the tag design. In this thesis three different passive UHF-RFID sensor tags which utilise stimuli-responsive polymers as sensing components are presented: an epidermal strain sensor, a solvent vapour sensor and a light sensor. In the case of the strain sensor and light sensor the tag designs dictated the choice of the stimuli-responsive polymers investigated for use. In contrast, the solvent vapour sensor tag was designed in reaction to the response of a polymer to solvent vapours.

## 1.4 Epidermal UHF-RFID strain sensor tag

One of the aims of the research in this thesis is to develop a prototype passive strain sensor tag using a stretchable slot antenna design proposed by Rakibet. The sensor proposed by Rakibet operates using

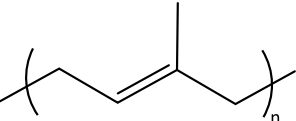
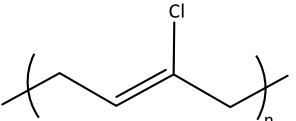
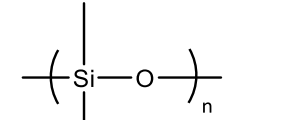
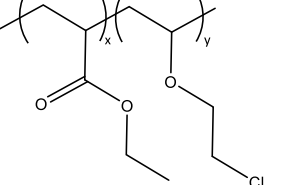
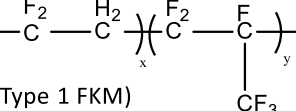
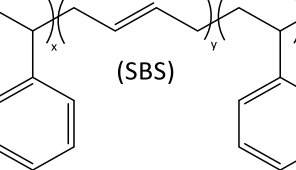
the principle of detuning slots – as the slot dimensions change with antenna stretching, the resonant frequency of the tag varies. Simulations highlighted that there was a linear relationship between stretch percentage and resonant frequency and the design could decipher between y and x directional strain. This stretchable slot antenna design shows promise in assisted living applications to allow paraplegic patients to control their wheelchair through facial muscle tweaking. For this design to operate experimentally, a stretchable elastic dielectric substrate was required. Designing RFID tags to be mounted onto the body is challenging as tag mismatching often occurs due to the high permittivity of skin. Though the use of a dielectric substrate can diminish the effect of the skin's high permittivity resulting in the tag retaining its performance even when mounted onto the body. In addition to being a dielectric the substrate also has to be stretchable to ensure strain transfer from the skin to the antenna occurs and elastic to ensure repeatability. Elastomeric materials present themselves to be superb candidates for the substrate required. They have many useful properties, though for this case the two most important being their elasticity and resilience. Elastomers have the ability to be deformed by either stretching, compression or torsion and return to their original shape once the force causing the deformation is removed (elasticity), while their resilience allows them to return to their original shape quickly.

## 1.5 Elastomeric materials

An elastomer can be defined as a polymeric material which when deformed reverts back to its original dimensions once the load responsible for the deformation is removed. For a polymer to exhibit elastomeric properties it must have the following three structural requirements: the polymer (i) must be above its glass transition temperature ( $T_g$ ) (ii) have a low degree of crystallinity and (iii) should be lightly cross-linked.<sup>41</sup> Elastomers can be divided into two categories: physically cross-linked or chemically cross-linked. Physical cross-links are not permanent and are either formed via hydrogen bonds, ionic bonds or polymer domains. Chemical cross-links are permanent and are formed through covalent bonding between the polymer and multifunctional molecules. Chemically cross-linked elastomers are referred to as thermoset elastomers, while physically cross-linked elastomers are referred to as thermoplastic elastomers. General properties of all elastomers include their rubber elasticity, low permeability and physical swelling in response to liquids and vapours. Thermoplastic elastomers have many of the same physical properties of thermoset elastomers, however, they can be processed like thermoplastic polymers i.e. when heated they can be remoulded. Natural rubber or vulcanised natural rubber (cis-polyisoprene) is the original elastomer, it is classified as a thermoset elastomer and is formed through the vulcanisation (cross-linking) of natural rubber latex with sulphur. Natural rubber latex is mainly sourced from the tree species *Hevea Brasiliensis* and was brought to the attention of Europe in 1493 by Columbus after he had witnessed the indigenous people of the Americas

using it in waterproof clothing and as bouncy balls. Unfortunately in colder climates natural rubber latex became brittle which limited its applications, though in 1770 Priestly discovered it could be used to rub out pencil marks and gave it the name rubber. It wasn't until 1839 that natural rubber was formed; Goodyear had mixed rubber (natural rubber latex) and sulfur together and accidentally spilled it onto a hot stove resulting in a cross-linked product that did not go brittle when cold or melt at high temperatures. Over the years a large range of different elastomers with widely varying properties have been developed. Acrylic (alkyl acrylate copolymer), butadiene, butyl (isobutylene-isoprene copolymer), bromobutyl, chlorobutyl, chlorinated polyethylene fluorocarbon, isoprene (synthetic cis-polyisoprene), chloroprene, silicone and nitrile rubbers are examples of thermoset elastomers. Styrenic block copolymers, thermoplastic polyurethanes and copolyether ester elastomers are examples of thermoplastic elastomers. The properties and applications of a select few elastomers are shown in Table 1.0. It should be noted that the basic properties of the different elastomers can be substantially modified by compounding. Compounding is when additional ingredients are added to the elastomer ingredients resulting in a compounded elastomer. Most commercially available elastomers are compounded, for example, a typical compounded Neoprene elastomers only contains about 30 – 50 % Neoprene by weight. Compounding ingredients have various roles including: accelerating the cross-linking reaction, improve processability and improve the elastomers properties. Examples of compounding ingredients include polymers (to form polymer blends), fillers (both reinforcing & non-reinforcing), accelerators, pigments and plasticisers. The specific properties of any elastomer depends on their polymer base chemical composition and structure, cross-linking, degree of cross-linking and any additional compounding ingredients.

Table 1.0: General properties and applications of a few select elastomers

| Elastomer            | Structure  | General Properties  | Applications  |
|----------------------|--|---|---|
| <b>Thermoset</b>     | <p>Natural Rubber (NR)</p>   | <ul style="list-style-type: none"> <li>• High resilience &amp; tensile strength</li> <li>• Good abrasion resistance</li> <li>• Good electrical resistance</li> <li>• Poor oil resistance</li> <li>• Low cost</li> </ul> | <ul style="list-style-type: none"> <li>• Large vehicle &amp; aircraft tyres</li> <li>• Waterproof clothing (Macintosh coats)</li> <li>• Protective gloves</li> </ul>  |
|                      | <p>Chloroprene Rubber (CR)<br/>(trade name Neoprene)</p>   | <ul style="list-style-type: none"> <li>• Good weather &amp; ozone resistance</li> <li>• Moderate oil resistance</li> <li>• Limited heat resistance</li> <li>• Low cost</li> </ul>                                       | <ul style="list-style-type: none"> <li>• General purpose seals</li> <li>• Seals in the refrigeration industry</li> <li>• Coatings</li> <li>• Wetsuit fabric</li> </ul>  |
|                      | <p>Silicone Rubber (SR)</p>    | <ul style="list-style-type: none"> <li>• Low tensile strength</li> <li>• Biocompatible</li> <li>• Good water resistance</li> <li>• Poor oil resistance</li> <li>• High heat resistance</li> </ul>                       | <ul style="list-style-type: none"> <li>• Medical equipment &amp; implants</li> <li>• Sealants in aircraft &amp; spacecraft applications</li> <li>• Adhesives &amp; Coatings</li> <li>• Kitchen equipment</li> </ul> |
|                      | <p>Acrylic Rubber (ACM)</p>   | <ul style="list-style-type: none"> <li>• Good oil resistance</li> <li>• Poor water resistance</li> <li>• Low resilience</li> <li>• High heat resistance</li> </ul>  | <ul style="list-style-type: none"> <li>• Sealants in the auto &amp; oil drilling industries (O-rings, gaskets etc.)</li> </ul>  |
|                      | <p>Fluorocarbon Rubber (FKM)</p>  <p>(Type 1 FKM)</p>  | <ul style="list-style-type: none"> <li>• Good oil resistance</li> <li>• Good heat resistance</li> <li>• Poor water &amp; steam resistance</li> </ul>  | <ul style="list-style-type: none"> <li>• Aircraft engine seals</li> <li>• General purpose seals</li> </ul>  |
| <b>Thermoplastic</b> | <p>Styrenic block copolymers:<br/>(SBS – styrene-butadiene-styrene)<br/>(SIS – styrene-isoprene-styrene)<br/>(SEBS – styrene-ethylene/butylene-styrene)</p>  | <ul style="list-style-type: none"> <li>• Good resilience</li> <li>• Poor oil resistance</li> <li>• Poor heat resistance</li> </ul>  | <ul style="list-style-type: none"> <li>• Adhesives (SIS)</li> <li>• Medical tubing (SEBS)</li> <li>• Footwear soles (SBS)</li> <li>• Plastic toys (SEBS)</li> </ul>   |



### 1.5.1 Mechanical properties of elastomers

Mechanical properties are the physical properties that a material displays upon application of force. Examples of mechanical properties are elasticity, plasticity, strength and toughness. Many materials are anisotropic which means that their mechanical properties will vary with the orientation of the applied force. Only uniaxial mechanical responses of elastomers are discussed here. Elasticity is the property of a material which when deformed returns back to its original dimensions once the force responsible for the deformation is removed. Elasticity is a characteristic of many materials but what sets elastomers apart is their extremely large reversible elongations. According to Hooke's law of elasticity, the change in length of a given body is proportional to the force acting upon that body provided it's within its elastic limit. In other words the stress on a material is proportional to the strain on that material and a linear stress-strain curve is observed as shown in Figure 1.3.

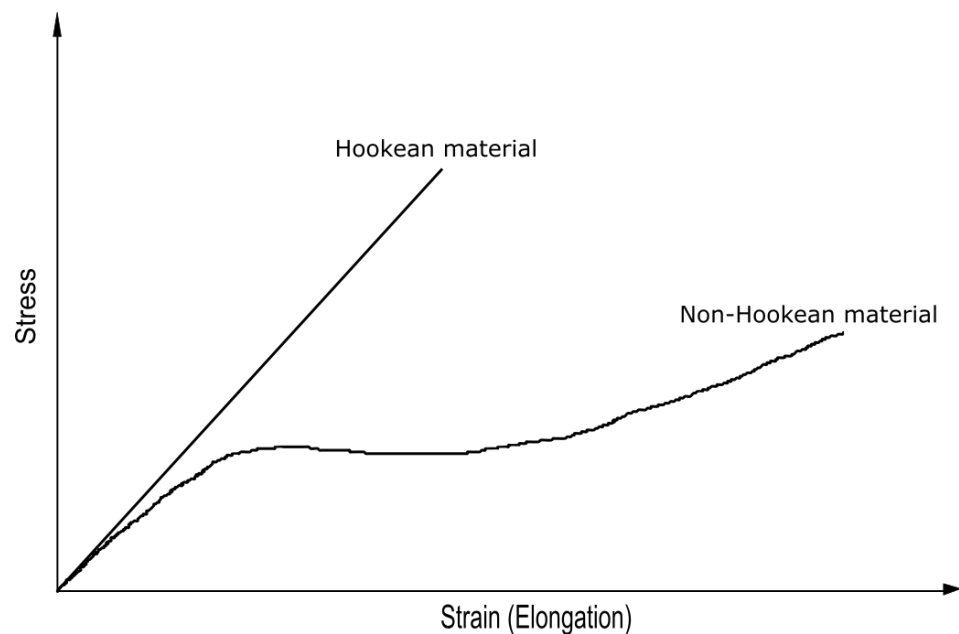


Figure 1.3: Illustration of Stress-strain plots for typical Hookean and non-Hookean materials.

However, elastomers do not follow Hooke's law at high strains and exhibit a non-linear stress strain curve. The modulus of elasticity, also referred to as Young's modulus describes how well the material resists deformation i.e. how stiff/rigid the material is and is the ratio of the stress to the corresponding strain of a material within the elastic limit:

$$E = \frac{\sigma}{\epsilon} \quad (\text{Equation 1.0})$$

Where  $E$  is Young's modulus,  $\sigma$  is stress and  $\epsilon$  is corresponding strain. The Young's modulus can be determined from the slope of a stress-strain curve. In the case of elastomers as the strain-curve is non-linear the initial slope is used to calculate the Young's modulus. Elastomers in general have very low modulus of elasticity and therefore regarded as soft i.e. easily deformed. Both the strength and toughness of a material can be gleaned from the stress-strain curve. Tensile strength is the

amount of force required to deform a material to breaking point. Elastomers tend to have low tensile strengths compared to other materials, however, it should be noted the elongation at tensile strength for elastomers is extremely large. Toughness is a measure of the energy a sample absorbs before it breaks and can be calculated from the area under a stress-strain curve. Figure 1.4 shows some typical stress-strain curves displayed by polymers.<sup>42,43</sup>

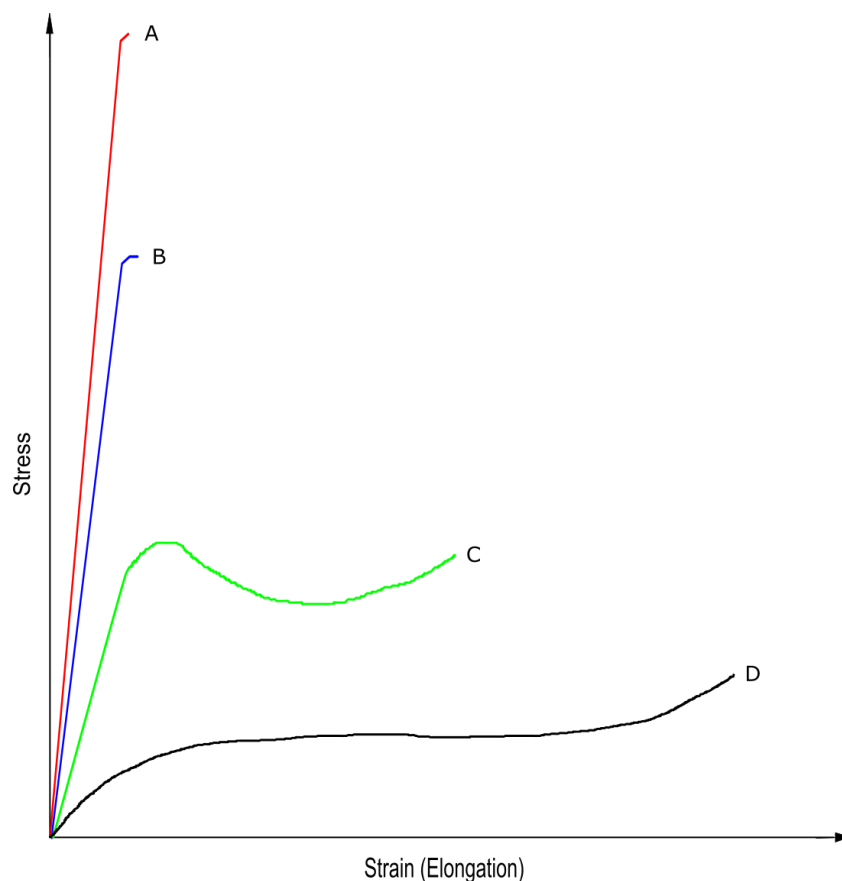


Figure 1.4: Illustration of stress-strain plots for various polymeric materials. The stress-strain curve A is typical of polymer fibres, curve B is typical of glassy polymers, curve C is typical of flexible plastics and curve D is typical of elastomers.

The stress-strain curve A is typical of polymer fibres such as nylon. Polymer fibres present a large Young's modulus, high tensile strength and low elongation at break. The stress-strain curve B is typical of amorphous or semi-crystalline polymers at temperatures below their glass transition temperature i.e. glassy polymers. Polymers that have high  $T_g$ 's such as polystyrene show the stress-strain behaviour observed in curve B. These polymers are often referred to as rigid plastics and display similar stress-strain behaviour to polymer fibres except they present a smaller Young's modulus and lower tensile strength. The stress-strain curve C is typical of amorphous or semi-crystalline polymers at temperatures above their  $T_g$ , often referred to as flexible plastics. Polyethylene and polypropylene are examples of flexible plastics. Along with elastic deformation, flexible plastics also display plastic deformation as shown by the plateau in curve C and often are labelled as ductile. Plastic deformation is defined as permanent deformation under the application of sustained force. While flexible plastics have a lower tensile strength and a smaller Young's modulus compared to polymer fibres and rigid plastics, they are tougher and have a larger elongation at break. The stress-strain curve D is typical of elastomers. Elastic deformation occurs

until very high strain deformations and a small Young's modulus combined with a low tensile strength compared to the other polymer types is observed. The type of elasticity displayed by elastomers is denoted as rubber elasticity.<sup>44</sup> Temperature can have a large effect on the mechanical properties of polymers; with increasing temperature a polymer can exhibit stress-strain behaviour ranging from rigid plastics to elastomer-like.<sup>42</sup>

Elastic strain can be due to chemical bond stretching, bond angle deformation or crystal structure deformation. The mechanism of elasticity in flexible polymers involves the deformation in the amorphous region which can cause interlamellar slip, separation or stack rotation. The plastic deformation shown in flexible plastics corresponds to deformation in the crystalline region where the interlamellar rearrange from a spherulite to fibrous morphology where parts of the interlamellar have unfolded.<sup>45</sup> The mechanism of elasticity in elastomers involves the kinetic movement of flexible polymer chains.<sup>46</sup> The chains in an unstrained elastomer exist in a random coiled structure linked via cross-links and uncoil to a linear structure with increasing strain. The mechanical properties of elastomers are largely dependent on type of chain, chain length, chain entanglement, degree of crystallinity and degree of crosslinking. As expected different types of elastomers show slightly different stress-strain curves, for example unreinforced natural rubber displays a sharp increase just before breaking point. This is due to the fact that at high strains the long chains that have been pulled into parallel alignment form a crystalline structure together – this process is known as strain crystallisation. An increased amount of force is required to break the bonding between the parallel chains.

## 1.6 Silicone Elastomers

Silicone elastomers are inorganic elastomers which are formed through the cross-linking of polysiloxanes. They have numerous advantages including; high temperature resistance, good release properties, good electrical insulation, good resistance to low concentration acids and bases, high gas permeability, non-toxic and odourless. Compared to other types of elastomers, silicone elastomers do exhibit reduced mechanical properties most notably a low tensile strength. Though their mechanical properties are retained at high temperatures and can be easily improved via the addition of reinforcing fillers such as silica. Another disadvantage of silicone elastomers is their low resistance to oils, non-polar solvents and strong acids and bases. Though the poor resistance to nonpolar solvents can be overcome by using polysiloxanes with trifluoropropyl side groups. The exact properties of a silicone elastomer are dependent on the polysiloxane, cure (cross-linking) system, cross-linker, cross-linking degree and any additional additives i.e. fillers used. Silicone elastomers are used in numerous industries including medical, construction and automotive. In biomedical applications silicone elastomers are commonly used for medical devices such as catheters and drains and for both aesthetic and prosthetic implants. In both the construction and

automotive industries silicone rubbers are used as sealants, coatings and adhesives. Silicone elastomers have also been used to fabricate sporting goods, toys and kitchen utensils.

### 1.6.1 Polysiloxanes

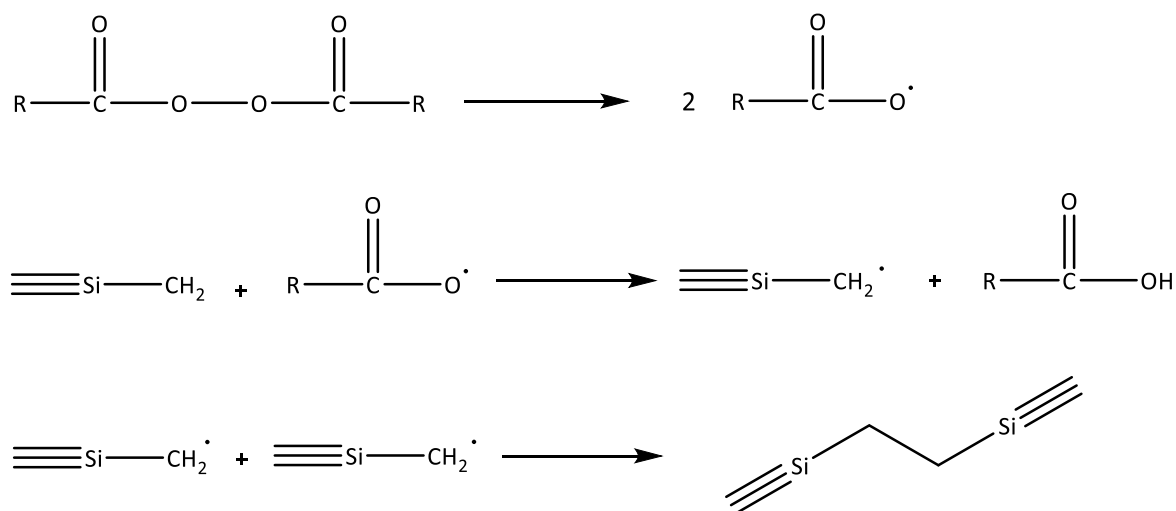
Polysiloxanes are the most common inorganic polymers and have a basic repeat unit of  $[\text{SiRR}'\text{-O}]_n$ . They have gained a large amount of interest due to their useful properties such as: high flexibility, gas permeability, low  $T_g$ , thermal stability and low surface energy. The polysiloxane that has had the most scientific and commercial interest is polydimethylsiloxane (PDMS). Polydimethylsiloxane is a member of the symmetrical dialkylpolysiloxanes with a repeat unit of  $[\text{Si}(\text{CH}_3)_2\text{-O}]_n$ . The large flexibility of the polysiloxanes arises from the unique characteristics of the Si – O bonds that make up the chain backbone. The Si – O bond is unusually long with a length of 1.64 Å in comparison to a C – C bond with a length of 1.53 Å. The long length of the Si – O bond combined with the fact that side groups are only present on every other atom of the backbone reduces steric hindrance. The reduced steric hindrance results in a low barrier to rotation. The Si – O – Si bond angle is larger than the angle in usual tetrahedral bonding, around 143° when compared to around 110°. Unlike in most hydrocarbon systems where the bond angles are fixed, the Si – O – Si bond shows much wider variability. The energy required to deform the Si – O – Si to 180° is extremely low – approx. 1.3 KJ/mol. The combination of the long length and large angle of the Si – O – Si bond results in polysiloxanes having both a large dynamic and equilibrium flexibility. Dynamic flexibility is the ability for a molecule to change spatial arrangements by rotation around its skeletal bond, while equilibrium flexibility is the ability of a chain to be compact when in the form of a random coil. The large dynamic and equilibrium flexibility of polysiloxanes is reflected in their low glass transition and melting temperatures, respectively. The flexibility of polysiloxanes can be reduced via several different methods: increasing the size of the side groups or inserting rigid groups into the chain backbone and this will result in an increase in both  $T_g$  and  $T_m$ . PDMS which has the most basic side group (methyl group) has one of the lowest  $T_g$  and  $T_m$  of the polysiloxanes, -125°C and -40°C, respectively. The low surface energy exhibited by polysiloxanes is due to the flexibility of the backbone chain. In general silicate based molecules have high surface energy, while hydrocarbons have low surface energy. However, the flexibility of the polysiloxane backbone means that the side groups (often alkyl or aryl groups) can be presented at the surface interface resulting in the low surface energy. The surface properties of polysiloxanes are associated with their side group characteristics. The movement of side groups to the surface interface also explains the hydrophobic nature of PDMS. The thermal stability property of polysiloxanes is due to the strength of the Si – O and Si – C bonds when compared to C – O and C – C bonds. The nature of the side groups can also change the bulk properties of polysiloxanes. For example, introducing fluorine side groups (commonly trifluoropropyl) can increase the thermal stability of the polysiloxane. The C – F bond is stronger than both a C – C bond and C – H bond.



## 1.6.2 Cross-linking mechanisms of polysiloxanes

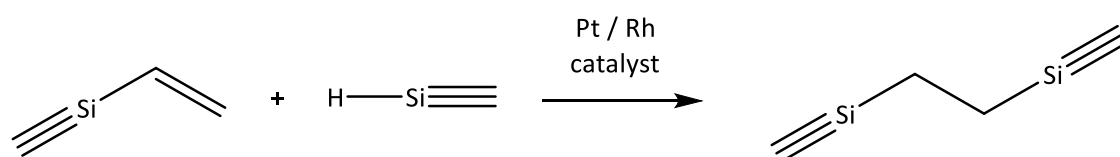
There are a variety of cross-linking mechanisms (which are also referred to as cure systems) available to use such as peroxide cure, addition cure and condensation cure.

Peroxide cure systems utilise free radicals to initiate the cross-linking reaction. This cure system is classified as a high temperature vulcanising (HTV) system. The free peroxide radicals are formed via the thermal decomposition of the peroxide curing agent. The peroxide radical undergoes a hydrogen abstraction reaction with the methyl side groups on the silicone polymer forming methylene radicals. Cross-linking is achieved via the dimerization of two methylene radicals.<sup>48</sup> Scheme 1.2 shows the peroxide free radical cross-linking of silicones. Post cures where the cured elastomer is exposed to elevated temperatures are performed to remove the volatile acid by-product. Vinyl containing silicones are often used to accelerate the cure rate and control the cross-linking reaction.<sup>43</sup> Peroxide curing agents that are used in cross-linking silicones are divided into two categories: general purpose and vinyl specific.



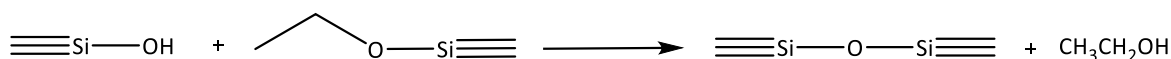
*Scheme 1.2: Peroxide free radical cross-linking of silicones.*

The crosslinking in addition cure systems occurs through a hydrosilylation reaction between vinyl groups on the polysiloxane chain and a multifunctional silicon hydride cross-linker<sup>49</sup> as shown in Scheme 1.3. The hydrosilylation reaction requires a catalyst which is often a platinum or rhodium complex, has no by-products and can be accelerated via heating. One of the most well-known and studied addition cured platinum catalysed PDMS elastomers is Sylgard<sup>®</sup> 184 which is a 2-part system. 2-Part addition cure systems are classified as room temperature vulcanising (RTV) systems.



*Scheme 1.3: Addition cure cross-linking reaction.*

Condensation cure systems are room temperature vulcanising systems and are classified into two groups: one component system (RTV-1) and two component system (RTV-2). RTV-1 cure systems are dependent on atmospheric moisture for curing. The curing begins at the surface and moves inwards according with the moisture diffusion rate. Typically an organometallic tin catalyst is used in RTV-1 systems. RTV-1 systems are further classified according to the by-product of the curing reaction - they can either be acidic, basic or neutral cure systems. Many commercial silicone sealants are RTV-1 cure systems. On the other hand while RTV-2 cure systems are not dependent on atmospheric moisture for curing, the presence of moisture can accelerate the curing reaction. Typically, RTV-2 systems use silanol terminated silicone polymers, alkoxy silane cross-linkers and an organotin salt as the catalyst. Scheme 1.4 shows the curing reaction of a RTV-2 cure system.



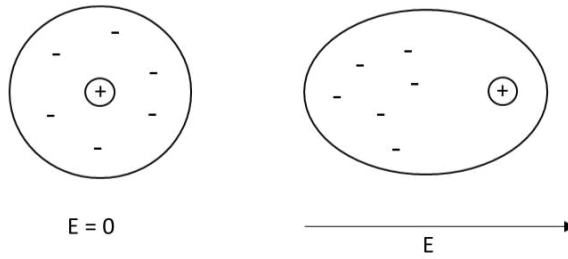
*Scheme 1.4: RTV-2 cure cross-linking reaction*

### 1.6.3 Compound design to introduce dielectric properties to silicone elastomers

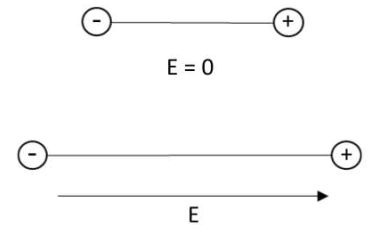
A dielectric material is an electrical insulator that can be polarised by an applied electric field. The electric charges are slightly displaced from their equilibrium positions at the atomic, molecular and bulk material levels causing what is referred to as dielectric polarisation.<sup>50</sup> Most dielectric materials have no free electrons and can have three forms: gas, liquid and solid. There are three types of solid dielectric materials: (i) Elemental solid dielectrics, these are materials that consist of single type of atoms, such as diamond; (ii) Ionic non-polar solid dielectrics, these are ionic crystals such as alkali halides; (iii) Polar solid dielectrics, which are made up of molecules that possess a permanent dipole moment. There are several different types of dielectric polarisation processes such as, orientation (dipole), ionic, electronic and space charge polarisation.<sup>51</sup> Orientation polarisation occurs in materials which possess a permanent dipole. When an electric field is applied the dipoles tend to line up along the direction of the electric field as shown in Figure 1.5 (c). Ionic polarisation occurs in ionic materials i.e. materials composed of anions and cations. In ionic materials each anion and cation pair is a dipole, however, the sum of the dipole moments over the whole material i.e. net dipole moment can still be zero. In the presence of an electric field, the anions and cations are displaced in opposite directions, with the cations moving in the direction of the electric field. The displacement of the ions relative to one another causes the dipole moment to increase resulting in an overall increase in the net dipole moment. All non-conducting materials are capable of electronic polarisation. In electronic polarisation the shift of the negative electron cloud relative to the nucleus to which it belongs induces a dipole moment. Within each atom or ion there is a positively charged nucleus surrounded by a negatively charged electron cloud. When an electric field is applied the positive nucleus moves in the direction of the applied field and the electron cloud distorts in the opposite direction. Space charge polarisation is found in ferrites (compounds composed of iron oxide combined with other metal oxides) and semi-conductors.

Space charge polarisation occurs due to the diffusion of ions along the direction of the electric field resulting in the accumulation of charges at the interfaces of the material.

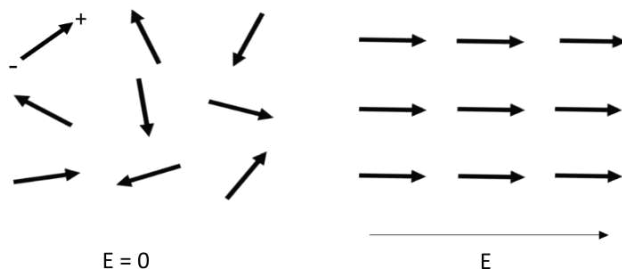
(a) Electronic polarisation



(b) Ionic polarisation



(c) Orientation polarisation



(c) Space charge polarisation

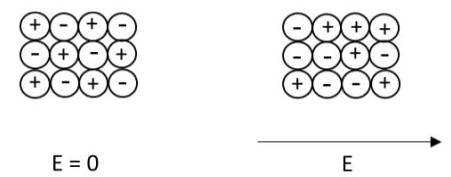


Figure 1.5: Illustration of the dielectric polarisation processes.  $E$  represents the applied electric field.

Both temperature and frequency can have an effect on the dielectric polarisation processes. Both electronic and ionic polarisation are independent of temperature. However, orientation and space charge polarisation processes are both affected by temperature. A decrease in orientation polarisation occurs with an increase in temperature. The molecules in a material always possess some energy which results in random motion. When the permanent dipoles are realigned due to an applied electric field, the molecules are still undergoing random motion which means that at a given instant not all the dipoles will be perfectly aligned. As the temperature is increased the molecules have more thermal energy which results in a larger amplitude of motion. The large amplitude of motion exhibited by the dipoles means that there is a greater range of deviation from perfect alignment with the electric field and therefore the orientation polarisation of the material is less. In contrast thermal energy facilitates the diffusion of ions and therefore space charge polarisation increases with increasing temperatures.



As highlighted above a dielectric material becomes polarised in an electric field. When the direction of the electric field is switched the polarisation will also switch direction to align with the new direction of the field. The time it takes for the polarisation to switch direction i.e. the time needed for rotation (orientation polarisation) or movement of charges (ionic, electronic and space charge polarisation) is called the relaxation time. Each polarisation process has a different relaxation time. If the relaxation time is lower than the frequency of the electric field the polarisation process ceases to contribute to the polarisation of the material as it cannot keep up with the alternating electric field. Electronic polarisation is the fastest dielectric polarisation process and therefore can occur at optical frequencies ( $\approx 10^{15}$  MHz). Space charge polarisation is the slowest of all the polarisation mechanism and occurs at low frequencies (less than  $10^2$  Hz). However, with increasing temperature space charge polarisation can occur at larger frequencies due to their increase in thermal energy. Ionic polarisation occurs at frequencies below  $10^{13}$  MHz and orientation polarisation occurs at frequencies below  $10^9$  MHz.<sup>52</sup> Figure 1.6 shows the frequency dependence of the dielectric polarisation processes.

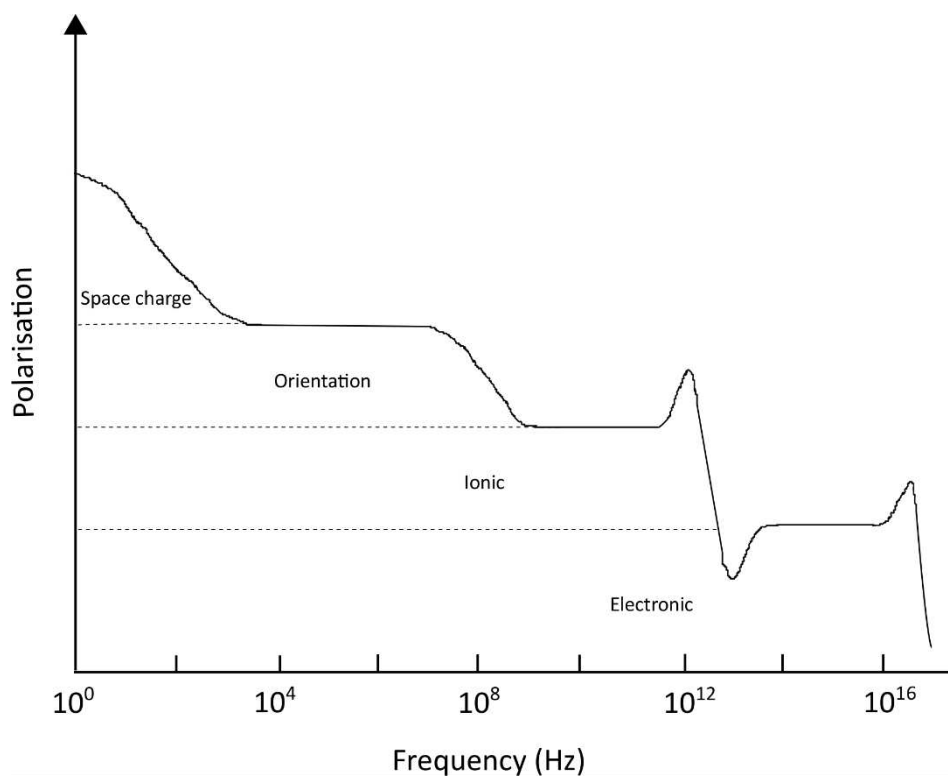


Figure 1.6: Frequency dependence of dielectric polarisation.

The dielectric constant or relative permittivity of a material determines its response to an applied external electric field. Materials which show greater polarisation in response to an applied electric field have larger dielectric constants / relative permittivities. The dielectric constant can be defined as the ability of a material to store electrical energy in an electric field and is the ratio of permittivity of a material to the permittivity of free space. Permittivity is a measure of how much the material opposes the external electric field. Table 1.1 shows the dielectric constant of some common

materials. It should be noted that the dielectric constants of the materials in Table 1.1 are not absolute as they can vary with both temperature and frequency as previously discussed.

*Table 1.1: Dielectric constants (relative permittivities) at room temperature for some common materials.*

| <b>Material</b> | <b>Dielectric constant</b> | <b>Material</b>          | <b>Dielectric constant</b> |
|-----------------|----------------------------|--------------------------|----------------------------|
| Vacuum          | 1                          | Silicon dioxide (silica) | 3.7 – 3.9                  |
| Air (1 atm)     | 1.0006                     | Neoprene rubber          | 6.7                        |
| Polyethylene    | 2                          | Acetonitrile             | 36                         |
| Benzene         | 2                          | Water                    | 80                         |
| PDMS            | 2.3 – 2.8                  | Titanium dioxide         | 100                        |
| Silicone rubber | 3.2 – 9.8                  | Barium titanate          | 500 - 5000                 |

As shown in Table 1.1, silicone rubber has quite a low dielectric constant. There are two methods that can be used to increase the dielectric constant of silicone rubber: one method is to incorporate dielectric moieties, such as polar moieties into the polymer backbone, side groups and cross-linkers. The other route is to introduce high dielectric materials into the polymer matrix such as fillers. The addition of ferroelectric/piezoelectric ceramics such as lead magnesium niobate-lead titanate (PMN-PT)<sup>53</sup>, titanium dioxide (TiO<sub>2</sub>)<sup>54</sup> and barium titanate (BaTiO<sub>3</sub>)<sup>55,56</sup> have shown to significantly increase the dielectric constant / relative permittivity of silicone elastomers. However, it should be noted that often an improvement of one property such as the dielectric constant in this case can come at the expense of another property. The addition of fillers to elastomers often results in an increase in the materials Young's modulus of elasticity and therefore makes the resulting polymer composite more rigid. This means that a larger amount of force is required to cause a smaller elongation. However, it has been shown that some fillers can act as reinforcing fillers and therefore the addition of these fillers improves both the mechanical and dielectric properties of the polymer composite. For example, loading silicone rubbers with titanium dioxide has shown an increase in the relative permittivity, elongation (%) at break and tensile strength of the silicone-TiO<sub>2</sub> composite.<sup>57</sup> It was found that the elongation at break and tensile strength reached maximum values at 35 wt % titanium dioxide loading. Composites with > 35 wt % TiO<sub>2</sub> loading saw a decline in mechanical properties which was attributed to the effects of titanium dioxide agglomeration within the composites.

## 1.7 UHF-RFID solvent vapour displacement sensor tag

Subsequently in this thesis the development of a vapour sensing passive RFID tag based upon the swelling of silicone elastomer where the elastomer would act as an actuator component will be described. The solvent vapour sensor tag design is shown in Figure 1.7. The displacement sensor tag consists of two antennas: the main antenna and feed loop antenna. The feed loop antenna is on a separate substrate and is the moving component of the tag. The tag sensor is designed to show optimum performance when the loop antenna is close to the main antenna. On exposure to solvent vapour the elastomer swells, pushing the feed loop away from the main antenna. As the distance between the feed loop and main antenna increases, the transmitted power increases and the tag's read range decreases. While the phenomenon of polymeric swelling has been utilised in a few other vapour sensor tag designs, none have used the swelling as a method to cause antenna displacement.

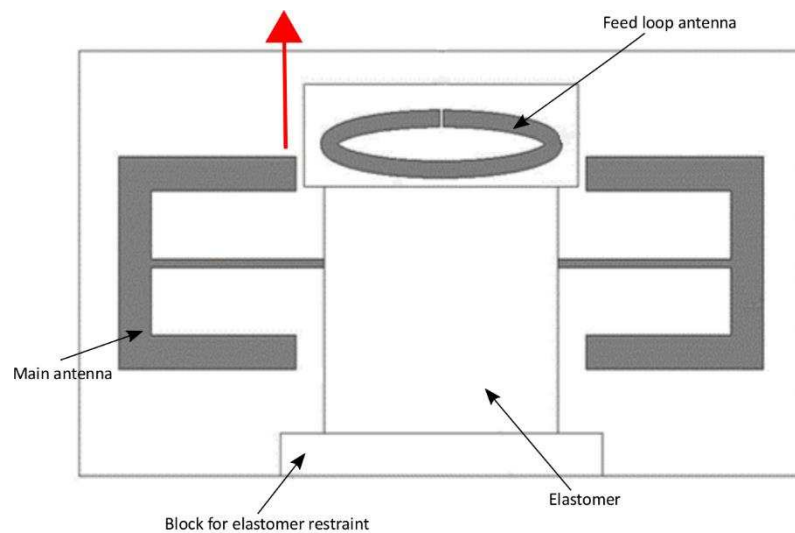


Figure 1.7: UHF-RFID solvent vapour displacement sensor tag design. The red arrow indicates the direction in which the feed loop antenna is pushed as a result of elastomer swelling.

## 1.8 Swelling phenomenon in elastomeric materials

As previously highlighted one of the common properties of all elastomers is their physical swelling in response to contact with liquid and vapours. The amount of swelling shown by elastomers can range from negligible amounts to large volume swelling of 100 – 150 % and is highly dependent on the compatibility of the elastomer and liquid. The property of elastomer swelling has in the past been seen as a negative, especially in microfluidic device and solid phase microextraction (SPME) applications. Though in recent years the swelling of elastomers has become a desirable property. PDMS sponge elastomers which swell in oil but not water have been investigated as potential oil spill cleaning materials. Swellable elastomers have also found applications in oilfields to seal undesired fluid flow and are used in either self-healing cements or swellable packers.<sup>58</sup> Oil-swellable, water-swellable and hybrid swellable elastomer systems for oilfield applications are commercially available. The mechanism of water-swelling elastomers is via osmosis while the mechanism of oil-swelling elastomers is through a diffusion process.<sup>59</sup> The swelling of elastomers

has also been used as a method to join silicone tubing to hard plastic or metal components such as barb fittings. In the past lubricants such as isopropyl alcohol (IPA) and silicone oil were often used by engineers for joining parts. However, using IPA makes the fitting process very time consuming as it does not evaporate quickly. Silicone oil-based lubricants, on the other hand, do not evaporate and can easily migrate to other surfaces resulting in additional clean-up to be required. Another limitation of silicone oil is that contamination risk is high as oil attracts dust and contaminants from the environment. The method of swelling the silicone tubing as a fitting method is attractive as the process is fast, mess free and produces a secure tight seal. MicroCare SwellEx<sup>®</sup> is a commercially available silicone swelling agent and is based on volatile methyl siloxanes.

The phenomenon of polymer swelling is the first stage of the process of polymer dissolution. Unlike non-polymeric materials where dissolution is instantaneous, the dissolution of polymers is generally a slow process. The dissolution of a polymer into a solvent comprises of two processes, solvent movement and chain disentanglement.<sup>60</sup> When a polymer is added to a solvent, forces of attraction or dispersion begin to act between the polymer and solvent according to their chemical nature, polarity and solubility parameter. If the polymer-solvent interactions are stronger than that of the polymer-polymer interactions the solvent can penetrate the polymer chains, causing the chains to disentangle and loosen out from their tightly coiled conformation resulting in an increase in polymer volume i.e. swelling. As the polymer chains begin to disentangle and unfold, more solvent can penetrate the space between the chains leading to an increase in the polymer-solvent interaction which in turn causes further polymer swelling. This process is the first stage of polymer dissolution. The phenomenon of swelling is dependant only on the forces of interaction between the solvent and polymer and cannot be influenced by agitation or stirring. When the polymer segments are fully solvated they diffuse out of the swollen polymer and disperse in the solvent phase. This is the second stage of polymer dissolution and is comparable to the diffusion process of non-polymeric and low molecular weight materials. The diffusion of polymer segments out of the swollen polymer occurs simultaneously and the rate of diffusion can be increased via agitation. The stages of polymer dissolution is shown in Figure 1.8. The dissolved polymer chains do not assume an extended straight chain but are found in an expanded coil structure where the space between the unfolded coils is occupied by solvent molecules.

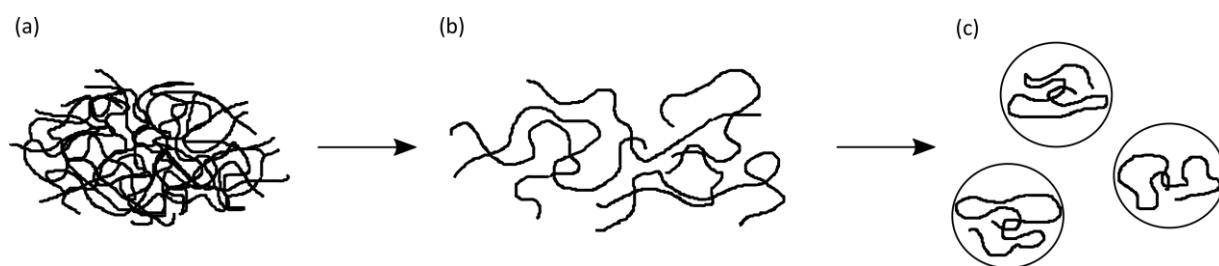


Figure 1.8: Schematic representation of polymer dissolution; (a) morphology of polymer chains just after being added to a solvent (b) first stage of polymer dissolution: polymer swelling due to the penetration of solvent molecules between the polymer chains and (c) second stage of polymer dissolution: polymer chains are fully solvated and dispersed into a solution.

Though some polymeric materials like elastomers only undergo the first stage of polymer dissolution i.e. they swell but do not dissolve. Examples of such polymeric materials are cross-linked polymers, highly crystalline polymers and polymers that exhibit strong interactions such as hydrogen bonding. In cross-linked polymers the cross-links act as anchors, preventing the polymer chains from diffusing out of the swollen polymer and in the case of highly crystalline and hydrogen bonded polymers the polymer-polymer interactions are stronger than that of the polymer-solvent interactions preventing full solvation of the polymer chains. Where the polymer-solvent interactions are weaker than the polymer-polymer interactions only a limited degree of swelling will occur. The swelling of elastomers is a reversible process and is similar to an elastic deformation<sup>61</sup> - in both cases the individual chains unfold to a linear structure. There are several factors that affect the degree of elastomer swelling, the most prominent being the compatibility of the solvent and the elastomer i.e. the strength of the polymer-solvent interactions. Other factors include the degree of elastomer cross-linking, presence of any compounding ingredients, and  $T_g$  of the base polymer which is associated with free volume.

Cohesion energy parameters or solubility parameters provide an easy method of predicting the adhesive and cohesive properties of a material. They have been used to predict the miscibility of materials and the swelling extent of elastomeric materials in solvents. The Hildebrand solubility parameter reflects the total intermolecular forces within a material and is derived from the cohesive energy density of that material. Miscibility will only result when the intermolecular forces between two materials are similar. These intermolecular forces are known as van der Waals forces of attraction. There are four types of van der Waal forces: hydrogen bonding, dipole-dipole interactions, dipole-induced dipole (polarisation) interactions and induced dipole-induced dipole interactions (London dispersion forces). The amount of van de Waals forces present in a material is indicated by the material's heat of vaporisation. The heat of vaporisation is the change in heat (enthalpy) required to change a liquid into a vapour i.e. the amount of energy required to break the van der Waal forces between the liquid molecules. The cohesive energy density of a material is expressed as:<sup>62</sup>

$$C = \frac{\Delta H - RT}{V} \quad \text{(Equation 1.1)}$$

where  $\Delta H$  is the heat of vaporisation,  $R$  is the gas constant,  $T$  is temperature and  $V$  is the molar volume. The term 'solubility parameter' was first introduced by Hildebrand and Scott and is the square root of the cohesive energy density:<sup>63</sup>

$$\delta = \sqrt{C} = \left( \frac{\Delta H - RT}{V} \right)^{1/2} \quad \text{(Equation 1.2)}$$

The solubility parameter,  $\delta$  expressed above is referred to as the Hildebrand solubility parameter. Hansen extended Hildebrand's research and showed that the heat of vaporisation could be divided

into the contributions of each type of van der Waal force.<sup>64</sup> Hansen calculated three solubility parameters (collectively known as the Hansen solubility parameters, HSP) for each material.  $\delta_d$  is the Hansen solubility parameter derived from the energy to break dispersion forces,  $\delta_p$  is the Hansen solubility parameter derived from the energy to break polar interactions and  $\delta_h$  is the Hansen solubility parameter derived from the energy to break hydrogen bonding between the molecules. The Hansen solubility parameters are additive resulting in what is known as the total Hansen solubility parameter,  $\delta_t$ :

$$\delta_t^2 = \delta_d^2 + \delta_p^2 + \delta_h^2 \quad (\text{Equation 1.3})$$

## 1.9 UHF-RFID light sensor tag

In this thesis the development of a light sensor tag design where tag mismatching is achieved by a short circuit within the tag antenna as a result of light exposure will be described. A material that becomes highly conductive as a result of light exposure is required to act as the short circuit. The material would be cast onto the tag where a short circuit could be achieved. Figure 1.9 shows the light sensor tag design. The advantage of this short circuit method is that conventional tags can be easily transformed into light sensor tags through simply casting the short circuit material onto the tag where a short circuit could be achieved. In addition to being light sensitive the final material has to offer simplicity in processing i.e. easy to cast onto the tags.

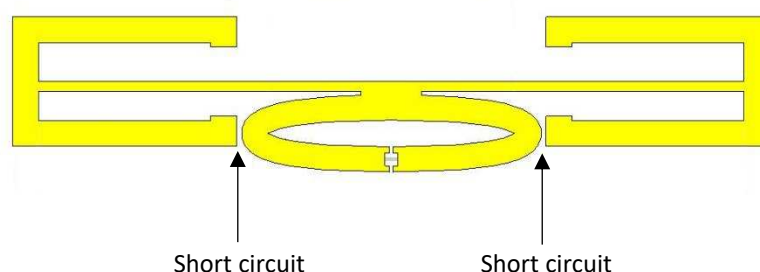
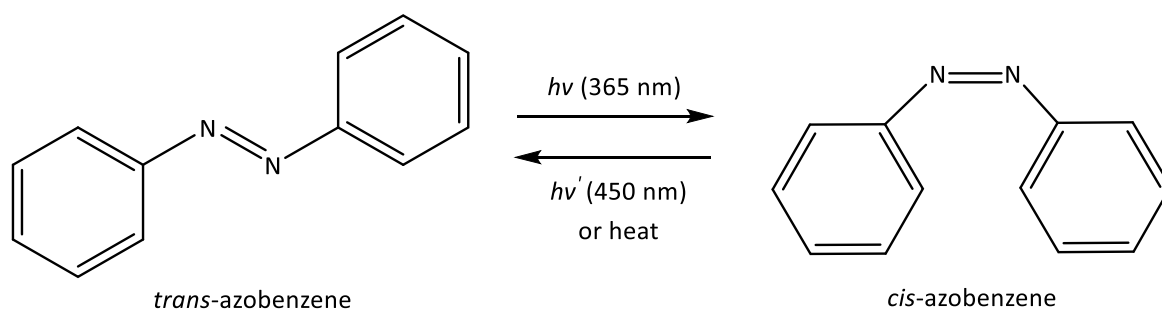


Figure 1.9: Light sensor tag design.

## 1.10 Light sensitive polymeric materials

There are numerous examples of light sensitive polymeric materials in literature whose response to light include a change in shape, phase, optic properties, mechanical strength, electrical or thermal properties. There are two main ways in which to achieve the desired light-sensitivity of polymeric materials; one method is to incorporate photoactive molecules as filler into the polymer matrix while the other method is to incorporate photoreactive moieties into the polymer structure either as groups on the backbone or side groups. The response of the light sensitive polymer will depend on the type of photoreaction that occurs.<sup>65</sup> Some of the most common photo-activated reactions used to obtain different light induced responses are: isomerization, dimerization, ring-opening, excitation and reduction.

Isomerization is the process in which a molecule is transformed into another molecule that has the same atoms but in a different arrangement. This change in the molecules configuration can have profound effects on the both the molecules geometry and dipole moment. One of the most well-known and utilised photoactive molecules that undergoes photo-isomerization is azobenzene and its derivatives. Azobenzene undergoes a trans-cis isomerisation upon exposure to UV light<sup>66</sup> as shown in Scheme 1.5. The advantage of this reaction is that it is reversible with either the application of heat or irradiation of visible light.

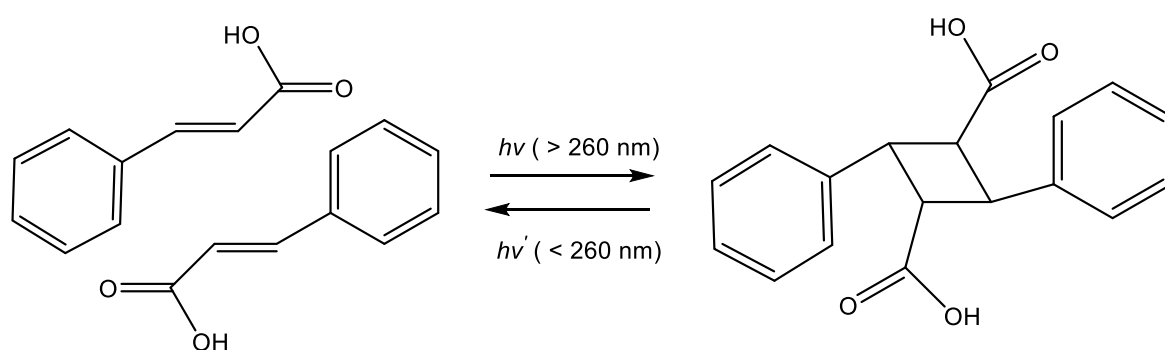


*Scheme 1.5: Trans-cis isomerisation of azobenzene.*

Due to the large change in the molecular length of azobenzene with isomerization: the distance between the para carbons decreases from 9.9 Å to 5.5 Å<sup>66</sup>, bending and contraction of azobenzene containing materials with light can be achieved. Yu *et al.* demonstrated a single film of a liquid-crystal network containing azobenzene chromophores that could be reversibly bent along any chosen direction using linearly polarised light.<sup>67</sup> The corresponding increase in the dipole moment of azobenzene from 0.5 D to 3.1 D with trans-cis isomerisation has been utilised in surfactant or amphiphilic block copolymer (BCP) micelle based controlled drug delivery systems.<sup>68</sup> The azobenzene moieties are incorporated into the structure of the hydrophobic block. With the increase in the dipole moment with UV exposure the hydrophobic block becomes more hydrophilic shifting the hydrophilic/lipophilic balance towards the destabilization of the micelles thus releasing their contents.

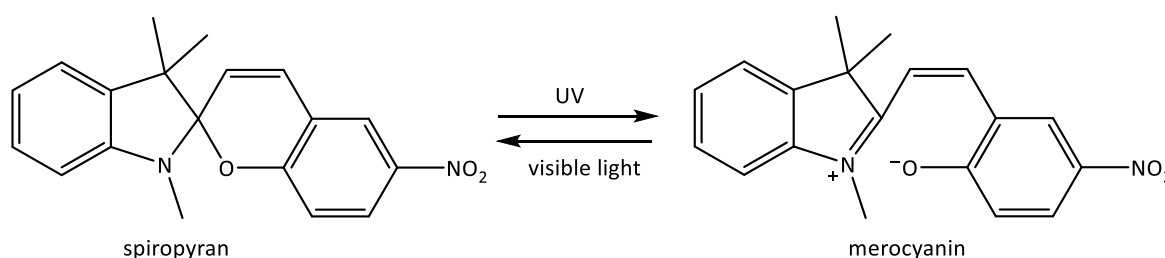
Photo induced dimerization involves an addition reaction between an excited molecule and unexcited molecule of the same species forming a dimer. The most common photo-dimerization reactions are [2+2] and [4+4] cycloadditions. There are a large variety of different molecules that undergo these photo reactions including cinnamic acid and anthracene derivatives. Photo-induced self-healing polymers<sup>69</sup> and photo-induced shape memory polymers<sup>70</sup> that utilise the photo induced dimerization of cinnamic acid have been demonstrated. In both cases the photo-dimerization reaction was used to form cross-links between the polymer chains. The photo-dimerization of cinnamic derivatives is a reversible reaction, thus the dimers formed are photo-responsive. In the case of the shape memory polymer presented, the polymer film was deformed and fixed into a temporary shape via the formation of dimer cross-links using UV irradiation ( $\lambda > 260 \text{ nm}$ ). The dimer

cross-links could then be cleaved apart using UV irradiation ( $\lambda < 260 \text{ nm}$ ) resulting in the polymer film to return to its original shape.



Scheme 1.6: Dimerization of cinnamic acid.

One of the most well-known photoactive molecules that undergoes photo-induced ring opening (photocycloreversion) is spiropyran. Spiropyran units undergo a transformation from a colourless ring closed spiropyran to a coloured open-ringed merocyanine form as a response to ultraviolet irradiation as shown in Scheme 1.7.<sup>71</sup> The reversible reaction (photocyclization) occurs through the irradiation with visible light. The photo-induced ring opening of the ring closed spiropyran to the ring-opened merocyanine is accompanied with a large change in polarity. This photo-induced transformation between hydrophobic spiropyran and hydrophilic merocyanine has been utilised in creating micelles that can undergo reversible disruption/regeneration as a response to light which is highly attractive for drug delivery and separation applications.<sup>72</sup> The large change in polarity accompanied by the photocycloreversion reaction of spiropyran has also been utilised in reversible solubility control of polystyrene<sup>73</sup> and reversible wetting of surfaces.<sup>71</sup> The reversible photocycloreversion of spiropyran has also been evaluated for use in optical switching<sup>72</sup> and as a photo-induced switch as part of a light-actuated molecular valve.<sup>74</sup>



Scheme 1.7: Photo induced ring-opening of spiropyran.

Photoconductive materials are materials that become more electrically conductive due to the absorption of light. They are used in numerous UV applications, though most notably in photocopy techniques (xerography), laser printers and as photoresistors in photodetectors. The absorption of photons energetically elevates electrons into the conduction band which results in the generation of electron holes. Both the excited electrons and electron holes can be used to carry electrical current and are classified as charge carriers.<sup>75</sup> The excited electrons can move through the material carrying the electrical current. In addition, other electrons are able to move through the material



by filling the electron holes. The latter mechanism is called hole conduction or hole transport as it appears that the electron holes migrate in the opposite direction of the excited electrons. Charge carriers can also be formed from photogenerated excitons. Excitons are bound excited electrons and electron holes which cannot transport charge. However, a free electron and electron hole (electron-hole pair) can be produced if two excitons collide or if the exciton is photoionised. Photoconductive materials can either be inorganic or organic in nature. Examples of inorganic photoconductors include cadmium sulfide, titanium oxide and selenium. There are several polymers which exhibit photoconductivity, such as polyvinyl fluoride, polyvinyl acetate, polyvinyl pyrene and poly *N*-vinyl carbazole (PVK).<sup>76</sup> Photoconductive polymers can be classified as p-type (hole transporting), n-type (electron transporting) or bipolar (combination of hole and electron transporting) though the majority of photoconductive polymers are p-type. Vinyl derivatives of polyaromatic compounds such as polyvinyl pyrene and poly *N*-vinyl carbazole have high photoconductive efficiencies, which is believed to be due to the fact these materials can form into a helical shape with the aromatic side chains in parallel to one another allowing easy charge carrier transfers. The backbone of the polymer is not involved in the photoconduction mechanism. Though one of the downsides of these materials is that they are only photoconductive in ultraviolet light.<sup>77</sup> It has been found that the addition of electron acceptor molecules such as 2, 4, 7-trinitrofluorenone (TNF) can enhance both the photoconductivity efficiency and spectral sensitivity. When TNF is added to poly *N*-vinyl carbazole (PVK), PVK becomes photoconductive in the visible region due to the formation of charge transfer complexes. It has been suggested that the increase in photoconductivity displayed by PVK: TNF complexes is caused by the transfer of the free electrons generated in the PVK molecule to TNF.<sup>78</sup> PVK transports charge via electron holes, however, TNF molecules have shown to be electron transporting and therefore contribute to the conductivity of the complex.

The photoreduction of silver salts to silver metal has been known for many years and is the basis of the photographic process.<sup>79</sup> The light sensitive silver halides (AgX, where X is Cl, Br or I) are used in photographic films for both black and white (B&W) and colour photography. In the case of colour photography the silver halides only act as mediators for transforming light into organic image dyes. B&W photographic films consist of two layers: a support base layer and the photosensitive layer which comprises of silver halide crystals suspended in a matrix, almost invariably gelatin. The silver halide suspensions are referred to as emulsions and the silver halide crystals within them are commonly termed grains. In general, emulsions contain a mixture of two silver halides. Photographic materials which contain both silver bromide and silver iodide are referred to as iodobromide materials and those that contain silver chloride and silver bromide as chlorobromide materials. The silver halide emulsions are prepared by reacting silver nitrate with alkali metal halides in the presence of gelatin. The resulting emulsion is cast onto a support layer (often polyethylene terephthalate or cellulose acetate) and cooled to ensure the sol to gel transition of

the emulsion takes place. When the photographic film is exposed to light a latent image is formed. The formation of a latent image is a multi-stage process and involves Frenkel defects. A light photon interacts with a halogen ion in the silver halide crystal liberating an electron as shown in the following reaction<sup>80</sup>:



The electron is free to move within the crystal lattice and migrates towards the interstitial silver ion that is a part of the Frenkel defect. The interstitial silver ion is subsequently reduced to form a silver atom:



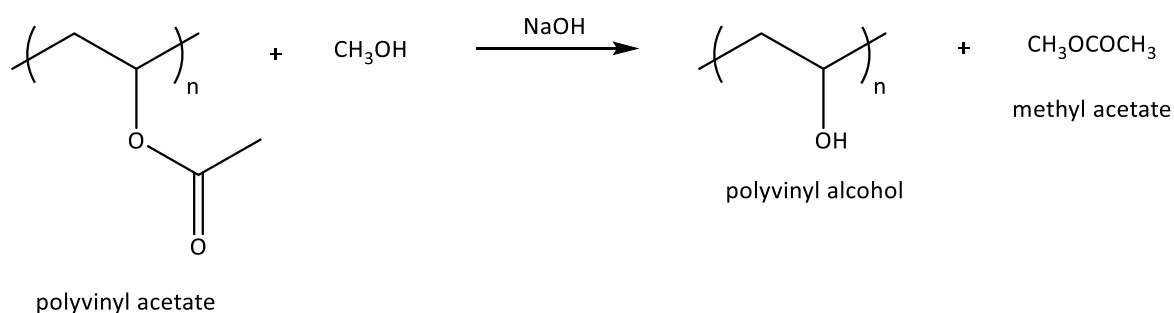
The above reaction is reversible meaning that the silver atom can revert back to a silver ion. However, the silver atom can be stabilised if another photon activates a nearby region in the crystal resulting in the formation of a silver atom cluster. A silver atom cluster can form via two different methods: the first method is where the silver atom traps the electron liberated by the second photon forming a negative silver ion. This negative silver ion is then neutralised by another interstitial silver atom producing a cluster of two silver atoms. The second method is where the second electron reacts with another interstitial silver forming a second silver atom. The two silver atoms then form a cluster of two silver atoms. It has been shown that a latent image is formed of a minimum of four silver atoms. To transform the latent image into a visual image, the photographic film is treated with a developer. Only the crystals that have a latent image are fully reduced to metallic silver by the developer. A fixer is then used which removes the silver halide crystals that contain no latent images from the emulsion and renders the photographic film insensitive to light. It should be noted that if the photographic film was left exposed to light rather than being developed the photoreduction reaction would continue until all the silver halides had been reduced to metallic silver.

Silver has one of the highest electrical conductivities of  $6.30 \times 10^7$  S/m and has in the past been utilised as a conducting filler to improve the electrical conductivity of traditionally insulating materials.<sup>81-83</sup> Therefore, the *in-situ* formation of silver through the photoreduction of silver salts presents an efficient method to increase the conductivity of a material via light exposure. The light sensitive material required for the light sensor tag design was based on photographic films. The use of silver halides, however, introduce processing limitations due to the fact that they are extremely light sensitive. They are also water insoluble which is the reason why they are formed in the gelatin matrix via the reaction with silver nitrate and alkali metal halides to ensure they are evenly distributed. Silver nitrate, whilst also a silver salt is not light sensitive - this is due to the fact that the nitrate ion cannot be oxidised and therefore an electron is not produced for the silver ion

to be reduced. However, it has been shown that silver nitrate can become light sensitive in the presence of organic materials. Silver nanoparticles have been produced via the photoreduction of silver nitrate in the presence of poly(N-vinylpyrrolidone),<sup>84,85</sup> cellulose acetate<sup>86</sup> and polyvinylalcohol (PVA).<sup>87-89</sup> These organic matrices act as the electron donors for the reduction of the silver ion.

## 1.11 Polyvinyl alcohol

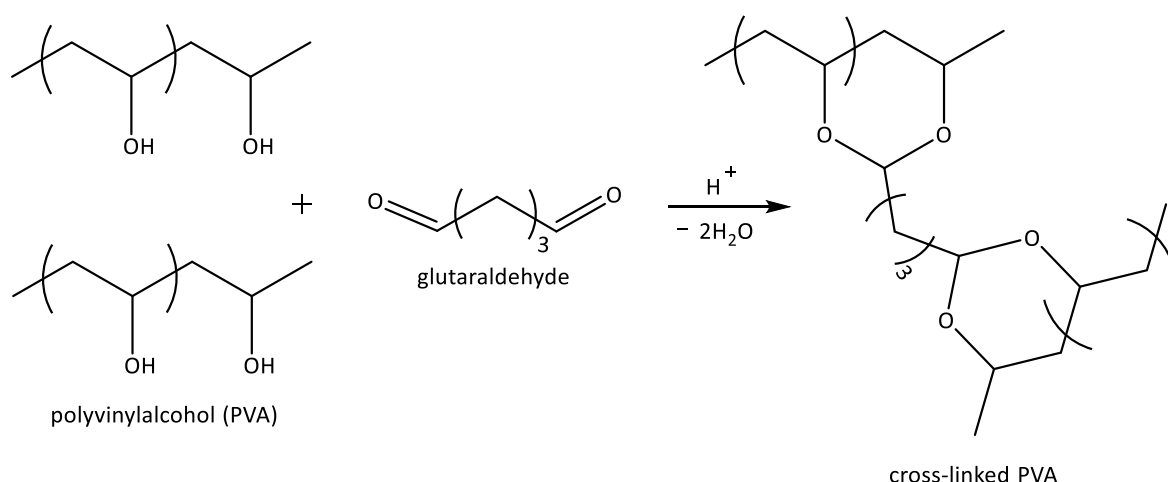
Polyvinyl alcohol (PVA) is a polyhydroxyl polymer with the structural formula  $(-\text{CH}_2\text{CHOH}-)_n(-\text{CH}_2\text{CHOCOCH}_3-)_m$  and was discovered in 1924 by scientists Herrman and Haehnel.<sup>90</sup> It is a dry solid which is white to yellow in colour and can be found in either granulated or powdered forms. PVA has many desirable properties which has led to its use in a range of products including lacquers, surgical threads, food packaging materials and adhesives. It is biodegradable, water soluble, non-toxic and hydrophilic. PVA is formed through either the acidic or alkaline hydrolysis of polyvinyl acetate,<sup>91</sup> though alkaline hydrolysis is the preferred method used in industry and is shown in Scheme 1.8.<sup>92</sup> This reaction is also referred to as saponification or transesterification. Typically sodium or potassium hydroxide catalysts are used along with methanol as the solvent.



*Scheme 1.8: Alkaline hydrolysis of polyvinyl acetate to polyvinyl alcohol*

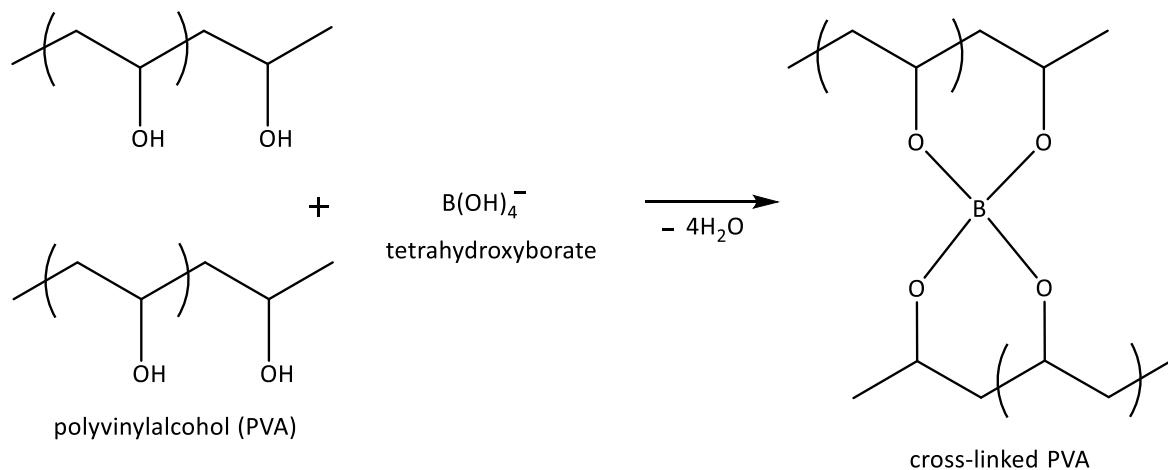
In the acidic hydrolysis of polyvinyl acetate, water is used as the solvent along with sulfuric acid as the catalyst and acetic acid is produced as the by-product. PVA can be classified according to the degree of hydrolysis, the three main commercial grades of PVA are: (i) fully hydrolysed (1 – 2 mol% residual acetate groups), intermediate hydrolysed (3 – 7 mol% residual acetate groups) and partially hydrolysed (10 – 15 mol% residual acetate groups). The degree of hydrolysis is extremely important as it dictates both the chemical and physical properties of the polymer,<sup>93</sup> for example PVA grades with a high degree of hydrolysis are less water soluble and are more difficult to crystallize. For a wide variety of applications including medical and water treatment PVA is cross-linked to form a hydrogel. A hydrogel can be described as a cross-linked network of hydrophilic polymer chains which swells in contact with water. PVA hydrogels can be synthesised by both chemical and physical methods. The most common methods of chemically cross-linking PVA is the use of dialdehyde cross-linkers such as glutaraldehyde, sodium borate cross-linkers and electron beam or  $\gamma$ -irradiation treatment. Physically cross-linked PVA hydrogels can be formed via ‘freeze/thawing’

methods. The 1, 3 diol units of PVA react with dialdehydes in the presence of acid, usually sulfuric acid to form acetal cross-links<sup>94</sup> as shown in Scheme 1.9. This reaction is known as acetalization.



*Scheme 1.9: PVA cross-linking reaction using a dialdehyde cross-linker.*

The cross-linking of PVA with sodium borate is an example of a condensation reaction. When sodium borate is dissolved in water it forms boric acid, H<sub>3</sub>BO<sub>3</sub> which accepts a further hydrogen from water resulting in the formation of tetrahydroxyborate B(OH)<sub>4</sub><sup>-</sup>. The condensation of tetrahydroxyborate and PVA results in borate ester cross-links (Scheme 1.10) and water which is trapped within the cross-linked PVA.



*Scheme 1.10: PVA cross-linking reaction using sodium borate as a cross-linker*

Radiation cross-linking of PVA offers several advantages over other chemical cross-linking methods: no catalysts or cross-linkers are required therefore no undesirable residues are left over and further purification is not required, the reaction conditions are mild and the gelation process is fast. When oxygen-free PVA solutions are irradiated, polymer radicals are formed via hydrogen abstraction by the  $\cdot\text{H}$  and  $\cdot\text{OH}$  radicals arisen from the water molecules. Hydrogen atoms are abstracted from the  $-\text{CH}(\text{OH})-$  and/or  $-\text{CH}_2-$  groups of PVA and the resulting polymer radicals can either interact with one another by disproportion or combination.<sup>95</sup> Physical cross-linking of PVA by freeze/thawing

methods is due to crystallite formation. This cross-linking method does not require the presence of a cross-linker and the resulting PVA hydrogels exhibit higher mechanical strengths compared to chemically cross-linked PVA hydrogels. The properties of these hydrogels formed via free/thawing methods depends on the PVA molecular weight, temperature of freezing, time of freezing and thawing and the number of freeze/thaw cycles. It has been shown that as the molecular weight and number of freeze/thaw cycles increase, the hydrogel structure becomes denser. Also, the number of crystallites increase with increasing PVA concentration.<sup>96</sup>

Another property that has made PVA so desirable for many applications is its film-forming ability. PVA films are formed through the removal of water from aqueous PVA solutions through drying. The characteristics and properties of PVA films are dependent on the drying process, for example the crystallinity of PVA can change during drying. It has been shown that as an aqueous PVA solution dries a 'skin' is formed above the PVA solution at the polymer-air interface.<sup>97</sup> This 'skin' is made up of a glassy polymer region. The glass transition temperature ( $T_g$ ) of PVA is lowered by the water and therefore as the water evaporates, the  $T_g$  increases resulting in a polymer transition from rubbery to glassy. At this point the resulting polymer solution is made up of two regions: a glassy region and rubbery region.<sup>98</sup> The glassy polymer region subsequently slows down the diffusion of water out of the PVA solution thus changing the rate of drying. The glassy region increases in size until a PVA film is formed. The polymer can undergo solvent-induced crystallisation, however, as the solvent is removed crystallisation cannot occur due to the limited mobility of the polymer. There are several methods in which polymer solutions can be deposited onto substrates such as, solution casting, dip coating and spin coating. Solution casting is simply when the polymer solution is deposited onto the surface and allowed to dry. Dip coating is a variation of solution casting except the substrate is dipped into the polymer solution and removed. The spin coating method uses centrifugal force to form polymer films with uniform heights. The polymer solution is deposited onto the centre of a substrate which is then spun at high speeds. As a result of centrifugal force the polymer solution flows outwards towards the edges coating the substrate. Evaporation of the solvent i.e. film drying also occurs during the spinning. The final film thickness depends mainly on the solution viscosity and spin speed.

## 1.12 Aims and Objectives

The overall aim of the work in this thesis is to fabricate and investigate the use of stimulus responsive polymers as sensing components in three UHF-RFID sensor tag designs; an epidermal strain sensor, a solvent vapour sensor and a light sensor. A further aim is to achieve ink-jet printing of a sensing component to work towards fully printed UHF-RFID tags.

Chapter one of this thesis has introduced RFID technology, RFID tags, passive UHF-RFID sensor tags and stimulus responsive polymers. In addition, the three UHF-RFID sensor tag designs; an

epidermal strain sensor, a solvent vapour sensor and a light sensor were described as well as the type of stimulus responsive polymers required to act as the sensing component for each design.

Chapter two of this thesis describes the investigation of PDMS elastomers as a substrate for an epidermal strain sensor design, along with the fabrication and performance testing of the tag prototype. The addition of a polar cross-linker and BaTiO<sub>3</sub> filler were the two methods explored to increase the permittivity of the PDMS elastomers to the desired value required for the tag design to function. Both adhesion using silicone glue and self-adhesion techniques were investigated as a means of attaching the antenna to the substrate. The performance of the prototype tag was achieved using an adjustable PTFE jig to vary the strain loadings. Results found in this chapter have been published in O. O. Rakibet, C. V. Rumens, J. C. Batchelor and S. J. Holder, *IEEE Antenna and Wireless Propag. Lett.*, 2014, **13**, 814-817.

Chapters three, four and five of this thesis are dedicated to the investigation of the swelling of PDMS elastomers in solvent vapours for use as an actuator mechanism in a displacement solvent vapour tag design. Chapter three investigated the swelling extent of PDMS elastomers and other polysiloxane networks in several solvent vapours. A relationship between the swelling extents of PDMS elastomers in solvent vapours and the solubility parameters and vapour pressure of the solvents was explored. The diffusion behaviour of the solvent vapours into the PDMS elastomers and polysiloxane networks was examined in chapter four. The performance of the solvent vapour sensor prototype tag exposed to a range of solvent vapours using a PDMS elastomer as the actuator mechanism was reported in chapter five. A selection of results found in chapters three, four and five have been published in C. V. Rumens, M. A. Ziai, K. Belsey, J. C. Batchelor and S. J. Holder, *J. Mater. Chem. C*, 2015, **3**, 10091-10098.

Chapter six of this thesis describes the investigation into ink-jet printing Sylgard 184<sup>®</sup>. Ink formulations containing varying amounts of Sylgard 184<sup>®</sup> were prepared and the surface tension of each ink was measured. The ink formulation with the surface tension closest to the value recommended for the ink-jet printer was used to print both discrete droplets and continuous films onto glass substrates.

Chapter seven of this thesis describes the investigation into using silver nitrate-PVA composites as a short circuit when exposed to light in a light sensor tag design. The photo-formation of silver nanoparticles within a PVA matrix was explored both in solution and thin films before the resistance of the silver nitrate-PVA composite films was measured over a period of light exposure time.

Chapter eight of this thesis presents the overall conclusions of the research undertaken in this thesis and describes any further work that could be undertaken.

## 1.13 References

- 1 C. M. Roberts, *Comput. Secur.*, 2006, **25**, 18-26.
- 2 J. Landt, *IEEE Potentials*, 2005, **24**, 8-11.
- 3 K. Domdouzis, B. Kumar and C. Anumba, *Adv. Eng. Inform.*, 2007, **21**, 350-355.
- 4 *US Pat.*, 3713148A, 1973.
- 5 A. R. Koelle, S. W. Depp and R. W. Freyma, *Proc. IEEE*, 1975, **63**, 1260-1261.
- 6 F. Thornton, B. Haines, A. M. Das, H. Bhargava, A. Campbell and J. Kleinschmidt (technical editor), *RFID Security*, Syngress, Rockland, 2006.
- 7 G. M. Gaukler and R. W. Seifert, in *Trends in supply chain design and management*, ed. H. Jung, F. F. Chen and B. Jeong, Springer-Verlag, London, 2007, ch. 2, pp. 29-48.
- 8 E. Ilie-Zudor, Z. Kemeny, P. Egri and L. Monostori, in *Proceedings of the 8<sup>th</sup> International Conference on The Modern Information Technology in the Innovation Processes of the Industrial Enterprises, MITIP 2006*, pp. 29-36.
- 9 K. Ahsan, H. Shah and P. Kingston, *IJCSI*, 2010, **7**, pp. 1-7.
- 10 L. Zhekun, R. Gadh and B. Prabhu, in *Proceedings of the ASME International Design Engineering Technical Conferences and Computers and Information in Engineering Conference*, 2004, vol. 4, pp. 123-129.
- 11 D. Wu, W. W. Ng, D. S. Yeung and H. Ding, in *Proceedings of the 8<sup>th</sup> International Conference on Machine Learning and Cybernetics*, 2009, pp. 2330-2335.
- 12 C. Rong, G. Zhao, L. Yan, E. Cayirci and H. Cheng, in *Computer and Information Security Handbook*, ed. J. R. Vacca, Morgan Kaufmann, Waltham, 2013, ch. 18, pp. 345-360.
- 13 R. Want, *IEEE Pervasive Computing*, 2006, **5**, 25-33.
- 14 E. C. Jones and C. A. Chung, *RFID in Logistics: A Practical Introduction*, CRC press, Boca Raton, 2007.
- 15 A. A. Babar, V. A. Bhagavati, L. Ukkonen, A. Elsherbeni, P. Kallio and L. Sydänheimo, *Int. J. Antenn. Propag.*, 2012, **2012**, 1-8.

- 16 A. Ruhanen, M. Hanhikorpi, F. Bertucelli, A. Colonna, W. Malik, D. Ranasinghe, T. S. López, N. Yan and M. Tavilampi, *BRIDGE*, 2008.
- 17 P. Puligundla, J. Jung and S. Ko, *Food Control*, 2012, **25**, 328-333.
- 18 L. Zhang and Z. Wang, in *Proceedings of the Fifth International Conference on Grid and Cooperative Computing Workshops*, IEEE, 2006, pp. 463-469.
- 19 A. Mainwaring, D. Culler, J. Polastre, R. Szewczyk and J. Anderson, in *Proceedings of the 1st ACM international workshop on Wireless sensor networks and applications*, 2002, pp. 88-97.
- 20 C. Englund and H. Wallin, *RFID in Wireless Sensor Network*, Technical Report, Department of Signals and Systems, Chalmers University of Technology, Sweden, 2004.
- 21 J. Fernández-Salmerón, A. Rivadeneyra, F. Martínez-Martí, L. F. Capitán-Vallvey, A. J. Palma and M. A. Carvajal, *Sensors*, 2015, **15**, 26769-26782.
- 22 J. Virtanen, L. Ukkonen, T. Björninen, L. Sydänheimo and A. Z. Elsherbeni, in *Sensors Applications Symposium (SAS)*, IEEE, 2011, pp. 312-317.
- 23 E. Abad, F. Palacio, M. Nuin, A. G. De Zarate, A. Juarros, J. Gómez and S. Marco, *J. Food Eng.*, 2009, **93**, 394-399.
- 24 N. Cho, S. Song, S. Kim, S. Kim and H. Yoo, in *Proceedings of ESSCIRC*, IEEE, 2005, pp. 279-282.
- 25 J. Gao, J. Sidén and H. Nilsson, in *Progress in Electromagnetics Research Symposium Proceedings*, 2010, pp. 845-848.
- 26 R. Bhattacharyya, C. Di Leo, C. Floerkemeier, S. Sarma and L. Anand, in *IEEE Sensors 2010 Conference Proceedings*, 2010, pp. 2363-2368.
- 27 J. Virtanen, L. Ukkonen, T. Björninen, A. Z. Elsherbeni and L. Sydänheimo, *IEEE Trans. Instrum. Meas.*, 2011, **60**, 2768-2777.
- 28 K. Chang, Y. Kim, Y. Kim and Y. J. Yoon, *Electron. Lett.*, 2007, **43**, 7-8.
- 29 J. Siden, X. Zeng, T. Unander, A. Koptuyug and H. Nilsson, in *IEEE Sensors 2007 Conference Proceedings*, 2007, pp. 308-311.
- 30 S. Manzari, C. Occhiuzzi, S. Nawale, A. Catini, C. Di Natale and G. Marrocco, *IEEE Sensors J.*, 2012, **12**, 2851-2858.



- 31 R. A. Potyrailo and W. G. Morris, *Anal. Chem.*, 2007, **79**, 45-51.
- 32 L. K. Fiddes and N. Yan, *Sensors Actuators B: Chem.*, 2013, **186**, 817-823.
- 33 C. Occhiuzzi, C. Paggi and G. Marrocco, *IEEE Trans. Antennas Propag.*, 2011, **59**, 4836-4840.
- 34 X. Yi, C. Cho, J. Cooper, Y. Wang, M. M. Tentzeris and R. T. Leon, *Smart Mater. Struct.*, 2013, **22**, 085009.
- 35 R. Bhattacharyya, C. Floerkemeier and S. Sarma, in 2009 IEEE International Conference on RFID Proceedings, IEEE, 2009, pp. 95-102.
- 36 S. Merilampi, P. Ruuskanen, T. Björninen, L. Ukkonen and L. Sydänheimo, in [\*the 3rd International Symposium on Applied Sciences in Biomedical and Communication Technologies \(ISABEL\) 2010 Proceedings\*](#), pp. 1-5.
- 37 E. M. Amin, R. Bhattacharyya, S. Sarma and N. C. Karmakar, in *Antennas and Propagation Society International Symposium Proceedings*, IEEE, 2014, pp. 1308-1309.
- 38 D. Schmaljohann, *Adv. Drug Deliv. Rev.*, 2006, **58**, 1655-1670.
- 39 M. A. C. Stuart, W. T. Huck, J. Genzer, M. Müller, C. Ober, M. Stamm, G. B. Sukhorukov, I. Szleifer, V. V. Tsukruk and M. Urban, *Nature Mater.*, 2010, **9**, 101-113.
- 40 B. Jeong and A. Gutowska, *Trends Biotechnol.*, 2002, **20**, 305-311.
- 41 R. J. Young and P. A. Lovell, *Introduction to Polymers*, CRC press, Boca Raton, 2011.
- 42 A. K. Bhowmick, in *Material Science and Engineering Volume 1*, ed. R. D. Rawlings, Eolss Publishers, Oxford, 2009, pp. 157-220.
- 43 H. F. Mark (ed.), *Encyclopedia of Polymer Science and Technology*, John Wiley & Sons, Hoboken, 2007.
- 44 D. François, A. Pineau and A. Zaoui, *Mechanical Behaviour of Materials Vol. 1: Micro- and Macroscopic Constitutive Behaviour*, Springer, London, 2012.
- 45 B. Xiong, PhD thesis, INSA Lyon, 2014.
- 46 R. A. Shanks and I. Kong, in *Advances in Elastomers I*, ed. P. M. Visakh, S. Thomas, A. K. Chandra and A. P. Mathew, Springer, New York, 2013, p. 11-45.

- 47 U. Schubert and N. Hüsing, *Synthesis of Inorganic Materials*, Wiley-VCH, Weinheim, 2012.
- 48 S. B. Lin, D. Durfee, A. A. Knott and G. K. Schallau II, in *Technology of Pressure-Sensitive Adhesives and Products*, ed. I. Benedek and M. M. Feldstein, CRC Press, Boca Raton, 2008, ch. 6, pp. 6/1-25.
- 49 D. Ahn and A. Dhinojwala, in *Silicone Surface Science*, ed. M. J. Owen and P. R. Dvornic, Springer, New York, 2012, ch. 2, pp. 23-54.
- 50 A. J. Pearmain and A. Haddad, in *Electrical Engineer's Reference Book*, ed. M. A. Laughton and D. F. Warne, Elsevier, Oxford, 2003, pp. 7/1-36.
- 51 W. Gao and N. M. Sammes, *An Introduction to Electronic and Ionic Materials*, World Scientific, Singapore, 1999.
- 52 J. Chen, in *Introduction to Organic Electronic and Optoelectronic Materials and Devices*, eds. S-S. Sun and L. R. Dalton, CRC Press, Boca Raton, 2017, ch. 28.
- 53 G. Gallone, F. Carpi, D. De Rossi, G. Levita and A. Marchetti, *Mater. Sci. Eng. C Mater. Biol. App.*, 2007, **27**, 110-116.
- 54 F. Carpi and D. D. Rossi, *IEEE Trans. Dielectr. Electr. Insul.*, 2005, **12**, 835-843.
- 55 E. A. Cherney, *IEEE Trans. Dielectr. Electr. Insul.*, 2005, **12**, 1108-1115.
- 56 Y. Shen, E. A. Cherney and S. H. Jayaram, in *the Conference Record of the 2004 IEEE International Symposium on Electrical Insulation*, 2004, pp. 320-323.
- 57 L. Yu and A. L. Skov, *International Journal of Smart and Nano Materials*, 2015, **6**, 268-289.
- 58 Y. Lou, A. Robisson, S. Cai and Z. Suo, *J. Appl. Phys.*, 2012, **112**, 034906.
- 59 S. Z. Qamar, M. Akhtar, T. Pervez and M. S. Al-Kharusi, *Mater. Design*, 2013, **45**, 487-496.
- 60 B. A. Miller-Chou and J. L. Koenig, *Prog. Polym. Sci.*, 2003, **28**, 1223-1270.
- 61 W. Woishnis and S. Ebnesajjad, *Chemical Resistance of Thermoplastics*, Elsevier, Oxford, 2011.
- 62 Q. Liu and M. C. Leu, in *Proceedings of the Materials & Processes for Medical Devices Conference*, Ed. S. Shrivastava, 2003, pp. 438-443.
- 63 C. M. Hansen, in *Paint and Coating Testing Manual*, Ed. J. V. Koleske, ASTM, Philadelphia, 1995, Ch. 35, pp. 383-406.

- 64 C. M. Hansen, *Hansen Solubility Parameters: A User's Handbook*, CRC press, Boca Raton, 2007.
- 65 D. Klinger, *Light-sensitive Polymeric Nanoparticles Based on Photo-Cleavable Chromophores*, Springer, New York, 2013.
- 66 F. P. Nicoletta, D. Cupelli, P. Formoso, G. De Filipo, V. Colella and A. Gugliuzza, *Membranes*, 2012, **2**, 134-197.
- 67 Y. Yu, M. Nakano and T. Ikeda, *Nature*, 2003, **425**, 145-145.
- 68 C. Alvarez-Lorenzo, L. Bromberg and A. Concheiro, *Photochem. Photobiol.*, 2009, **85**, 848-860.
- 69 C. Chung, Y. Roh, S. Cho and J. Kim, *Chem. Mater.*, 2004, **16**, 3982-3984.
- 70 A. Lendlein, H. Jiang, O. Jünger and R. Langer, *Nature*, 2005, **434**, 879-882.
- 71 S. Samanta and J. Locklin, *Langmuir*, 2008, **24**, 9558-9565.
- 72 H. Lee, W. Wu, J. K. Oh, L. Mueller, G. Sherwood, L. Peteanu, T. Kowalewski and K. Matyjaszewski, *Angew. Chem. Int. Ed.*, 2007, **119**, 2505-2509.
- 73 M. Irie, T. Iwayanagi and Y. Taniguchi, *Macromolecules*, 1985, **18**, 2418-2422.
- 74 A. Kocer, M. Walko, W. Meijberg and B. L. Feringa, *Science*, 2005, **309**, 755-758.
- 75 C. A. Daniels, *Polymers: Structure and Properties*, Technomic Publishing Company Ltd., Lancaster, 1989.
- 76 A. Ravve, *Principles of Polymer Chemistry*, Springer, New York, 2012.
- 77 M. Goosey, in *Specialty Polymers*, ed. R. W. Dyson, Blackie, Glasgow, 1987, pp. 83-109.
- 78 M. Stolka, in *Special Polymers for Electronics and Optoelectronics*, ed. J. A. Chilton and M. Goosey, Springer Science+Business Media, Dordrecht, 1995, pp. 284-314.
- 79 S. Fujita, in *Organic Chemistry of Photography*, Springer-Verlag, Heidelberg 2004.
- 80 R. Jacobson, S. Ray, G. G. Attridge and N. Axford, *Manual of Photography*, Focal Press, Oxford, 2000.
- 81 P. C. Ma, B. Z. Tang and J. Kim, *Carbon*, 2008, **46**, 1497-1505.

- 82 S. Mahendia, A. Tomar and S. Kumar, *J. Alloys Compounds*, 2010, **508**, 406-411.
- 83 H. Jiang, K. Moon, Y. Li and C. Wong, *Chem. Mater.*, 2006, **18**, 2969-2973.
- 84 H. Huang, X. Ni, G. Loy, C. Chew, K. Tan, F. Loh, J. Deng and G. Xu, *Langmuir*, 1996, **12**, 909-912.
- 85 S. Maruo and T. Saeki, *Optics Express*, 2008, **16**, 1174-1179.
- 86 W. K. Son, J. H. Youk and W. H. Park, *Carbohydr. Polym.*, 2006, **65**, 430-434.
- 87 G. Gaddy, J. McLain, E. Steigerwalt, R. Broughton, B. Slaten and G. Mills, *J. Cluster Sci.*, 2001, **12**, 457-471.
- 88 A. Kutsenko and V. Granchak, *Theoretical and Experimental Chemistry*, 2009, **45**, 313-318.
- 89 S. Clemenson, D. Léonard, D. Sage, L. David and E. Espuche, *J. Polym. Sci. A Polym. Chem.*, 2008, **46**, 2062-2071.
- 90 C. Haweel and S. Ammar, *Iraqi J. Chem. Petrol. Eng.*, 2008, **9**, 15-21.
- 91 K. K. M. Nthoiwa, C. A. Diaz and Y. Chaudhari, in *Handbook of Thermoplastics*, ed. O. Olabisi and K. Adewale, CRC press, Boca Raton, 2016, ch. 2.
- 92 I. Sakurada, *Polyvinyl Alcohol Fibers*, Marcel Dekker Inc., New York, 1985.
- 93 T. S. Gaaz, A. B. Sulong, M. N. Akhtar, A. A. H. Kadhum, A. B. Mohamad and A. A. Al-Amiery, *Molecules*, 2015, **20**, 22833-22847.
- 94 W. H. Philipp and L. Hsu, Technical Report, NASA Lewis Research Center, 1979.
- 95 V. M. Nikolic, A. Krkljes, Z. K. Popovic, Z. V. Lausevic and S. S. Miljanic, *Electrochem. Commun.*, 2007, **9**, 2661-2665.
- 96 S. K. Mallapragada and S. McCarthy-Shroeder, in *Handbook of Pharmaceutical Controlled Release Technology*, ed. D. L. Wise, Marcel Dekker Inc., New York, 2000, ch. 2.
- 97 S. Ghoshal, P. Denner, S. Stapf and C. Mattea, *Macromolecules*, 2012, **45**, 1913-1923.
- 98 M. O. Ngui and S. K. Mallapragada, *Polymer*, 1999, **40**, 5393-5400.

# Chapter 2: Fabrication of BaTiO<sub>3</sub>-PDMS composites as substrates for passive wireless epidermal UHF-RFID strain sensors

## 2.0 Introduction

Passive RFID strain sensors have found applications in both structural health monitoring (SHM) of damaged structures and vehicles and the monitoring of human body movements. These sensors are ideal for both applications due to their low cost, wireless monitoring with a non-line of sight operation capabilities, long read range and ability to be embedded into objects. A passive RFID strain sensor design based on a meander-line antenna (MLA) was proposed by Occhiuzzi *et al.*<sup>1</sup> A copper wire MLA with one turn either side of a tuning T-match section was used. This sensor can measure strain through a change in the antenna's input impedance and radiation performance caused by the elongation of the MLA when vertical stress is applied. A RFID folded patch antenna sensor design has shown the ability to detect strain changes from 20  $\mu\epsilon$  to as high as 10,000  $\mu\epsilon$ .<sup>2</sup> This sensor relies on a shift in resonance frequency caused by antenna deformation as a result of applied strain, which introduces mismatching between the chip and antenna. The authors found a linear relationship between normalised frequency change and strain.

A slot stretchable antenna design for a passive strain gauge sensor was proposed by Rakibet.<sup>3</sup> The sensor operated using the principle of detuning slots; as the slot dimensions changed as a result of antenna stretching, the resonant frequency of the antenna varied. Simulations using a single port slot antenna showed x-axis stretching of the antenna caused an increase in resonant frequency, while y-axis stretching caused a decrease as shown in Figure 2.0. In both cases there was a linear relationship between resonant frequency and stretch percentage. These results showed the viability of this antenna design as a strain sensor which could be used as an actuator in assisted living applications due to its ability to determine strain direction. For example, this design could be used to allow paraplegic patients to control their wheelchair through facial muscle tweaking.

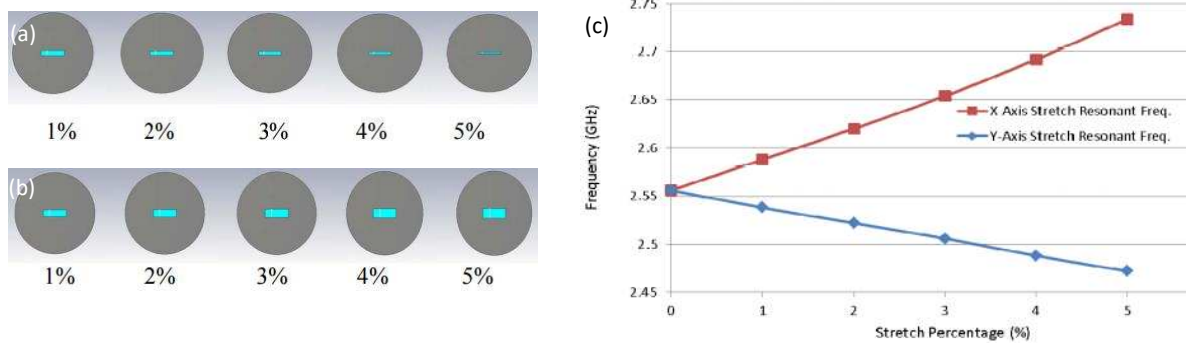


Figure 2.0: (a) X-axis and (b) Y-axis stretching effect on single slot stretchable antenna design. (c) Simulation results showing the effect of stretch percentage on resonant frequency © 2012 IEEE.<sup>3</sup>

For this sensor design to operate experimentally for the previous application, the following two design challenges had to be met: (1) fabrication of an elastic dielectric substrate that can withstand repetitive stretching and (2) fabrication of a stretchable conductive antenna and formulate a method to attach it to the substrate.

Polydimethylsiloxane (PDMS) elastomers showed great promise as the candidate for the tag substrate. They have many desirable properties such as chemical and heat resistance, a non-toxic nature<sup>4</sup>, good flexibility and elastic properties. The one disadvantage of PDMS is its low permittivity (dielectric constant) of around 2.3. The simulations of the proposed strain gauge design by Rakibet used a silicone substrate with a permittivity of 3.1, therefore the aim was to produce a PDMS substrate with a similar permittivity value. A larger permittivity also prevents the mismatching between the antenna and chip that is often caused when the tag is placed on a high dielectric surface, such as the human body. Addition of polar groups could be used to increase the relative permittivity of the PDMS elastomer as materials with polar groups in their molecular structure have high relative permittivities because their dipoles are able to orient in an electric field and have large dipole moments.<sup>5</sup> There has been much interest in increasing the polarity or hydrophilicity of PDMS for applications such as microfluidic and biomedical devices through PDMS surface functionalisation via oxygen plasma, UV ozone and chemical treatment. However, surface polar functionalisation alone would not contribute to the increase in permittivity of the bulk material desired. Another method is to use a polar functionalised siloxane copolymer. Gankema *et al.* synthesised a siloxane copolymer containing cyanopropyl groups by anionic copolymerisation of functionalised cyclotetrasiloxanes.<sup>6</sup> The polarity of the final siloxane copolymer could be tuned by varying the amount of cyanopropyl functionalised cyclotetrasiloxane used in the copolymerisation. Instead of using a polar functionalised siloxane homopolymer or copolymer, a polar functionalised cross-linker - 2-cyanotriethoxysilane (TESPN) was chosen.

Another well-established method to improve polymer permittivity is the use of high permittivity inorganic fillers. Addition of ferroelectric/piezoelectric ceramics such as lead magnesium niobate-lead titanate (PMN-PT),<sup>7</sup> titanium dioxide (TiO<sub>2</sub>)<sup>8,9</sup> and barium titanate (BaTiO<sub>3</sub>)<sup>10,11</sup> have shown to

significantly increase polymer permittivity. Multi-fillers and the addition of powder metals, such as aluminium have also shown to increase polymer permittivity.<sup>12</sup> Barium titanate was chosen in this study as the filler material as it has shown to exhibit extremely high permittivity values, it is commercially available and there have been well reported methods for its incorporation into polymers. Silver Lycra® (polyether/polyurea urethane polymer fibres embedded with silver nanoparticles) was chosen as the antenna material as it is conductive and can retain both its shape and electrical properties after repeated stretching.

In this chapter, both the introduction of a more polar cross-linker TESPN and addition of barium titanate to PDMS elastomers were investigated as methods to increase the permittivity of the PDMS elastomers to the desired value of 3.1.<sup>3</sup> The best method of attaching the silver Lycra® antenna to the PDMS substrate was also explored and a UHF RFID epidermal strain-sensor tag prototype was fabricated and tested under varying strain loadings.

## 2.1 Experimental

### 2.1.1 Materials and Apparatus

Silanol-terminated polydimethylsiloxane cSt 1000 (DMS-S31) (M. W. 26,000, Fluorochem Ltd.), silanol-terminated polydimethylsiloxane cSt 18000 (DMS-S42) (M. W. 77,000, Fluorochem Ltd.), tin (II) 2-ethylhexanoate (95%, Sigma Aldrich), toluene (analytical reagent grade, Fisher Chemicals), tetraethyl orthosilicate (99%, Sigma Aldrich), 2-cyanoethyltriethoxysilane (Fluorochem Ltd.) and barium titanate (< 2µm 99.9% trace metal basis, Sigma Aldrich), medical silicone adhesive (Makeup International), Telesis silicone adhesive, Skin Tite silicone adhesive ([www.smooth-on.com](http://www.smooth-on.com)), silver Lycra® (0.5 mm thickness) ([www.mindsetonline.co.uk](http://www.mindsetonline.co.uk)), NXP UHF RFID chip (Higgs3 RFID chip provided by Alien Technology), copper clad Mylar sheet (DuPont Teijin Films) and flexible filling knife were used as received. Homogenous mixing of composite components was achieved using a RCT basic IKA labortechnik speed-mixer and all moulds used were fabricated out of PTFE to ensure easy removal of the cured composite.

### 2.1.2 Synthesis of TEOS and TESPN cross-linked elastomers

Silanol-terminated PDMS (16.5 g, 1.27 mmol), and tetraethyl orthosilicate (with the ratio of SiOH groups in PDMS to SiOR groups in TEOS at 1:1 and 1:4) or 2-cyanoethyltriethoxysilane (with the ratio of SiOH groups in PDMS to SiOR groups in TESPN at 1:1 and 1:3) were added to a glass beaker and speed-mixed for 30 seconds. Table 2.2 displays the moles of tetraethyl orthosilicate and 2-cyanoethyltriethoxysilane used. Tin (II) 2-ethylhexanoate dissolved in toluene (0.755 cm<sup>3</sup>, 1.51 mmol) was then added to the mixture and speed-mixed for 30 seconds before being poured into the rectangular mold (width = 3 cm, length = 5.8 cm). The elastomers were allowed to cure at room temperature for 10-15 minutes before being placed into an oven at 60 °C overnight. Heating in an

oven ensures the full removal of ethanol and makes sure the elastomers were completely cured. The elastomers structures were confirmed by FTIR spectroscopy.

*FTIR (cm<sup>-1</sup>) PDMS:* 2966 (CH<sub>3</sub>, CH str); 1438 (Si – CH<sub>3</sub>, CH<sub>3</sub> asym def); 1261 (Si – CH<sub>3</sub>, CH<sub>3</sub> sym def); 1103, 1020 (Si-O-Si str); 786 (Si - C str and CH<sub>3</sub> rock); 862, 704, 646 (not identified).

*FTIR (cm<sup>-1</sup>) TEOS:* 2981 (CH<sub>3</sub>, C – H asym str); 2929 (CH<sub>2</sub>, C – H asym str), 2890 (C-H asym str); 1443 (CH<sub>3</sub>, C - H asym bend); 1391 (CH<sub>3</sub>, C – H sym bend); 1294 (C – H twist/wag); 1164, 995 (CH<sub>3</sub>, C – H rock); 1072 (C – O asym str); 779 (SiO<sub>4</sub> asym); 525 (O – C – C def); 1203 (not identified).

*FTIR (cm<sup>-1</sup>) TESPN:* 2981 (CH<sub>3</sub>, C – H asym str); 2929 (CH<sub>2</sub>, C – H asym str), 2890 (C-H asym str); 2245 (C – N str); 1443 (CH<sub>3</sub>, C - H asym bend); 1391 (CH<sub>3</sub>, C – H sym bend); 1319 (C – C (ethyl) str); 1294 (C – H twist/wag); 1196 (C – C(N) str); 1164, 995 (CH<sub>3</sub>, C – H rock); 1072 (C – O asym str); 1004, 880, 742 (CH<sub>2</sub> rock); 642 (C – C – C bend) 525 (O – C – C def); 1203 (not identified).

### 2.1.3 Synthesis of BaTiO<sub>3</sub>-PDMS composite elastomers

Silanol-terminated PDMS (12 g, 0.156 mmol) and BaTiO<sub>3</sub> (particle loading in the range of 0 – 40 weight %) were added to a glass beaker and speed-mixed for 30 minutes. Tetraethyl orthosilicate (0.070 cm<sup>3</sup>, 0.336 mmol) was then added to the mixture and speed-mixed for 30 seconds. Tin (II) 2-ethylhexanoate dissolved in toluene (0.074 cm<sup>3</sup>, 0.148 mmol) was then added to the mixture and speed-mixed for 10 seconds before being poured into the rectangular mould. The elastomer was allowed to cure overnight at room temperature. The composites structure and distribution of BaTiO<sub>3</sub> was verified using FTIR, XRD spectra and SEM micrographs. The sample for FTIR and XRD analysis was a composite with 27.8 wt% barium titanate loading.

*FTIR (cm<sup>-1</sup>) BaTiO<sub>3</sub>-PDMS composite:* 2966 (CH<sub>3</sub>, CH str); 1450 (BaTiO<sub>3</sub>, carbonate ion impurities); 1438 (Si – CH<sub>3</sub>, CH<sub>3</sub> asym def); 1261 (Si – CH<sub>3</sub>, CH<sub>3</sub> sym def); 1103, 1020 (Si-O-Si str); 786 (Si - C str and CH<sub>3</sub> rock); 520 (Ti – O vibration); 865 and 660 (not identified).

### 2.1.4 Synthesis of BaTiO<sub>3</sub> pellet

Barium titanate (powder, < 2µm, 99% trace metal basis, Sigma Aldrich) was used as the starting material. The material was ground for 40 minutes using a mortar machine (Agate and General stonecutters Ltd) to ensure good packing of the pellet. Pellets for impedance measurements were pressed for 30 minutes at 1 ton pressure and fired at 1350°C overnight. Electrodes were prepared by coating the top and bottom of the pellet with silver conductive paint. The structure of the pellet was confirmed using X-ray diffraction (XRD) spectroscopy.

### 2.1.5 Measurements and Instruments

FTIR spectroscopic measurements were performed using a Shimadzu IRAffinity-1 spectrometer with a Specac Golden Gate™ ATR sampling accessory each sample was scanned 64 times at room temperature and atmospheric pressure with a resolution of 4 cm<sup>-1</sup>. For the FTIR spectroscopic



measurements the samples were clamped down using the Golden Gate™ to ensure a good optical contact between the sample and diamond was achieved. XRD measurements of the BaTiO<sub>3</sub> pellet and BaTiO<sub>3</sub>-PDMS composite was performed by L. V. Stimpson using a Bruker D8 Advance. Relative permittivity of the TEOS and TESP cross-linked PDMS elastomers and BaTiO<sub>3</sub>-PDMS composites was measured using both a rectangular waveguide (transmission/reflection line method) and dielectric assessment kit (DAK) (Speag) (coaxial probe method) attached to a vector network analyser. For the waveguide measurements the edge of the elastomers were tapered to produce a sloped edge and placed in the middle of the waveguide supported by polystyrene foam. Before any permittivity measurements of the elastomers were performed, a calibration measurement where the waveguide was empty apart from the supporting polystyrene foam was completed. For the permittivity measurements using the DAK, the probe was placed flush against the surface of the elastomers. Before any permittivity measurements, a calibration measurement using distilled water was performed. In the case of the calibration measurement the probe was placed under the surface of the water ensuring there were no air bubbles present on the underside of the probe. The permittivity of the elastomers was measured over the frequency range 3 – 6 GHz for both methods and the average permittivity was calculated. An impedance analyzer (4192A LF Impedance Analyzer 5 Hz – 13 Hz, Hewlett Packard) was used to measure the capacitance of the BaTiO<sub>3</sub> pellet which was in turn used to calculate relative permittivity. Electrodes were prepared by coating the top and bottom of the pellet with silver conductive paint and the pellet dimensions were measured using a micro meter, 0-25 mm range and 0.01 mm increment (T5450, Agar Scientific). Resistance measurements of the tag antenna were done using a resistance meter (ISO-TECH, IDM 201). The resistance was measured a total of 5 times and the average resistance was calculated. All tag simulations and RFID measurements were performed by O. O. Rakibet. Tag simulations were done using CST Microwave Studio and the RFID measurements were performed using the Voyantic TagperformanceLite UHF RFID characterisation system. In all RFID measurements, the sample was placed at a distance of 30 cm from the Voyantic TagperformanceLite antenna. For the RFID measurements of the prototype RFID stain sensor tag at varying strain loadings, an adjustable PTFE jig was constructed. The prototype tag was clamped into the jig at the right and left edges and top and bottom edges so strain along both the y axis and x axis could be achieved. The jig was placed at a distance of 30 cm from the Voyantic TagperformanceLite antenna and the transmitted power, dB was measured between 700 – 1200 MHz with a frequency step of 5 MHz for each strain measurement. Each strain measurement was repeated five times and the average was calculated.

## 2.2 Results and Discussion

### 2.2.1 Characterisation of TEOS and TESPON cross-linked PDMS elastomers, BaTiO<sub>3</sub>-PDMS elastomers and BaTiO<sub>3</sub> pellet

#### 2.2.1.1 TEOS and TESPON cross-linked PDMS elastomers

The elastomers produced were transparent and rubber like in appearance. As anticipated the elastomers with the higher cross-link density i.e. containing the larger ratio of cross-linker were slightly firmer. The FTIR spectra of pure PDMS, TEOS cross-linked PDMS elastomers and TEOS are shown in Figure 2.1 for comparison. Assignment of the FTIR absorption bands were made in accordance with literature reports.<sup>13,14</sup> As shown in figure 2.1, there is no broad absorption band around 3600 – 3100 cm<sup>-1</sup> for the Si-OH in pure PDMS due to the low relative concentration of OH to (CH<sub>3</sub>)<sub>2</sub>Si units. Therefore the hydroxyl groups could not be used as markers to show the cross-linking condensation reaction. It was also clear that the newly formed Si – O – Si groups as a result of cross-linking could not be distinguished from the large number of such bonds already present at 1020 and 1091 cm<sup>-1</sup> in pure PDMS. It has been shown that copolymerisation between Si-OH groups of hydrolysed TEOS and Si-OH groups of PDMS is characterised by an absorption band at 850 cm<sup>-1</sup>.<sup>1,14</sup> However, this characteristic absorption band was absent in the FTIR spectra of either elastomer though this could be due to masking by the band at 864 cm<sup>-1</sup>. The disappearance of the absorption band attributed to TEOS (2929 cm<sup>-1</sup>) in the FTIR spectra of the elastomers suggested cross-linking had occurred.

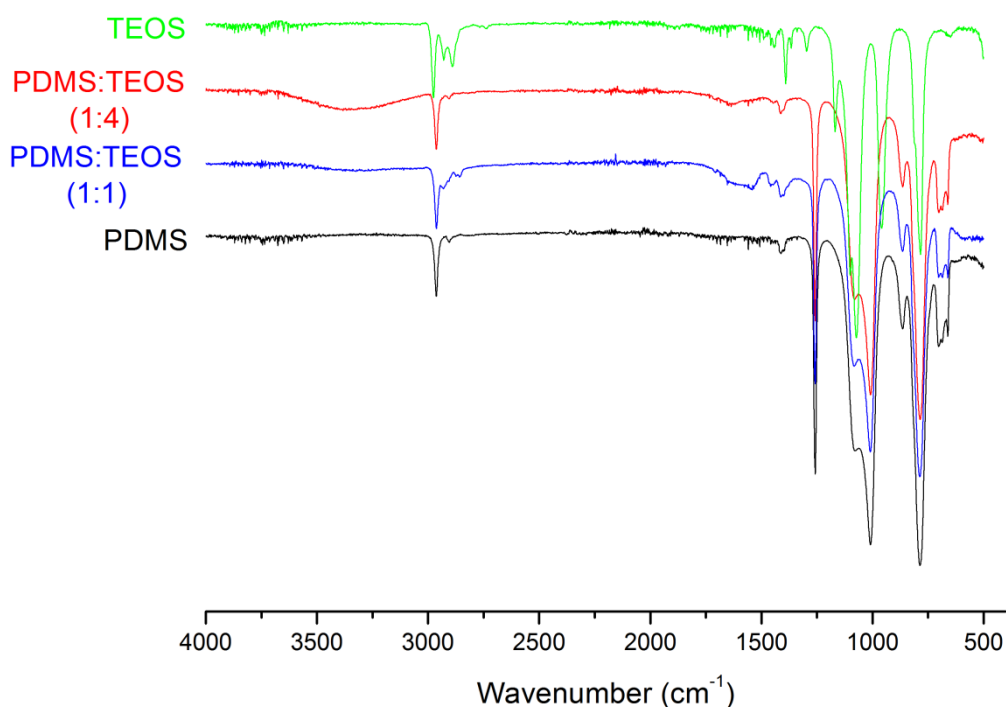


Figure 2.1: FTIR spectrum of pure PDMS, cross linked PDMS elastomers with varying ratio of TEOS cross linker and pure TEOS.

The broad absorption band at  $3400\text{ cm}^{-1}$  in the FTIR spectrum of the PDMS-TEOS 1:4 elastomers was attributed to hydrolysed excess TEOS. TEOS can undergo hydrolysis in acidic conditions before forming  $\text{SiO}_2$  via a water condensation reaction.<sup>15</sup> Evidence of hydrolysed TEOS was not shown in the FTIR PDMS-TEOS 1:1 elastomers confirming cross-linking had occurred. The absence of absorption bands at  $3391$  and  $881\text{ cm}^{-1}$  confirmed the by-product of the cross-linking reaction ethanol had been removed by heating during the curing process.

Figure 2.2 shows the FTIR spectra of pure PDMS, TESPN cross-linked PDMS elastomers and TESPN. TESPN displayed similar characteristic FTIR absorption bands as TEOS apart from the absence of the band at  $779\text{ cm}^{-1}$  ( $\text{SiO}_4$  asym str) and additional absorption bands associated with the propionitrile group ( $2245, 1319, 1196, 1004, 880, 742$  and  $642\text{ cm}^{-1}$ ).<sup>16</sup> None of these absorption bands were observed in the FTIR spectra of either PDMS-TESPN elastomer due to the low relative concentration of the propionitrile group within the elastomers.

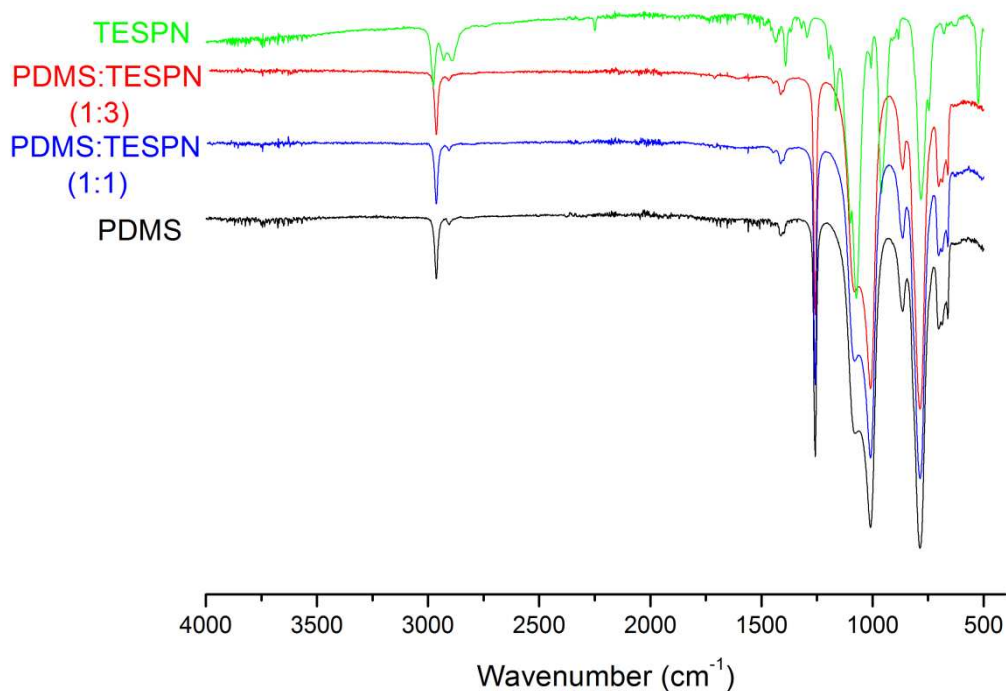


Figure 2.2: FTIR spectrum of pure PDMS, cross-linked PDMS elastomers with varying ratios of the TESPN cross linker and pure TESPN.

#### 2.2.1.2 BaTiO<sub>3</sub>-PDMS elastomers

Both FTIR spectroscopy and XRD was used to investigate the structure of the BaTiO<sub>3</sub>-PDMS elastomers, while SEM imaging was used to investigate the distribution of barium titanate within the composite elastomer. The FTIR spectra of pure BaTiO<sub>3</sub>, PDMS and a BaTiO<sub>3</sub> PDMS composite are shown in Figure 2.3. In the case of pure BaTiO<sub>3</sub>, a broad absorption band around  $500\text{ cm}^{-1}$ , due to the Ti-O vibration was observed.<sup>17</sup> Another absorption band was observed at around  $1450\text{ cm}^{-1}$ , previous research has attributed this peak to carbonate ion impurities.<sup>18</sup> In the FTIR spectra of the BaTiO<sub>3</sub> PDMS composite, characteristic absorption bands due to both BaTiO<sub>3</sub> and PDMS are

observed. There is no disappearance of PDMS absorption bands in the composite FTIR spectra indicating that there is no or minimal chemical interaction between the PDMS and BaTiO<sub>3</sub>. The broad absorption band due to BaTiO<sub>3</sub> at around 500 cm<sup>-1</sup> in the BaTiO<sub>3</sub> PDMS composite has a smaller transmission than the corresponding absorption band in pure BaTiO<sub>3</sub>. This difference is observed because of the concentration of BaTiO<sub>3</sub> (27.8 wt % in this case) compared to the PDMS. On decreasing the BaTiO<sub>3</sub> weight % in the composite, the absorption band at 500cm<sup>-1</sup> would predictably decrease or not even be observed at the lowest weight percentage. Only one of the BaTiO<sub>3</sub> absorption bands is observed in the composite FTIR spectra. The second BaTiO<sub>3</sub> absorption band at around 1450 cm<sup>-1</sup> is most likely masked by the CH<sub>3</sub> asymmetric deformation of Si-CH<sub>3</sub> in PDMS at around the same wavenumber (1438 cm<sup>-1</sup>).

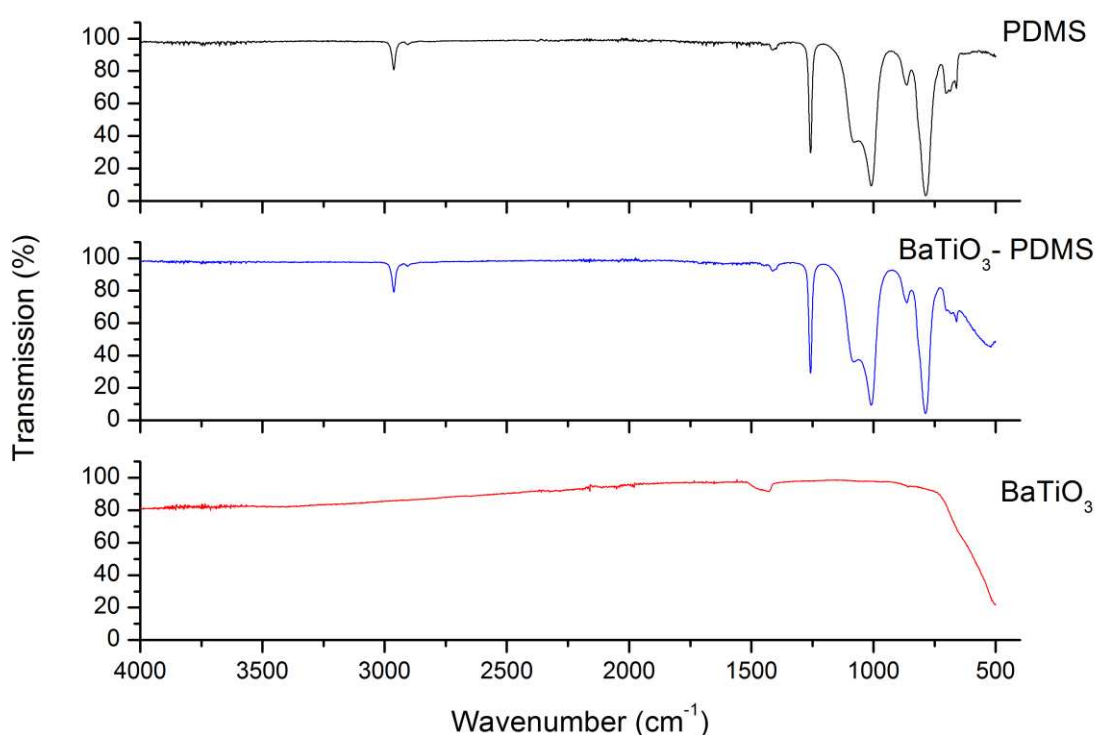


Figure 2.3: FTIR spectra of BaTiO<sub>3</sub>, PDMS and 27.8 wt% BaTiO<sub>3</sub> PDMS composite.

XRD patterns of pure barium titanate and barium titanate PDMS composite are shown in Figure 2.4. In the XRD pattern of the barium titanate PDMS composite, there was no change in the reflection peaks compared to the pure barium titanate indicating there had been no change in the morphology of barium titanate. There is some slight noise in the XRD pattern of the barium titanate PDMS composite due to the amorphous nature of the PDMS matrix.

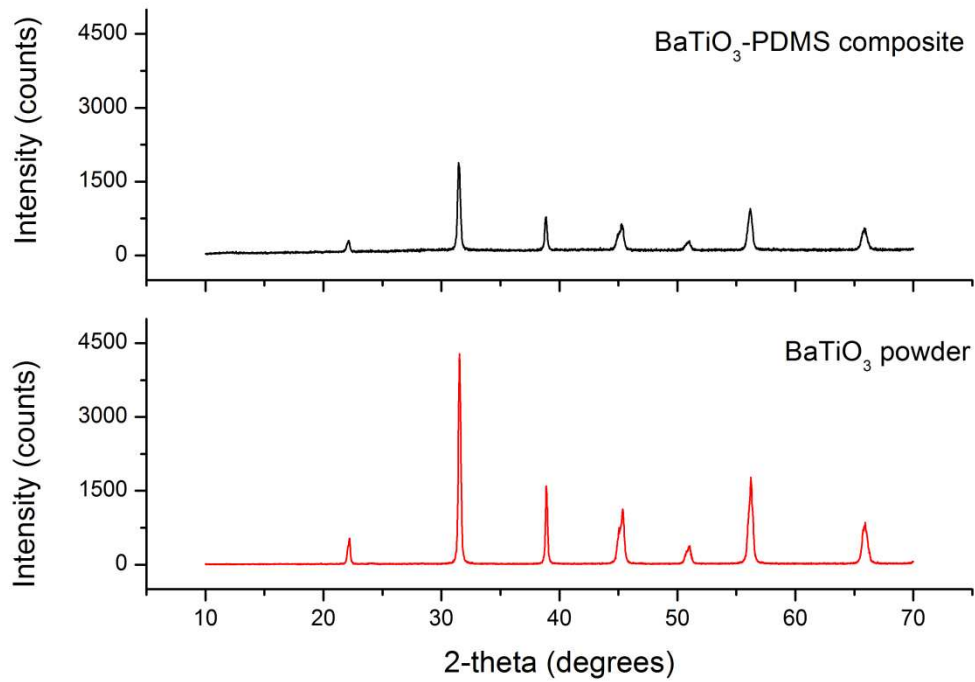


Figure 2.4: XRD of barium titanate powder and 27.8 wt% BaTiO<sub>3</sub>-PDMS composite.

Scanning electron microscopy micrographs of the PDMS-barium titanate composites with various amounts of BaTiO<sub>3</sub> are shown in Figure 2.5. The micrographs show unconnected and homogeneously distributed barium titanate particles in the PDMS matrix. At low particle loadings, the ceramic powder is well dispersed in the PDMS matrix without apparent agglomeration. However, at the higher loading level (36.6 wt %) slight agglomeration of BaTiO<sub>3</sub> in the composite was observed.

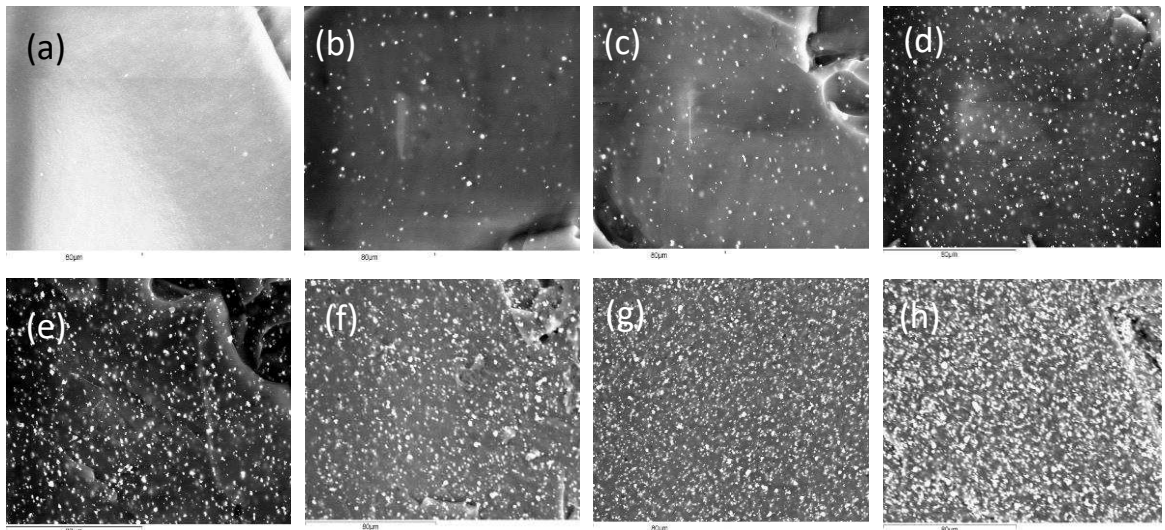


Figure 2.5: Distribution of barium titanate (a) 0 wt% (b) 1.0 wt% (c) 1.9 wt% (d) 4.6 wt% (e) 8.8 wt% (f) 16.3 wt% (g) 27.8 wt% and (h) 36.6 wt%.

### 2.2.1.3 BaTiO<sub>3</sub> Pellet

Characterisation by XRD was applied to the pellet and was compared to BaTiO<sub>3</sub> powder. This was performed to ensure that the heating process necessary to form the pellet did not cause a phase transformation. It is important the BaTiO<sub>3</sub> is in the tetragonal phase as in this phase, BaTiO<sub>3</sub>

demonstrates interesting properties, such as a high dielectric constant and ferroelectricity. Figure 2.6 shows larger splitting of the two peaks corresponding to (200) and (002) at 45° for the pellet compared to the powder. This splitting identifies the barium titanate pellet is in the tetragonal phase. In the cubic system, there is no splitting at 45° and heating will cause this peak to broaden. The XRD of the pellet also shows further splitting of all peaks compared to the starting powder. Further splitting is fostered by the sintering (heating) process and will cause the *c/a* ratio to increase. The *c/a* ratio of the barium titanate pellet was 1.00976 compared to 1.00455, the *c/a* ratio of the powder. Even with the *c/a* ratio increase, the barium titanate pellet is still in the tetragonal phase.

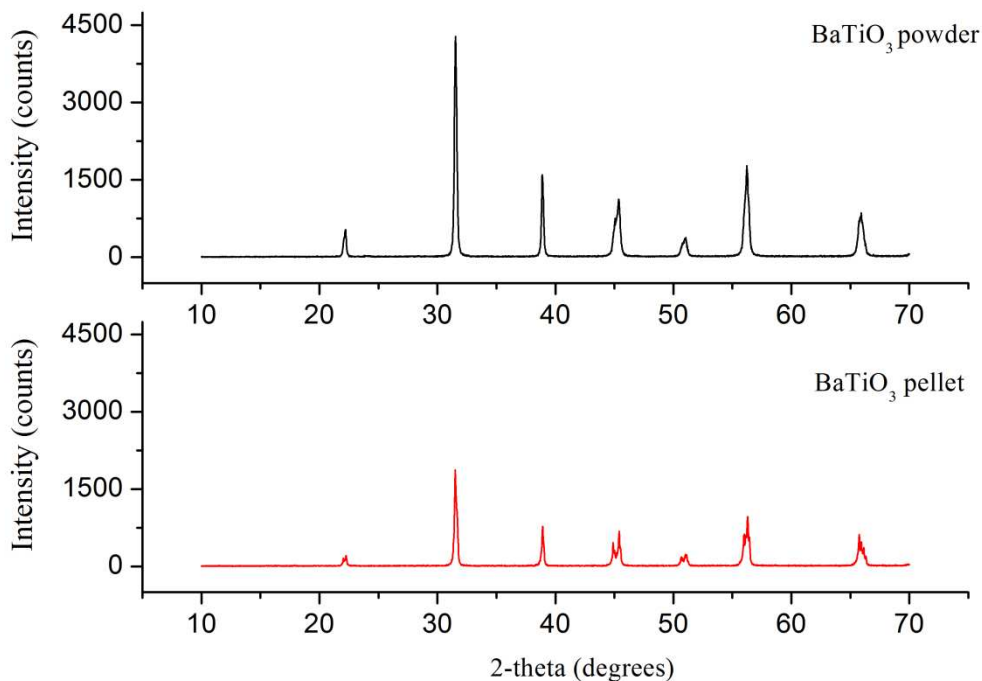


Figure 2.6: XRD of barium titanate powder and barium titanate pellet.

## 2.2.2 Effect of chemical modification and inorganic filler on permittivity of PDMS

### 2.2.2.1 Permittivity

The dielectric constant or relative permittivity of a material determines its response to an applied external electric field in dielectric materials.<sup>19</sup> Relative permittivity is the ratio of the absolute permittivity of a medium to the permittivity of free space (equation 2.0)

$$\epsilon_r = \frac{\epsilon}{\epsilon_0} \quad (\text{Equation 2.0})$$

Where  $\epsilon_r$  is relative permittivity,  $\epsilon$  is absolute permittivity and  $\epsilon_0$  is permittivity of free space at  $8.85 \times 10^{-12}$  F/m.

There are several ways to measure permittivity, in this chapter the relative permittivity of the elastomers was measured via both the transmission/reflection line method (waveguide) and coaxial

probe method (DAK) and the relative permittivity of the BaTiO<sub>3</sub> pellet was calculated via capacitance measurements. The transmission/reflection line method measures the reflected (S<sub>11</sub>) and transmitted (S<sub>21</sub>) S-parameters, which are used to calculate relative permittivity. S-parameters describe the electrical behaviour of linear electrical networks when undergoing electrical signals and are always frequency dependent.<sup>20</sup> In this case, the network is a two-port S-parameter network as there are two ports (one either end) of the waveguide. The S<sub>11</sub> parameter is the input port voltage reflection coefficient and S<sub>21</sub> is the forward voltage gain. Figure 2.7 illustrates both S<sub>11</sub> and S<sub>21</sub> parameters. The transmitted (S<sub>21</sub>) and reflected (S<sub>11</sub>) wave will have changed in amplitude and phase from the incident wave. It is the change in amplitude that is important in permittivity measurements.

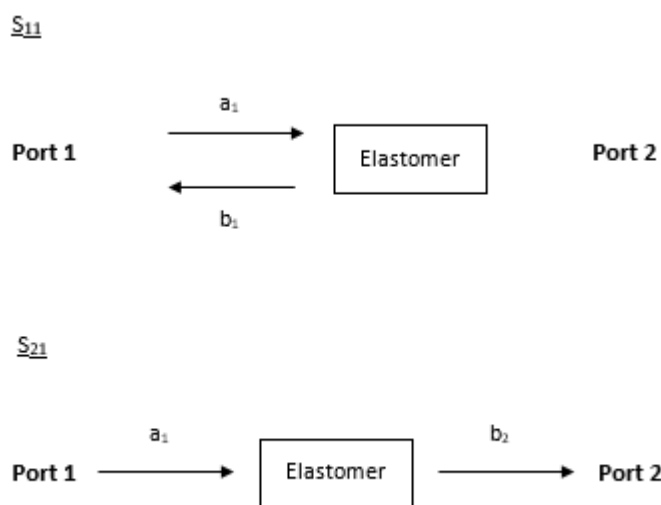


Figure 2.7: Illustration of S<sub>11</sub> and S<sub>21</sub> parameters. S<sub>11</sub> refers to the reflected signal where  $S_{11} = b_1/a_1$ . S<sub>21</sub> refers to the transmitted signal where  $S_{21} = b_2/a_1$ .

It was found that the straight edge of the elastomer (90 degrees to the incident wave) caused large reflections within the waveguide preventing an accurate result. To prevent this from happening, the edge of the elastomer was tapered to produce a slope to offer the incident wave a gradual transition from air to the elastomer at the air/elastomer interface. In the case of the coaxial probe method only the S<sub>11</sub> parameter is measured and used to calculate relative permittivity. The relative permittivity of the BaTiO<sub>3</sub> pellet was calculated using the following equation:

$$\epsilon_r = \frac{(C \times d)}{(\epsilon_0 \times A)} \quad \text{(Equation 2.1)}$$

Where  $\epsilon_r$  is relative permittivity,  $C$  is capacitance measured,  $d$  was the thickness of the pellet,  $A$  was the area of the pellet and  $\epsilon_0$  is the permittivity of free space.

### 2.2.2.2 Effect of TESPON cross-linker on permittivity

The relative permittivity values of the TEOS and TESPON cross-linked elastomers are listed in Table 2.0. It was found that both the TEOS and TESPON cross-linked elastomers displayed similar permittivity values to pure PDMS, which has a permittivity value of around 2.3. There was minimal difference between the permittivity of the TEOS cross-linked and TESPON cross-linked elastomers which was unexpected as it was thought the inclusion of the highly polar cyano groups would increase the overall relative permittivity of the elastomer. It was also noted that the amount of cross-linker had no effect on the relative permittivity. Both the concentration and resultant moments of a polar group in a polymer chain determine the permittivity of the polymer.<sup>21</sup> Therefore, it could be suggested that the concentration of polar groups within the TESPON cross-linked elastomers were too low to display an increase in permittivity. However, increasing the polar group concentration may not increase permittivity as dipole moments of polar groups are also effected by the spatial requirements imposed by the polymer chain. Popielarz and co-workers have shown that at high frequencies the mobility (dipole moment) of the polar groups in polymer chains is too slow to contribute to the relative permittivity.<sup>22</sup> This indicates that at high frequencies the permittivity becomes dependent primarily on the polymer chain, which in this case has a low permittivity.

Table 2.0: Relative permittivity of TEOS and TESPON cross-linked PDMS elastomers measured using the waveguide method.

| Elastomer        | TEOS (mmol) | TESPON (mmol) | PDMS (mmol) | (SiOR) : PDMS (SiOH) | Mean Relative Permittivity*<br>Waveguide |
|------------------|-------------|---------------|-------------|----------------------|--|
| PDMS-TEOS(1:1)   | 1.34        | -             | 1.27        | 0.95 : 1             | 2.6                                      |
| PDMS-TEOS(1:4)   | 5.18        | -             | 1.27        | 3.78 : 1             | 2.6                                      |
| PDMS-TESPON(1:1) | -           | 1.31          | 1.27        | 1.03 : 1             | 2.5                                      |
| PDMS-TESPON(1:3) | -           | 3.86          | 1.27        | 3.04 : 1             | 2.5                                      |

\*Permittivity measurements performed between 3 – 6 GHz

### 2.2.2.3 Effect of barium titanate filler on permittivity

Barium titanate is a ferroelectric material. A ferroic can be defined “as a material processing two or more orientation states or domains which can switched from one to another through the application of one or more appropriate forces.”<sup>23</sup> Therefore, ferroelectrics are materials in which the orientation state of spontaneous polarization can be changed with the application of an electric field. BaTiO<sub>3</sub> possess four different crystal phases – cubic, tetragonal, orthorhombic and rhombohedral. Above 120°C (393K) BaTiO<sub>3</sub> has a cubic structure, with the Ba<sup>2+</sup> ions in the centre, Ti<sup>4+</sup> ions at the corners of the cube and an octahedron of O<sup>2-</sup> ions around each titanium ion. In this structure BaTiO<sub>3</sub> is not a ferroelectric as it does not have a net dipole moment as the charges are symmetrically positioned. Between 120 °C and 5 °C BaTiO<sub>3</sub> has a tetragonal structure (Figure 2.8)



as the Ti atom moves off-centre along a Ti-O bond which gives rise to a spontaneous polarisation.<sup>24</sup>

If displacement occurs in all the  $\text{TiO}_6$  octahedra, a net polarisation is seen.

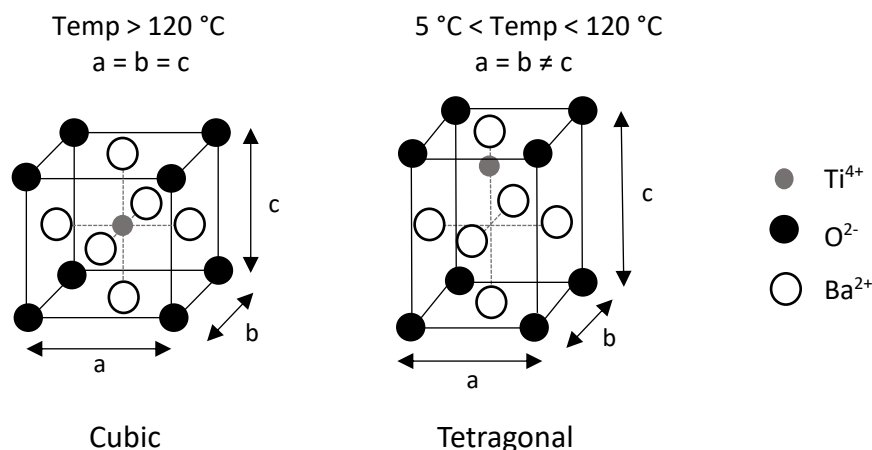


Figure 2.8: Cubic and tetragonal phases of  $\text{BaTiO}_3$ .

Tetragonal  $\text{BaTiO}_3$  is a ferroelectric material and its relationship between spontaneous polarisation and voltage is characterised by a hysteresis loop rather than the linear relationship shown by dielectrics.<sup>25</sup>  $\text{BaTiO}_3$  contains domain structures, which are variable in size. Within a single domain there is net polarisation (the dipoles have a common orientation), but different domains have their polarisation in different orientations. In tetragonal  $\text{BaTiO}_3$ , the titanium atom can be off-centre in six directions along any of the Ti-O bonds and therefore neighbouring domains can only have polarisations that are at  $90^\circ$  or at  $180^\circ$  to each other as shown in Figure 2.9. The net polarisation is the vector resultant of the polarisations of the individual domains. When an external electric field is applied a change in net polarisation can occur. This change in net polarisation can be caused by  $180^\circ$  or  $90^\circ$  domain switching (where the direction of polarisation of the domains changes) and domain wall migration. Domain wall migration is the process where favourably orientated domains grow in size at the expense of the less favourably orientated domains until the whole crystal has its dipoles aligned, known as saturation polarisation.

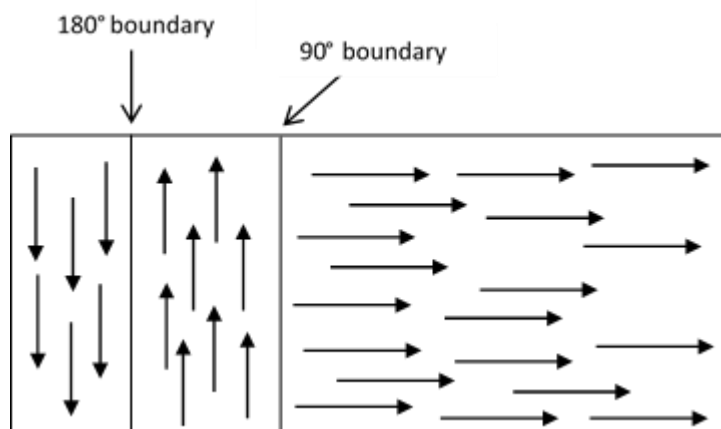


Figure 2.9: Sketch of domains in  $\text{BaTiO}_3$  showing  $90^\circ$  and  $180^\circ$  boundaries.

Permittivity of bulk barium titanate ( $\text{BaTiO}_3$  pellet) was determined over a low frequency range (100 –  $1\text{E}7$  Hz) using an impedance analyzer and shown in figure 2.10. Barium titanate has shown to

have permittivity values up to 4000 at room temperature<sup>10</sup>, however such large values were not observed. The BaTiO<sub>3</sub> exhibited a high relative permittivity of around 850 between 100 Hz and 100 KHz. Above 100 KHz the permittivity drops then stabilizes until 1 MHz and decreases further. Overall, permittivity decreases as the frequency increased. This was expected as the two polarisation processes that are responsible for the permittivity of BaTiO<sub>3</sub> (ionic and electronic polarisation)<sup>26</sup> are frequency dependent. As frequency increases, ionic polarisation contributions decrease as the ionic molecules can no longer follow the oscillations and at the point of optical frequencies (around 1E16 Hz) there is no contribution by ionic polarisation.<sup>27</sup> This suggests that the effect of barium titanate filler on the composite permittivity at high frequencies will not be as large as expected.

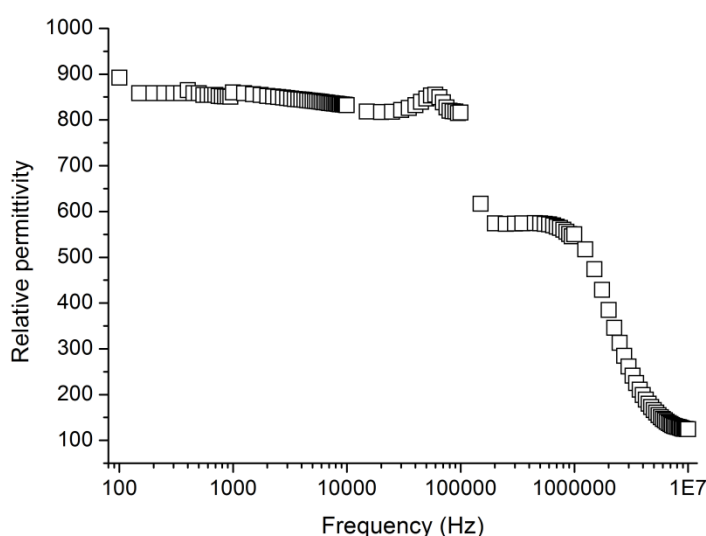


Figure 2.10: Relative permittivity of barium titanate pellet.

Permittivity is also dependant on temperature and the materials synthesis route including purity, density and grain size.<sup>28</sup> For example, BaTiO<sub>3</sub> synthesised via the sol gel method has shown permittivity values of 500 – 650 at 1 MHz<sup>29</sup> compared to 2000 at 1 KHz exhibited by BaTiO<sub>3</sub> synthesised via the hydrothermal method.<sup>30</sup> As previously highlighted the permittivity of the bulk barium titanate in this case did not reach values of 4000 previously shown in literature. The low permittivity was attributed to the low pellet density. Pellet densities have a large effect on measured permittivity values. Low density usually indicates a highly porous pellet which will have a significantly lower permittivity compared to a solid body as the pores will contain air which has a low relative permittivity of about 1. The pellet density was calculated at 0.0514 g cm<sup>-3</sup>, corresponding to 0.85 % of the theoretical density of BaTiO<sub>3</sub> (6.012 g cm<sup>-3</sup>).<sup>31</sup> Therefore, it is most likely that the bulk permittivity of the barium titanate used is much larger than observed in figure 2.10. However, the BaTiO<sub>3</sub>-PDMS composites are not expected to exhibit permittivity values as large as bulk BaTiO<sub>3</sub> as it has already been previously shown that the permittivity of BaTiO<sub>3</sub> in cross-linked PDMS is 93% smaller than the permittivity of BaTiO<sub>3</sub> in PDMS before cross-linking.<sup>32</sup> This is

attributed to the fact that the BaTiO<sub>3</sub> particles are unable to orientate and align in the electric field in the cross-linked polymer resulting in weak dipole moments.

The permittivity of the BaTiO<sub>3</sub>-PDMS composites were determined between 3 – 6 GHz using the waveguide method and shown in figure 2.11. It was found that the relative permittivity of the composites increased with wt% loading of BaTiO<sub>3</sub>. A positive linear relationship ( $R^2 = 0.9443$ ) was observed which agreed with previous findings that used %vol barium titanate loading.<sup>33</sup> The relative permittivity of 0 wt% BaTiO<sub>3</sub> loading was 2.6 compared to 4.2 shown for 36.6 wt% BaTiO<sub>3</sub> loading. It was found that barium titanate loading of 27.8 wt% provided a relative permittivity value of 3.4 close to the ideal value of 3.1 previously mentioned. Therefore, all further composites synthesised had a barium titanate loading of around 27.8 wt%. Shen and co-workers reported a permittivity of 6 with 40 wt% barium titanate filler at 120 Hz<sup>11</sup> and Babar *et al.* reported a permittivity of 8 with 15 % vol (around 50 wt%) barium titanate filler.<sup>34</sup> As shown in figure 2.11, the permittivity of the 36.6 wt% BaTiO<sub>3</sub>-PDMS composite was about 30 % lower compared to the permittivity of the 40 wt% composite reported by Shen *et al.* The difference in permittivity was attributed to the fact that the permittivity value from literature was gained at a low frequency. It has already been shown in figure 2.9, that the permittivity of BaTiO<sub>3</sub> decreases with increasing frequency. Even though the permittivity measurements performed by Babar *et al.* were done at ultra-high frequencies, it was still found that the permittivity value at 50 wt% extrapolated from figure 2.11 was still around 45 % lower. However, the composites reported in literature contained BaTiO<sub>3</sub> with smaller grain sizes, 80 nm *versus* ~2  $\mu$ m used to make the composites in this chapter.

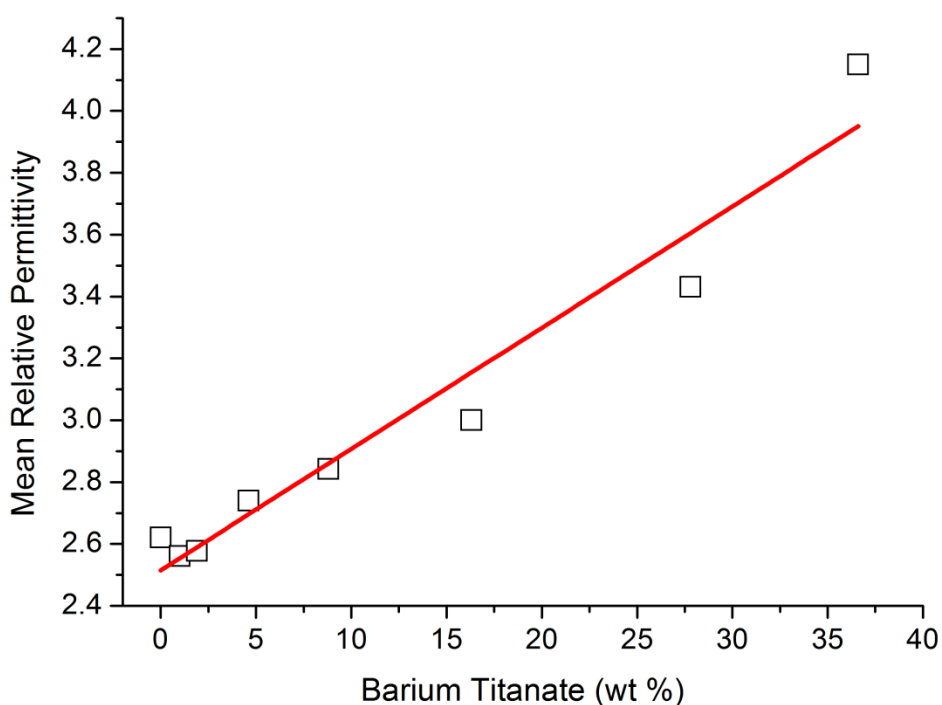


Figure 2.11 Relative permittivity of barium filled PDMS composites (permittivity measurements performed between 3 - 6 GHz).

#### 2.2.2.4 Comparison between waveguide and DAK measurements

Table 2.1 shows the permittivity values obtained using both the waveguide method and coaxial probe method (DAK) for each sample. For all samples, the permittivity value obtained was larger using the DAK method. The slight difference between the permittivity values measured using the waveguide and DAK could be contributed to the dielectric loss of the material. Along with the permittivity results, the DAK method also measured the loss tangent of the BaTiO<sub>3</sub>-PDMS composites. It was observed that the loss tangent for all the composites regardless to the percentage of barium titanate filler was extremely low as shown in Table 2.1. Waveguide measurements are not as effected by the loss tangent compared to the DAK measurements. As the waveguide is filled with air and completely closed off, no power is lost through radiation and dielectric loss is negligible. However, in the case of the coaxial probe method (DAK) if a sample has a low loss tangent a thicker sample is required to prevent all the electromagnetic waves reflecting back from the samples boundaries which results in the impression of a sample with a larger permittivity value. This was confirmed in Table 2.1 as all the DAK measurements were slightly larger than the waveguide measurements. Therefore, it was concluded that the difference between the DAK and waveguide measurements was due to the low tangent loss of the BaTiO<sub>3</sub>-PDMS composites and the permittivity values measured using the waveguide method were accurate.

Table 2.1: Permittivity results from both waveguide and DAK measurements.

| Sample                            | $\epsilon_r$ Waveguide | $\epsilon_r$ DAK | $\Delta\epsilon_r = \epsilon_r$<br>waveguide - $\epsilon_r$<br>DAK | Tangent Loss<br>(from DAK) |
|-----------------------------------|------------------------|------------------|--|----------------------------|
| PDMS-TEOS(1:1)                    | 2.6                    | 2.7              | -0.1   | 0.020                      |
| PDMS-TEOS(1:4)                    | 2.6                    | 2.7              | - 0.1  | 0.020                      |
| PDMS-TESPN(1:1)                   | 2.5                    | 2.7              | - 0.2  | 0.022                      |
| PDMS-TESPN(1:3)                   | 2.5                    | 2.7              | - 0.2  | 0.028                      |
| 1.0 wt% BaTiO <sub>3</sub> -PDMS  | 2.6                    | 2.7              | - 0.1  | 0.022                      |
| 1.9 wt% BaTiO <sub>3</sub> -PDMS  | 2.6                    | 2.7              | - 0.1  | 0.020                      |
| 4.6 wt% BaTiO <sub>3</sub> -PDMS  | 2.7                    | 2.8              | - 0.1  | 0.021                      |
| 8.8 wt% BaTiO <sub>3</sub> -PDMS  | 2.8                    | 2.9              | - 0.1  | 0.022                      |
| 27.8 wt% BaTiO <sub>3</sub> -PDMS | 3.4                    | 3.7              | - 0.3  | 0.023                      |
| 36.6 wt% BaTiO <sub>3</sub> -PDMS | 4.2                    | 4.3              | - 0.1  | 0.024                      |

#### 2.2.3 High molecular weight PDMS composites

As discussed in section 2.2.2 composites with a barium titanate loading of around 27.8 wt% showed an ideal relative permittivity value of 3.4. However, it has been shown that the addition of fillers causes an increase in the composites elastic modulus. Denver *et al.* observed an elastic modulus increase of around 30% for PDMS composites with a loading of 5 vol% nickel nanoparticles.<sup>35</sup> The

addition of ceramic fillers (a rigid phase) increases the stiffness of the composite. Along with a permittivity value of around 3.4, the final composite for the strain-sensor design has to exhibit good elasticity to withstand repetitive stretching. Therefore, a compromise was made to ensure high permittivity while maintaining the flexibility of the PDMS network. A high molecular weight PDMS (cSt 1000, M. W. 77,000) was used, as a high molecular weight PDMS has a lower elastic modulus than the low molecular weight used (cSt 18000, M. W. 26,000).

However, the high molecular weight PDMS posed a new problem. High molecular weight PDMS inherently has a high viscosity due to the increase in chain entanglements and this high viscosity brought difficulties to the synthesis of the composite in regards to mixing and pouring. The mixing stage of the synthesis route was extremely important to ensure the barium titanate and tin catalyst was homogeneously distributed. In order to reduce the viscosity of the PDMS, addition of different solvents at varying weight ratios to PDMS were investigated. Addition of a solvent to a polymer can cause two effects: plasticization and dilution. In this case the former is the effect desired, as plasticization causes a decrease in the glass transition temperature which lowers the viscosity of the polymer.<sup>36</sup> Varying amounts of tin catalyst and methods of curing (i.e. under pressure, change in temperature) were also investigated alongside the addition of solvent to produce a composite with a smooth shiny surface.

The following experiments were all performed with a barium loading *circa* 28.2 – 28.5 wt% and a ratio of SiOH groups in PDMS to SiOR groups in TEOS at 1:4. It was found the addition of toluene at a weight ratio to PDMS of 0.25:1 lowered the viscosity to a manageable level. A 1:3.8 molar ratio of PDMS to catalyst and curing method of being left at room temperature until the composite became tacky before being placed into a 60°C oven overnight (method A) produced a composite which had a highly patterned rough surface and was flexible. However, at the time this combination of factors seemed to prove to be the best and was used in the synthesis of the BaTiO<sub>3</sub>-PDMS composites for the antenna attachment experiments in section 2.2.4.

A 1:0.9 molar ratio of PDMS to catalyst and curing method of 1 hour at room temperature before being placed in the oven at 60°C overnight (method B) was found to be the best combination and resulted in a composite which was flexible with a smooth shiny surface. This method was used to synthesise the composite for the antenna resistance measurements in section 2.2.5. The latter composite's (method B) structure and distribution of BaTiO<sub>3</sub> was verified using FTIR and SEM micrographs. There were no FT-IR absorption peak differences between the high molecular weight BaTiO<sub>3</sub> (28.5 wt%)-PDMS<sub>77,000</sub> composite and the low molecular weight BaTiO<sub>3</sub> (27.8 wt%)-PDMS<sub>26,000</sub> composite (figure 2.12 (a)), indicating that increasing the molecular weight of PDMS has no effect on the minimal chemical reaction between PDMS and BaTiO<sub>3</sub>. The absence of characteristic peaks associated with toluene (3099, 2925, 1086 and 1506 cm<sup>-1</sup>) in the FTIR spectra of the BaTiO<sub>3</sub>-PDMS<sub>77,000</sub> composite confirmed that the toluene was removed completely during the composite curing

process. SEM micrographs of the  $\text{BaTiO}_3$  (28.5 wt%)-PDMS<sub>77,000</sub> are shown in Figure 2.12(b – d). The SEM micrographs showed homogeneously dispersed barium titanate within the polymer matrix indicating that adding toluene to the mixture encouraged the dispersion process during mixing and there was no observed settling of barium titanate at the upper and lower surfaces which means an even permittivity throughout the composite should be achieved.

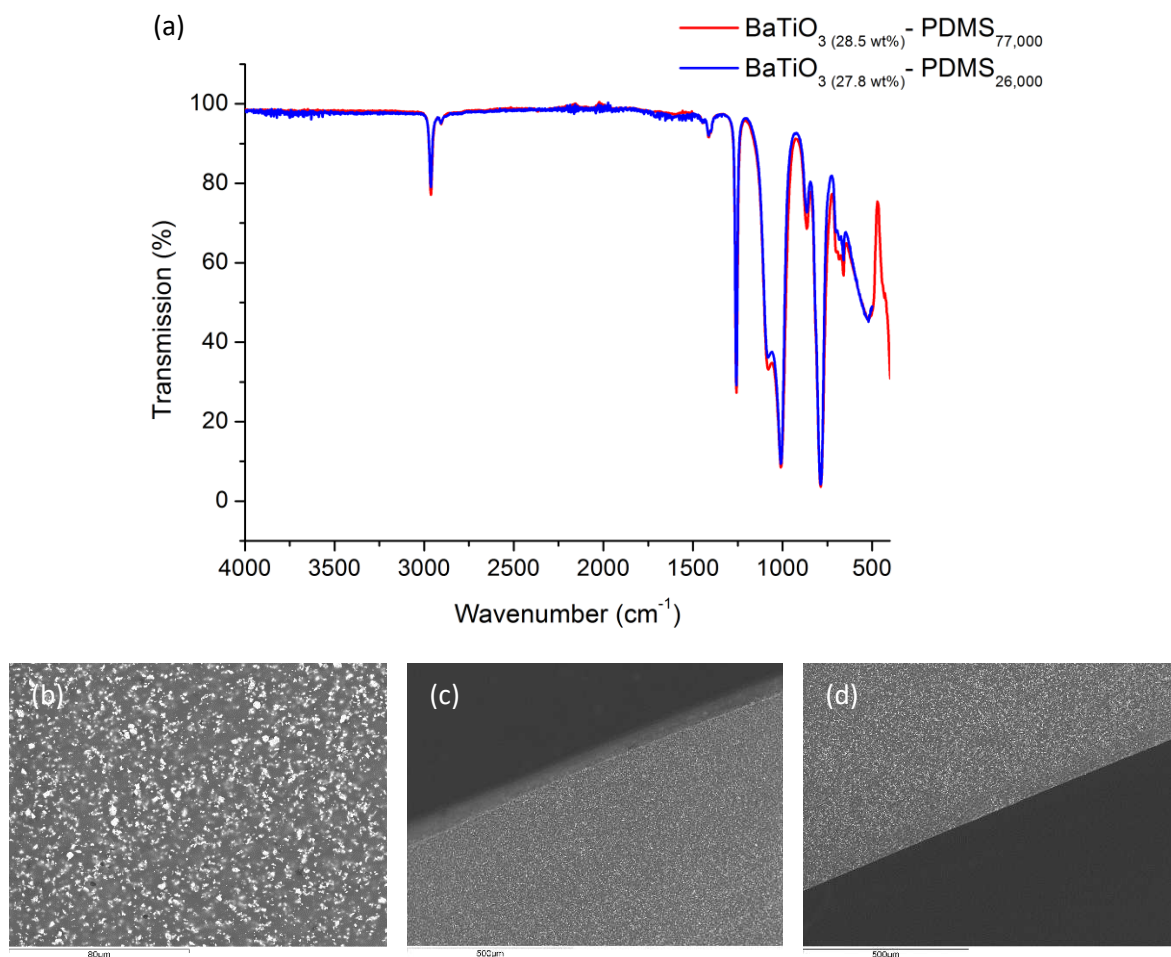


Figure 2.12: (a) FTIR of  $\text{BaTiO}_3$  (28.5 wt%)-PDMS<sub>77,000</sub> composite fabricated using method B section 2.2.3 and  $\text{BaTiO}_3$  (27.8 wt%)-PDMS<sub>26,000</sub>. SEM micrographs of  $\text{BaTiO}_3$  (28.5 wt%)-PDMS<sub>77,000</sub> (a) cross section (b) corner edge of cross-section and upper surface and (c) corner edge of cross-section and lower surface.

## 2.2.4 Antenna attachment

Silver Lycra® with a thickness of 0.5mm was chosen as the antenna material. Silver is a well-known and a commonly used conductor on account of the high conductivity it shows even when oxidised. Silver is relatively easy to work with and can be incorporated within polymers as seen in silver Lycra®. Lycra® is a polyether/polyurea urethane<sup>37</sup> which forms fibres (as seen in Figure 2.13). These fibres are highly elastic and are ideal for stretching. Figure 2.13(b) shows that the silver particles (the white spots) are embedded along the Lycra fibres. Silver particles are observed as white spots in the SEM micrograph because silver has a high density compared to the polymer fibre.

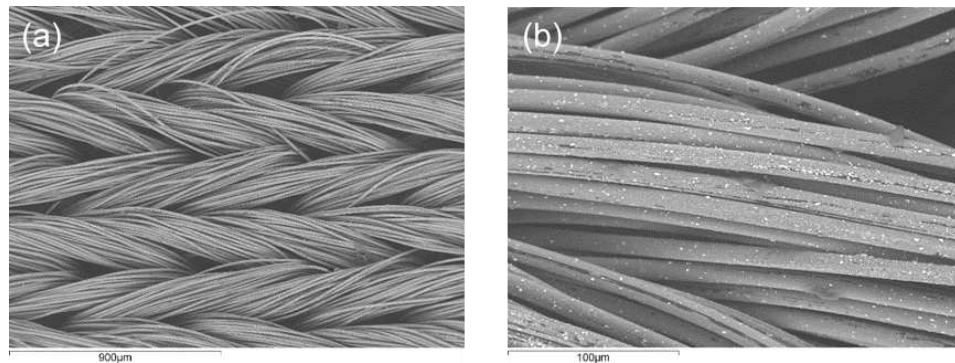


Figure 2.13: SEM micrographs of Silver Lycra® at magnification (a) x 65 and (b) x 474.

A method to attach the antenna to the BaTiO<sub>3</sub>-PDMS composite which resulted in good antenna-substrate adhesion that can withstand repetitive straining and no loss in the antenna's electrical properties was required. Self-adhesion of the antenna to the composite during the curing process was the most desirable method. In this case, the tag was designed to a specific substrate permittivity; a self-adhesion method would eliminate the use of an adhesive which would form a layer with a different permittivity to that of the substrate between the antenna and substrate. This could potentially stop the tag from functioning.

The antenna in Figure 2.14 was used for the self-adhesion attachment experiments. Laser cutting was used to achieve the desired shape of the antenna.



Figure 2.14: Image of antenna with silicone IC chip attached.

A simulation to predict the received frequency of the tag using the antenna design in Figure 2.14 was performed. The antenna (slot dimensions length = 20.08 mm, width = 4 mm, radius = 20 mm, feed thickness = 2 mm) was simulated in CST Microwave Studio on a Mylar sheet (permittivity = 3, thickness = 0.046 mm) attached to a BaTiO<sub>3</sub>-PDMS composite (diameter = 6 cm, height = 0.2 cm).

and permittivity = 3.43) which was placed on top of a rectangular phantom used to represent human tissue. The phantom comprised of a 26 mm top layer of combined skin and fat (permittivity = 14.5, conductivity = 0.25 S/m) and a bottom layer of 20 mm thick muscle (permittivity = 55.1, conductivity = 0.25 S/m). The simulations performed by Rakibet showed the maximum read range of the tag was 831 MHz, which is close to the desired 865.6 - 867.6 MHz frequency band for the United Kingdom.<sup>38</sup> For optimal performance, the maximum read range of the tag from experimental results should be between 781 - 911 MHz (there can be a difference of 50 MHz between simulated and experimental results).

Two tags were fabricated; one with the antenna placed onto the surface and the other with the antenna placed just under the surface of the substrate. The substrate was fabricated following method A in section 2.2.3 (composite diameter = 6 cm, height = 0.2 cm). The IC chip was glued to the antenna feed lines using conductive silver epoxy glue. The placement of the antenna onto the surface of the composite was performed at 9 minutes 40 seconds into the BaTiO<sub>3</sub>-PDMS curing time – a stage where the composite had become slightly tacky. The placement of the antenna just under the composite surface was performed as soon as possible after the BaTiO<sub>3</sub>-PDMS mixture had been poured into the mould. From looking at the two tags, a good antenna adhesion had been achieved. However, both tags exhibited poor RFID performance even when stretched. The tag with the antenna just under the surface was the worse of the two sample, showing a small theoretical maximum read range of around 0.5 meters outside of our optimal frequency range (781 – 911 MHz). The reason for this poor performance was visually clear by looking at the sample. With the antenna under the substrate surface, the individual silver Lycra<sup>®</sup> fibres are surrounded by the BaTiO<sub>3</sub>-PDMS mixture, giving the antenna a white appearance. The BaTiO<sub>3</sub>-PDMS substrate is inherently an insulator and as a result the antenna's resistance and impedance had changed causing the antenna to be no longer conjugate matched with the microchip. It is the lack of conjugate impedance matching that results in the tags poor performance. The tag with the antenna on the surface showed the same effects as the other tag, as the BaTiO<sub>3</sub>-PDMS mixture had seeped through between the silver Lycra<sup>®</sup> fibres.

It was hypothesised the resistance of the silver Lycra changed due to the interaction with the BaTiO<sub>3</sub>-PDMS substrate. A preliminary experiment was performed to investigate if the resistance of the silver Lycra<sup>®</sup> does increase when placed onto the composite. A resistance meter (ISO-TECH, IDM 201) was used to measure the resistance of Lycra<sup>®</sup> before and after placed onto a BaTiO<sub>3</sub>-PDMS substrate. The resistance measurement performed after Lycra<sup>®</sup> placement was completed once the substrate had completely cured. The substrate was synthesised following method B in section 2.2.12 (dimension diameter = 8 cm, height 0.1 cm) and four silver Lycra<sup>®</sup> pieces (dimensions width = 2 cm, length = 2cm) were placed onto the substrate at 25 minutes into curing. SEM micrographs were performed to investigate the self-adhesion of the Lycra<sup>®</sup> to the substrate.



Resistance measurements performed by Rakibet showed that the resistance of the silver Lycra<sup>®</sup> pieces increased fourfold. The large increase in resistance was caused by the silver Lycra<sup>®</sup> being embedded in the substrate as shown in Figure 2.15. At first glance of Figure 2.15, it could be suggested that the Lycra<sup>®</sup> was embedded from the mechanical cutting required to produce a cross-section for SEM analysis. However, Figure 2.15 shows silver Lycra<sup>®</sup> strands protruding from within the substrate – a phenomena that is not caused by mechanical cutting but from the Lycra<sup>®</sup> being embedded within the composite. A method to prevent the large resistance change could be to place the Lycra<sup>®</sup> onto the substrate further into the curing time.

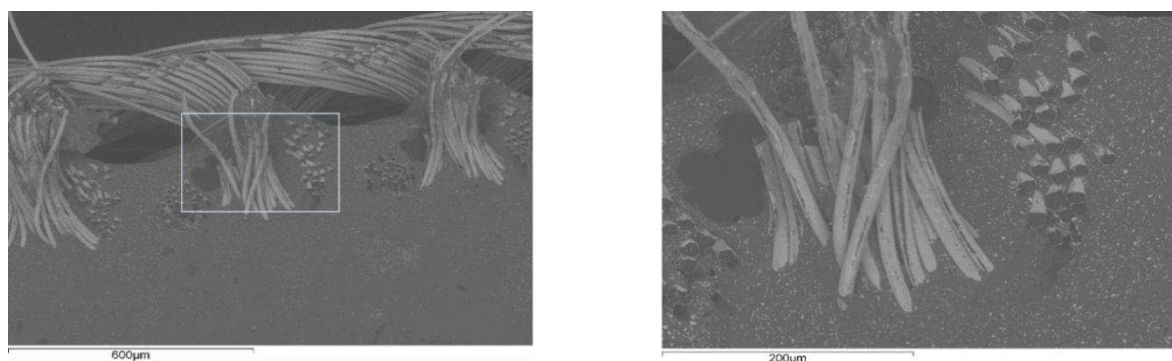


Figure 2.15: SEM micrograph (a) cross-section of silver Lycra<sup>®</sup> adhered to BaTiO<sub>3</sub> - PDMS substrate (b) expanded image of highlighted area in micrograph (a).

### 2.2.5 Antenna resistance

As discussed above in section 2.2.4, placing the Lycra<sup>®</sup> onto the substrate further into the curing time could prevent the large resistance change previously observed. This hypothesis was tested by measuring the resistance of silver Lycra<sup>®</sup> pieces placed onto a substrate at varying curing times. The substrate was fabricated following method B in section 2.2.3 and six silver Lycra<sup>®</sup> pieces (dimensions width = 0.5 cm, length = 2 cm) were placed onto the composite 4 minutes apart beginning at 24 minutes into curing. As adhesion is reliant on the interaction between the Lycra<sup>®</sup> and substrate, the adhesion of the silver Lycra<sup>®</sup> pieces were noted as it could become poor as time into curing increases. Resistance of the Lycra<sup>®</sup> was measured before and after placed onto the BaTiO<sub>3</sub>-PDMS substrate, as well as one week later to investigate if a change is observed. The resistance of the Lycra<sup>®</sup> was also investigated using three silicone based adhesives – Medical, Telesis 5 and Skin Tite. Following the same procedure as above the resistance of the Lycra<sup>®</sup> was measured before and after placement and one week later. In the case of the adhesives, the Lycra<sup>®</sup> pieces were attached to a fully cured substrate.

Table 2.2 shows the resistance measurements of Lycra<sup>®</sup> placed on at different times into the curing process. It was the resistance difference between Lycra<sup>®</sup> on PDMS (1 week later) and Lycra<sup>®</sup> on air that was examined. Premature placing (32 minutes and below) of the silver Lycra<sup>®</sup> caused an increase in the Lycra's electrical resistance. However, affixing of the Lycra<sup>®</sup> above 40 minutes displays maintenance of the Lycra's resistance and the Lycra<sup>®</sup> placed onto the substrate at 44 minutes into curing still exhibited excellent adhesion. Table 2.2 shows that as the time into curing

increases, the resistance difference decreases. However, the resistance difference at 28 minutes into curing does not follow this generalisation. As seen in Figure 2.16, the silver Lycra<sup>®</sup> placed at 28 minutes (second from furthest left) shows a large white area where the BaTiO<sub>3</sub>-PDMS has seeped through. This was most likely caused by using slightly too much pressure when placing the silver Lycra<sup>®</sup> piece onto the substrate.

Table 2.2: Electrical resistance (R) of silver Lycra<sup>®</sup> placed on elastomers at varying times into the curing process.

| R (Ω) of Lycra <sup>®</sup> on air | Curing time substrate (mins) | R (Ω) of lycra on fully cured substrate | ΔR (Ω) = R(substrate) – R(air) | R (Ω) of Lycra <sup>®</sup> on substrate 1 week later | ΔR (Ω) = R(elastomer 1 week later) – R(air) |
|------------------------------------|------------------------------|---|--------------------------------|---|---|
| 13.3 ± 0.2                         | 24                           | 16.2 ± 0.2                              | 2.9                            | 28.7 ± 0.1  | 15.4  |
| 14.0 ± 0.2                         | 28                           | 22.3 ± 0.6                              | 8.3                            | 34.1 ± 0.3  | 20.1  |
| 11.4 ± 0.2                         | 32                           | 11.6 ± 0.4                              | 0.2                            | 20.0 ± 0.2  | 8.6   |
| 12.9 ± 0.2                         | 36                           | 10.6 ± 0.2                              | -2.3                           | 17.1 ± 0.1  | 4.2   |
| 13.3 ± 0.3                         | 40                           | 11.1 ± 0.2                              | -2.2                           | 16.2 ± 0.2  | 2.9   |
| 13.4 ± 0.2                         | 44                           | 10.7 ± 0.2                              | -2.7                           | 15.0 ± 0.2  | 1.6   |

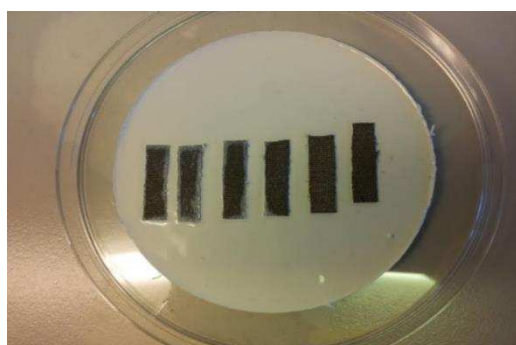


Figure 2.16: Silver Lycra placed on substrate at varying times (4 minutes apart) during the curing process (far left is 24 minutes into curing, far right is 44 minutes into curing).

Table 2.3 shows the resistance measurements of Lycra<sup>®</sup> using three silicone adhesives. An extremely low resistance difference was observed when using two of the adhesives – Medical and Telesis 5. However, a very large resistance difference of 11.6 Ω was seen when using Skin Tite adhesive. From studying the sample, it was expected that the resistance difference using Skin Tite would be large as the silver Lycra<sup>®</sup> fibres were stuck together. This suggests that the Skin Tite adhesive has coated the fibres providing them with an insulating layer ceasing the conductivity, resulting in the increase of resistance. Even though two of the adhesives exhibited very low resistance differences, self-adhesion of the antenna was still preferred and a difference of 1.6 Ω is tolerable and should not affect the tags RFID performance.

Table 2.3: Electrical resistance ( $R$ ) of silver Lycra® placed onto PDMS using different silicone adhesives.

| $R$ ( $\Omega$ ) of Lycra® on air | Adhesive  | $R$ ( $\Omega$ ) of lycra on fully cured substrate | $\Delta R$ ( $\Omega$ ) = $R(\text{substrate}) - R(\text{air})$ | $R$ ( $\Omega$ ) of Lycra® on substrate 1 week later | $\Delta R$ ( $\Omega$ ) = $R(\text{elastomer 1 week later}) - R(\text{air})$ |
|-----------------------------------|-----------|--|---|--|--|
| 11.1 $\pm$ 0.2                    | Medical   | 10.9 $\pm$ 0.2                                     | -0.2  | 10.9 $\pm$ 0.2                                       | -0.2   |
| 11.2 $\pm$ 0.2                    | Telesis 5 | 11.6 $\pm$ 0.1                                     | 0.4   | 10.5 $\pm$ 0.2                                       | -0.7   |
| 11.2 $\pm$ 0.1                    | Skin Tite | 11.3 $\pm$ 0.2                                     | 0.1   | 23.0 $\pm$ 0.2                                       | 11.6   |

## 2.2.6 Design and Fabrication of Prototype RFID strain sensor

The antenna design was further optimised and the final design shown in Figure 2.17 (full antenna dimensions shown in Table 2.4) was developed from an UHF RFID tattoo transfer tag which exhibited good RFID performance when mounted on skin. Laser cutting was used to acquire the antenna shape. The slot was originally rectangular in shape, however, due to over-burn at the slot ends the delicate feed lines were often compromised. Therefore, the slot was rounded as shown in Figure 2.17 which solved the previous problem.

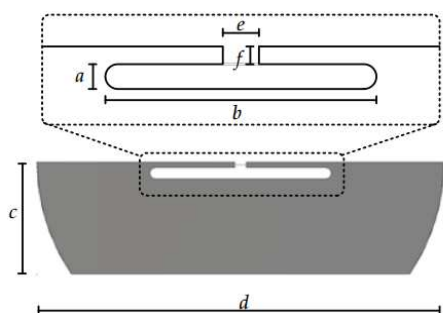


Figure 2.17: Prototype RFID strain sensor antenna design.

Table 2.4: RFID antenna dimensions

| Parameters          | Symbol | Length (mm) |
|---------------------|--------|-------------|
| Slot width          | $a$    | 2           |
| Slot length         | $b$    | 32          |
| Antenna width       | $c$    | 20          |
| Antenna length      | $d$    | 72          |
| chip length         | $e$    | 2           |
| Feed line thickness | $f$    | 1           |

The antenna was simulated in CST Microwave Studio on a Mylar sheet (permittivity = 3, thickness = 0.046 mm) attached to the BaTiO<sub>3</sub>-PDMS substrate (permittivity = 3.43, dimensions diameter = 80 mm, height = 1 mm) which was placed on top of a rectangular phantom used to represent skin. The phantom comprised of a top layer of combined skin and muscle (permittivity = 14.5, conductivity = 0.25 S/m) and a bottom layer of muscle (permittivity = 55.1, conductivity = 0.93 S/m). The simulation performed by O. O. Rakibet showed the maximum read range of the tag was at 849 MHz.

Silanol-terminated PDMS cSt 18000 (12 g, 0.156 mmol), BaTiO<sub>3</sub> (4.8 g, 20.6 mmol), tetraethyl orthosilicate (0.070 cm<sup>3</sup>, 0.313 mmol) and toluene (3.47 cm<sup>3</sup>, 35.6 mmol) were added to a glass beaker and speed-mixed for 30 minutes. Tin(II) 2-ethylhexanoate dissolved in toluene (0.074 cm<sup>3</sup>, 0.148 mmol) was then added to the mixture which was speed-mixed for a further 60 seconds before

being poured into a PTFE circular mold (diameter = 80 mm, height = 1 mm). A flexible filling knife was drawn down over the mold to ensure a uniform height elastomer. As discussed previously in section 2.2.5, premature placing of the silver Lycra® onto the curing composite lead to a loss in antenna conductivity. With the new antenna design, it was found that the narrow feed lines were more susceptible to conductivity degradation compared to the main body. Therefore, the feed lines were placed down onto the composite further into the curing time. The main body of the antenna was placed onto the composite 75 minutes into curing while the feed lines were placed at 95 minutes. The composite was left to cure at room temperature for a further 25 minutes before being placed into a 60°C oven for 72 hours. The resulting tag prototype showed excellent antenna adhesion with no visible PDMS seepage (Figure 2.18(a)).

### 2.2.7 Strain sensor RFID measurements

The results from the tag simulation using the new antenna design from section 2.2.6 showed the radiation efficiency to be -12.5 dB. To verify this result and to establish the accuracy of the body phantom, the read range of the tag prototype was measured over a range of frequencies using the Voyantic Lite measurement system. For the measurements, a NXP UHF RFID chip with -15 dB sensitivity was attached to the tag prototype using silver conductive epoxy glue and the tag was placed onto the skin of a volunteer's forearm using adhesive tape. The prototype tag exhibited a maximum read range of 1.6 m at 868 MHz, which corresponded to the results of the simulation.

An antenna of the same design as Figure 2.17 was etched onto a copper clad thin Mylar sheet and an UHF RFID chip was attached. Two prototype tags were fabricated using this one copper antenna; one where the antenna was placed on a BaTiO<sub>3</sub>-PDMS substrate as shown in Figure 2.18 (substrate synthesised following method in section 2.2.6) and the other where the antenna was placed onto a Perspex substrate.

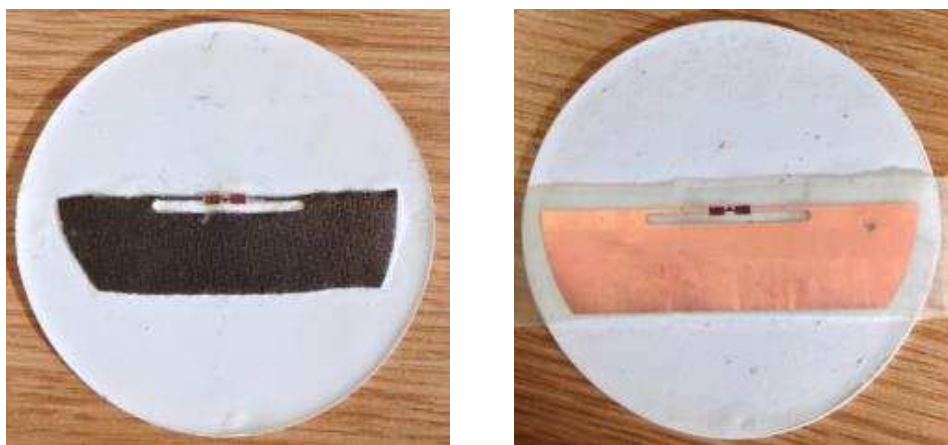


Figure 2.18: Image of (a) silver Lycra® antenna BaTiO<sub>3</sub>-PDMS tag prototype (b) copper antenna BaTiO<sub>3</sub>-PDMS tag prototype.

Perspex was chosen as it has the same permittivity value, 3.4 as the BaTiO<sub>3</sub>-PDMS substrate. The read range of both tags was measured and found to be identical, confirming the BaTiO<sub>3</sub>-PDMS substrate fabricated in section x had a permittivity of around 3.4. The read range of the silver Lycra®

antenna BaTiO<sub>3</sub>-PDMS prototype tag placed on skin was compared to the copper antenna BaTiO<sub>3</sub>-PDMS prototype tag. The silver Lycra® antenna tag showed a lower read range, 60 % of the copper antenna tag. This was expected as the conductivity of silver Lycra® is much lower than copper. However, the maximum read range for both tags occurred at 868 MHz.

Figure 2.19 shows the RFID prototype strain sensor tag in the PTFE jig used for the RFID strain measurements. Strain, in this case stretch along the x axis caused the slot of the antenna to become longer and narrower. Whereas, stretch along the y axis caused the slot to become shorter and wider. The strain in all of the following measurements was expressed as a percentage change in the slots width, where a positive value was a stretch along the x axis and negative value along the y axis. To assess the tag performance over time, the tag was kept in the PTFE jig at 10% strain for 1 week and then the experiment was repeated.

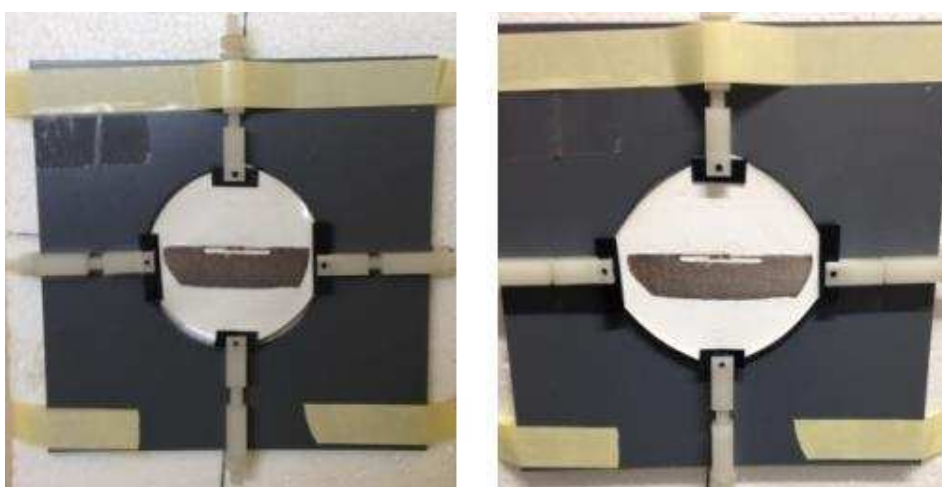


Figure 2.19: Prototype tag on PTFE jig for strain measurements (a) no strain (b) 10% strain.

Figure 2.20 shows the transmitted power *versus* frequency of the prototype tag under both y axis (negative stretch %) and x-axis (positive stretch %) strain. The transmitted power required to activate the chip was much larger when the tag was under y-axis strain when compared to x-axis strain. As the slot became shorter and wider during y-axis strain, impedance mismatching between the antenna and chip occurred resulting in the increase of power required and essentially a less efficient tag. The impedance mismatching was not only observed through the large transmitted power but also through the small frequency range where measurements could be recorded. Therefore, this strain sensor design could not be used to monitor y-axis strain. However, this is not a limitation as this means that this sensor design can differentiate between y and x-axis strain. However, by rotating the tag within the PTFE jig by 90° the prototype sensor tag would be able to monitor y-axis strain as the antenna slot would become narrower and longer instead of shorter and wider. This highlights the importance of the angle of mounting on the performance of the prototype tag design described in this chapter.

The performance of the prototype tag over time was also analysed and compared to the original measurements as shown in Figure 2.20. It was clear that the difference between the original and

new measurements (measurements performed after the tag was left at 10% stretch for 1 week) was minimal - a difference of 0.2 dB at the operating frequency (868 MHz) for the tag experiencing 10.40% stretch was observed. The minimal difference between the original and new measurements indicates that the prototype tag recovers well after being kept stretched. This recovery after stretching is an important requirement for the proposed application (an actuator to allow paraplegic patients to control their wheelchair through muscle tweaking) of the prototype tag in terms of longevity.

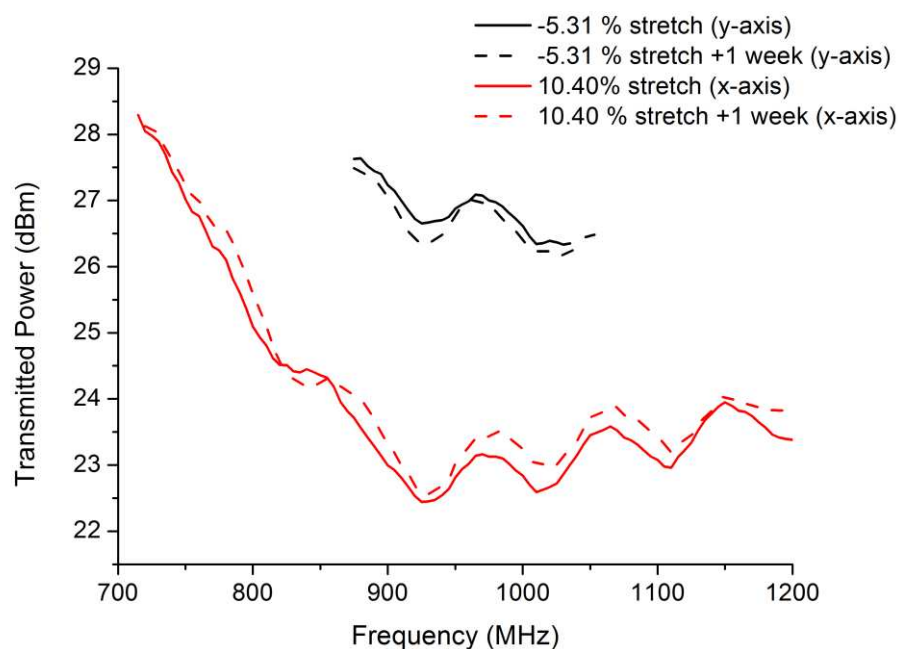


Figure 2.20: Transmitted power versus frequency.

Figure 2.21 showed the transmitted power of the prototype tag as a function of stretch. A linear relationship was observed and statistical analysis showed there was a strong correlation between the two properties (correlation coefficient = -0.97).

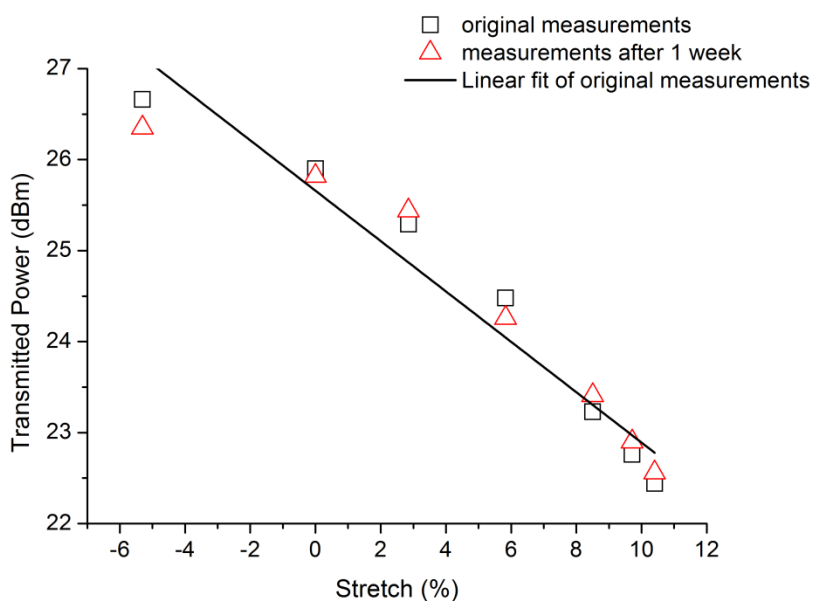


Figure 2.21: Transmitted Power of the prototype tag as a function of stretch (%).

This relationship could allow for accurate prediction of the tags RFID response under strain not measured in this experiment. The transmitted power was again measured for the prototype tag under various strains after being left for 1 week at around 10 % strain. As shown in Figure 2.21, the measurements after 1 week all lie very close to the original measurements suggesting the prototype tag's performance does not degrade over time.

## 2.3 Conclusions

PDMS elastomers were successfully synthesised using both TEOS and TESPN cross-linkers. As expected the PDMS-TEOS elastomers displayed similar relative permittivity values as pure PDMS. However, the PDMS-TESPN elastomers showed no increase in relative permittivity. It was concluded that at high frequencies, polar groups cannot and do not contribute to permittivity. Therefore, the addition of polar cross-linkers was not a reliable method to improve permittivity at high frequencies. Barium titanate filler was chosen to increase the permittivity of the PDMS elastomer. It was found to be in the tetragonal crystal phase and displayed high permittivity values of 900 at 100Hz and 150 at 10MHz. Frequency and pellet density showed to display a substantial effect on permittivity values of the bulk barium titanate. Barium titanate loaded PDMS elastomers were successfully synthesised. FTIR spectrum confirmed minimal to no chemical interaction between the PDMS and BaTiO<sub>3</sub>, while SEM micrographs confirmed homogenous distribution of the barium titanate within the elastomer. Increase in barium titanate loading led to an increase in permittivity values. In conclusion permittivity values of the elastomer could be controlled by varying the weight percentage of BaTiO<sub>3</sub>. Elastomers with around 27.8 wt% BaTiO<sub>3</sub> loading showed the ideal relative value,  $\epsilon_r = 3.4$  for the strain – sensor design.

High molecular weight PDMS-BaTiO<sub>3</sub> composites were successfully synthesised. The addition of toluene at a weight ratio to PDMS of 0.25:1 caused plasticization of the PDMS allowing homogenous mixing. Silver Lycra was chosen as the antenna material as it demonstrates high conductivity and elasticity. Self-adhesion of the antenna was achieved by placing the silver Lycra onto the elastomer during the curing process. It was found that premature placing of the antenna caused an increase in resistance (loss in conductivity), as the semi cured elastomer would coat and embed the silver Lycra fibres. However, the placement of the antenna 40 minutes into curing displayed resistance maintenance.

A prototype strain sensor RFID tag was successfully produced using the high molecular weight PDMS-BaTiO<sub>3</sub> composite as the substrate. RFID measurements showed the prototype strain sensor could differentiate between y and x-axis strains and could monitor an increase in x-axis strain up to 10.4% via a decrease in transmitted power. The tag was left under around 10 % strain for 1 week before the RFID measurements were repeated and it was concluded the tag showed good performance over time as the 1 week later measurements were not significantly different from the original measurements.

## 2.4 References

- 1 C. Occhiuzzi, C. Paggi and G. Marrocco, *IEEE Trans. Antennas Propag.*, 2011, **59**, 4836-4840.
- 2 X. Yi, C. Cho, J. Cooper, Y. Wang, M. M. Tentzeris and R. T. Leon, *Smart Mater. Struct.*, 2013, **22**, 085009.
- 3 O. O. Rakibet, J. C. Batchelor and S. W. Kelly, in *Antennas and Propagation Conference (LAPC) Proceedings*, IEEE, 2012, pp. 1-4.
- 4 J. Lötters, W. Olthuis, P. Veltink and P. Bergveld, *J. Micromech. Microeng.*, 1997, **7**, 145.
- 5 M. T. Goosey, in *Plastics for electronics*, ed. M. T. Goosey, Kluwer Academic Publishers, London, 1999, Chapter 1, pp. 1-24.
- 6 H. Gankema, R. J. Lugtenberg, J. F. Engbersen, D. N. Reinhoudt and M. Möller, *Adv. Mater.*, 1994, **6**, 944-947.
- 7 G. Gallone, F. Carpi, D. De Rossi, G. Levita and A. Marchetti, *Mater. Sci. Eng. C. Mater. Biol. Appl.*, 2007, **27**, 110-116.
- 8 F. Carpi and D. D. Rossi, *IEEE Trans. Dielectr. Electr. Insul.*, 2005, **12**, 835-843.
- 9 T. Tanaka, *IEEE Trans. Dielectr. Electr. Insul.*, 2005, **12**, 914-928.
- 10 E. A. Cherney, *IEEE Trans. Dielectr. Electr. Insul.*, 2005, **12**, 1108-1115.
- 11 Y. Shen, E. A. Cherney and S. H. Jayaram, in [Conference Record of the 2004 IEEE International Symposium on Electrical Insulation](#), IEEE, 2004, pp. 320-323.
- 12 G. Momen and M. Farzaneh, *Rev. Adv. Mater. Sci.*, 2011, **27**, 1-13.
- 13 F. Rubio, J. Rubio and J. Oteo, *Spectrosc. Lett.*, 1998, **31**, 199-219.
- 14 L. Tellez, J. Rubio, F. Rubio, E. Morales and J. Oteo, *J. Mater. Sci.*, 2003, **38**, 1773-1780.
- 15 C. Brinker, *J. Non Cryst. Solids*, 1988, **100**, 31-50.
- 16 C. Wurrey, W. Bucy and J. Durig, *J. Phys. Chem.*, 1976, **80**, 1129-1136.



- 17 H. C. Pant, M. K. Patra, A. Verma, S. R. Vadera and N. Kumar, *Acta Materialia*, 2006, **54**, 3163-3169.
- 18 R. Mara, G. Sutherland and H. Tyrell, *Phys. Rev.*, 1954, **96**, 801.
- 19 D. Fleisch, *A Student's Guide to Maxwell's Equations*, Cambridge University Press, Cambridge, 2008.
- 20 M. S. Bakir and J. D. Meindl (eds.), *Integrated Interconnect Technologies for 3D Nanoelectronic Systems*, Artech House, Norwood, 2009.
- 21 W. Baker and W. Yager, *J. Am. Chem. Soc.*, 1942, **64**, 2171-2177.
- 22 R. Popielarz, C. Chiang, R. Nozaki and J. Obrzut, *Macromolecules*, 2001, **34**, 5910-5915.
- 23 C. N. R. Rao and K. J. Rao, in *Solid State Chemistry Compounds*, ed. A. K. Cheetham and P. Day, Oxford University Press, Oxford, 1992, pp. 281-296.
- 24 L. Smart and E. Moore, *Solid State Chemistry: An Introduction*, Chapman & Hall, Cheltenham, 1996.
- 25 A. R. West, *Basic Solid State Chemistry*, John Wiley & Sons Inc., Chichester, 1999.
- 26 J. C. Slater, in *Ferroelectricity: The Fundamentals Collection*, ed. J. A. Gonzalo and B. Jimenez Wiley-VCH, Weinham, 2005, pp. 66-79.
- 27 V. Rajendran and A. Marikani, *Materials Science*, Tata McGraw-Hill Education, New Delhi, 2004.
- 28 L. Guo, H. Luo, J. Gao, L. Guo and J. Yang, *Mater. Lett.*, 2006, **60**, 3011-3014.
- 29 P. Arya, P. Jha, G. Subbanna and A. Ganguli, *Mater. Res. Bull.*, 2003, **38**, 617-628.
- 30 M. Vijatović, J. Bobić and B. Stojanović, *Sci. Sinter.*, 2008, **40**, 235-244.
- 31 S. Gablenz, H. Abicht, E. Pippel, O. Lichtenberger and J. Woltersdorf, *J. Eur. Ceram. Soc.*, 2000, **20**, 1053-1060.
- 32 D. Khastgir and K. Adachi, *J. Polym. Sci. Part B Polym. Phys.*, 1999, **37**, 3065-3070.
- 33 C. Chiang, R. Popielarz and L. Sung, in *Mat. Res. Soc. Symp. Proc.*, 2001, pp. N6. 9. 1 - N6. 9. 6.
- 34 A. Babar, V. Bhagavati, L. Ukkonen, A. Elsherbeni, P. Kallio and L. Sydänheimo, *Int. J. Antennas Propag.*, 2012, **2012**.

- 35 H. Denver, T. Heiman, E. Martin, A. Gupta and D. Borca-Tasciuc, *Nsti Nanotech 2008*, 2008, 301-303.
- 36 J. A. Rogers and H. H. Lee, in *Unconventional Nanopatterning Techniques and Applications*, ed. J. A. Rogers and H. H. Lee, John Wiley & Sons, Hoboken, 2008, Chapter 3, pp. 27-66.
- 37 P. C. Painter and M. M. Coleman, *Essentials of Polymer Science and Engineering*, DEStech Publications Inc., Lancaster, 2008.
- 38 [http://www.gs1.org/docs/epc/UHF\\_Regulations.pdf](http://www.gs1.org/docs/epc/UHF_Regulations.pdf), (accessed October 2015).

# Chapter 3: Swelling of polysiloxane networks in solvent vapours; applications for passive UHF-RFID wireless sensors

## 3.0 Introduction

The absorbent, permeable and partitioning properties of polydimethylsiloxane (PDMS) have led to PDMS being widely used as a material in many analytical techniques including solid phase microextraction (SPME)<sup>1</sup>, gas chromatography<sup>2</sup>, and membrane inlet mass spectroscopy. However, it was also found that PDMS tended to swell in non-polar solvents such as pentane and xylene but not so much in polar solvents such as water.<sup>3</sup> While this property of PDMS to swell in more non-polar solvents has been shown to be advantageous in water remediation techniques, such as removing oil from water<sup>4</sup>, it was seen as a large disadvantage in microfluidic systems that used non-polar solvents and in SPME. In the case of SPME, severe swelling can cause the PDMS coating to be damaged when it is retracted into the needle resulting in the sample to be lost. Lee *et al.* determined the extent of PDMS swelling in a range of solvents and found swelling degree correlated with the similarity between the solubility of the solvent and PDMS.<sup>3</sup> Though the swelling of PDMS is often seen as a negative characteristic for many applications, it can be exploited and utilised as an actuator mechanism in a passive RFID solvent vapour sensor tag.

Passive RFID sensors are highly desirable as they are low cost, energy-efficient, wireless and lightweight. There has also been much interest in developing passive RFID volatile organic compound (VOC) sensors for a number of applications including; monitoring food quality in packaging<sup>5</sup> and homeland security.<sup>6</sup> The majority of gas and vapour sensors rely on the variation of electrical properties of a material in response to an analyte as a sensing material. Fiddes and Yan demonstrated an RFID tag array, which utilised carbon black/polymer composites integrated into conventional RFID tags.<sup>7</sup> As the carbon black/polymer composite swells in vapour, the distance between the carbon black changes resulting in a conductive change which in turn changes the signal frequency transmitted from the RFID tag to change. Each of the RFID tags has a different polymer as the sensing element, therefore producing a unique pattern of signals for each vapour. Potyrailo and Morris coated conventional RFID tags with a thin layer of Nafion polymer electrolytes (co-polymer of tetrafluoroethylene and sulfonyl fluoride vinyl ether); the resistance and capacitance of this polymer layer changes in response to vapour absorption.<sup>8</sup> Chemicapacitor systems have also been used as vapour sensors and have previously utilised the known swelling of PDMS in chemical vapour. Polymer-based capacitor sensors detect organic vapours through the absorption of vapour by the polymer, which results in variation of the polymer's permittivity leading to an overall change

in capacitance of the sensor.<sup>9</sup> However, the variance in the polymer's permittivity can be extremely subtle which has led to either the addition of highly conductive additives to PDMS<sup>10</sup> or to measure the change in both permittivity (dielectric) and deformation of the polymer to increase sensitivity.<sup>11</sup>

Rather than rely on capacitance variance, the RFID solvent vapour prototype tag used in chapter 5 takes advantage of the large physical deformation of PDMS elastomers when exposed to vapours using a displacement sensor design. RFID displacement sensors have previously been used in structural health monitoring in the place of using strain gauges, however, a displacement tag design has not yet been used in vapour sensing. Therefore, the aim of this chapter was to fabricate PDMS elastomers to be used in the RFID solvent vapour sensor prototype in chapter 5, investigate their swelling extent in a range of solvent vapours and to understand if the degree of swelling by solvent vapours can be correlated with solubility as shown when swelling occurred in solvents. Swelling studies of 2-cyanoethyltriethoxysilane (TESPN) cross-linked PDMS elastomers, polytrifluoropropylmethylsiloxane (PTFPMS) elastomers, 40 wt% BaTiO<sub>3</sub>-PDMS composites and PDMS sponges were also performed to investigate the effect of chemical modification within the cross-links, chemical modification on the polymer backbone, introduction of fillers and pores, respectively, on the degree of swelling with the intention of possibly creating an array of solvent vapour sensor tags. The property of PDMS swelling was also evaluated as a mechanism for solvent scrubbing.

## 3.1 Experimental

### 3.1.1 Materials and Apparatus

Silanol-terminated polydimethylsiloxane (PDMS) (cSt 1000, M. W. 26 000), silanol-terminated polytrifluoropropylmethylsiloxane (PTFPMS) (cSt 150-250, M. W. 2977) (molecular weight of PTFPMS was calculated *via* <sup>1</sup>H NMR) and 2-cyanoethyltriethoxysilane (TESPN) was obtained from Fluorochem Ltd. Tin(II) 2-ethylhexanoate (95%), tetraethyl orthosilicate (99%) and barium titanate (< 2µm 99.9% trace metal basis) were purchased from Sigma Aldrich. All the above chemicals were used as received. Acetone (lab grade), acetonitrile (HPLC grade), butan-1-ol (analytical grade), chlorobenzene (analytical grade), diethyl ether (analytical grade), ethanol (analytical grade), ethyl acetate (analytical grade), hexane (lab grade), methanol (analytical grade), methylene dichloride (HPLC grade), pentan-1-ol (analytical grade), propan-2-ol (analytical grade), tetrahydrofuran (HPLC grade), toluene (HPLC grade) and xylene (mixture of isomers with meta-xylene as the predominant isomer determined *via* <sup>1</sup>H NMR spectroscopy) (analytical grade) were purchased from Fisher Scientific and used as received. Granulated and caster sugar (Tate and Lyle®) was purchased from the local supermarket. Homogenous mixing of the elastomer components was achieved using a DAC 150FV2-K speedmixer and elastomers were formed in PTFE square moulds (mould width = 2 cm, length = 2 cm and height = 0.2 cm).

### 3.1.2 Synthesis of polysiloxane networks: Sn catalysed condensation method

#### 3.1.2.1 Synthesis of standard PDMS elastomers

Silanol-terminated PDMS (8.00 g,  $3.08 \times 10^{-4}$  mol), cross-linking agent tetraethyl orthosilicate (0.13 g,  $6.24 \times 10^{-4}$  mol) (ratio of SiOH groups in PDMS to SiOR groups in TEOS, 1:4) and catalyst tin (II) 2-ethylhexanoate (0.18 cm<sup>3</sup>, 1 M solution in toluene) were speed-mixed at 3500 rpm for 90 seconds in total. The mixture was poured into square moulds and allowed to cure at room temperature for 2 hours before being placed into an oven at 60 °C overnight.

#### 3.1.2.2 Synthesis of TESPN cross-linked PDMS elastomers

Silanol-terminated PDMS (8.00,  $3.08 \times 10^{-4}$ ), cross-linking agent 2-cyanoethyltriethoxysilane (0.13 g,  $5.98 \times 10^{-4}$ ) (ratio of SiOH groups in PDMS to SiOR groups in TESPN, 1:3) and catalyst tin (II) 2-ethylhexanoate (0.18 cm<sup>3</sup>, 1 M solution in toluene) were speed-mixed at 3500 rpm for 90 seconds in total. The mixture was poured into square mould and allowed to cure at room temperature for 2 hours before being placed into an oven at 60 °C overnight.

#### 3.1.2.3 Synthesis of PDMS sponges

Sugar templates were fabricated using either granulated or caster sugar. Distilled water (1.5 cm<sup>3</sup>) and either granulated or caster sugar (25 g) was thoroughly mixed and packed into square moulds before being kept under vacuum overnight to ensure the full removal of water. To fabricate a PDMS sponge a sugar template was placed into a petri dish which was in turn placed into an ice bath. An ice bath was used to slow the rate of the cross-linking reaction to ensure full saturation of the sugar template by the elastomer mixture could occur. Several preliminary experiments showed that by decreasing the catalyst to slow the rate of the cross-linking reaction rather than the use of an ice bath ensured full saturation of the sugar template but produced sticky not fully cured sponges. Silanol terminated PDMS (15.00 g,  $5.77 \times 10^{-4}$  mol), cross-linking agent tetraethyl orthosilicate (0.24 g,  $1.15 \times 10^{-3}$  mol) and catalyst tin (II) 2-ethylhexanoate (0.36 cm<sup>3</sup>, 1 M solution in toluene) were speed-mixed at 3500 rpm for 90 seconds in total. The mixture was poured around the sugar template until it was level with the top of the template ensuring full immersion of the template did not occur. The mixture was left to infiltrate the spaces between the sugar particles via capillary action. After 30 minutes, the partially saturated template was removed from the mixture and turned over into a clean petri dish in an ice bath. The remaining mixture was again poured around the sugar template and left to infiltrate for a further 30 minutes. The fully saturated sugar template was removed along with any excess mixture. The saturated template was allowed to cure for 2 hours at room temperature and placed in a 60 °C oven overnight. The sugar template was removed by dissolution in an 80 °C water bath and the resulting PDMS sponges were left to dry at room temperature. It was found that full immersion of the sugar template within the elastomer mixture caused an inner pocket within the PDMS sponges that was not desired. The full removal of the sugar template from the PDMS sponge was confirmed by FTIR spectroscopy. SEM micrographs

were used to determine pore morphology along with estimated pore size and nitrogen physisorption was used to determine the pore size distribution and surface area of the sponges.

*FTIR ( $\text{cm}^{-1}$ ) PDMS sponge using caster sugar template:* 3323 (O–H); 2963, 2905 (CH stretching of  $\text{CH}_3$ ); 1416 ( $\text{CH}_3$  asymmetric deformation of Si– $\text{CH}_3$ ); 1258 ( $\text{CH}_3$  symmetric deformation of Si– $\text{CH}_3$ ); 1080, 1009 (Si–O–Si stretching vibrations); 789 (Si–C stretching and  $\text{CH}_3$  rocking); 864, 698, 662 (not identified).

*FTIR ( $\text{cm}^{-1}$ ) PDMS sponge using granulated sugar template:* 3343 (O–H); 2963, 2903 (CH stretching of  $\text{CH}_3$ ); 1412 ( $\text{CH}_3$  asymmetric deformation of Si– $\text{CH}_3$ ); 1258 ( $\text{CH}_3$  symmetric deformation of Si– $\text{CH}_3$ ); 1082, 1009 (Si–O–Si stretching vibrations); 787 (Si–C stretching and  $\text{CH}_3$  rocking); 862, 698, 662 (not identified).

#### 3.1.2.4 Synthesis of 40 wt% BaTiO<sub>3</sub>-PDMS composites

Silanol terminated PDMS (8.00 g,  $3.08 \times 10^{-4}$  mol), cross-linking agent tetraethyl orthosilicate (0.13 g,  $6.24 \times 10^{-4}$  mol) and barium titanate (5.39 g, 0.02 mol) were speed-mixed for x minutes. The catalyst tin (II) 2-ethylhexanoate (0.18 cm<sup>3</sup>, 1 M solution in toluene) was added to the mixture and speed-mixed at 3500 rpm for a further 90 seconds. The mixture was poured into square moulds and allowed to cure at room temperature for 2 hours before being placed into an oven at 60 °C overnight.

#### 3.1.2.5 Synthesis of polytrifluoropropylmethylsiloxane (PTFPMS) elastomers

Silanol-terminated PTFPMS (8.00 g,  $2.69 \times 10^{-3}$  mol), cross-linking agent tetraethyl orthosilicate (1.12 g,  $5.38 \times 10^{-3}$  mol) and catalyst tin (II) 2-ethylhexanoate (1.62 cm<sup>3</sup>, 1 M solution in toluene) were speed-mixed at 3500 rpm for 90 seconds in total. The mixture was poured into square moulds and allowed to cure at room temperature for 2 hours before being placed into an oven at 60 °C overnight. The PTFPMS elastomer structures were confirmed by FTIR spectroscopy.

*FTIR ( $\text{cm}^{-1}$ ):* 2965 (CH stretching of  $\text{CH}_3$ ); 2913 ( $\text{CH}_2$  asymmetric C–H stretching); 1447, 1422 ( $\text{CH}_3$  asymmetric deformation of Si– $\text{CH}_3$ ); 1369, 1315, 1123 (C–F stretching vibration); 1261 (symmetric bending vibration of Si– $\text{CH}_3$ ); 1206 (Si– $\text{CH}_2\text{CH}_2\text{CF}_3$ ); 1063, 1009 (Si–O–Si asymmetric stretching vibration); 799 (rocking vibration of Si– $\text{CH}_3$ ); 764 (C–F symmetric deformation vibration); 895, 837, 718, 673, 638, 552 (not identified).

#### 3.1.3 Characterisation of the polysiloxane networks

The following instruments were used to characterise the polysiloxane networks before solvent vapour absorption experiments were performed. FTIR measurements of the PTFPMS elastomers and PDMS sponges were performed using a Shimadzu IRAffinity-1 spectrometer, each sample was scanned 64 times at room temperature and atmospheric pressure with a resolution of 4 cm<sup>-1</sup>. BSE SEM (Back Scattering Electrons Scanning Electron Microscopy) images of the PDMS sponges were performed using a SEM (Hitachi SE-3400)/EDX (Oxford instruments X-Max 80) integrated system.

Nitrogen physisorption analysis of the PDMS sponges were performed using a Thermo Scientific Surfer Gas Adsorption Porosimeter. Full characterisation of the standard PDMS elastomers, TESPN cross-linked elastomers and BaTiO<sub>3</sub>-PDMS composites have already been performed and can be found in full detail in chapter 2.

#### 3.1.4 Swelling experiments

The PDMS elastomers were used as prepared (length = 2 cm, width = 2cm and height = 0.2 cm) and were placed in a saturated atmosphere of each solvent vapour for 72 hours. To achieve a saturated atmosphere, 25 cm<sup>3</sup> of each solvent was poured into the bottom of a dessicator (internal seal diameter of 10.1 cm). The circular perforated shelf was placed back into the dessicator with a PDMS elastomer in a petri dish placed on top. The dessicator was sealed and at the end of 72 hours excess solvent was still present indicating a saturated atmosphere was achieved. The volume and weight of each PDMS elastomer was measured before and after solvent vapour exposure. To measure the extent of PDMS swelling, the volume swelling ratio ( $Q_v$ ), defined as the ratio of the volume of swollen PDMS to its dry volume was calculated along with the weight swelling ratio ( $Q_w$ ), defined as the ratio of the weight of swollen PDMS to its dry weight. The volume of the PDMS elastomer was measured using digital calipers (0-150 mm). PDMS swelling experiments for each solvent were performed three times in total.

#### 3.1.5 Solvent scrubber experiments

To investigate if the standard elastomers could 'mop up' solvent in an enclosed space several solvent scrubber experiments using toluene, chlorobenzene, ethyl acetate, acetone, hexane and diethyl ether were performed. Only solvents that caused either large or mid-range PDMS swelling were used. The standard PDMS elastomers were originally weighed and the maximum weight of each of the six solvents that the PDMS elastomer could absorb was calculated using the weight swelling ratio ( $Q_w$ ). 90 wt% of the maximum weight of the solvent that the standard PDMS elastomer could absorb was weighed in a crucible which was then placed within a dessicator (internal seal diameter of 10.1 cm) with a pre-weighed PDMS elastomer in a petri dish. The dessicator was sealed and at the end of 72 hours the PDMS elastomer was re-weighed and the presence of any remaining solvent within the crucible was noted. This procedure was repeated for all six solvents.

## 3.2 Results and Discussion

### 3.2.1 Polysiloxane Network Characterisation

#### 3.2.1.1 PDMS sponges

The PDMS sponges produced were white in appearance with visible pores and could be manually compressed without any breakage. Visual inspection of the sponges confirmed the pores were interconnected throughout the whole sample and no large internal cavities of air were present. It

was found in preliminary experiments that if the sugar template was immersed in the PDMS mixture during the saturation process, a sponge with a large air cavity was formed. It was observed that the PDMS sponges formed using the caster sugar template appeared to possess smaller pores than the sponges formed using the granulated sugar template, which was expected as the granulated sugar crystals are much larger than caster sugar crystals. To further investigate the size of the pores and the surface area of the PDMS sponges both SEM micrographs were taken and nitrogen physisorption was performed. SEM micrographs of the cross-section and surfaces of both PDMS sponges are shown in figures 3.0 and 3.1.

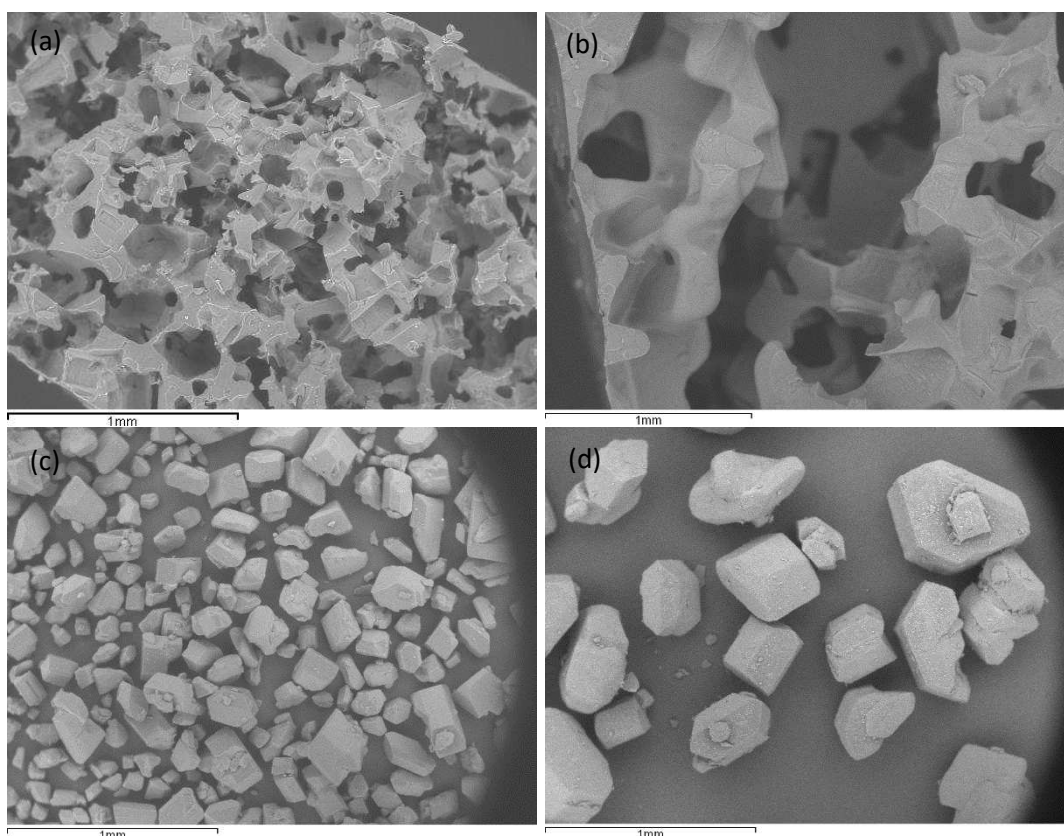


*Figure 3.0: SEM micrograph of PDMS sponge prepared using (a) caster sugar template and (b) granulated sugar template. SEM micrograph of (c) caster sugar and (d) granulated sugar. Scale bar is 1 mm in length.*



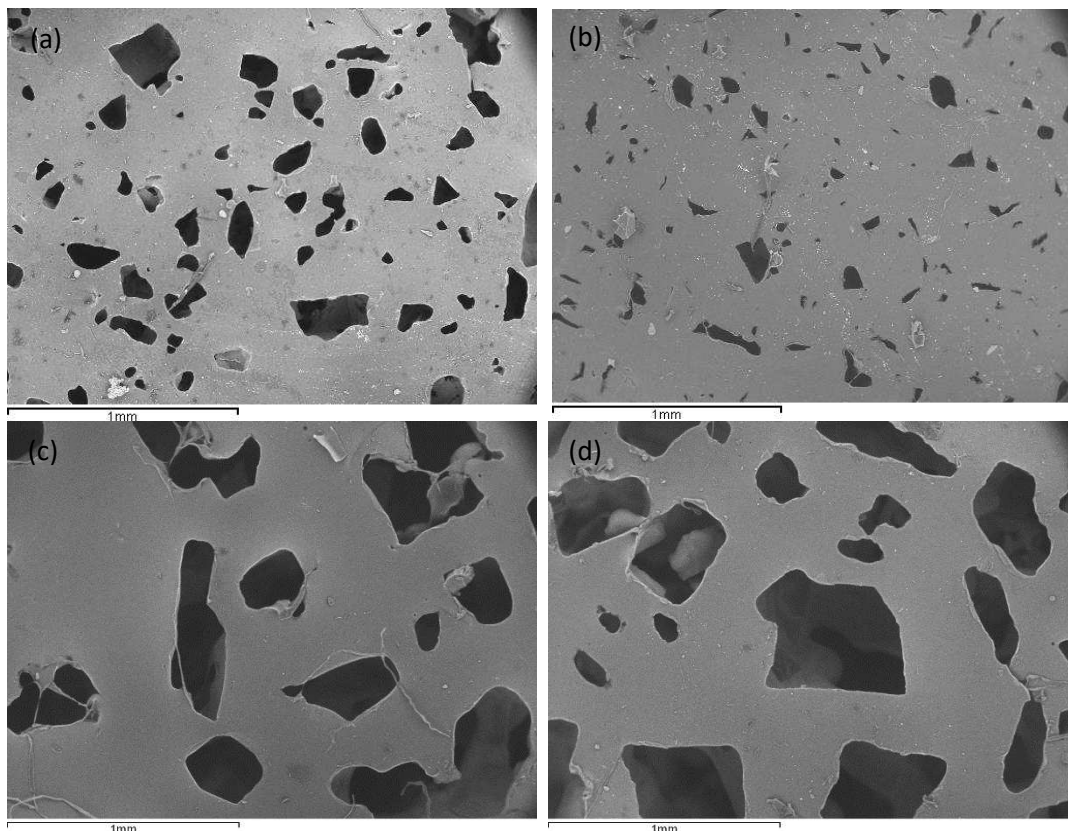


Figure 3.1: SEM micrographs of (a) top surface and (b) bottom surface of PDMS sponge prepared using a caster sugar template and (c) top surface and (d) bottom surface of PDMS sponge prepared using a granulated sugar template. Scale bar is 1 mm in length.

Figures 3.0 and 3.1 confirmed that both sponges exhibited an interconnected three-dimensional framework and showed that both the top and bottom surface of the sponges were also porous. The pores within the sponges did not exhibit the cube-like shape of the sugar crystals (figure 3.0) as expected. The irregular shape of the pores was attributed to the random packing of the sugar crystals in the sugar template. The walls of the pores appeared to be smooth, however striations were observed from the mechanical cutting required to produce a cross-section for SEM analysis. To obtain a rough guideline of pore size, the calliper function in INCA (SEM software) was used to measure the pore sizes of both PDMS sponges. Pore sizes up to 342  $\mu\text{m}$  were found when caster sugar templates were used. In comparison, pore sizes up to 867  $\mu\text{m}$  were observed when granulated sugar templates were used. The sponge fabricated using the caster sugar template exhibited a type III  $\text{N}_2$ -physisorption isotherm (Figure 3.2) which is typically associated with macroporous or non-porous materials with weak adsorbent-adsorbate interactions. The  $\text{N}_2$ -physisorption isotherm confirmed the pore size measured from the SEM micrograph.

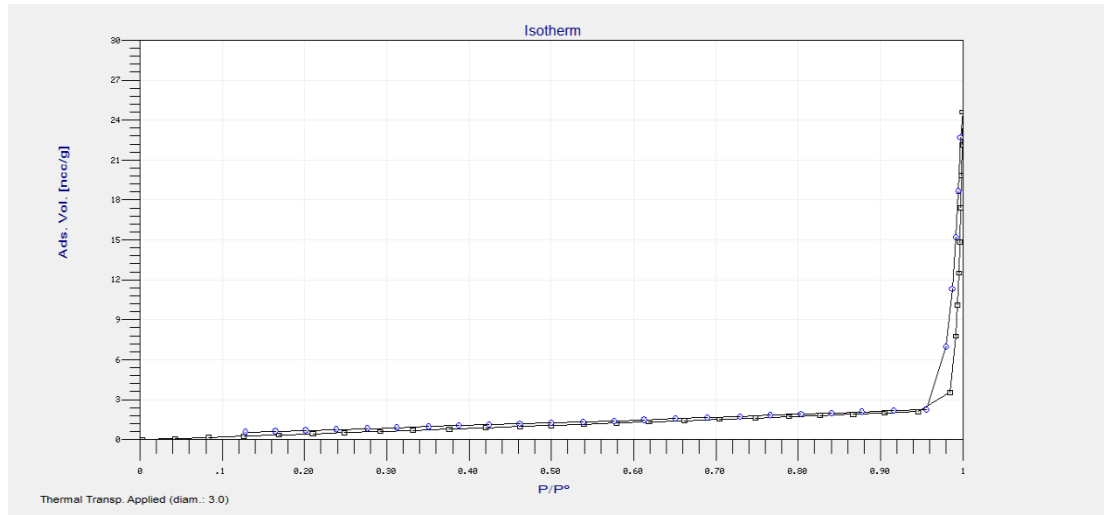


Figure 3.2: Nitrogen physisorption isotherm of PDMS sponges fabricated using a caster sugar template.

The BET (Brunauer, Emmett and Teller) method is commonly used to determine the surface area of the material. BET theory describes multilayer adsorption with the following assumptions:- (i) the adsorbent surface is made of equivalent sites where molecules are adsorbed randomly (ii) no lateral interactions between adsorbed molecules occur therefore, the probability of a site being occupied is independent of a neighbouring site being occupied and (iii) the molecules in the first layer act as sites for the molecules in the second layer and so forth forming multi-layers.<sup>12</sup> The derived BET equation is as follows:

$$\frac{1}{w[(P^0/P)-1]} = \frac{1}{w_m c} + \frac{c-1}{w_m c} (P/P^0) \quad (\text{Equation 3.0})$$

Where  $P$  is the partial pressure of the adsorbate gas,  $P^0$  is the saturated pressure of the adsorbate gas,  $w$  is the weight of gas adsorbed at standard temperature and pressure (STP),  $w_m$  is the weight of gas adsorbed at STP to produce a monolayer of adsorbate on the adsorbent surface and  $c$  is the BET constant that is related to the enthalpy of adsorption of the adsorbate gas on the adsorbent surface. To calculate surface area using the BET method, the physisorption isotherm is transformed into a BET plot ( $1/w [(P^0/P)-1]$  versus  $P/P^0$ ) from which the  $w_m$  and  $c$  can be derived.<sup>13</sup> A typical BET plot is a straight line in the relative pressure region,  $0.05 \leq P/P^0 \leq 0.35$ .<sup>14</sup> The slope,  $s$  and intercept,  $i$  of a BET plot are:

$$s = \frac{c-1}{w_m c} \quad (\text{Equation 3.1})$$

$$i = \frac{1}{w_m c} \quad (\text{Equation 3.2})$$

The two previous equations can be solved to derive both the  $w_m$  and  $c$  as follows:<sup>15</sup>

$$w_m = \frac{1}{s+i} \quad (\text{Equation 3.3})$$

$$c = \frac{s}{i} + 1 \quad \text{(Equation 3.4)}$$

The calculated  $w_m$  is then used to calculate the total surface area ( $S_t$ ). By dividing the total surface area by the weight of the sample, the specific surface area (also known as the BET surface area) of the sample is found. The equation for total surface area is as follows:

$$S_t = \frac{w_m \bar{N} A_x}{\bar{M}} \quad \text{(Equation 3.5)}$$

Where  $\bar{N}$  is Avogadro's number,  $A_x$  is the cross sectional area of the adsorbate and  $\bar{M}$  is the adsorbate molecular weight. However, it has been highlighted that the BET method is not applicable to a material which exhibits a type III physisorption isotherm<sup>16</sup> which was observed for the PDMS sponge. The BET constants ( $c$ ) of type III isotherms are typically very small at around 1 or 2 and when this value is so small any small change can have a profound effect on the calculated  $w_m$ . Also, the values of  $w$  are extremely small over the relative pressure range used in the BET plot which leads to inaccurate BET surface areas. As a result, the BET surface area was not calculated and nitrogen physisorption was not performed on either the standard PDMS elastomer or PDMS sponge fabricated using the granulated sugar template. It has been suggested that using a different adsorbate could enable the BET equation to be used to calculate the sponge's surface area.<sup>15</sup> As shown in figure 3.2 the sponge exhibited a type III isotherm which means that the adsorbate – adsorbent interaction is weak. If the adsorbent was changed, the adsorbate – adsorbent interaction could increase which in turn could change the isotherm into one where the BET method to calculate surface area was applicable i.e. type II isotherm.

FTIR spectroscopy was used to determine if the sugar template was completely removed through dissolution and to confirm the structure of the PDMS sponges. Figure 3.3 shows the FTIR spectrum of a PDMS sponge fabricated using a caster sugar template, a PDMS sponge fabricated using a granulated sugar template, a standard PDMS elastomers and neat caster sugar. The FTIR spectrum of caster and granulated sugar were exactly the same which was expected as the only difference between the two sugars should be the sugar particle size. The FTIR spectra of both sponges were almost identical to the FTIR spectrum of the PDMS elastomer apart from the appearance of a small broad absorption band around  $3300 \text{ cm}^{-1}$  assigned to O–H stretching. The absorption band at around  $3300 \text{ cm}^{-1}$  in the PDMS sponges could be caused by either the presence of sugar, hydrolysed TEOS groups or water. It has been previously discussed that TEOS undergoes hydrolysis under acid catalysis. In this case excess TEOS was used which results in free hydrolysed TEOS not being used in the cross-linking reaction. However, it has been shown that hydrolysed TEOS can form silica via a water condensation reaction with other hydrolysed TEOS molecules<sup>17</sup> therefore potentially only a small amount or if any hydrolysed TEOS would be left in the PDMS elastomer. As shown in figure 3.3, there were no other characteristic FTIR absorption bands for sugar observed in the FTIR spectra of the sponges, which strongly suggested that the sugar template had been completely removed

through the dissolution process. The complete removal of the sugar template was also confirmed through SEM micrographs, as no sugar particles were observed in the PDMS sponges. It is most likely that the FTIR absorption band at around  $3300\text{ cm}^{-1}$  was caused by the presence of a small amount of water which was a result of incomplete drying of the PDMS sponges after the dissolution process.

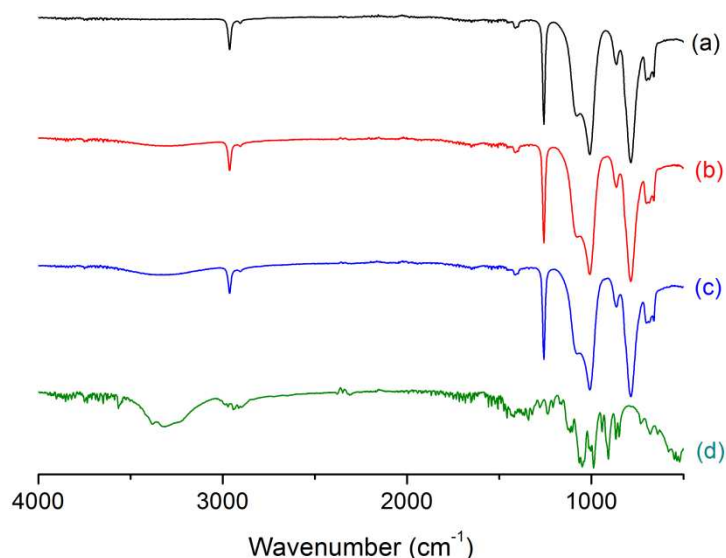


Figure 3.3: FTIR spectra of (a) standard PDMS elastomer, (b) PDMS sponge formed using a caster sugar template, (c) PDMS sponge formed using a granulated sugar template and (d) caster sugar

### 3.2.1.2 PTFPMS elastomers

The resulting PTFPMS elastomers were opaque and white in appearance. Compared to the PDMS elastomers, the PTFPMS elastomers were slightly firmer and held a distinctive mottled pattern on the top surface. FTIR spectrum of pure PTFPMS, cross-linked PTFPMS elastomers and pure TEOS are shown in figure 3.4. FTIR absorption bands have been identified with different functional groups of the cross-linked elastomers in section 3.1.2.5. As shown in figure 3.4 there was a small absorption band around  $3600\text{ cm}^{-1}$  assigned to the O–H stretch for the pure silanol terminated PTFPMS polymer. As previously discussed in chapter 2, a decrease in intensity or absence of the O–H absorption band in the FTIR spectrum of the cross-linked PTFPMS elastomer can be used as a marker to show the cross-linking reaction. The disappearance of the absorption band around  $3600\text{ cm}^{-1}$  observed in the FTIR spectrum of the cross-linked PTFPMS confirmed a full cross-linking reaction had occurred. Further FTIR markers for the polycondensation cross-linking reaction are the appearance of the band at  $850\text{ cm}^{-1}$  and the bands  $1000\text{--}1100\text{ cm}^{-1}$  assigned to the Si–O–Si cross-link. However, neither of these FTIR markers could be used to investigate the cross-linking reaction. As shown in figure 3.4, the absorption bands at  $1063$  and  $1009\text{ cm}^{-1}$  assigned to the Si–O–Si asymmetric stretching vibration in the FTIR spectrum of the cross-linked PTFPMS elastomer did not increase in intensity nor did the absorption band at  $837\text{ cm}^{-1}$ . The presence of ethanol – the by-product of the polycondensation reaction – was not detected in the FTIR spectrum which confirmed

removal of the solvent was achieved through heating during the curing process. The FTIR spectra of the PTFPMS elastomer was extremely similar to that of the PDMS elastomer, apart from the additional absorption bands at 1206, 1315, 1367, 1123 and 764  $\text{cm}^{-1}$  that are characteristic of the trifluoropropyl group.

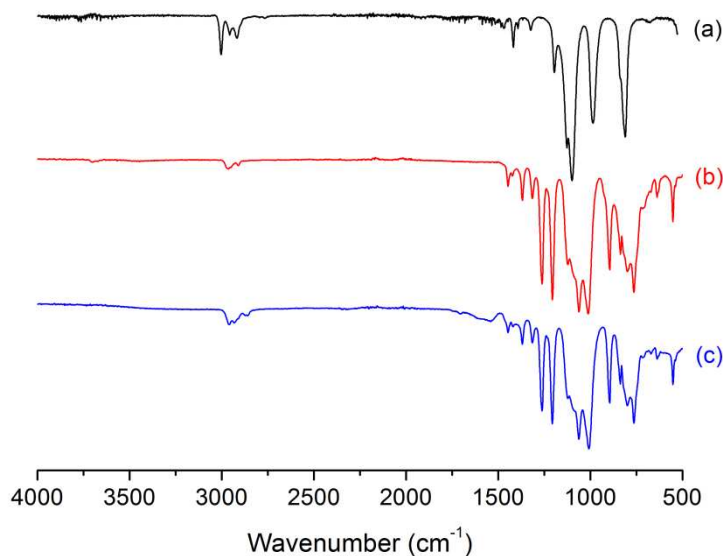


Figure 3.4: FTIR spectra of (a) TEOS (b) silanol terminated PTFPMS (pure polymer) and (c) cross-linked PTFPMS elastomer.

The morphology of the PTFPMS elastomers was investigated using SEM. SEM micrographs of the top and bottom surface along with a cross-section of a PTFPMS elastomer was shown in figure 3.5. The lacerations shown in figure 3.5 (e) were a result of the mechanical cutting required to obtain the cross-section of the elastomer. White circles were observed throughout the PTFPMS elastomer as shown in figure 3.5 (b), (d) and (e). EDX analysis was performed to examine the composition of the white circles compared to the surrounding area. The EDX spectra showed that while the same elements (carbon, oxygen, silicone, fluorine and tin) were detected within both the white circles and surrounding area, a larger concentration of tin was found within the white circles. This suggested that the white circles are a result of slight phase separation between the polymer and tin catalyst and are essentially capsules of tin catalyst. This phase separation was not observed in the SEM micrographs of standard PDMS elastomers.

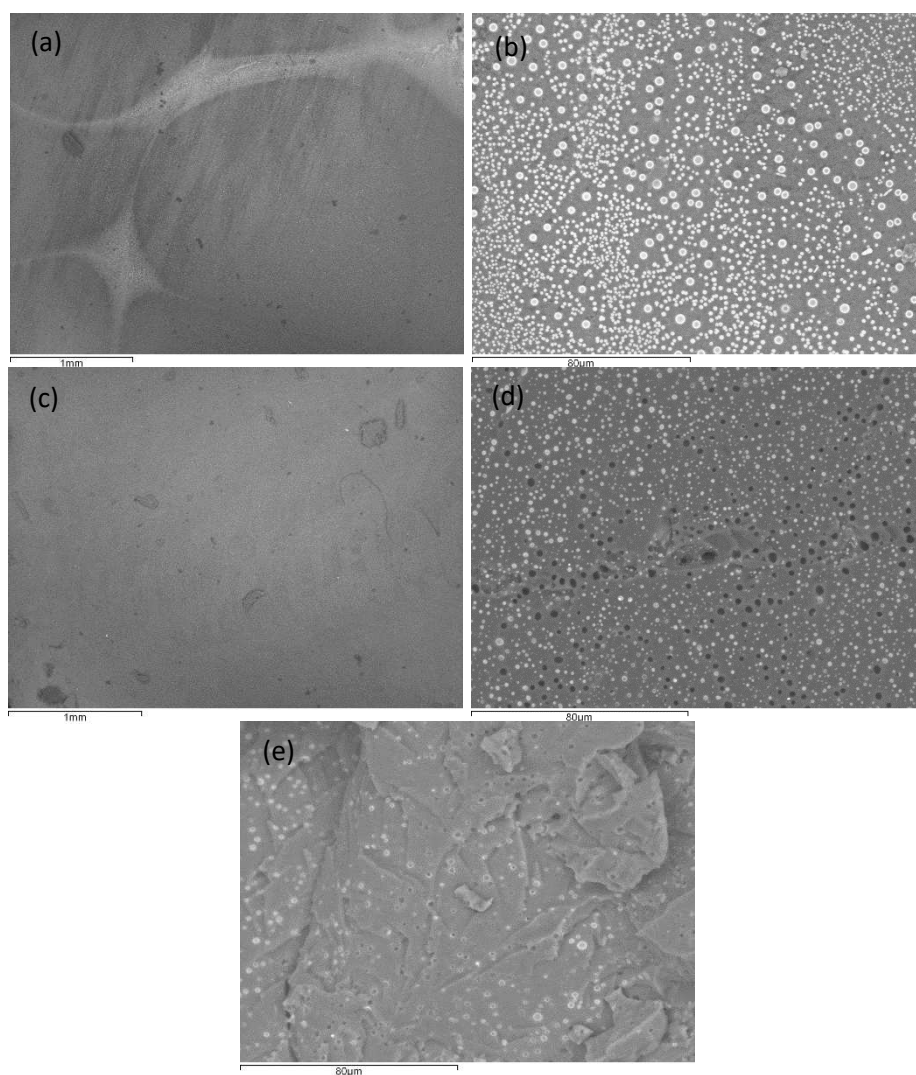


Figure 3.5: SEM micrographs (a-b) top surface, (c-d) bottom surface and (e) cross-section of PTFPMS elastomer. Scale bar for (a) and (c) is 1 mm and for (b), (d) and (e) is 80  $\mu\text{m}$  in length.

### 3.2.2 Standard PDMS swelling

The standard PDMS elastomers were placed in a saturated atmosphere of each of the fifteen chosen solvent vapours for 72 hours. The long solvent exposure time was chosen to ensure the PDMS elastomer reached their maximum swelling. Figure 3.6 shows the swelling ratio in terms of both weight and volume of the elastomer after vapour exposure. Each of the swelling experiments were performed a total of three times and the standard error (standard deviation of the mean) was calculated. As shown in figure 3.6 the standard errors were small indicating the maximum swelling values of the PDMS elastomers in each solvent vapour were reliable.

Generally PDMS shows a degree of solvent vapour specificity with non-polar to weakly polar solvent vapours with ethers (diethyl ether and tetrahydrofuran), hexane and DCM causing the largest swelling, ( $Q_v > 2.0$ ) and polar solvent vapours, alcohols (pentan-1-ol, butan-1-ol, propan-2-ol, ethanol and methanol) and acetonitrile causing the least swelling ( $Q_v = 1.0-1.3$ ) which was expected

for PDMS. As expected there were some observed differences between  $Q_V$  and  $Q_W$  which was attributed to the density differences between the solvents. For solvents with densities  $> 1 \text{ g ml}^{-1}$   $Q_V < Q_W$  and solvents with densities  $< 1 \text{ g ml}^{-1}$   $Q_V > Q_W$ . The differences between  $Q_V$  and  $Q_W$  are greater for solvents that cause a larger degree of swelling. Thus dichloromethane which possesses a large density and caused large PDMS swelling showed the largest difference between  $Q_V$  and  $Q_W$ . Along with  $Q_V$  and  $Q_W$ , the moles of absorbed solvent vapour were also calculated. Further analysis was performed using all three methods of describing PDMS swelling, however, more focus has been placed on using the volume swelling ratio as the RFID tag antenna relies on the lateral deformation of the substrate. Figure 3.7 shows the swelling extent in terms of moles of solvent vapour absorbed into the standard PDMS elastomer after vapour exposure.

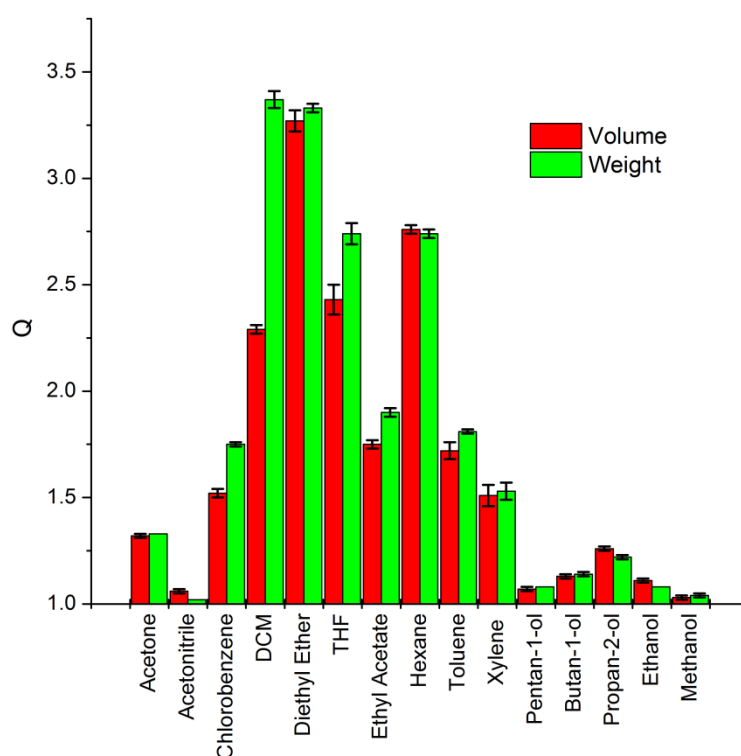


Figure 3.6: Swelling ratio ( $Q$ ) of PDMS elastomer after 72 hours exposure to a range of solvent vapours.

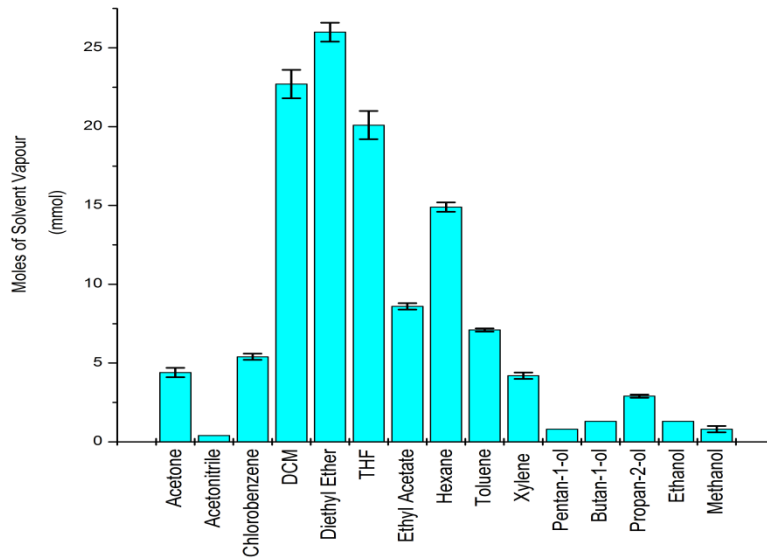


Figure 3.7: Moles of solvent vapour absorbed into elastomer after 72 hours exposure.

### 3.2.3 Correlation between swelling and solubility parameters

Previous research investigated PDMS swelling by the direct absorption of solvents (liquid-solid interface) and found that the extent of swelling could be correlated with the Hildebrand solubility parameter ( $\delta$ ,  $\text{cal}^{1/2} \text{cm}^{-3/2}$ ). In the Hildebrand model, solubility can be related to the cohesive energy of the molecule:<sup>18,19</sup>

$$\delta = (-E/V)^{1/2} \quad \text{(Equation 3.6)}$$

Where  $\delta$  is the Hildebrand solubility parameter,  $-E$  is the molecular cohesive energy and  $V$  is the molar volume. The cohesive energy of the molecule is derived from the heat of vaporisation. Lee *et al.* observed that solvents with a solubility parameter close to that of PDMS caused the largest swelling (Figure 3.8).<sup>20</sup> However, the authors did note a significant lack of correlation was observed for certain solvents where those with similar solubility parameter caused significantly different degrees of PDMS swelling. The differences were attributed to the solvent polarity differences and the authors used the dipole moment of the solvent to explain the difference observed swelling and represent the polar contributions to the overall solubility. Generally Hildebrand solubility parameters are good predictors for the compatibility of materials with non-polar and weakly polar solvents but are often poor for solvent with significant polar and/or hydrogen bonding properties.



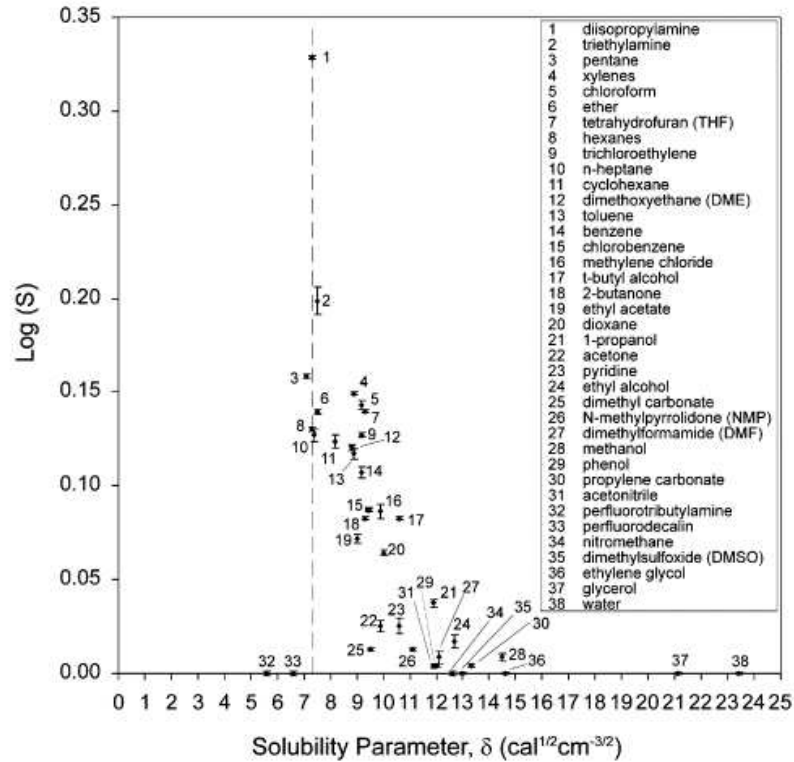


Figure 3.8: Swelling ratio,  $S$  of PDMS in various solvents versus the solvent's Hildebrand solubility parameter,  $\delta$ . Figure reprinted with permission from J. N. Lee, C. Park and G. M. Whitesides, *Anal. Chem.*, 2003, **75**, 6544-6554. Copyright © 2003, American Chemical Society.

As an extension of the Hildebrand method, Hansen suggested that the cohesive energy should be divided into three components: dispersion interactions ( $\delta_d$ ), dipolar interactions ( $\delta_p$ ) and hydrogen bonding interactions ( $\delta_h$ ).<sup>21,22</sup> These three components are known as the Hansen solubility parameters (MPa<sup>1/2</sup>) and are additive:

$$\delta_t^2 = \delta_d^2 + \delta_p^2 + \delta_h^2 \quad (\text{Equation 3.7})$$

Solubility often follows the general rule of 'like dissolves like' and therefore two materials to be soluble the Hansen solubility parameters of each material must be similar. In this chapter, the Hansen solubility parameters (HSPs) rather than the Hildebrand solubility parameter were used to investigate PDMS swelling in a number of solvent vapours. To measure the similarity of the HSP of PDMS to the HSP of each solvent, the Ra defined as the distance between the HSP's of two molecules was calculated for each solvent using the following equation:<sup>22,23</sup>

$$Ra = \sqrt{(\delta_{dp} - \delta_{ds})^2 + (\delta_{pp} - \delta_{ps})^2 + (\delta_{hp} - \delta_{hs})^2} \quad (\text{Equation 3.8})$$

Where  $p$  and  $s$  indicate the polymer and solvent contributions, respectively. The smaller the Ra value the higher degree of absorption and the higher swelling of PDMS. The Hansen solubility parameters and calculated Ra values for each solvent was shown in Table 3.0. Figure 3.9 showed

the calculated Ra values for each of the solvents *versus*  $Q_w$ ,  $Q_v$  and moles of solvent absorbed. In general solvents with a  $R_a < 8.0$  show the largest PDMS swelling and solvents with a  $R_a > 8.0$  show the least PDMS swelling. However, it was clear that there was no simple relationship between the value of  $R_a$  and the extent of PDMS swelling. Solvents with low polarities are ranked accurately in swelling ability, however, more polar solvents are not.

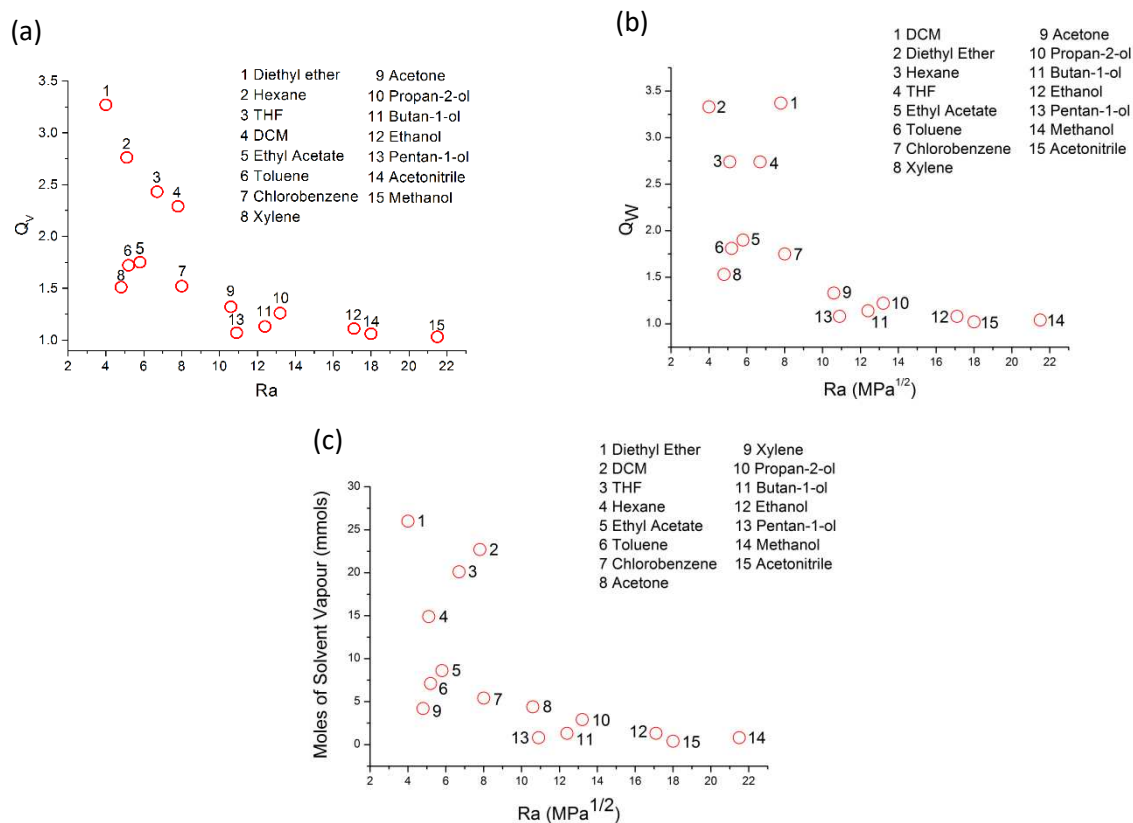


Figure 3.9: (a)  $Q_v$  (b)  $Q_w$  and (c) moles of absorbed solvent vapour versus  $R_a$  for each solvent. The numbers relate to the ranking of the solvents swelling ability.

Henry's Law states that the overall absorbed concentration of gas,  $C$  (maximum PDMS swelling in this case) is directly proportional to the partial pressure of the gas,  $P$  and solubility,  $S$ :

$$C = SP \quad \text{(Equation 3.9)}$$

To investigate the effect of the solvent's vapour pressure on the extent of PDMS swelling,  $Q_w$ ,  $Q_v$  and moles of solvent vapour absorbed were plotted against the solvents vapour pressure as shown in Figure 3.10(a) and (b), respectively.

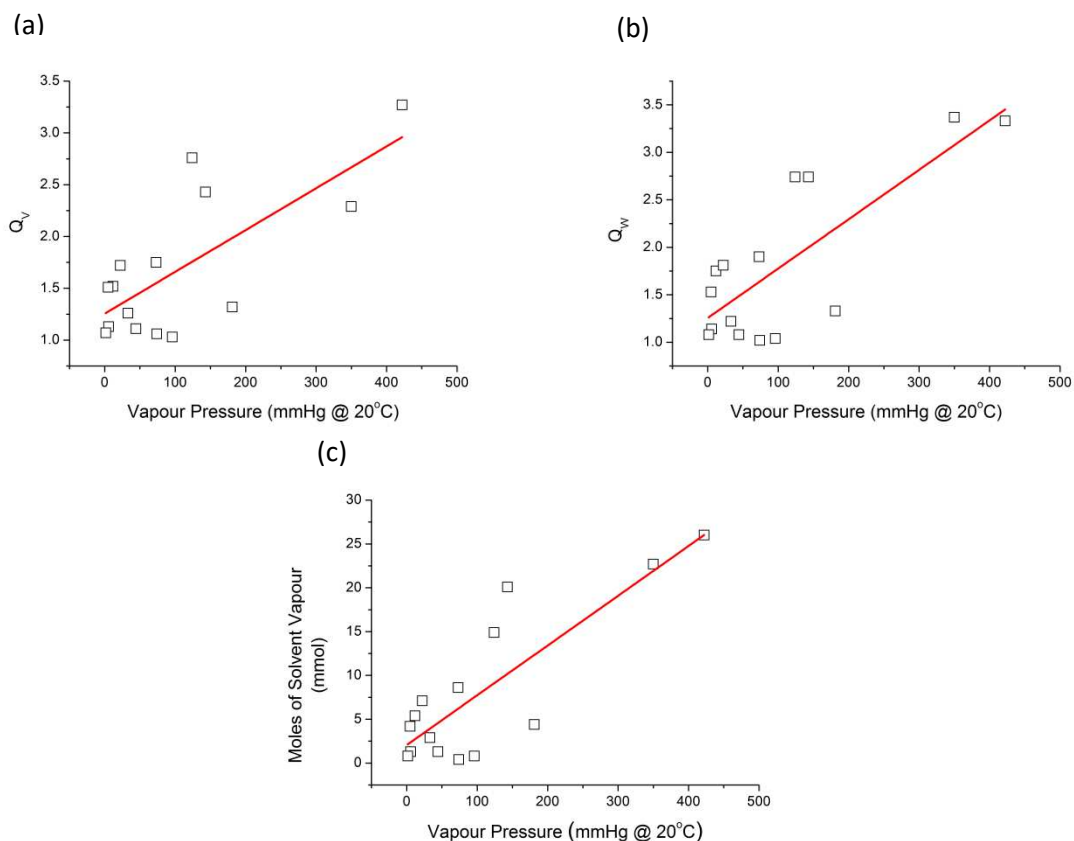


Figure 3.10: (a)  $Q_v$  versus vapour pressure (b)  $Q_w$  versus vapour pressure and (c) moles of solvent vapour in swollen elastomer versus vapour pressure.

None of the three graphs exhibited a linear relationship, however the Pearson correlation coefficient values obtained via linear fitting of the graphs using Origin software showed there was a strong correlation between swelling degree and vapour pressure. The Pearson correlation coefficient of figure 3.10(a), (b) and (c) was 0.73, 0.79 and 0.83, respectively. As previously discussed the extent of PDMS swelling has shown a strong correlation between both solubility and vapour pressure. Therefore, in accordance with Henry's law the relationship between both the total Hansen solubility parameter ( $\delta_t$ ), vapour pressure of the solvent and extent of PDMS swelling was plotted (figure 3.11). It was observed that the difference in  $Q_v$  for solvents with similar total solubility parameters could be explained by the difference in the solvent's vapour pressures. Generally, a solvent with a high vapour pressure exhibits a larger  $Q_v$  than a solvent with a similar  $\delta_t$  and a low vapour pressure. This was also observed when  $Q_w$  and moles of absorbed solvent vapour was used to describe the degree of elastomer swelling. Linear regression analyses were performed using a range of x (independent) variables; including Hansen solubility parameters, Ra, vapour pressure, molar volume and water content.

Table 3.0: Volume and weight swelling ratios (standard PDMS elastomers), Hansen solubility parameters, Ra and ranking for each solvent. Ranking refers to the order of the solvent swelling ability with rank 1 being the best solvent.

| Solvent         | Q <sub>v</sub> | Q <sub>w</sub> | Solvent vapour<br>(mmol) | Hansen Solubility Parameters (MPa <sup>1/2</sup> ) |                |                |                | Ra (MPa <sup>1/2</sup> ) | Rank (Q <sub>v</sub> ) | Rank (Q <sub>w</sub> ) | Rank (mmol) | P <sub>VP</sub> (mmHg @ 20°C) |
|-----------------|----------------|----------------|--------------------------|--|----------------|----------------|----------------|--------------------------|------------------------|------------------------|-------------|-------------------------------|
|                 |                |                |                          | δ <sub>d</sub>                                     | δ <sub>p</sub> | δ <sub>h</sub> | δ <sub>t</sub> |                          |                        |                        |             |                               |
| Acetone         | 1.32           | 1.33           | 4.4                      | 15.5   | 10.4           | 7.0            | 19.9           | 10.6                     | 9                      | 9                      | 8           | 181.0                         |
| Acetonitrile    | 1.06           | 1.02           | 0.4                      | 15.3   | 18.0           | 6.1            | 24.2           | 18.0                     | 14                     | 15                     | 15          | 74.0                          |
| Butan-1-ol      | 1.13           | 1.14           | 1.3                      | 16.0   | 5.7            | 15.8           | 23.2           | 12.4                     | 11                     | 11                     | 11          | 5.5                           |
| Chlorobenzene   | 1.52           | 1.75           | 5.4                      | 19.0   | 4.3            | 2.0            | 19.6           | 8.0                      | 7                      | 7                      | 7           | 11.7                          |
| Diethyl Ether   | 3.27           | 3.33           | 26.0                     | 14.5   | 2.9            | 5.1            | 15.6           | 4.0                      | 1                      | 2                      | 1           | 422.0                         |
| Ethanol         | 1.11           | 1.08           | 1.3                      | 15.8   | 8.8            | 19.4           | 26.5           | 17.1                     | 12                     | 12                     | 12          | 44.3                          |
| Ethyl Acetate   | 1.75           | 1.90           | 8.6                      | 15.8   | 5.3            | 7.2            | 18.2           | 5.8                      | 5                      | 5                      | 5           | 73.0                          |
| Hexane          | 2.76           | 2.74           | 14.9                     | 14.9   | 0.0            | 0.0            | 14.9           | 5.1                      | 2                      | 3                      | 4           | 124.0                         |
| Methanol        | 1.03           | 1.04           | 0.8                      | 15.1   | 12.3           | 22.3           | 29.6           | 21.5                     | 15                     | 14                     | 14          | 96.0                          |
| DCM             | 2.29           | 3.37           | 22.7                     | 18.2   | 6.3            | 6.1            | 20.2           | 7.8                      | 4                      | 1                      | 2           | 350.0                         |
| Pentan-1-ol     | 1.07           | 1.08           | 0.8                      | 15.9   | 5.9            | 13.9           | 21.9           | 10.9                     | 13                     | 13                     | 13          | 1.5                           |
| Propan-2-ol     | 1.26           | 1.22           | 2.9                      | 15.8   | 6.1            | 16.4           | 23.6           | 13.2                     | 10                     | 10                     | 10          | 33.0                          |
| Tetrahydrofuran | 2.43           | 2.74           | 20.1                     | 16.8   | 5.7            | 8.0            | 19.5           | 6.7                      | 3                      | 4                      | 3           | 143.0                         |
| Toluene         | 1.72           | 1.81           | 7.1                      | 18.0   | 1.4            | 2.0            | 18.2           | 5.2                      | 6                      | 6                      | 6           | 22.0                          |
| Xylene          | 1.51           | 1.53           | 4.2                      | 17.8   | 0.9            | 1.8            | 17.9           | 4.8                      | 8                      | 8                      | 9           | 4.8                           |
| PDMS            | -              | -              | -                        | 15.9   | 0.1            | 4.7            | 16.6           | -                        | -                      | -                      | -           | -                             |

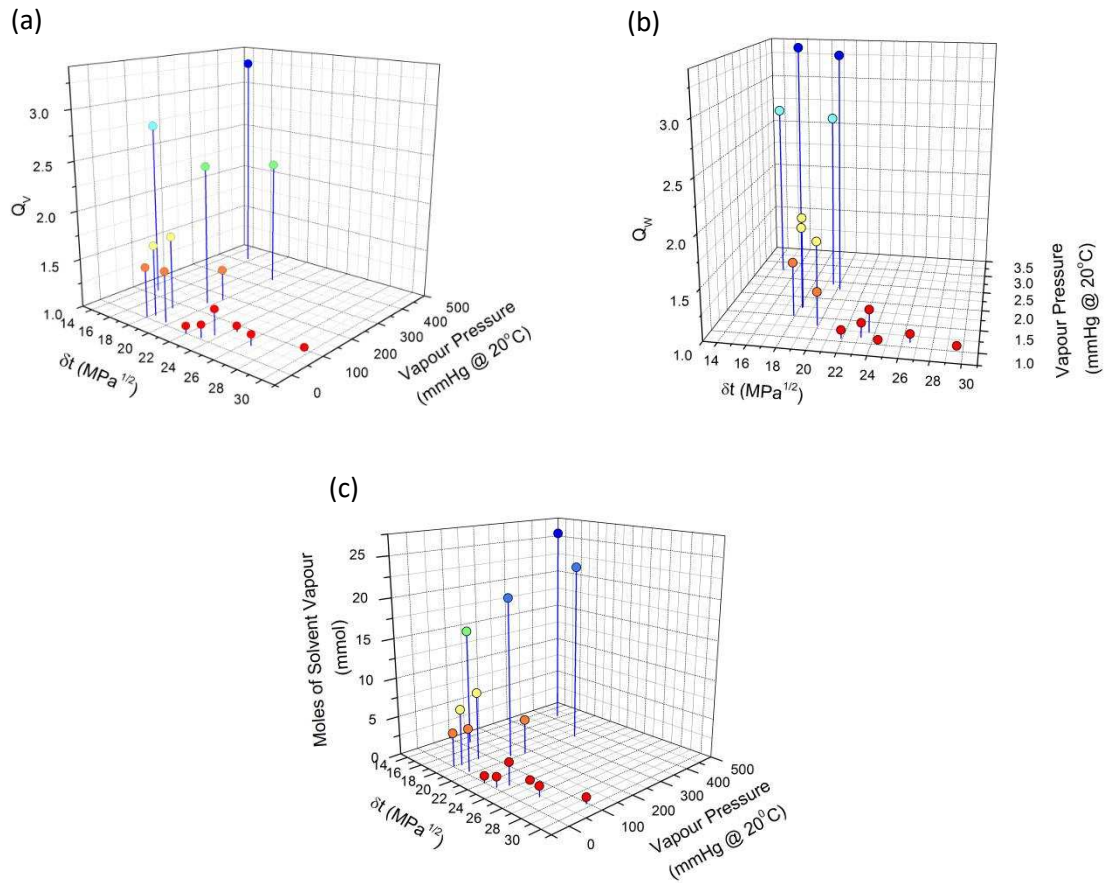


Figure 3.11: (a)  $Q_V$  versus the total Hansen solubility parameter and vapour pressure of each solvent (b)  $Q_W$  versus the total Hansen solubility parameter and vapour pressure of each solvent and (c) moles of solvent in swollen elastomer versus the total Hansen solubility parameter and vapour pressure of each solvent.

The analyses were also performed presuming that maximum PDMS swelling had been reached after 72 hours solvent vapour exposure. Two sets of variables were found to produce the best linear fits;  $R_a$  and vapour pressure (equation 3.10) and the HSPs and vapour pressure (equation 3.11).

$$Q_V = a + (b_{R_a} \times R_a) + (b_{P_{vp}} \times P_{vp}) \quad \text{(Equation 3.10)}$$

$$Q_V = a + (b_{\delta_d} \times \delta_d) + (b_{\delta_p} \times \delta_p) + (b_{\delta_h} \times \delta_h) + (\delta_{P_{vp}} \times P_{vp}) \quad \text{(Equation 3.11)}$$

Where  $a$  was the calculated intercept,  $b$  was the calculated slope from each independent variable,  $P_{vp}$  is the vapour pressure,  $\delta_d$  is the dispersion solubility parameter,  $\delta_p$  is the polarity solubility parameter and  $\delta_h$  is the hydrogen bonding solubility parameter. The full results of the linear regression analyses are found in Table 3.1. To ensure the association between the extent of PDMS swelling ( $Q_V$ ,  $Q_W$  and moles of absorbed solvent) and each of the two sets of variables used in equation (3.10) and (3.11) was statistically significant, the  $F$ -test for regression was performed at a confidence level of 95 %. The  $F$ -test calculates the probability of the null hypothesis – in this case that the association between the swelling ratio and each of the two set of variables was not statistically significant and that the fit was purely by chance. The  $F$ -test results as indicated by significance  $f$  from the linear regression output were all  $< 0.05$  as shown in Table 3.1. The small significance  $f$  calculated led to the rejection of the null hypothesis and therefore confirmed the

validity of the linear fit. The predicted  $Q_V$  values calculated using equation 3.10 and 3.11 were plotted against the measured values of  $Q_V$  as shown in Figure 3.12(a) and (b), respectively. The predicted-measured plot was used to visually assess the prediction error for each of the predicted values and therefore how well the linear regression model fitted the data. A few outliers (deviations from the line) were noted, with the largest deviation from the line being THF and the other smaller two outliers being xylene and acetone. However, it was found that the linear regression model was a good fit as the majority of the predicted values lay close to or directly on, the linear fit line. This relationship could be used to gauge the extent of PDMS swelling by other solvent vapours that were not used in this chapter. Predicted-measured plots for both  $Q_W$  and moles of absorbed solvent vapour were shown in Figure 3.13 and 3.14. The linear regression model was found to be a good fit even when using  $Q_W$  or moles of absorbed solvent vapour to measure degree of PDMS swelling.

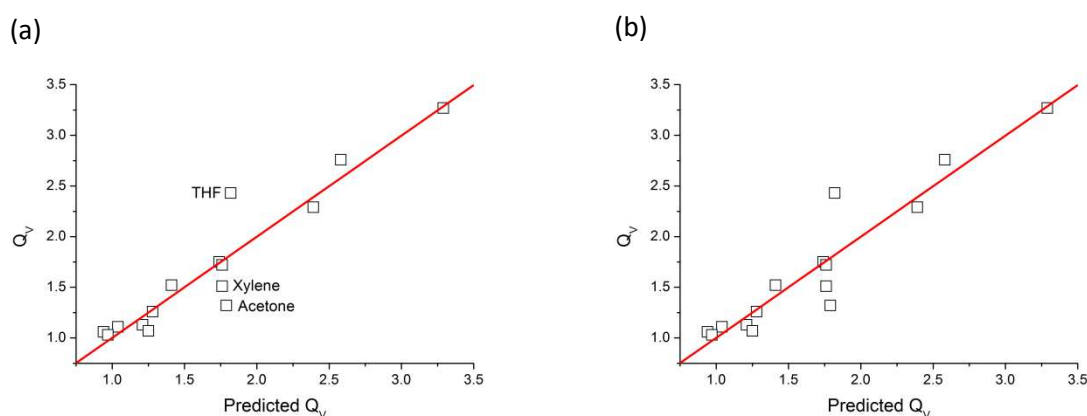


Figure 3.12: (a) Measured volume swelling ratio versus predicted swelling ratio calculated using results from linear regression analysis.  $R_a$  and vapour pressure variables used (equation 3.10) (b) Measured volume swelling ratio versus predicted swelling ratio calculated using results from linear regression analysis.  $\delta_d$ ,  $\delta_p$ ,  $\delta_h$  and vapour pressure variables used (equation 3.11).

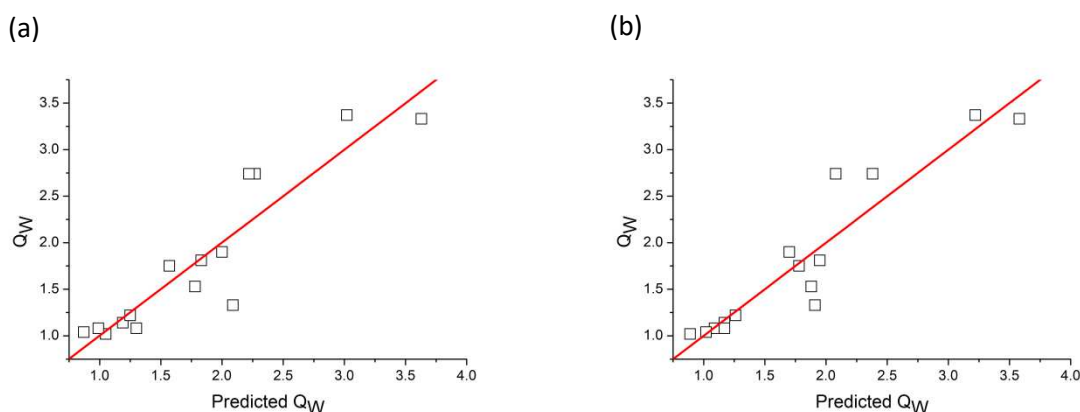


Figure 3.13: (a) Measured weight swelling ratio versus predicted swelling ratio calculated using results from linear regression analysis.  $R_a$  and vapour pressure variables used (equation 3.10) (b) Measured weight swelling ratio versus predicted swelling ratio calculated using results from linear regression analysis.  $\delta_d$ ,  $\delta_p$ ,  $\delta_h$  and vapour pressure variables used (equation 3.11).

Table 3.1: Results from the linear regression analysis. The intercept and variables were used in equation 3.10 and 3.11 to predict swelling for  $Q_v$ ,  $Q_w$  and moles of absorbed solvent vapour.

|                       | $Q_v$                    |                          | $Q_w$                    |                          | Moles of Solvent Vapour |              |
|-----------------------|--------------------------|--------------------------|--------------------------|--------------------------|-------------------------|--------------|
|                       | Eq 3.10                  | Eq 3.11                  | Eq 3.10                  | Eq 3.11                  | Eq 3.10                 | Eq 3.11      |
| <b>R<sup>2</sup></b>  | 0.820032972              | 0.8870684                | 0.851629341              | 0.879732317              | 0.870788294             | 0.870921352  |
| <b>Significance f</b> | $3.39749 \times 10^{-5}$ | $9.98399 \times 10^{-5}$ | $1.06681 \times 10^{-5}$ | $1.35841 \times 10^{-4}$ | $4.65 \times 10^{-6}$   | 0.000192     |
| <b>Intercept (a)</b>  | 2.061165316              | 3.733022915              | 2.1428168                | 0.758810704              | 10.00094586             | -0.383922955 |
| <b>b<sub>Ra</sub></b> | -0.071008207             | -                        | -0.078272575             | -                        | -0.700582178            | -            |
| <b>b<sub>δd</sub></b> | -                        | -0.105318594             | -                        | 0.06699796               | -                       | 0.459577803  |
| <b>b<sub>δp</sub></b> | -                        | -0.069508359             | -                        | -0.063754836             | -                       | -0.606956017 |
| <b>b<sub>δh</sub></b> | -                        | -0.029037386             | -                        | -0.020349323             | -                       | -0.128322476 |
| <b>b<sub>VP</sub></b> | 0.00317938               | 0.00338831               | 0.004261646              | 0.005060529              | 0.048357022             | 0.055789896  |

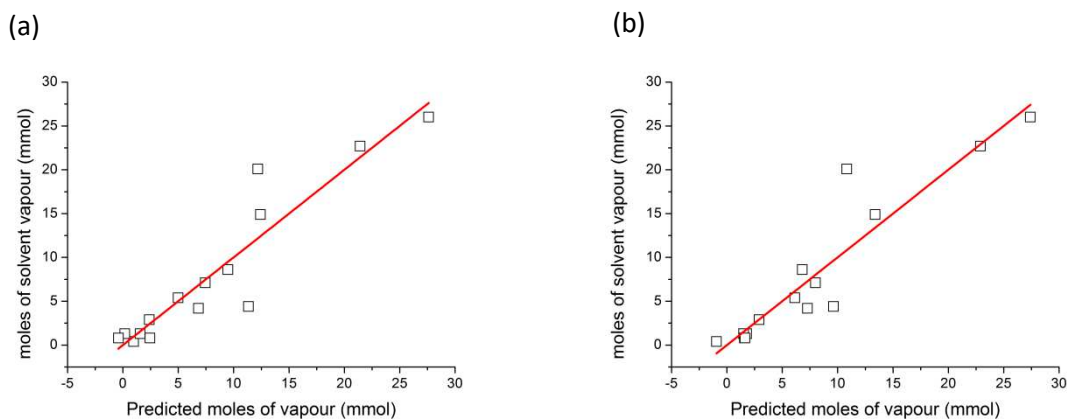


Figure 3.14: (a) Measured moles of solvent vapour in swollen elastomer versus predicted moles of vapour calculated using results from linear regression analysis.  $R_a$  and vapour pressure variables used (equation 3.10) (b) Measured moles of solvent vapour in swollen elastomer versus predicted moles of vapour calculated using results from linear regression analysis.  $\delta_d$ ,  $\delta_p$ ,  $\delta_h$  and vapour pressure variables used (equation 3.11).

### 3.2.4 Effect of polymer morphology on equilibrium swelling

#### 3.2.4.1 Fillers

The 40 wt% BaTiO<sub>3</sub>-PDMS composites were placed in a saturated atmosphere of diethyl ether, acetone and methanol for 72 hours at room temperature. Figure 3.15 shows the  $Q_v$  and  $Q_w$  of the BaTiO<sub>3</sub>-PDMS composites compared to the measured swelling ratios of the PDMS standard elastomers in the three solvent vapours.

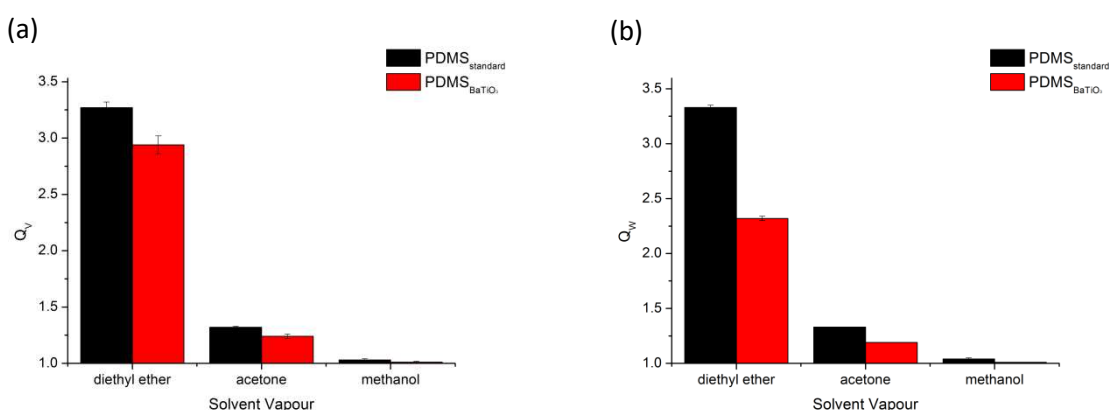


Figure 3.15: (a)  $Q_v$  and (b)  $Q_w$  of standard PDMS elastomers and BaTiO<sub>3</sub>-PDMS composites after 72 hours exposure to a range of solvent vapours.

Both the  $Q_v$  and  $Q_w$  of the BaTiO<sub>3</sub>-PDMS composites followed the same pattern as the PDMS standard in which diethyl ether caused the largest swelling and methanol caused the least swelling. This suggests that the barium titanate filler has no overall effect on the Hansen solubility parameters of the PDMS composite. As shown in figure 3.15 the  $Q_v$  of the standard PDMS and BaTiO<sub>3</sub>-PDMS composite was similar for all three solvents, while the  $Q_w$  of the BaTiO<sub>3</sub>-PDMS composite for all three solvents is slightly lower compared to the standard PDMS elastomers. Previous research has shown that the addition of certain fillers such as silicates and zeolites causes a decrease in the extent of PDMS swelling in solvents.<sup>24</sup> The decrease in BaTiO<sub>3</sub>-PDMS swelling relative to PDMS is caused through the interaction of the filler with the polymer which in turn



effectively increases the cross-linking density of the PDMS matrix. In the FTIR spectrum of the BaTiO<sub>3</sub>-PDMS composite, characteristic absorption bands due to both BaTiO<sub>3</sub> and PDMS are observed. There was no disappearance of PDMS absorption bands in the composite FTIR spectrum which indicates that there is no or minimal chemical interaction between the PDMS and BaTiO<sub>3</sub> which explains why the  $Q_V$  of the BaTiO<sub>3</sub>-PDMS composite was so similar to the  $Q_V$  of the PDMS standard. Nayak *et al.* confirmed the lack of interaction between barium titanate and PDMS and revealed that BaTiO<sub>3</sub> acts as a nonreinforcing filler for PDMS.<sup>25</sup> The authors observed a reduction in mechanical properties as a function of BaTiO<sub>3</sub> wt% filler, a positive slope in the Kraus plot and similar glass transition temperature's (T<sub>g</sub>) for the BaTiO<sub>3</sub>-PDMS composites and neat PDMS.

### 3.2.4.2 Porosity

The sponges fabricated using granulated sugar templates were extremely fragile and difficult to handle, therefore swelling experiments were only performed using the sponges fabricated using caster sugar templates. Materials with high porosity have shown enhanced solvent absorption as the pores act as additional space (free volume) where the solvent molecules can be held.<sup>26</sup>

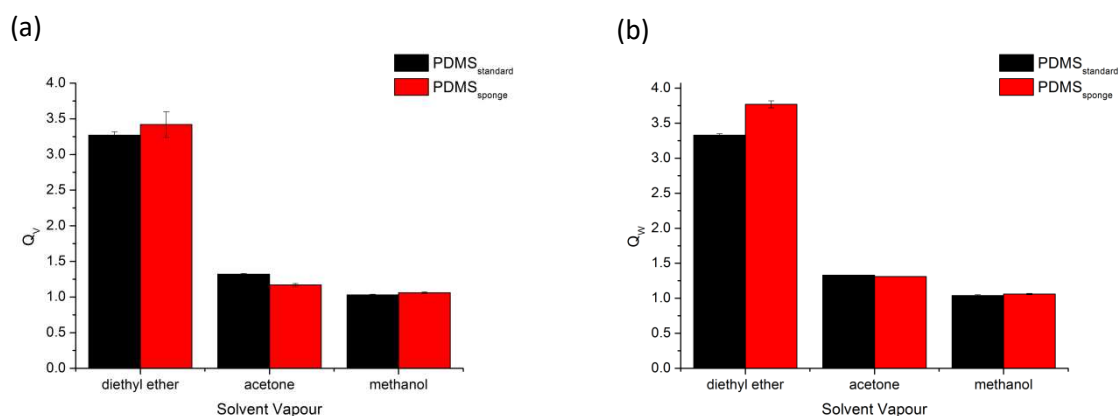


Figure 3.16: (a)  $Q_V$  and (b)  $Q_W$  of standard PDMS elastomers and PDMS sponges after 72 hours exposure to a range of solvent vapours.

However, as shown in figure 3.16 the  $Q_V$  and  $Q_W$  of the PDMS sponges were similar to that of the  $Q_V$  and  $Q_W$  of the standard PDMS elastomer. The similar swelling extents observed for the standard PDMS elastomer and sponges was attributed to the size of pores. As shown in section 3.2.1, the sponges fabricated had macro sized pores (up to 342  $\mu\text{m}$ ), which lead to the sponges to contain less cross-linked polymer than the standard elastomers. This was highlighted by the original weight of the sponges and standard elastomers of the same dimensions. It was found that the weight of the standard elastomers was almost three times as large as the weight of the PDMS sponges. Therefore, within the PDMS sponges there is less free volume associated with the cross-linked polymer. Rather than providing additional free volume compared to the standard elastomers, the pores within the PDMS sponge made up the amount of free volume lost due to the smaller amount of cross-linked polymer present.

### 3.2.4.3 Nature of cross-links

Arima *et al.* observed that the chemical nature of the cross-links within a polymer network was an important factor in the swelling extent of the polymer network.<sup>26</sup> The authors found that increasing cross-linking density generally decreased sorption of polyethylmethacrylate polymers. However, if cross-links with hydrophilic ether linkages were used, water sorption of the polymer increased with cross-link concentration. These findings clearly demonstrated that the chemical nature of the cross-links can have a more profound effect on polymer swelling than cross-linking density. The effect of cross-linking density on the extent of polymer swelling is discussed further in section 3.3.3.4. Further swelling experiments of the TESPN cross-linked elastomers were performed using xylene, DCM and acetonitrile in addition to the original swelling experiments using diethyl ether, acetone and methanol.

As shown in figure 3.17, the swelling extent of the TESPN cross-linked elastomers are slightly higher than the standard PDMS elastomers except in acetonitrile solvent vapour. The  $Q_v$  of the TESPN cross-linked elastomer in methanol was found to be below 1 indicating the elastomer shrunk and no swelling had occurred. However, as the  $Q_w$  of the TESPN cross-linked elastomer in methanol was larger than 1, it was concluded that swelling had occurred and the small  $Q_v$  could be attributed to a small error in measuring the elastomer. Following the findings of Arima *et al.* the addition of the cyanoethyl group within the cross-links was expected to increase the swelling extent of the elastomers in more polar solvents. However, as shown in figure 3.17 an increase in swelling extent was also observed in the non-polar solvents DCM, xylene and diethyl ether. Also, even though the cross-links (TESPN) and acetonitrile both shared the same group (cyano group), the TESPN cross-linked elastomers did not show an increase in swelling extent compared to the standard elastomer (cross-linked with TEOS) in acetonitrile. These results showed that in this case, the main influence on the swelling behaviour of the TESPN cross-linked elastomer was not the chemical nature of the cross-links. As with the standard PDMS elastomers, an excess of TESPN was used - the ratio of SiOH groups in PDMS to SiOR groups in TESPN was 1:3. Apart from the difference in the chemical nature of the two cross-links, there was a difference between the cross-link functionality of the two resulting elastomers. The standard PDMS elastomer was composed of tetrafunctional cross-links, where as the TESPN cross-linked elastomer was composed of trifunctional cross-links. The cyano group within the trifunctional cross-link would not take up as much volume as a linked PDMS chain, therefore the TESPN cross-linked elastomers would have a small additional amount of free volume compared to the TEOS cross-linked elastomer (standard PDMS elastomers). This small additional free volume could have resulted in the slightly larger swelling extent observed for the TESPN cross-linked elastomers compared to standard PDMS. Both the standard PDMS elastomers and TESPN cross-linked elastomers contained silica as a result of the excess cross-linker<sup>27</sup> used in both cases. Silica reinforces the elastomers which as discussed previously in section 3.3.3.1 results in a decrease in swelling extent. As the cross-linker TESPN is a trifunctional cross-linker compared to TEOS (cross-

linker in the standard PDMS elastomers) which is tetrafunctional, the TESPN cross-linked elastomers would contain slightly less reinforcing silica material. The slight difference in the amount of reinforcing silica could also explain the slightly larger swelling extent observed for the TESPN cross-linked elastomers compared to the standard PDMS elastomers.

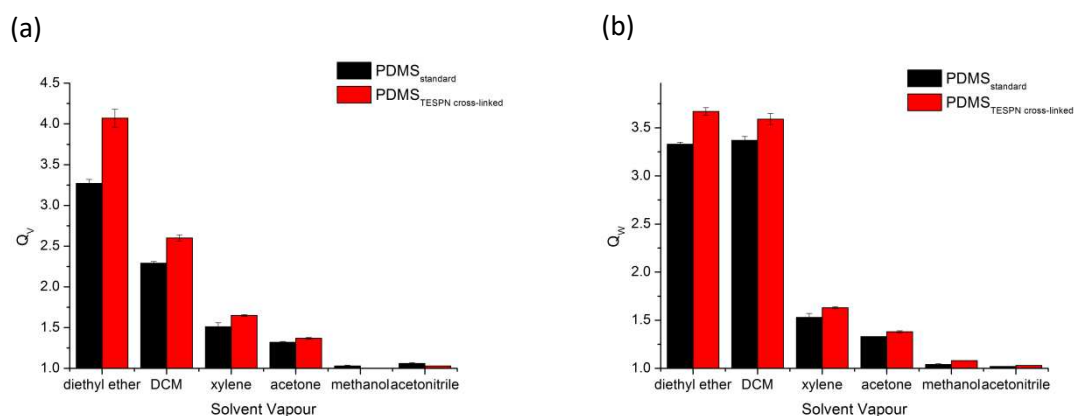


Figure 3.17: (a)  $Q_v$  and (b)  $Q_w$  of standard PDMS elastomers and TESPN cross-linked PDMS elastomers after 72 hours exposure to a range of solvent vapours.

#### 3.2.4.4 Fluoro containing Polysiloxanes

Further swelling experiments of the PTFPMS elastomers were performed using hexane, toluene, DCM and ethanol in addition to the original swelling experiments using diethyl ether, acetone and methanol. The swelling extent of PTFPMS in acetone could not be measured accurately as after 72 hours acetone vapour exposure the PTFPMS elastomers had broken. It was also found that there was an extremely large difference between the swelling ratio of the PDMS elastomers and PTFPMS elastomer in diethyl ether vapour. Therefore, to gain further insight into the swelling behaviour of PTFPMS supplementary swelling experiments were performed. Figure 3.18 shows the  $Q_w$  and  $Q_v$  of PTFPMS compared to PDMS in a selection of solvent vapours.

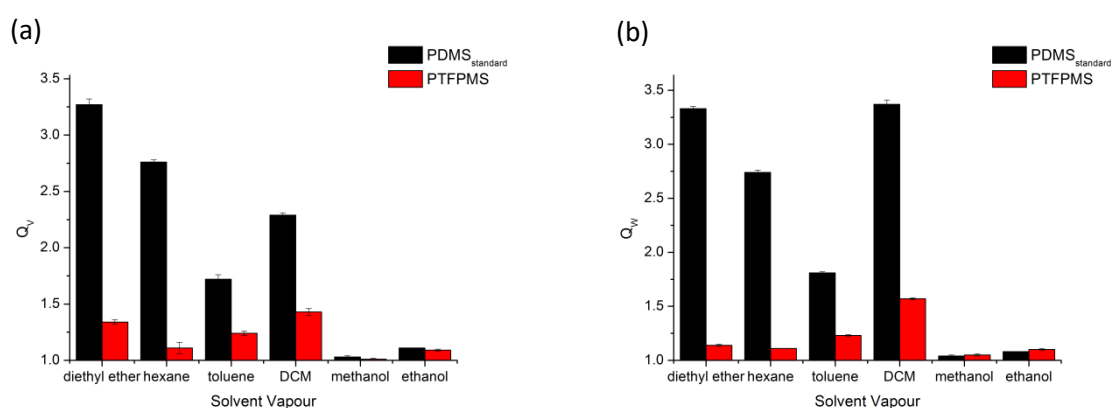


Figure 3.18: (a)  $Q_v$  and (b)  $Q_w$  of standard PDMS elastomers and PTFPMS elastomers after 72 hours exposure to a range of solvent vapours.

It was clear that in all solvent vapours the swelling extent of PTFPMS was lower than PDMS; the difference in swelling extent was much larger for the solvents that caused the largest and middle range PDMS swelling. The difference in swelling extent of the PDMS and PTFPMS elastomers was attributed to the effect of the trifluoropropyl group and cross-linking degree of the siloxane elastomers. Previous research has shown the extent of PDMS swelling can change considerably with varying cross-linking degree.<sup>28-30</sup> In fact, swelling experiments on polymer networks can be performed to determine the molecular weight between two cross-links using the Flory – Rehner equation<sup>31</sup> (equation 3.13). The Flory – Rehner equation follows from the Flory – Huggins equation (equation 3.12) but considers the free energy of elastic deformation as an additional contribution factor to the free energy change on swelling an elastomer.<sup>32</sup> The Flory-Huggins theory is a mathematical model of the thermodynamics of polymer-solvent solutions and considers both the enthalpy and entropy of mixing contributions to the free energy of mixing pure polymer and pure solvent as follows:

$$\ln a_s = [\ln (1 - \phi_p) + \phi_p] + (\chi \phi_p^2) \quad (\text{Equation 3.12})$$

Where  $a_s$  is the activity of the solvent,  $\phi_p$  the volume fraction of the polymer and  $\chi$  is the Flory-Huggins interaction parameter. The first term (in the squared brackets) corresponds to the entropy contribution while the second term to the enthalpy contribution. Flory and Rehner introduced a further term to equation 3.12 to consider the free energy of elastic deformation as a contribution factor to the free energy of mixing solvents and cross-linked polymer networks.

$$\ln a_s = [\ln (1 - \phi_p) + \phi_p] + (\chi \phi_p^2) + \left[ \frac{V_s}{\bar{v} M_c} \left( \phi_p^{1/3} - \frac{1}{2} \phi_p \right) \right] \quad (\text{Equation 3.13})$$

Where  $M_c$  is the molecular weight between two cross-links. In the case of cross-linked polymers, as the volume of solvent increases within the polymer network as a result of thermodynamically favoured mixing, the chains are deformed and an elastic force develops which causes a decrease in entropy. The extent of deformation and resulting elastic force depends on the chain length between cross-links (hence the  $M_c$  inclusion into equation 3.13). In the case of a small  $M_c$  the elastic resistance to the swelling stress is stronger than a large  $M_c$ . Therefore it is clear that the degree of cross-linking has an effect on polymer network swelling.

The molecular weight of both PDMS and PTFPMS chains were determined using NMR spectroscopy and were found to be 24266 g mol<sup>-1</sup> and 2977 g mol<sup>-1</sup>, respectively. As the same ratio of cross-linker was used i.e. the ratio of SiOH groups in PDMS or PTFPMS to SiOR groups in TEOS was 1:4 it is clear that the PTFPMS elastomers have a larger cross-link density compared to the PDMS elastomers due to their much smaller chain length. In both cases the Si-OH groups were at the end of the polymer chains, therefore the average molecular weight between cross-links,  $M_c$ , should be similar or equal to the molecular weight of the polymer chains before cross-linking. Essentially the cross-linking reaction occurring between the silanol terminated PDMS or PTFPMS and the TEOS is an end-linking

reaction which forms tetrafunctional cross-links. The TEOS was added in excess which ensures full cross-linking occurs as well as simultaneously forming silica which reinforces the elastomer.<sup>27</sup> As previously discussed in section 3.3.3.1 a reinforcing filler can cause a decrease in swelling extent as it effectively increases the cross-link density. However as an excess of TEOS was used for both the PDMS and PTFPMS elastomers, the effect of the reinforcing silica does not need to be considered. The  $M_c$  of the PDMS is almost 10 times as large as the  $M_c$  of the PTFPMS which explains the large difference in  $Q_w$  and  $Q_v$  observed for the two polymer networks (figure 3.18). However, it has been highlighted that for solvents that cause poor swelling, the elastic deformation contribution present in the Flory-Rehner equation would be negligible as it assumes the neighbouring polymer chains do not react with one another which only happens in highly swollen polymers.<sup>29</sup> This accounts for the small difference observed between the swelling extent of PDMS and PTFPMS for both ethanol and methanol.

Another reason for the large difference between the  $Q_w$  and  $Q_v$  of the PDMS and PTFPMS elastomers was the effects of the trifluoropropyl group compared to the methyl group. Previous research has shown the substitution of the methyl group with the trifluoropropyl group on the silicone backbone increases the polymer's resistance to both non-polar solvents and oils.<sup>33</sup> The trifluoropropyl group is larger and more rigid than the methyl group and therefore inhibits the rotational mobility of the polymer chain. As a result PTFPMS has a higher glass transition temperature and lower fractional free volume than PDMS as shown in Table 3.2. The smaller the free volume, the lower capacity for absorption.

Table 3.2: Fractional free volume ( $V_f$ ), glass transition temperature ( $T_g$ ) and Hansen solubility parameters of PDMS and PTFPMS

| Polymer | $V_f$ | $T_g$ °C | Hansen Solubility Parameters (MPa <sup>1/2</sup> ) |            |            |            |
|---------|-------|----------|--|------------|------------|------------|
|         |       |          | $\delta_d$   | $\delta_p$ | $\delta_h$ | $\delta_t$ |
| PDMS    | 0.33  | -125     | 15.9   | 0.1        | 4.7        | 16.6       |
| PTFPMS  | 0.29  | -70      | 15.5   | 7.2        | 5.7        | 17.9       |

The substitution of one methyl group with a trifluoropropyl group also has an effect on the polymer's total Hansen solubility parameter. The total Hansen solubility parameter of PTFPMS and PDMS is 17.9<sup>34</sup> and 16.6 MPa<sup>1/2</sup><sup>35</sup>, respectively. As previously discussed, it has been found the extent of PDMS swelling in solvent vapour can be correlated to the solvents vapour pressure and the similarity between the Hansen solubility parameters of both solvent and PDMS. Therefore, as the Hansen solubility parameters of PTFPMS are different from PDMS, a difference between the swelling extent of PDMS and PTFPMS was expected. Along with the large difference between the  $Q_w$  and  $Q_v$  of the PDMS and PTFPMS elastomers, it was observed that the PTFPMS elastomers do not follow the same swelling pattern as PDMS. For example, the PTFPMS elastomers swell more in

toluene than they do in hexane whereas the PDMS elastomers swell more in hexane than they do in toluene. This was solely attributed to the difference in the Hansen solubility parameters of the two polymers. Linear regression analysis using either  $R_a$  and vapour pressure or the Hansen solubility parameters and vapour pressure as the independent variables, were not performed for the PTFPMS elastomers as it was felt there was not enough swelling data to produce an accurate fit. However, both the  $Q_w$  and  $Q_v$  of PTFPMS versus the total Hansen solubility parameter and vapour pressure of each solvent was plotted (Figure 3.19).

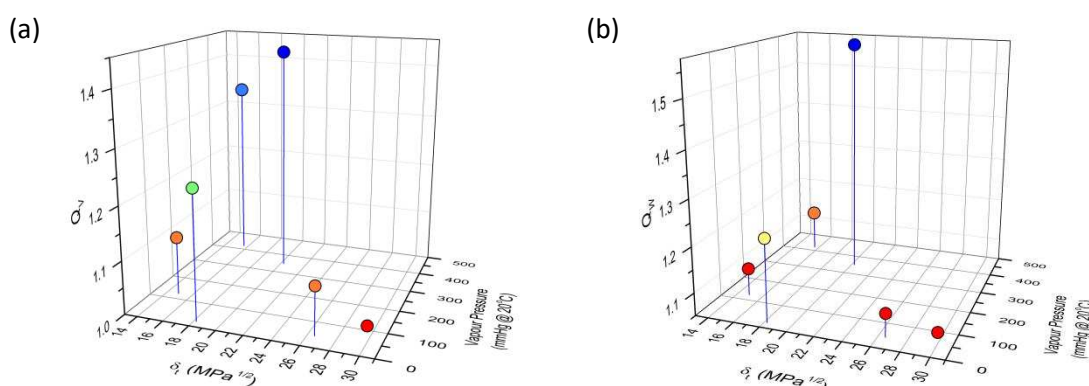


Figure 3.19: (a)  $Q_v$  versus the total Hansen solubility parameter and vapour pressure of each solvent (b)  $Q_w$  versus the total Hansen solubility parameter and vapour pressure of each solvent

It was observed that solvents with a similar  $\delta_t$  to that of PTFPMS exhibited the largest swelling and any differences in the swelling extent for solvents with similar  $\delta_t$  could be explained by the difference in the solvent's vapour pressure. As with PDMS elastomers, generally a solvent with a high vapour pressure caused larger swelling than a solvent with a similar  $\delta_t$  and a low vapour pressure. Previously it was noted that the PTFPMS elastomers broke apart when swollen in acetone vapour. Acetone has a  $\delta_t$  value close to that of PTFPMS and a mid-range vapour pressure (181.0 mmHg @ 20°C) therefore it was not expected to cause the largest swelling.

As previously discussed a large difference between the swelling extent of PDMS and PTFPMS in solvents such as diethyl ether, hexane, toluene and DCM was observed. A PDMS/PTFPMS elastomer was fabricated and swelling studies were performed to investigate its use as an actuator component in a RFID vapour sensor. Two different PDMS/PTFPMS elastomers were fabricated: a double layered elastomer and a PTFPMS elastomer with a PDMS tip (illustrated in figure 3.20).

PTFPMS elastomer (section 3.1.2.5), however the PTFE square moulds were only filled half way with the PTFPMS mixture. Once the PTFPMS mixture was partially cured and was tacky to touch, a PDMS mixture (synthesis method 3.1.2.1) was poured on top of the semi-cured PTFPMS elastomer. The resulting PTFPMS/PDMS elastomer was left to cure for 2 hours at room temperature before being placed into a 60°C overnight. EDX analysis was performed on a cross-sectional area of the double layered elastomer to examine if the two polymers had merged together or if there was a definite edge where the two polymers are joined. The PTFPMS elastomer with a PDMS tip was fabricated by first fabricating a PTFPMS elastomer following the method in section 3.1.2.5. A slice about 5 mm in width, 1mm in height and 20 mm in length was removed using a scalpel. The remaining part of the PTFPMS elastomer was placed back into the square mould before a PDMS mixture (synthesis method 3.1.2.1) was poured to fill the hole formed by the missing PTFPMS slice. The resulting elastomer was left to cure for 2 hours at room temperature and placed in an oven overnight at 60 °C. The PTFPMS elastomer with a PDMS tip was cut into strips of around 5 mm in width. The PTFPMS/PDMS elastomers were placed into a saturated diethyl ether atmosphere following the method in section 3.1.4. Images of the elastomers were taken at intervals during diethyl ether exposure to observe their swelling behaviour. The swelling of the double layered elastomer and PTFPMS elastomer with a PDMS tip in diethyl ether vapour was shown in figure 3.21 and 3.22 respectively.

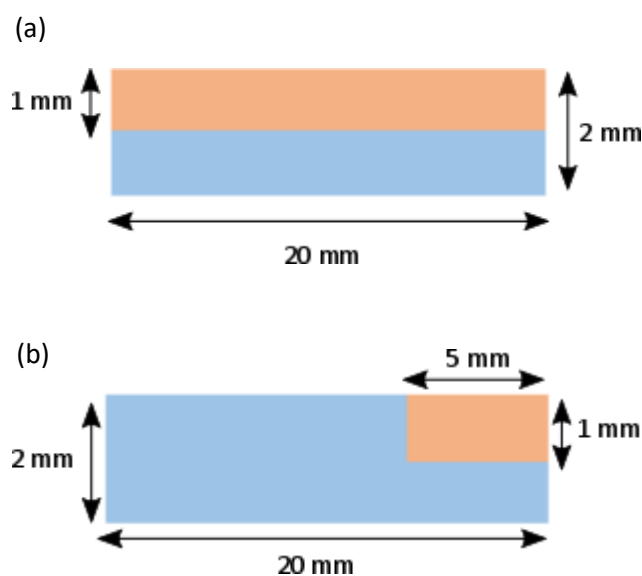


Figure 3.20: Side on view illustration of (a) double layered elastomer and (b) PTFPMS elastomer with a PDMS tip. Orange represents PDMS and blue represents PTFPMS.

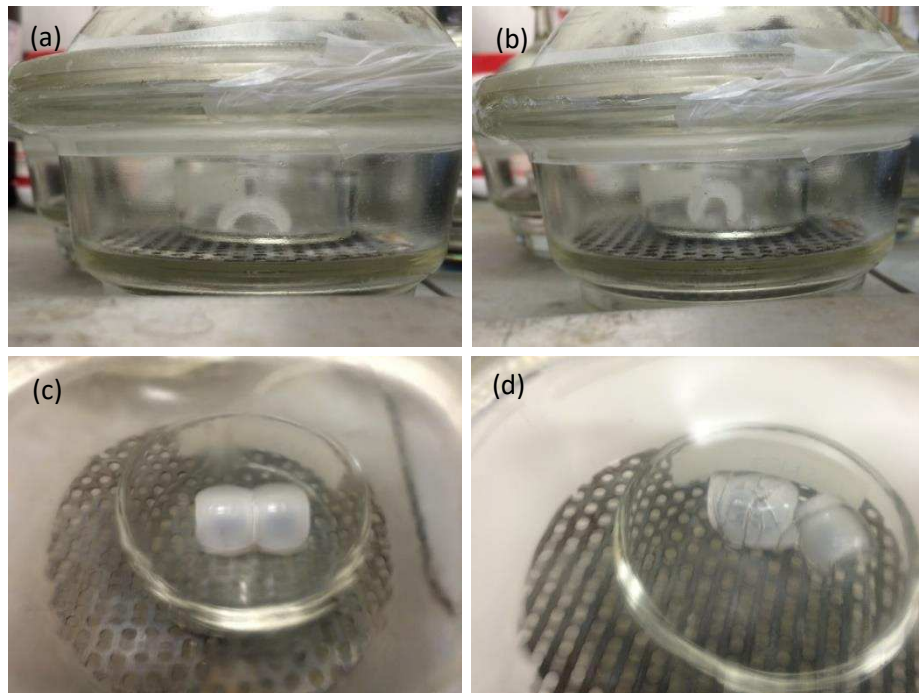


Figure 3.21: Images of 2 cm<sup>2</sup> double layered PTFPMS/PDMS elastomer exposed to diethyl ether vapour for (a) 90 minutes (b) 5 hours (c) 5 hours (same elastomer sample as figure 3.21 (b) but the image was taken from a different angle) and (d) 46.5 hours

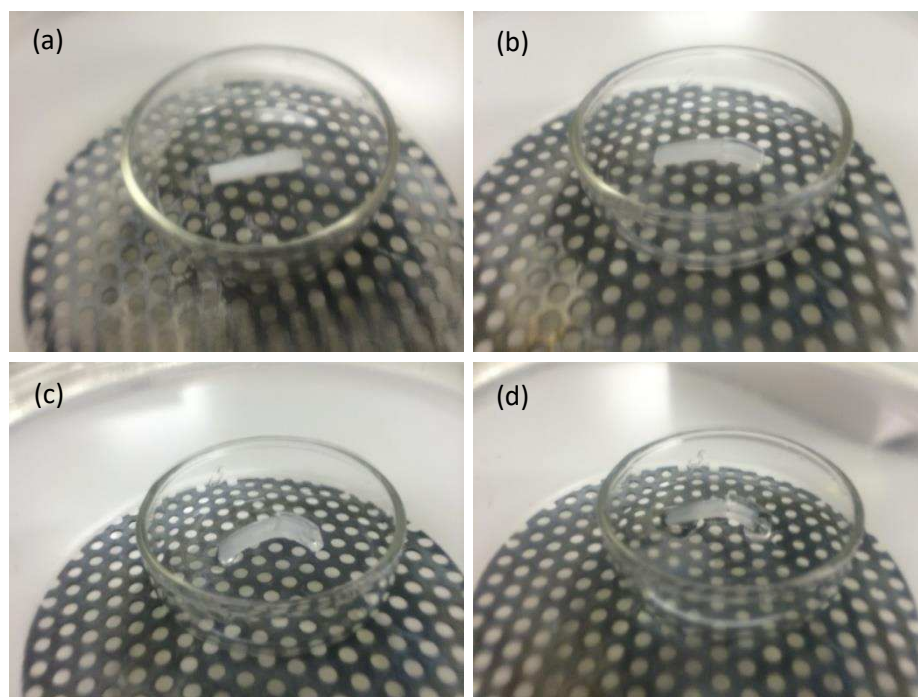


Figure 3.22: Images of PTFPMS strip with PDMS tip after (a) 0 minutes (b) 1 hour (c) 5 hours and (d) 72 hours diethyl ether exposure time.

The double layered elastomer used in the swelling experiment was placed onto the petri dish with the PTFPMS half facing down. As shown in figure 3.21, the elastomer formed an arch shape which became taller and narrower before forming into a hollow tube and breaking apart as the diethyl ether exposure time increased. A fault line in the middle of the curved elastomer appeared after 5 hours exposure to diethyl ether and it was at this fault line that the elastomer broke apart after 46.5 hours vapour exposure. Fractures were also observed in the broken elastomer. It was found that if the double layered elastomer was placed with the PTFPMS half facing up, the elastomer



formed a U-shape in which the ends would connect to form a hollow tube before again breaking apart with increased diethyl ether time exposure. This swelling behaviour was completely different to what was observed for the individual PDMS and PTFPMS elastomers. Along with the swelling behaviour of a 2 cm<sup>2</sup> double layered elastomer the swelling behaviour of a double layered elastomer strip around 5 mm in width was also investigated. The double layered elastomer strip formed an arch shape which became taller and narrower with diethyl ether exposure time as observed with the 2 cm<sup>2</sup> sample. However, after 110 minutes vapour exposure time, the elastomer fell onto its side before curling up to form a donut shape. With increase vapour exposure time (24 hours) the donut shaped elastomer did not break, though fractures within the PTFPMS layer were seen.

As shown in figure 3.22, the PTFPMS strip with PDMS tip forms an arch shape which becomes narrower and higher with diethyl ether exposure time. Unlike the double layered elastomer, the swollen PTFPMS strip with PDMS tip did not fall over, form into a donut-shape or break apart. The desorption behaviour of the PTFPMS strip with a PDMS tip was also investigated. The PTFPMS elastomer with a PDMS tip returned to its original shape though a few fractures within the elastomer were formed. Further experiments would have to be performed to investigate if the PTFPMS elastomer with a PDMS tip could be re-used and if the same swelling behaviour was achieved each time. The PTFPMS strip with a PDMS tip design showed more promise as an actuator component than the double layered design as the former design had the advantages of controlled buckling - a clearly pronounced arch shape which did not change shape, fall down or break with solvent vapour exposure time – and possibly the ability to be re-used. RFID sensors containing these PDMS/PTFPMS elastomer are potentially advantageous as they could be more chemically specific than sensors containing just PDMS or PTFPMS components since the swelling behaviour is reliant on the unique difference between the swelling extent of PTFPMS and PDMS in each solvent vapour.

Energy-dispersive x-ray spectroscopy (EDX) analysis was used to investigate the boundary where the two different polymer layers met within the double layered PDMS/PTFPMS elastomer. This was performed to discover if the two different polymers merged with one another creating a thin PDMS/PTFPMS mixed layer or if there was a distinct boundary between the two polymer layers. A SEM micrograph of the cross-section of the double layered PDMS/PTFPMS was shown in figure 3.23 where one polymer layer was at the top of the image and the other polymer layer at the bottom of the image. EDX analysis was performed at points spaced at regular intervals running down the image at almost a 90 degree angle to the two layers. As the chemical composition of both polymers was so similar, the presence and magnitude of fluorine in the EDX spectrum at around 0.677 was used to confirm the presence of the PTFPMS elastomer. The EDX spectra numbered 1 – 8 exhibited large fluorine peaks indicating the top layer (according to the image) was PTFPMS. This was visually confirmed as the top layer had white speckled dots which were observed in the SEM micrographs

of the PTFPMS elastomers in section 3.2.1.2. The EDX spectra numbered 11 – 15 exhibited extremely small fluorine peaks indicating the bottom layer was predominately PDMS. As shown in figure 3.23, spectrum 9 exhibited a large fluorine peak while spectrum 10 showed a small fluorine peak which indicated the boundary between the two polymers was between these two points. The distance between these two points was measured at 8.7  $\mu\text{m}$  using Image J software. The small distance measured between points 9 and 10 suggested that there was little or no polymer migration between the two polymer layers and therefore a distinct boundary was present in the double layered elastomer. Even though it has been shown that there was a distinct boundary between the two polysiloxane elastomer layers, the double layered elastomer did not break apart at this boundary after swelling confirming good adhesion between the layers had been achieved. The lacerations observed in figure 3.23 were attributed to the mechanical force of cutting to achieve a cross-section of the double layered elastomer.

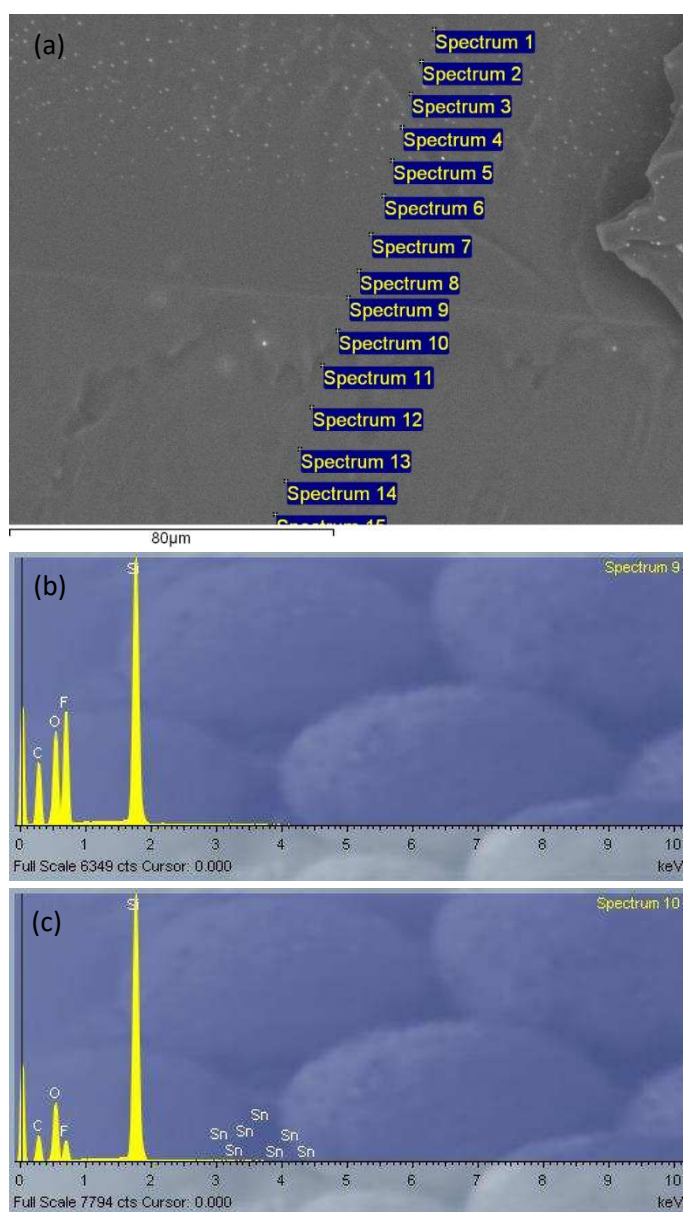


Figure 3.23: (a) SEM micrograph of double layered elastomer. EDX spectra of (b) point 9 and (c) point 10 on SEM micrograph

### 3.2.5 PDMS elastomers as solvent scrubbers

The solvent scrubber experiments were performed using the standard PDMS elastomers and toluene, chlorobenzene, ethyl acetate, acetone, hexane and diethyl ether as the chosen solvents. Table 3.3 shows the weight of the solvent in the crucible at 0 minutes (90 wt% of the maximum weight of the solvent that the standard PDMS elastomer can absorb – calculated from  $Q_w$ ) and the weight of the solvent absorbed by the PDMS elastomer after 72 hours. As shown in Table 3.3 it is clear that not all the solvent has been absorbed by the elastomer after 72 hours, however, there was no visual solvent left in the crucible. In a sealed container a certain amount of solvent will evaporate into the headspace forming a saturated atmosphere. This amount of solvent,  $n$  was calculated using the following equation:

$$n = \left( \frac{P_{VP} \times \text{internal volume of the desiccator}}{R \times T} \right) \times M.W. \text{ of solvent} \quad (\text{Equation 3.14})$$

Where  $P_{VP}$  is the vapour pressure of the solvent at 20°C in Pascal, the internal volume of the desiccator was approximately  $5.35 \times 10^{-4} \text{ m}^3$ ,  $R$  is the ideal gas constant (8.314 J/mol) and  $T$  is the temperature in Kelvin (293.15 K). The amount of solvent that will be lost from the crucible to form a saturated atmosphere was shown in Table 3.3 and it was found that this did not account for the rest of the solvent that was not absorbed by the PDMS elastomer. It was concluded that the desiccator was not in fact air tight and the solvent that had not been absorbed by the standard PDMS elastomer escaped. It was noted that the desiccators in this experiment were sealed in the same manner as the desiccators in the swelling experiments in section 3.1.4 and therefore it could be concluded that a proportion of solvent vapour would have also escaped in the swelling experiments. However, as such a large excess of solvent was used in the swelling experiments the loss of escaped solvent vapour had no effect on the extent of the polysiloxane network swelling i.e. maximum swelling was achieved. This was supported by the fact that there was still a large amount of solvent left in the desiccators after the swelling experiments were completed.

Table 3.3: Weight of solvent in the crucible at 0 minutes and weight of solvent absorbed by the PDMS elastomer after 72 hours.

| Solvent Vapour | Amount of Solvent (g)   |                         |  |   |
|----------------|-------------------------|-------------------------|--|---|
|                | In crucible (0 minutes) | In elastomer (72 hours) | $\Delta$ solvent weight = In elastomer – In crucible | Will evaporate from crucible to create saturated atmosphere |
| Toluene        | 0.5631                  | 0.2909                  | -0.2722  | 0.0593  |
| Chlorobenzene  | 0.5194                  | 0.3229                  | -0.1965  | 0.0385  |
| Ethyl acetate  | 0.6766                  | 0.2430                  | -0.4336  | 0.1890  |
| Acetone        | 0.2350                  | 0.0216                  | -0.2134  | 0.3080  |
| Hexane         | 1.1370                  | 0.3875                  | -0.7495  | 0.3130  |
| Diethyl ether  | 1.7170                  | 0.2387                  | -1.4783  | 0.9190  |

\*calculated from equation 3.14

The PDMS elastomers still show promise as solvent scrubber materials as in all cases the elastomers absorbed a certain amount of solvent vapour. However, further experiments would have to be conducted in an air tight container.

### 3.3 Conclusions

A selection of polysiloxane networks; standard PDMS elastomers, TESPN cross-linked elastomers, PDMS sponges, 40 wt% BaTiO<sub>3</sub>-PDMS elastomer and PTFPMS elastomers were successfully synthesised and exposed to a range of solvent vapours. As expected non-polar solvents were found to cause the largest standard PDMS swelling and polar solvents caused the least. It was found that the swelling extent (using either  $Q_v$ ,  $Q_w$  or moles of solvent vapour absorbed) of standard PDMS elastomers could be directly correlated with the Hansen solubility parameters,  $\delta_d$ ,  $\delta_p$  and  $\delta_h$  and the vapour pressure of the solvent vapour used. This relationship has allowed for a method to predict polymer swelling by a range of solvent vapours. It was found that neither the introduction of barium titanate filler or pores nor the use of a more polar cross-linker had a profound effect on the extent of polymer swelling. On the other hand the swelling extent of the PTFPMS elastomers was much lower compared to the standard PDMS elastomers due to their larger cross-link density. A PTFPMS elastomer strip with a PDMS tip was successfully synthesised and exhibited controlled buckling as a result of diethyl ether vapour exposure. This dual component elastomer design showed good promise as a potential actuator and has the advantage of being more specific than the one component elastomers as its swelling behaviour is reliant on the unique difference between the swelling extent of PTFPMS and PDMS in each solvent vapour. Further experiments would have to be performed to investigate the full potential of the standard PDMS elastomers as solvent scrubber materials.

### 3.4 References

- 1 S. Balasubramanian and S. Panigrahi, *Food Bioprocess Tech.*, 2011, **4**, 1-26.
- 2 S. Seethapathy and T. Górecki, *Anal. Chim. Acta*, 2012, **750**, 48-62.
- 3 J. N. Lee, C. Park and G. M. Whitesides, *Anal. Chem.*, 2003, **75**, 6544-6554.
- 4 S. Choi, T. Kwon, H. Im, D. Moon, D. J. Baek, M. Seol, J. P. Duarte and Y. Choi, *ACS Appl. Mater. Interfaces*, 2011, **3**, 4552-4556.
- 5 R. A. Potyrailo, N. Nagraj, Z. Tang, F. J. Mondello, C. Surman and W. Morris, *J. Agric. Food Chem.*, 2012, **60**, 8535-8543.

- 6 R. A. Potyrailo, N. Nagraj, C. Surman, H. Boudries, H. Lai, J. M. Slocik, N. Kelley-Loughnane and R. R. Naik, *TrAC Trends in Analytical Chemistry*, 2012, **40**, 133-145.
- 7 L. K. Fiddes and N. Yan, *Sensors Actuators B: Chem.*, 2013, **186**, 817-823.
- 8 R. A. Potyrailo and W. G. Morris, *Anal. Chem.*, 2007, **79**, 45-51.
- 9 S. Patel, T. Mlsna, B. Fruhberger, E. Klaassen, S. Cemalovic and D. Baselt, *Sens. Actuators B Chem.*, 2003, **96**, 541-553.
- 10 S. Dissanayake, C. Vanlangenberg, S. V. Patel and T. Mlsna, *Sens. Actuators B Chem.*, 2015, **206**, 548-554.
- 11 U. Altenberend, A. Oprea, N. Barsan and U. Weimar, *Anal. Bioanal. Chem.*, 2013, **405**, 6445-6452.
- 12 K. Sing, *Colloids Surf. Physicochem. Eng. Aspects*, 2001, **187**, 3-9.
- 13 S. Lowell and J. E. Shields, *Powder Surface Area and Porosity*, Springer Science & Business Media, Netherlands, 1991.
- 14 K. K. Aligizaki, *Pore Structure of Cement-Based Materials: Testing, Interpretation and Requirements*, Taylor & Francis, Oxon, 2006.
- 15 S. Lowell, J. E. Shields, M. A. Thomas and M. Thommes, *Characterization of Porous Solids and Powders: Surface Area, Pore Size and Density*, Kluwer Academic Publishers, Dordrecht, 2004.
- 16 B. Viswanathan, in *Catalysis: Principles and Applications*, ed. B. Viswanathan, S. Sivasanker and A. Ramaswamy, Narosa Publishing House, New Delhi, 2002, Chapter 1, pp. 1-33.
- 17 C. Brinker, *J. Non Cryst. Solids*, 1988, **100**, 31-50.
- 18 A. F. Barton, *Chem. Rev.*, 1975, **75**, 731-753.
- 19 H. A. Benesi and J. Hildebrand, *J. Am. Chem. Soc.*, 1949, **71**, 2703-2707.
- 20 J. N. Lee, C. Park and G. M. Whitesides, *Anal. Chem.*, 2003, **75**, 6544-6554.
- 21 C. M. Hansen, *Prog. Org. Coat.*, 2004, **51**, 77-84.
- 22 C. M. Hansen, *Hansen Solubility Parameters: A User's Handbook*, CRC press, Boca Raton, 2007.
- 23 T. Lindvig, M. L. Michelsen and G. M. Kontogeorgis, *Fluid Phase Equilib.*, 2002, **203**, 247-260.

- 24 L. E. Gevers, I. F. Vankelecom and P. A. Jacobs, *J. Membr. Sci.*, 2006, **278**, 199-204.
- 25 S. Nayak, T. K. Chaki and D. Khastgir, *Ind. Eng. Chem. Res.*, 2014, **53**, 14982-14992.
- 26 J. L. Ferracane, *Dent. Mater.*, 2006, **22**, 211-222.
- 27 D. McCarthy, J. Mark and D. Schaefer, *J. Polym. Sci. B Polym. Phys.*, 1998, **36**, 1167-1190.
- 28 N. Stafie, D. Stamatialis and M. Wessling, *Sep. Purif. Technol.*, 2005, **45**, 220-231.
- 29 Q. TrongáNguyen, *J. Chem. Soc. Faraday Trans.*, 1993, **89**, 4339-4346.
- 30 S. C. George and S. Thomas, *J. Membr. Sci.*, 1999, **163**, 1-17.
- 31 W. Chassé, M. Lang, J. Sommer and K. Saalwächter, *Macromolecules*, 2011, **45**, 899-912.
- 32 N. Neuburger and B. Eichinger, *Macromolecules*, 1988, **21**, 3060-3070.
- 33 M. Dawir, *Sealing Technology*, 2008, **2008**, 10-14.
- 34 S. Charati and S. Stern, *Macromolecules*, 1998, **31**, 5529-5535.
- 35 T. Uragami, I. Sumida, T. Miyata, T. Shiraiwa, H. Tamura and T. Yajima, *Mater. Sci. Appl.*, 2011, **2**, 169.

# Chapter 4: Diffusion rate of solvent vapours into polysiloxane networks; applications for passive UHF-RFID wireless sensors

## 4.0 Introduction

Diffusion is the process by which molecules, ions or other particles move from one part of a system to another. Diffusion into polymers have been studied using several techniques such as gravimetry<sup>1</sup>, fluorescence<sup>2,3</sup> and membrane permeation.<sup>4</sup> There are many applications in which the study of diffusion in polymers is important, such as controlled release of drugs<sup>5</sup>, gas barrier properties for coatings and food packaging<sup>6</sup> and selectivity for gas separation membranes<sup>7</sup> and sensors.<sup>8</sup> In chapter 3, the extent of swelling of polysiloxane networks in a range of solvent vapours was investigated for the purpose to be used in a RFID solvent vapour sensor tag design which utilises the often regarded negative characteristic of PDMS – swelling in non-polar solvents. Along with the swelling properties, the diffusion properties of the solvent vapours into the polysiloxane networks is also very important. The study of the solvent vapour diffusion into the polysiloxane networks would provide knowledge on the rate of swelling i.e. the rate of the RFID sensor response and selectivity between solvent vapours which cause similar equilibrium swelling values. The understanding of both response rate and selectivity is essential for sensor applications. Therefore, the main aim of this chapter is to investigate the diffusion rate of the solvent vapours into the various polysiloxane networks used in chapter 3. The diffusion into the polysiloxane networks was studied via their area increase in response to a saturated atmosphere of solvent vapour. Area increase was chosen as it is the lateral growth of the polysiloxane networks that causes the feed loop displacement. In this chapter, the diffusion rates of six chosen solvent vapours (diethyl ether, hexane, DCM, xylene, toluene and acetone) into a range of polysiloxane networks:- standard PDMS elastomers (TEOS cross-linked), TESPN cross-linked PDMS, PDMS sponges, 40 wt% BaTiO<sub>3</sub>-PDMS elastomers and polytrifluoropropylmethylsiloxane (PTFPMS) elastomers were investigated.

## 4.1 Experimental

### 4.1.1 Materials and Apparatus

A full list of materials and apparatus used in this chapter can be found in chapter 3 section 3.1.1.

### 4.1.2 Synthesis of polysiloxane networks: Sn catalysed condensation method

Standard PDMS elastomers, TESPN cross-linked PDMS elastomers, PDMS sponges fabricated from caster sugar templates, 40 wt% BaTiO<sub>3</sub>-PDMS composites and polytrifluoropropylmethylsiloxane

(PTFPMS) elastomers were synthesised following the methods described in chapter 3 section 3.1.2. Full characterisation of standard PDMS elastomers, TESPN cross-linked PDMS elastomers and BaTiO<sub>3</sub>-PDMS composites can be found in chapter 2. Full characterisation of PDMS sponges and PTFPMS elastomers can be found in chapter 3.

#### 4.1.3 Absorption Rate Experiments

Measurement of the absorption rates of the polysiloxane networks were performed by placing the polysiloxane elastomers into a dessicator (internal seal diameter of 15.2 cm) with 50 cm<sup>3</sup> of a chosen solvent for either 24 hours or 72 hours. The polysiloxane networks were placed onto 1 mm square grid paper for scaling purposes and rather than the usual concave dessicator lid, a flat glass lid was used to seal the dessicator to ensure good visual access to the elastomer. To measure the lateral swelling of the polysiloxane elastomers over solvent vapour exposure time, photographs of the polysiloxane networks were taken at either 30 minute or 15 minutes intervals from a heights of 2.5 cm (distance between the dessicator lid and camera). Image J software was used to calculate the area of the polysiloxane elastomers from each photograph and the area swelling ratio ( $Q_A$ ), defined as the ratio of the area of the swollen polysiloxane elastomer to its original area, was calculated.

## 4.2 Results and Discussion

### 4.2.1 Absorption Rate / swelling kinetics of polysiloxane networks

Absorption rate experiments were originally performed on the standard PDMS elastomers using six solvent vapours; two vapours that caused the largest PDMS swelling (diethyl ether and DCM), two vapours which caused mid-range PDMS swelling (acetone and xylene) and two vapours that caused the least PDMS swelling (methanol and acetonitrile). To prevent continually removing the PDMS elastomers from the saturated vapour atmosphere for measurements, the area of the elastomer was measured rather than the volume or weight. Figure 4.0 shows the relationship between PDMS area swelling,  $Q_A$  and solvent vapour exposure time over a period of 24 hours.



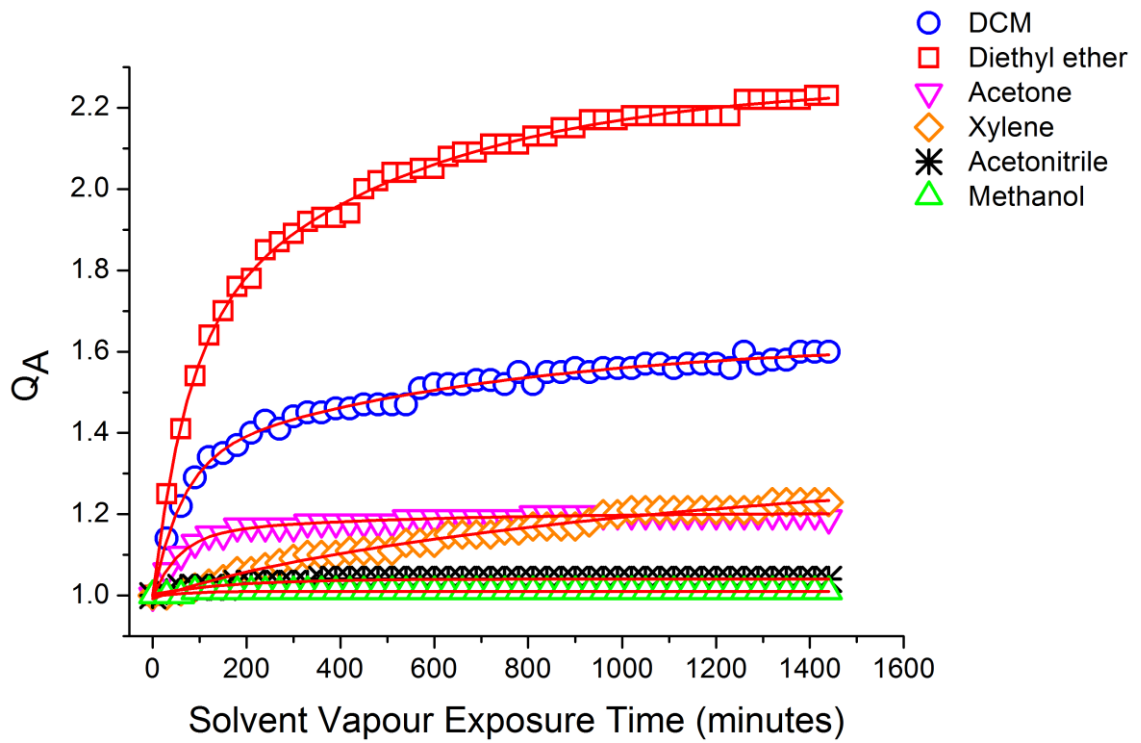


Figure 4.0: Area swelling ratio versus solvent vapour exposure time for standard PDMS elastomers.

It was found that the curves best fit was achieved using a 2-phase exponential association model:

$$Q_V = Q_{V_0} + A_1 \left(1 - e^{-\frac{t}{t_1}}\right) + A_2 \left(1 - e^{-\frac{t}{t_2}}\right) \quad (\text{Equation 4.0})$$

Adjusted R-square values were calculated for the 2-phase exponential association model fits and shown in Table 4.0. R-square describes how well the model describes the variance of the data i.e. how well the model fits the data. R-square values can range from 0 to 1 with values close to 1 indicating a good data fit. As shown in Table 4.0, the r-square values of the fitted absorption data for standard PDMS were all close to 1 demonstrating the 2-phase exponential association model was a good fit and could be used to predict the maximum area swelling.

Table: 4.0: Adjacent R-square values for the 2-phase exponential association model fits of the absorption data of each polysiloxane network.

| Solvent Vapour | Adj. R-square values for 2-phase exponential association model fit |                         |             |                                 |                     |
|----------------|--|-------------------------|-------------|---------------------------------|---------------------|
|                | Polysiloxane networks  |                         |             |                                 |                     |
|                | Standard PDMS  | TESPN cross-linked PDMS | PDMS sponge | 40 wt% BaTiO <sub>3</sub> -PDMS | PTFPMS              |
| Diethyl ether  | 0.99806  | 0.99814                 | 0.99814     | 0.99824                         | 0.64354             |
| Hexane         | 0.9982   | 0.99917                 | 0.99799     | 0.99906                         | 0.98562<br>0.97913* |
| DCM            | 0.99238  | 0.99648                 | 0.99700     | 0.99665                         | 0.98631             |
| Acetone        | 0.98948  | 0.99292                 | 0.98075     | 0.99335                         | 0.99850             |
| Toluene        | 0.99853  | 0.99753                 | 0.99734     | 0.99851                         | 0.98979<br>0.98820* |
| Xylene         | 0.98948  | 0.99731                 | 0.99836     | 0.99549                         | 0.98636<br>0.98667* |
| Methanol       | 0.90141  | N/A                     | N/A         | N/A                             | N/A                 |
| Acetonitrile   | 0.94949  | N/A                     | N/A         | N/A                             | N/A                 |

\* Adj. R-square values for the 2-phase exponential association model fit of 72 hours absorption data.

The maximum area swelling of the standard PDMS elastomers in the six chosen solvents was calculated using equation 4.0 where  $t$  was set at  $1 \times 10^{12}$  minutes and used to investigate the swelling kinetics and diffusion behaviour of the standard PDMS elastomers. Many diffusion processes through elastomeric polymer can be described by Fick's first law of diffusion:<sup>9</sup>

$$J = -D \left( \frac{\delta_c}{\delta_x} \right) \quad (\text{Equation 4.1})$$

Where the flux,  $J$  is directly proportional to the concentration gradient ( $\delta_c/\delta_x$ ) and  $D$  is the diffusion coefficient. The swelling kinetics of the standard PDMS in all six chosen solvent vapours was shown in figure 4.1. The swelling kinetics of the standard PDMS in methanol and acetonitrile were not further analysed due to the limited number of data points in the initial swelling region as shown in figure 4.1. The limited number of data points was attributed to the poor swelling ability of the two solvent vapours i.e. it takes minimal time for a small maximum swelling to be reached. Therefore, it was decided that vapours that caused minimal PDMS swelling would not be used for swelling kinetics and diffusion analysis. A further two solvent vapours were chosen for the absorption rate experiments; one that caused mid-range PDMS swelling (toluene) and one that caused large PDMS swelling (hexane) shown in Figure 4.2.

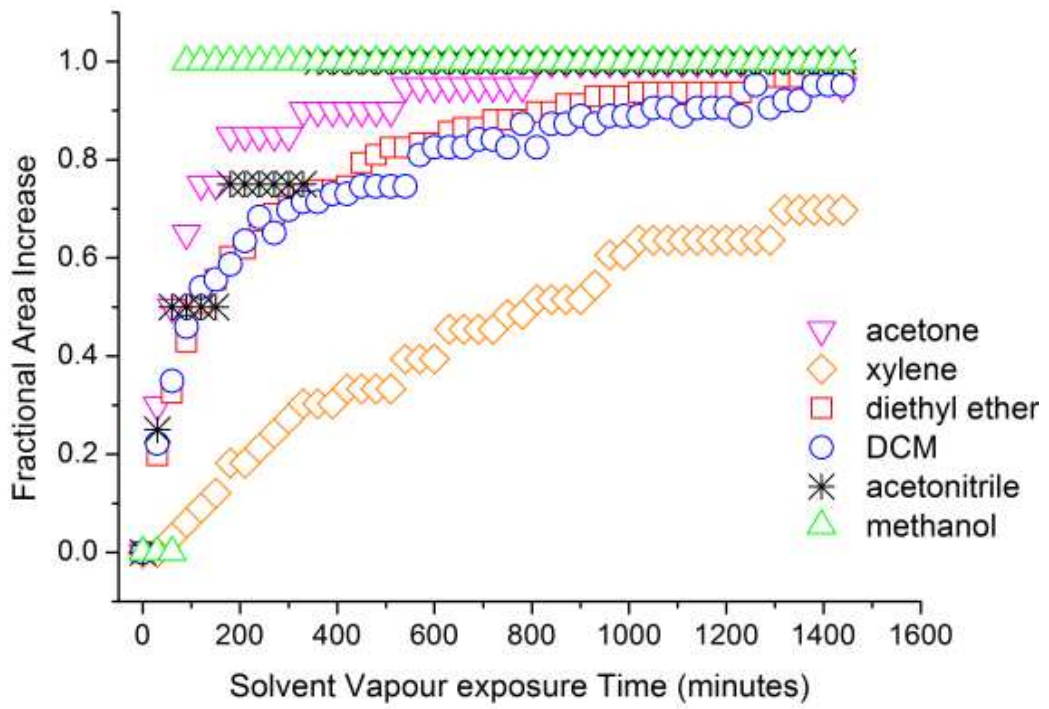


Figure 4.1: Swelling kinetics of standard PDMS elastomers in acetone, xylene, diethyl ether, DCM, acetonitrile and methanol solvent vapour.

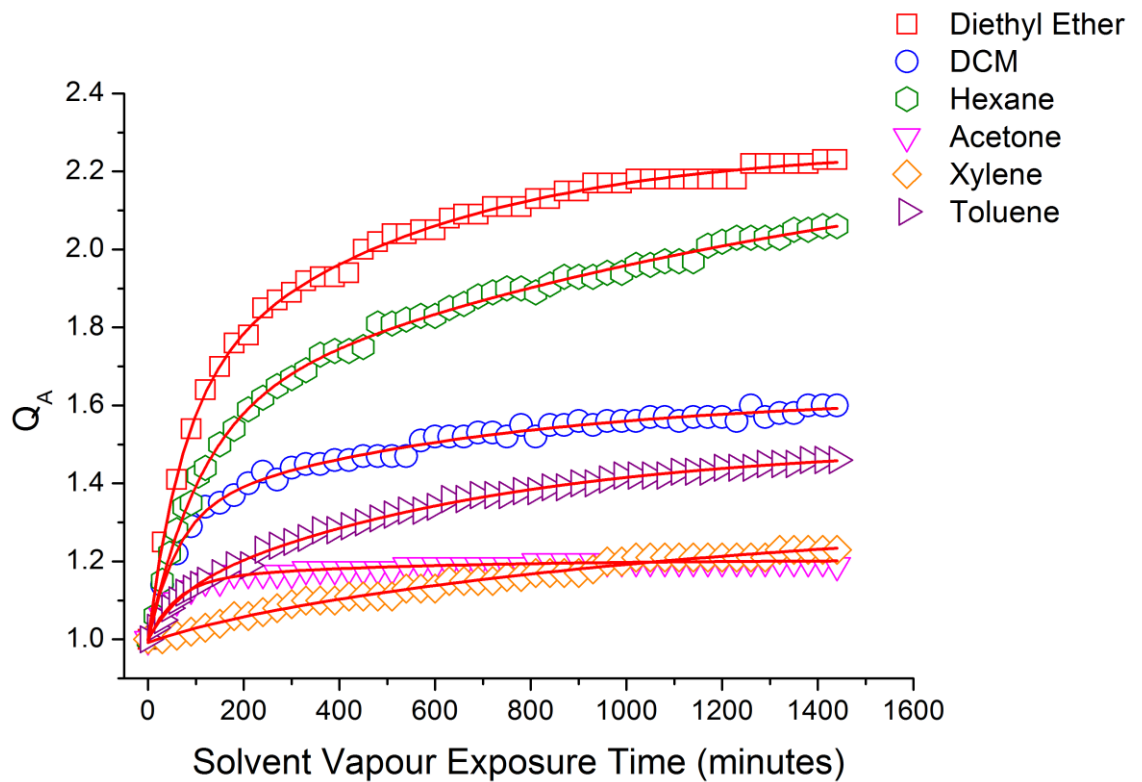


Figure 4.2: Relationship between PDMS area swelling,  $Q_A$  and solvent vapour exposure time. Inclusion of the solvent vapours toluene and hexane.

The swelling kinetics of the standard PDMS elastomers in diethyl ether, DCM, hexane, acetone, toluene and xylene solvent vapours was shown in Figure 4.3 (a). The first 55 % swelling by the six solvent vapours (Figure 4.3 (b)) displayed a linear relationship associated with Fickian diffusion.

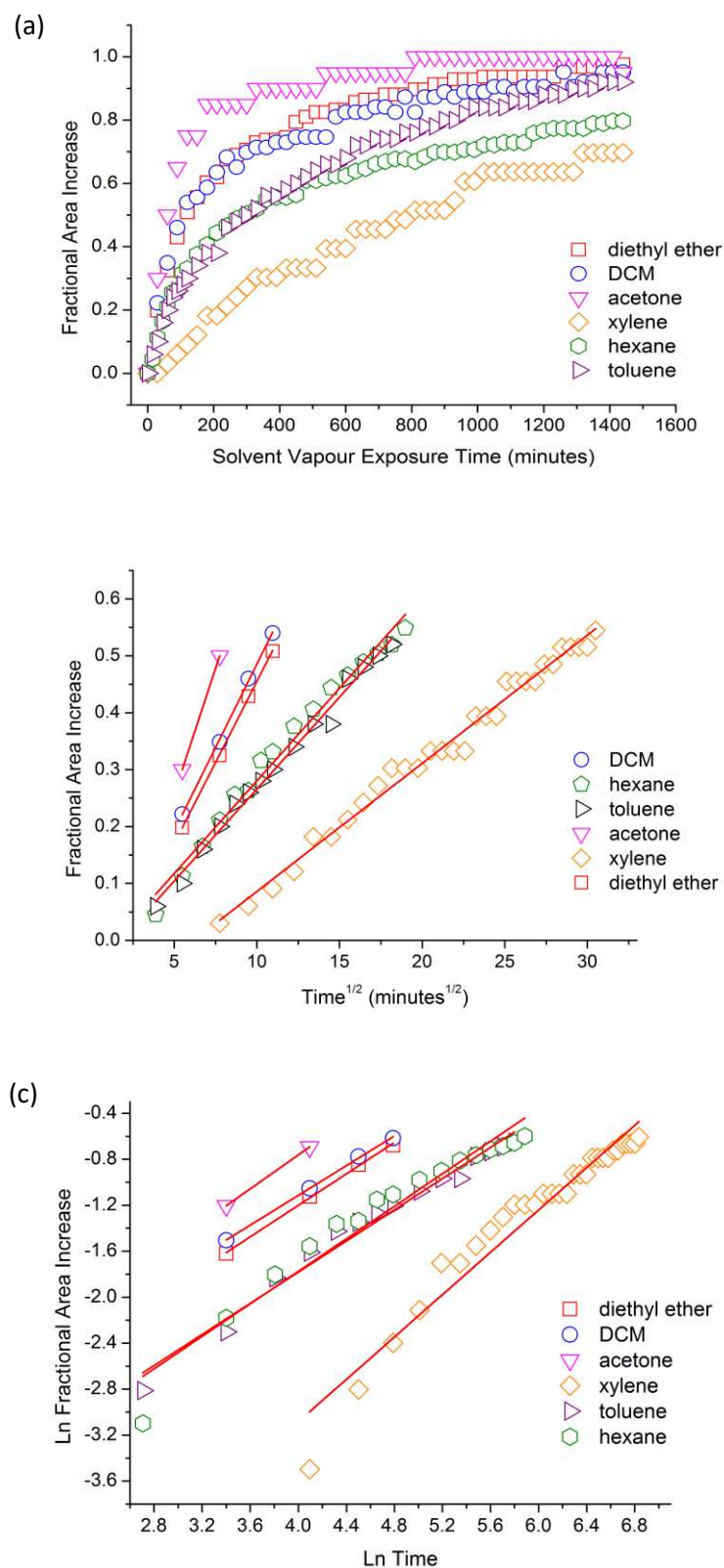


Figure 4.3: (a) Swelling kinetics, (b) the first 55 % swelling data versus the square root of time for the standard PDMS elastomers and (c) plot to determine diffusion exponent,  $n$  and polymer characteristic constant,  $k$  for the swelling of standard PDMS in diethyl ether, DCM, acetone, xylene, toluene and hexane.

This linear relationship further suggests case 1 Fickian diffusion where the mobility of the diffusant is slower than the polymer chain relaxation. In order to determine the mechanism of transport the swelling data was fitted into the following equation:<sup>10,11</sup>

$$\text{Ln} \frac{M_t}{M_\infty} = \text{Ln} k + n \text{Ln}(t) \quad (\text{Equation 4.2})$$

Where  $\frac{M_t}{M_\infty}$  is the fractional solvent vapour mass uptake of the polymer at time t, k is a constant that depends on the structural properties of the polymer and n is the diffusion characteristic of the polymer solvent vapour system. The slope and intercept of a plot  $\text{Ln} \frac{M_t}{M_\infty}$  versus  $\text{Ln} t$  gives the value of n and k, respectively.<sup>5</sup> Equation 4.2 only applies up until the first 60 % swelling. If n = 0.5 the mechanism of transport is Fickian (case 1) in which the rate limiting step is the diffusion rate. If n = 1.0 the mechanism of transport is case II where the rate of diffusion is faster compared to polymer relaxation, therefore the rate limiting step is the polymer relaxation. Values of n between 0.5 and 1 indicate anomalous behaviour which occurs through coupling between Fickian and non-Fickian behaviour.<sup>10</sup> The values of diffusion exponent, n and polymer characteristic constant K were found by plotting  $\text{Ln}$  fractional area increase versus  $\text{Ln}$  time (figure 4.3 (c)) and recorded in Table 4.1. The first 55 % swelling data was used for figure 4.3(c). Values of n for the standard PDMS elastomers were found to be between 0.5 and 1.0 indicating the transport mechanism was anomalous transport rather than case 1 Fickian diffusion, which was expected. The deviation from case 1 Fickian diffusion is most likely due to the swelling of the elastomers. The polymer characteristic constant, k can be used to describe the interaction between the solvent and the polymer, the larger the value of k the increased interaction between the solvent vapour and polymer. As shown in Table 4.1, the value of k did not relate to the swelling ability of the solvent vapour. The largest k value was for xylene, which caused mid-range swelling of the PDMS elastomers (chapter 3).

It was found that in diethyl ether, DCM, hexane, acetone, toluene and xylene solvent vapour the standard PDMS elastomers had reached 97.6 %, 95.2 %, 79.7 %, 95.0 %, 92.0 % and 69.7 % maximum swelling, respectively after 24 hours of vapour exposure. In all the solvent vapours apart from xylene and hexane, PDMS had almost reached maximum swelling after 24 hours which confirmed the assumption in chapter 3 that after 72 hours solvent vapour exposure maximum swelling was achieved. The 2-phase exponential association model was also used to predict the area swelling of the standard PDMS elastomers at 72 hours and it was found the predicted maximum area swelling in all solvent vapours was predicted to be reached at this time. To assess the accuracy of the use of the 2-phase exponential association model to predict maximum area swelling and therefore the accuracy of the swelling kinetics, the absorption rate experiments for the other polysiloxane networks were performed for 72 hours. The 2-phase exponential model was fitted to only 24 hours of the absorption data and the predicted maximum area swelling and measured area swelling at 72 hours was compared. It was found that the absorption data for all

the polysiloxane networks could be fitted to the 2- phase exponential association model with all the r-square values apart from the value for the fitted absorption data of diethyl ether by PTFPMS being very close to 1 as shown in Table 4.0. The low r-square value observed for the fit of the absorption data of diethyl ether in PTFPMS was most likely a result of the curling deformation of the PTFPMS elastomer during swelling. The sides of the PTFPMS elastomer curled inwards with swelling causing the area to decrease in size as shown in figure 4.4(d). Even with the lower r-square value, the 2-phase exponential association model fit was still the best fit for the swelling data of PTFPMS in diethyl ether. Even though the r-square values were close to 1 for the PTFPMS elastomers in toluene, hexane and xylene solvent vapour it was found that the maximum area ratios calculated from equation 4.0 were unreasonably large with values in the millions. As the swelling extents for the PTFPMS elastomers were so small in the previous three solvent vapours, the area ratio did not increase significantly in 24 hours causing the 2-phase exponential association model to extrapolate indefinitely. To obtain reasonable data fits for the absorption data of the PTFPMS elastomers in toluene, hexane and xylene, the area ratios measured at 72 hours were included to inform the model the area ratio levelled off rather than increased indefinitely. The r-square values for the fitted 72 hours absorption data of toluene, hexane and xylene by PTFPMS was shown in Table 4.0 labelled \* and were found to be close to the value of 1. Figure 4.4 shows the relationship between the other polysiloxane networks (PDMS sponge, TESPN cross-linked PDMS, 40 wt % BaTiO<sub>3</sub>-PDMS and PTFPMS) and solvent vapour exposure time.

Table 4.1: Diffusion exponent,  $n$  and polymer characteristic constant,  $k$  values in the various polysiloxane networks using different solvent vapours.

| Solvent<br>Vapour | $n$ values       |                |                                    |                             |        | $k$ values       |                |                                    |                             |        |
|-------------------|------------------|----------------|------------------------------------|-----------------------------|--------|------------------|----------------|------------------------------------|-----------------------------|--------|
|                   | Standard<br>PDMS | PDMS<br>sponge | 40 wt%<br>BaTiO <sub>3</sub> -PDMS | TESPN cross-<br>linked PDMS | PTFPMS | Standard<br>PDMS | PDMS<br>sponge | 40 wt%<br>BaTiO <sub>3</sub> -PDMS | TESPN cross-<br>linked PDMS | PTFPMS |
| Diethyl<br>ether  | 0.68             | 0.81           | 0.72                               | 0.70                        | 0.70   | 3.94             | 4.09           | 4.09                               | 4.12                        | 3.11   |
| DCM               | 0.65             | 0.65           | 0.70                               | 0.64                        | 1.04   | 3.70             | 3.36           | 3.86                               | 3.56                        | 4.85   |
| Hexane            | 0.71             | 0.88           | 0.81                               | 0.79                        | 1.02   | 4.60             | 4.41           | 4.80                               | 4.72                        | 5.35   |
| Acetone           | 0.74             | 1.32           | 0.71                               | 0.68                        | 0.79   | 3.71             | 5.25           | 3.72                               | 3.50                        | 4.07   |
| Toluene           | 0.68             | 0.87           | 0.61                               | 0.72                        | 0.89   | 4.49             | 5.18           | 4.26                               | 4.87                        | 5.19   |
| Xylene            | 0.92             | 0.66           | 0.60                               | 0.63                        | 0.63   | 6.77             | 4.44           | 4.45                               | 4.55                        | 4.64   |

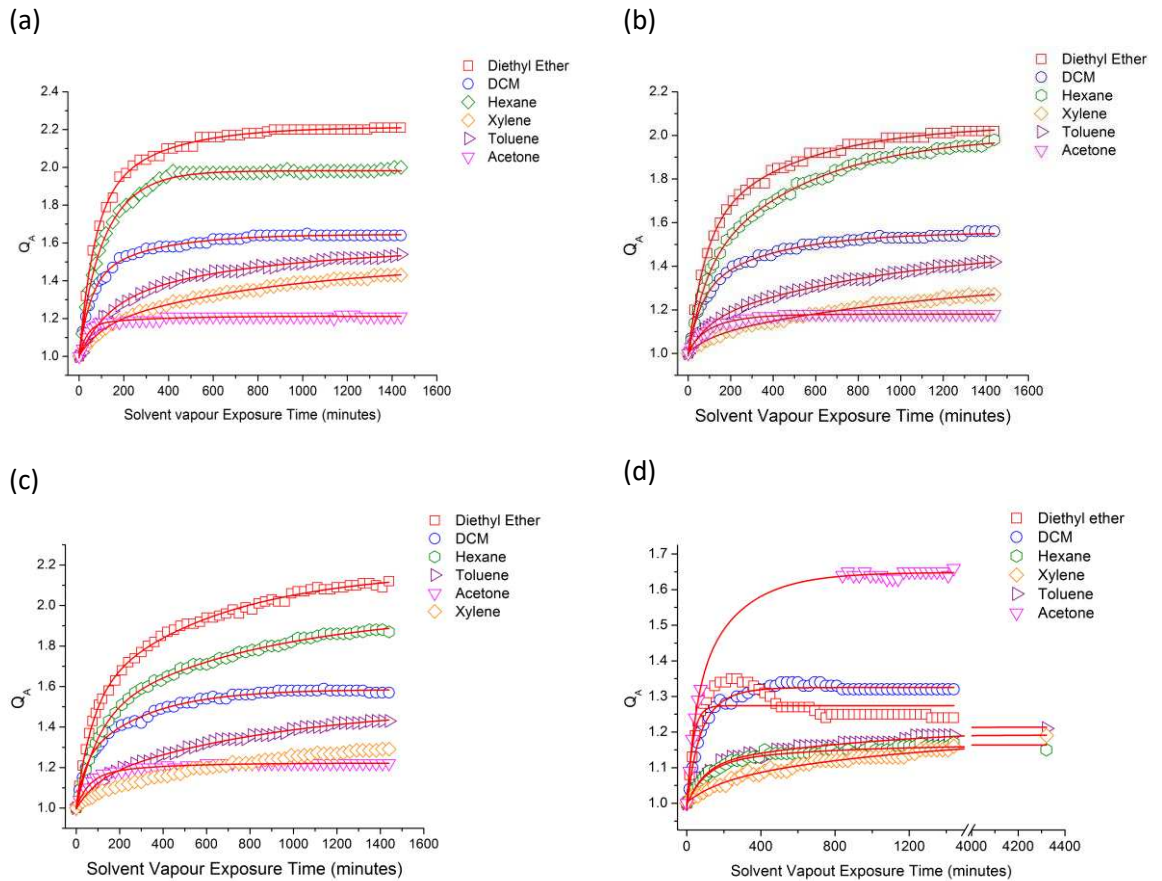


Figure 4.4: Area swelling ratio versus solvent vapour exposure time for (a) PDMS sponges (b) 40 wt% BaTiO<sub>3</sub>-PDMS elastomers (c) TESPN cross-linked PDMS elastomers and (d) PTFPMS elastomers. The data gap observed in (d) for acetone was due to the camera going out of focus which meant the area could not be accurately measured.

The predicted maximum area ratio swelling (calculated from equation 4.0) and measured area ratio swelling at 72 hours was compared for each polysiloxane network in the following solvent vapours: diethyl ether, hexane, DCM, toluene, acetone and xylene as shown in Table 4.2. It was observed that for about half of the solvent vapour polysiloxane systems the measured area ratio at 72 hours was larger than the predicted maximum area ratio swelling. As this was not the case for the majority it was concluded that the 2-phase exponential association model fit did not underestimate the extrapolated value. The largest area ratio difference (predicted max.-measured) of -0.16 was observed for 40 wt% BaTiO<sub>3</sub>-PDMS composite in hexane. An area difference of -0.16 relates to a 64 mm<sup>2</sup> area difference presuming the area of the pre-swollen polysiloxane networks was 400 mm<sup>2</sup>. An area difference of 64 mm<sup>2</sup> was deemed to be within acceptable error in this case. The difference observed was most likely a result of reasonable error associated with the measuring technique. As shown in Table 4.2 for three of the solvent vapour polysiloxane systems – standard PDMS in hexane, TESPN cross-linked PDMS in DCM and 40 wt% BaTiO<sub>3</sub>-PDMS in acetone - no difference between the predicted and measured area ratio was observed. As a result of the r-squared values of the 2-phase exponential fit all being very close to 1 (Table 4.0) and the small area ratio swelling difference between predicted maximum and measured at 72 hours it was concluded that the 2-phase exponential model was the best fit and could accurately predict the maximum swelling ratio area.



The small area ratio swelling difference also confirmed the assumptions made in chapter 3 that the maximum swelling ratio is reached by 72 hours solvent vapour exposure.

The values of diffusion exponent,  $n$  and polymer characteristic constant  $K$  were found for the PDMS sponges, TESPN cross-linked PDMS elastomers, 40 wt% BaTiO<sub>3</sub>-PDMS and PTFPMS elastomers and are shown in Table 4.1. The diffusion exponent was again found to be between 0.5 and 1.0 except for the swelling of the PDMS sponge in acetone and PTFPMS elastomers in DCM and hexane where the diffusion exponent was  $n = > 1$  which indicated super case II diffusion. Super case II diffusion is when the rate of diffusion of the penetrant molecule is much faster than the relaxation of the polymer. Therefore, the limiting step is the rate of polymer relaxation. There was not a large difference between the  $k$  constants for the standard PDMS elastomers and 40 wt% BaTiO<sub>3</sub>-PDMS composites apart from xylene, which suggested that the addition of the barium titanate filler did not have an effect on the interaction between the solvent vapour and the polymer. To compare the diffusion rate of the solvent vapours into each polysiloxane network and the effect of polymer morphology on the vapour diffusion rate, the diffusion coefficient for each different swelling system was calculated.

Table 4.2: Comparison between predicted maximum area ratio swelling (using equation 4.0 where  $t = 1 \times 10^{12}$  minutes) and measured area ratio swelling at 72 hours for all polysiloxane networks in diethyl ether, hexane, DCM, acetone, toluene and xylene.

| Solvent Vapour       | Polysiloxane network            | Predicted Maximum area ratio | Measured area ratio at 72 hrs solvent vapour exposure | $\Delta$ area ratio = predicted max. – measured at 72 hrs |
|----------------------|---------------------------------|------------------------------|---|---|
| <b>Diethyl ether</b> | Standard PDMS                   | 2.26                         | N/A   | N/A   |
|                      | TESPN cross-linked PDMS         | 2.17                         | 2.29  | -0.12   |
|                      | 40 wt% BaTiO <sub>3</sub> -PDMS | 2.05                         | N/A   | N/A   |
|                      | PDMS sponge                     | 2.21                         | N/A   | N/A   |
|                      | PTFPMS                          | 1.27                         | 1.23  | 0.04  |
| <b>Hexane</b>        | Standard PDMS                   | 2.33                         | 2.33  | 0.00  |
|                      | TESPN cross-linked PDMS         | 1.97                         | 2.02  | -0.05   |
|                      | 40 wt% BaTiO <sub>3</sub> -PDMS | 2.00                         | 2.16  | -0.16   |
|                      | PDMS sponge                     | 1.98                         | 2.01  | -0.03   |
|                      | PTFPMS                          | 1.16                         | 1.15  | 0.01  |
| <b>DCM</b>           | Standard PDMS                   | 1.63                         | N/A   | N/A   |
|                      | TESPN cross-linked PDMS         | 1.59                         | 1.59  | 0.00  |
|                      | 40 wt% BaTiO <sub>3</sub> -PDMS | 1.56                         | 1.59  | -0.03   |
|                      | PDMS sponge                     | 1.65                         | 1.70  | -0.05   |
|                      | PTFPMS                          | 1.33                         | 1.29  | 0.04  |
| <b>Acetone</b>       | Standard PDMS                   | 1.20                         | N/A   | N/A   |
|                      | TESPN cross-linked PDMS         | 1.22                         | 1.23  | -0.01   |
|                      | 40 wt% BaTiO <sub>3</sub> -PDMS | 1.18                         | 1.18  | 0.00  |
|                      | PDMS sponge                     | 1.21                         | 1.22  | -0.01   |
|                      | PTFPMS                          | 1.65                         | 1.58  | 0.07  |
| <b>Toluene</b>       | Standard PDMS                   | 1.50                         | 1.63  | -0.13   |
|                      | TESPN cross-linked PDMS         | 1.51                         | 1.55  | -0.04   |
|                      | 40 wt% BaTiO <sub>3</sub> -PDMS | 1.51                         | 1.55  | -0.04   |
|                      | PDMS sponge                     | 1.57                         | 1.65  | -0.08   |
|                      | PTFPMS                          | 1.22                         | 1.21  | 0.01  |
| <b>Xylene</b>        | Standard PDMS                   | 1.33                         | N/A   | N/A   |
|                      | TESPN cross-linked PDMS         | 1.35                         | 1.41  | -0.06   |
|                      | 40 wt% BaTiO <sub>3</sub> -PDMS | 1.35                         | 1.39  | -0.04   |
|                      | PDMS sponge                     | 1.50                         | 1.52  | -0.02   |
|                      | PTFPMS                          | 1.20                         | 1.19  | 0.01  |

#### 4.2.2 Diffusion Coefficient

The diffusion coefficient, D is a physical constant that describes how well a substance can self-diffuse or diffuse into a certain media - in this case the diffusion of solvent vapours into the polysiloxane networks. Therefore, to compare the diffusion of the different solvent vapours into the varying polysiloxane networks the diffusion coefficient for each solvent in each media was calculated. There are several methods where the empirical correlations were derived from mathematical models for Fickian sorption and can be used to estimate the diffusion coefficient. The first method is known as the half-time method where D can be calculated using the following equation:<sup>12</sup>

$$D = \frac{0.0492}{(t_{1/2}/h^2)} \quad (\text{Equation 4.3})$$

where  $t_{1/2}$  is the time it takes for the polymer to absorb 50 % of the total solvent vapour absorbed at equilibrium and h is the height of the polymer sample. The second method is known as the initial slope method where D can be calculated using the following expression:

$$\frac{M_t}{M_\infty} = 4 \left( \frac{Dt}{\pi h^2} \right)^{1/2} = Kt^{1/2} \quad (\text{Equation 4.4})$$

Where  $M_t/M_\infty$  is the fractional solvent vapour mass uptake of the polymer and K is the slope of a  $M_t/M_\infty$  versus  $t^{1/2}$  plot. Equation 4.4 can be further simplified to:

$$D = \left( \frac{Kh}{4} \right)^2 \pi \quad (\text{Equation 4.5})$$

Both equations 4.4 and 4.5 are dependent on the geometry of the sample and are representative of a plane sheet polymer sample. Royer *et al.* highlighted that substituting  $h$  with  $h_\infty$  (height of the sample at equilibrium) and  $M_t/M_\infty$  with  $R_t/R_\infty$  (R is the degree of swelling) into equation 4.4 produces an equation which relates swelling to the diffusion coefficient:<sup>13</sup>

$$\frac{R}{R_\infty} = 4 \left( \frac{Dt}{\pi h_\infty^2} \right)^{1/2} \quad (\text{Equation 4.6})$$

However, the new equation is only valid if the volume expansion of the polymer is equivalent to the mass uptake of the polymer i.e. ideal solution behaviour. In this case area expansion rather than volume expansion was used to describe swelling degree. However, as the swelling of the polysiloxane networks by solvent vapour is believed to be equal in all three spatial directions (x, y and z) the area expansion would be related to mass uptake. As previously shown in chapter 3 section 3.3.1 the PDMS-solvent vapour systems did not exhibit ideal solution behaviour and therefore equation 4.6 could not be used to accurately determine D of the solvent vapours in the polysiloxane networks. As accurate diffusion coefficients could not be calculated, the slopes of the fractional area increase *versus*  $t^{1/2}$  plots for the first 55 % swelling were used to compare the

diffusion rates of the different solvents. The slope of a straight line indicates the rate at which a change in  $x$  produces a change in  $y$ . Relating this to the fractional area increase *versus*  $t^{1/2}$  plots, a larger slope equals a larger fractional area increase at any particular time and therefore the magnitude of the slope is indicative of the diffusion rate. As shown in equation 4.5, the magnitude of the slope is also related to the magnitude of the diffusion coefficient.

#### 4.2.3 Solvent Vapour Diffusion Rates

As previously discussed, the slope of the fractional area increase *versus*  $t^{1/2}$  plots for the first 55 % swelling can be used to indicate the diffusion rate of the solvent vapours into the polysiloxane networks. There are several factors which influence the rate of diffusion of molecules into polymers including: (i) size and shape of the penetrant molecule; (ii) morphology of the polymer; (iii) solubility of the penetrant molecule in the polymer and (iv) diffusion conditions i.e. temperature. The first 55 % swelling by all six solvents in each of the polysiloxane networks is shown in figure 4.5 and the slope of each graph was recorded in Table 4.3.

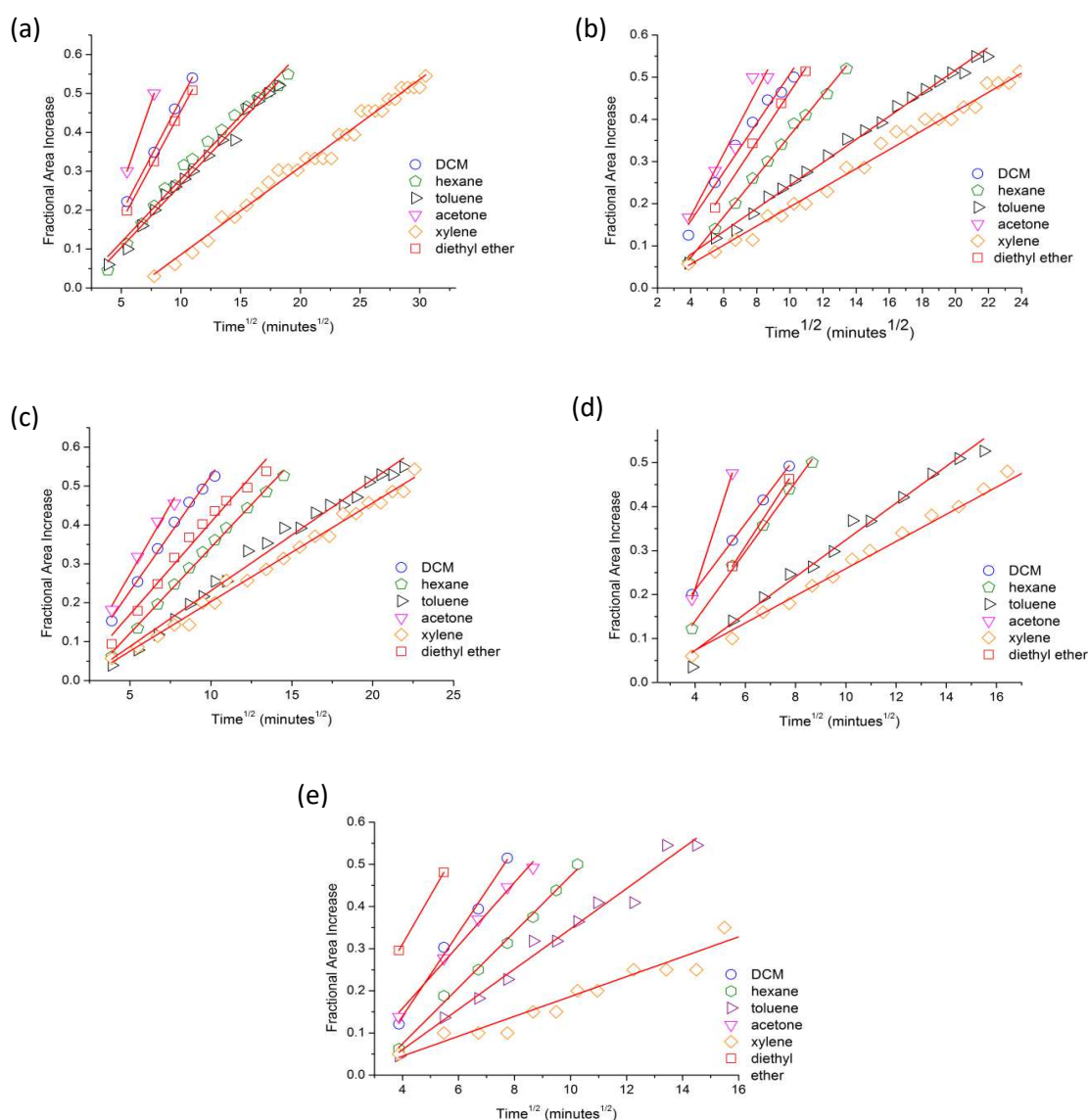


Figure 4.5: First 55 % swelling data versus the square root of time for (a) PDMS standard elastomers (b) 40 wt% BaTiO<sub>3</sub>-PDMS elastomers (c) TESPN cross-linked elastomers (d) PDMS sponges and (e) PTFPMS elastomers.

Table 4.3: Diffusion rates of the solvent vapours into the different polysiloxane networks and the diffusion coefficient in air of each solvent vapour.

| Diffusion rate in polysiloxane networks i.e. slope of graphs in figure 4.5 |                   |                   |                         |                                 |                   |   |
|--|-------------------|-------------------|-------------------------|---------------------------------|-------------------|---|
| Solvent Vapour   | PDMS standard     | PDMS sponge       | TESPN cross-linked PDMS | 40 wt% BaTiO <sub>3</sub> -PDMS | PTFPMS elastomer  | Diffusion Coefficient in air (cm <sup>2</sup> /s) |
| Diethyl Ether  | 0.05692 ± 0.00067 | 0.08771 ± N/A     | 0.04738 ± 0.00235       | 0.05909 ± 0.00274               | 0.11532 ± N/A     | 0.074   |
| DCM  | 0.05858 ± 0.00116 | 0.07539 ± 0.00043 | 0.05940 ± 0.00225       | 0.05821 ± 0.00399               | 0.09926 ± 0.00568 | 0.101   |
| Hexane   | 0.03255 ± 0.00112 | 0.07895 ± 0.00226 | 0.04412 ± 0.00086       | 0.04831 ± 0.00091               | 0.06640 ± 0.00192 | 0.200   |
| Toluene  | 0.03233 ± 0.00081 | 0.04186 ± 0.00154 | 0.02862 ± 0.00078       | 0.02732 ± 0.00045               | 0.04777 ± 0.00234 | 0.087   |
| Acetone  | 0.08815 ± N/A     | 0.17828 ± N/A     | 0.07165 ± 0.00612       | 0.07474 ± 0.01020               | 0.07472 ± 0.00352 | 0.124   |
| Xylene   | 0.02251 ± 0.00046 | 0.03089 ± 0.00068 | 0.02541 ± 0.00053       | 0.02266 ± 0.00045               | 0.02358 ± 0.00106 | 0.070   |

For all the polysiloxane networks, xylene showed the slowest diffusion and apart from the PTFPMS elastomers acetone showed the fastest diffusion rate. The rate of diffusion into the standard PDMS elastomers decreased in the solvent vapour order:

Acetone > DCM > diethyl ether > hexane > toluene > xylene

It has been highlighted the diffusion coefficient of a molecule into a polymer decreases with an increase in a molecules size.<sup>7</sup> According to the volume of the solvent vapours, the rate of diffusion would be expected to be in the order:

DCM > acetone > diethyl ether > toluene > xylene > hexane

However, as this order of diffusion rate was not observed for the solvent vapours diffusing into the standard PDMS elastomers it was clear that the diffusion rate of the solvent vapours was not influenced by size effects alone. Saleem *et al.* showed that exceptions to the general rule of small molecules diffuse faster were attributed to difference in shape of the molecule.<sup>14</sup> The authors found that *o*-xylene has the lowest diffusion coefficient compared to the other xylene isomers despite being the smallest molecule in size. It was suggested that the two adjacent methyl group on *o*-xylene distorts the molecules symmetry which in turn reduces the molecules mobility resulting in a low diffusion coefficient. The authors also highlighted that an increase in the number of chlorine atoms within a penetrant molecule was seen to decrease the diffusion coefficient. Chlorine atoms are rather bulky and therefore reduce the mobility of the penetrant molecule. Therefore, even though DCM is smaller than acetone the lack of chlorine atoms in acetone compensates for its larger size resulting in acetone having a faster diffusion rate than DCM. The research also highlighted that small ring structured molecules have lower diffusion coefficients than larger linear molecules which explains why hexane was found to have a faster diffusion rate than both toluene and xylene. It has been previously found that the diffusion rate of a solvent is dependent on the dielectric constant of the solvent.<sup>15</sup> The order of solvents according to their dielectric constant is as follows:

Acetone > DCM > diethyl ether > xylene > toluene > hexane

When compared to the order of the rate of diffusion of the solvent vapours into the standard PDMS elastomers, it was found in general that the larger the dielectric constant the faster the diffusion rate of the solvent vapour. However, the effect of the solvent's dielectric constant alone does not explain why xylene was observed to have the slowest diffusion rate of all the solvent vapours investigated but has a larger dielectric constant than both toluene and hexane. Therefore, while the diffusion rate of the solvent vapours may be weakly dependent on the dielectric constant the main factors effecting the solvent vapour's diffusion rate was found to be the size and shape of the solvent. The order of diffusion into the TESPN cross-linked elastomers was the same as the standard

elastomers. In the case of the 40 wt% BaTiO<sub>3</sub>-PDMS elastomers, PDMS sponges and PTFPMS elastomers the order of solvent vapour diffusion varied slightly compared to the order shown in the standard PDMS elastomers. The order of diffusion into both the 40 wt% BaTiO<sub>3</sub>-PDMS elastomers and PDMS sponges were similar to the standard elastomers apart from the fact that diethyl ether showed a larger diffusion rate than DCM in both networks and in the PDMS sponges hexane showed a larger diffusion rate than DCM as follows:

The rate of diffusion into the 40 wt% BaTiO<sub>3</sub>-PDMS decreased in the order:

Acetone > diethyl ether > DCM > hexane > toluene > xylene

In addition the rate of diffusion into the PDMS sponges decreased in the order:

Acetone > diethyl ether > hexane > DCM > toluene > xylene

In the case of the PTFPMS elastomers the rate of diffusion decreased in the solvent order:

Diethyl ether > DCM > acetone > hexane > toluene > xylene

Taking into account the slope (diffusion rate) error, it was found that the diffusion rates of DCM and diethyl ether were similar in both the standard PDMS and 40 wt% BaTiO<sub>3</sub>-PDMS elastomers and therefore the order of solvent vapour diffusion into the 40 wt% BaTiO<sub>3</sub>-PDMS was the same as the standard PDMS elastomers. However, even taking into account the slope errors the diffusion rate of DCM was still faster than diethyl ether into the TESPN cross-linked elastomers. This possibly suggests that in the TESPN cross-linked elastomers penetrant size effects were more profound than shape effects on the penetrant diffusion rate. The order of the solvent vapour diffusion rates in the following polysiloxane networks – PDMS sponges and PTFPMS - could not be explained by just the size and shape of the penetrant molecule suggesting that in these two vapour-polymer systems, the morphology of the polymer has an effect on the penetrant diffusion coefficient. The effect of polymer morphology on the diffusion rate of a particular solvent vapour was discussed in more detail in section 4.2.4. In the case of the PTFPMS elastomers the high diffusion rate shown by diethyl ether may not be accurate. As shown in figure 4.4 once the area ratio of the PTFPMS elastomer in diethyl ether solvent vapour reached its maximum value, it decreased before levelling out. This was due to the fact that the sides of the PTFPMS elastomers began to curl inwards during the swelling process. As a result to this slight folding exhibited by the PTFPMS elastomers, the true area growth was difficult to measure and most likely underestimated which in turn would cause the maximum area growth calculated from the 2-phase exponential association model to be underestimated. This underestimation of the maximum area ratio would lead to an overestimated diffusion rate. Not taking into account the diffusion rate of diethyl ether as it is most likely slightly overestimated, the solvent vapour diffusion rate order into the PTFPMS elastomers apart from hexane follows the expected order predicted by the size of the penetrant molecule. For the PTFPMS elastomers, it appears the shape effects of the bulky chlorine group do not have the same effect on

the diffusion rate of DCM as what was seen in the standard PDMS elastomers. This observation was attributed to the different side groups in PTFPMS and PDMS. As transient free volume which facilitates diffusion is caused by the movement of polymer chains, the shape of the resulting volume must be dictated by the chain side groups. In the case of the PTFPMS elastomers it was suggested that the shape of the transient free volume facilitates the mobility of DCM negating the shape effects observed in standard PDMS.

#### 4.2.4 Effect of the polymer morphology on the diffusion rate of a solvent vapour

##### 4.2.4.1 Barium titanate fillers

The effects of filler on the diffusion properties of polymer-filler composites have been previously investigated. In the majority of cases it was found that the diffusion coefficient decreased with increasing filler concentration. However, Aminabhavi and Harlapur found that the diffusion coefficient of solvents into carbon black filled fluoroelastomers were independent of carbon black loading.<sup>16</sup> It has been suggested that fillers which are compatible with the polymer matrix, occupy the free volume of the polymer<sup>10</sup> and act as obstacles to the penetrants increasing the diffusion path length resulting in a decreased diffusion coefficient. Cohen and Turnbull proposed a mathematical relation between the diffusion coefficient of a penetrant in a liquid of hard spheres and free volume:<sup>17</sup>

$$D = A \exp\left(\frac{-\gamma v^*}{v_f}\right) \quad (\text{Equation 4.7})$$

Where  $A$  and  $\gamma$  are constants,  $v^*$  is the minimum volume of the void required to fit the penetrant volume and  $v_f$  is the free volume of the material available for penetrant transport. According to equation 4.7, the penetrant diffusion coefficient would decrease with decreasing available free volume. Therefore, a decrease in diffusion coefficient with filler loading would be expected if the filler was occupying the polymer's free volume. However, Merkel *et al.* found that the diffusion coefficient of penetrants increased with increased fumed silica loading in high free volume glassy poly(4-methyl-2-pentyne).<sup>7</sup> The authors discovered that with increased fumed silica loading, the available free volume of the polymer actually increased resulting in the increased diffusion coefficients. However, with the increased free volume a decrease in diffusion selectivity was observed as expected. As free volume increases, larger penetrants can easily diffuse into the polymer. It was suggested that rubbery polymers can accommodate obstacles such as fillers, without introducing additional free volume and therefore follows the Maxwell model which can be used to estimate the diffusivity of a penetrant in a filled polymer system. The Maxwell model assumes the non-porous fillers act as obstacles and perfect bonding between the fillers and the polymer matrix occurs.



The Maxwell model is as follows:<sup>18</sup>

$$D_{i,m} = D_{i,p} \left[ \frac{2-2V_f+(1+2V_f)\frac{D_{i,f}}{D_{i,p}}}{2+2V_f+(1-2V_f)\frac{D_{i,f}}{D_{i,p}}} \right] \quad (\text{Equation 4.8})$$

Where  $D_{i,m}$  is the diffusivity of a penetrant  $i$  in the filled polymer  $m$ ,  $D_{i,p}$  is the diffusivity of a penetrant in the unfilled polymer  $p$ .  $V_f$  is the volume fraction of the fillers and  $D_{i,f}$  is the diffusivity of a penetrant in the filler. Equation 4.8 can be approximated to:

$$D_{i,m} = D_{i,p} \left[ \frac{2-2V_f}{2+2V_f} \right] \quad (\text{Equation 4.9})$$

If both the volume fraction of the filler ( $V_f$ ) and  $\left(\frac{D_{i,f}}{D_{i,p}}\right)$  are small, according to equation 4.9, the diffusion coefficient of a penetrant will decrease with increasing non-porous filler concentration. It has been suggested that fillers not only affect free volume by acting as obstacles but via adherence to the polymer matrix (reinforcement). Free volume is redistributed continuously and diffusion of penetrants via free volume occurs through transient gaps in the polymer.<sup>19</sup> The transient gaps connect sections of free volume and are caused by micro-Brownian motions of the polymer chains. However, good adherence of the fillers to the polymer hinders the Brownian motions of the polymer chains, resulting in a decrease in transient gaps.<sup>20</sup> The hindering of polymer chain movements also causes the  $T_g$  of the composite to increase. The effect of  $T_g$  on the diffusion coefficient is further discussed in section 4.2.4.3. The diffusion rate of each solvent vapour into the 40 wt% BaTiO<sub>3</sub>-PDMS elastomers and the standard PDMS elastomers are compared in figure 4.6.

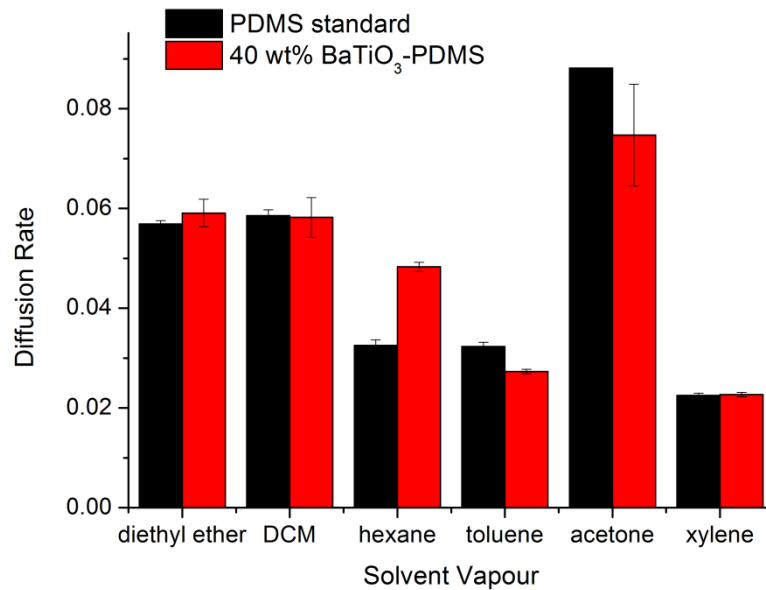


Figure 4.6: Comparison of the diffusion rate of solvent vapours into standard PDMS elastomers and 40 wt% BaTiO<sub>3</sub>-PDMS elastomers

It was clear that the introduction of fillers does not appear to have a large effect on the solvent vapour diffusion rates and therefore does not follow either the mathematical expression presented by Cohen and Turnbull (equation 4.7) or the Maxwell model (equation 4.9). The similarity between the diffusion rates into standard PDMS elastomers and 40 wt% BaTiO<sub>3</sub>-PDMS elastomers was attributed to the poor adherence between the barium titanate filler and PDMS matrix. As previously discussed in Chapter 3 section 3.3.3 it has been shown that there is a lack of chemical interaction between BaTiO<sub>3</sub> and PDMS. Imperfect bonding or filler incompatibility with the polymer introduces voids which facilitate facile diffusion and increases the available free volume.<sup>9</sup> Therefore, in this case the Maxwell model is invalid and the introduction of defects and voids caused by filler/polymer incompatibility balances out the original loss of free volume caused by the presence of the BaTiO<sub>3</sub> filler.

#### 4.2.4.2 Porosity

Comparisons were made between the diffusion rate of each solvent vapour into the PDMS sponges and the standard PDMS elastomers. The increase in the diffusion rates of the solvent vapours into the sponges compared to the standard PDMS elastomers as shown in Figure 4.7 was expected.

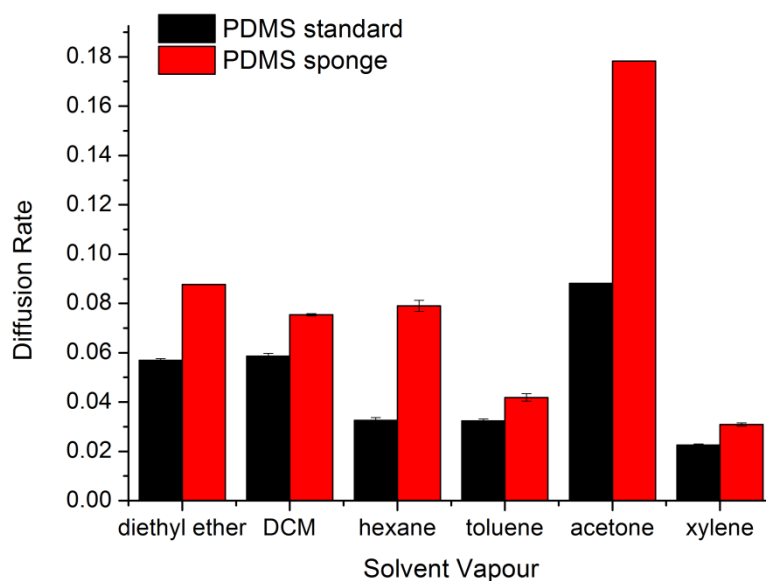


Figure 4.7: Comparison of the diffusion rate of solvent vapours into standard PDMS elastomers and PDMS sponges.

As previously discussed diffusion (transport) of molecules into polymeric systems relies on both the free volume of the polymer and segmental mobility of the polymer chains. The introduction of pores, which are essentially free space increases the overall free volume of the polymer network. Therefore, following equation 4.7 a porous material will increase the penetrant diffusion coefficient. The diffusion through the pore space is much faster than the diffusion through the free volume associated with the polymer. In the case of the PDMS sponges, the interconnected pores allowed for fast facile penetrant diffusion before diffusion through the free volume associated with the polymer occurred. Essentially, the interconnected pores of the PDMS sponge increased the

surface area where penetrant diffusion into the polymer chains transpires. The degree of porosity can be mathematically related to penetrant diffusion coefficient.<sup>8</sup> The volume fraction porosity of a material,  $V_p$  (volume of the material which is occupied by pores) is related to both the surface area of the pores,  $A_p$  and the average pore radius  $R_h$  as follows:

$$V_p = R_h A_p \quad (\text{Equation 4.10})$$

The permeability of a penetrant,  $P$  through a porous material can be given by the following equation:

$$P = (1 - p)R_h^2 / f_s f_T \quad (\text{Equation 4.11})$$

Where  $p$  is the relative density of the film and  $f_s$  and  $f_T$  are factors that account for the shape of the pores and non-linear pathway the penetrant has to take in the material respectively. The diffusion coefficient,  $D$  is related to permeability as follows:

$$D = \frac{P}{S} \quad (\text{Equation 4.12})$$

Where  $S$  is solubility of the penetrant. Combining equations 4.11 and 4.12, it was found that  $D$  is directly proportional to the average pore radius squared,  $R_h^2$  assuming constant solubility. Therefore, it could be concluded that an increase in material porosity would cause an increase in the diffusion coefficient of the penetrant. This relationship confirmed the increased diffusion rates observed for the PDMS sponges. Jin *et al.* also observed an increase in penetrant diffusion coefficient with an increase in pore size of porous hydrogels.<sup>21</sup> The difference between the diffusion rates into the two different polymer morphologies was not the same for each solvent vapour. It was found that hexane displayed the largest difference in diffusion rate between the PDMS sponges and PDMS standards (diffusion into sponge was 2.4 faster than into standard) where as DCM and toluene showed the least (diffusion into sponge was 1.3 faster than into standard). The solvent vapours were placed in order according to how much faster they diffuse into the PDMS sponge compared to the standard PDMS elastomer:

Hexane > Acetone > Diethyl Ether > xylene > DCM = Toluene

In the case of the PDMS sponges where the interconnected pores were filled with air the diffusion rate of the solvent vapour in air combined with the size and shape of the penetrant influenced the measured diffusion rate. The diffusion coefficient of all six solvent vapours in air are shown in Table 4.3. A penetrant with a larger diffusion coefficient in air would diffuse faster through the interconnected pores allowing for diffusion into the free volume of the polymer to occur at several points within the PDMS sponge. In the case of the standard PDMS elastomer, diffusion into the free volume of the polymer originally occurs at the edge of the elastomer before moving inwards.

The solvent diffusion in air decreased in the order:

Hexane > Acetone > DCM > Diethyl Ether > Toluene > xylene

The order of the solvent diffusion coefficient in air does not match the order of how much faster the solvent vapours diffuse into the PDMS sponge compared to the standard PDMS elastomer. Therefore, it was clear that effect of the size and shape of the penetrant (as previously discussed in section 4.2.3) on diffusion is not completely overcome by the effect of the diffusion coefficient of the penetrant in air. However, the inclusion of the effect of the penetrant diffusion rate in air does explain why the diffusion rate of hexane was affected so much with the inclusion of pores to the PDMS network and why the solvent diffusion rate order into the PDMS sponges differed from the standard PDMS elastomers.

#### 4.2.4.3 Nature of cross-links

The diffusion rate of the solvent vapours into the TESPON cross-linked PDMS elastomers were compared with the diffusion rates into the standard PDMS elastomers as shown in Figure 4.8. There was minimal difference in the diffusion rates of DCM, toluene and xylene between the two different polymer morphologies. The diffusion rates of both diethyl ether and acetone were slower into the TESPON cross-linked elastomers than into the PDMS elastomers. It was found that hexane was the only solvent vapour that diffused faster into the TESPON cross-linked elastomers.

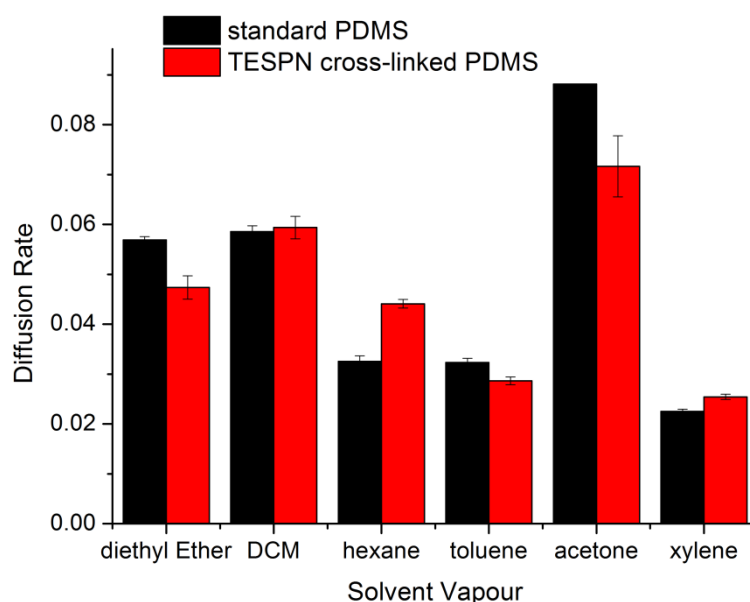


Figure 4.8: Comparison of the diffusion rate of solvent vapours into standard PDMS elastomers and TESPON cross-linked PDMS elastomers.

One well known method to reduce cross-link density in thermoset polymers is to decrease the monomer functionality.<sup>22</sup> A decrease in cross-link functionality should work the same way and cause a reduction in the final cross-link density of the cross-linked polymer. As previously highlighted in chapter 3, apart from the chemical difference between the two cross-linkers used

(TEOS and TESPN), the two cross-linkers also have different functionalities. TEOS has a functionality of 4 compared to TESPN that has a functionality of 3. Therefore, it would be expected that the TESPN cross-linked polymers have a slightly lowered cross-link density compared to the standard PDMS elastomers (TEOS cross-linked). A reduction in cross-link density is shown in the reduction of the  $T_g$  of the cross-linked polymer.<sup>23</sup> Previous research has shown that the diffusion coefficient of a penetrant molecule is larger in polymers with a low  $T_g$ .<sup>9</sup> Thus, a reduction in cross-link functionality would cause an increase in the diffusion coefficient of a penetrant molecule. As the functionality of TESPN is smaller than TEOS it would be expected that the diffusion rate into the TESPN cross-linked elastomers would be faster than into the standard PDMS elastomers. However, as shown in figure 4.8 this was not the case. It is most likely that a difference of 1 cross-link function (3 compared to 4) does not have a large effect on the cross-link density of the polymer and therefore the  $T_g$  of the polymers are most likely very similar.

#### 4.2.4.4 Fluoro-containing Polysiloxanes

As shown in Table 4.3 and figure 4.9, it was clear that the diffusion of the solvent vapours apart from acetone was faster into PTFPMS compared to the PDMS elastomers. This was not in agreement with previous research that found the diffusion of  $\text{CO}_2$  and  $\text{CH}_4$  into PTFPMS was much slower than into PDMS.<sup>24</sup> The substitution of a methyl group with a large bulky group such as trifluoropropyl as in the case of PTFPMS decreases the polymer's fractional free volume to 0.29 compared to 0.33 of PDMS and reduces the mobility of the polymer chains as reflected in the increased glass transition temperature  $T_g$  of the polymer.<sup>25</sup> The  $T_g$  of PTFPMS is  $-70\text{ }^\circ\text{C}$  while the  $T_g$  of PDMS is  $-125\text{ }^\circ\text{C}$ . A decrease in both free volume and chain mobility of a polymer is expected to be accompanied with a decrease in the diffusion coefficient of a penetrant molecule.

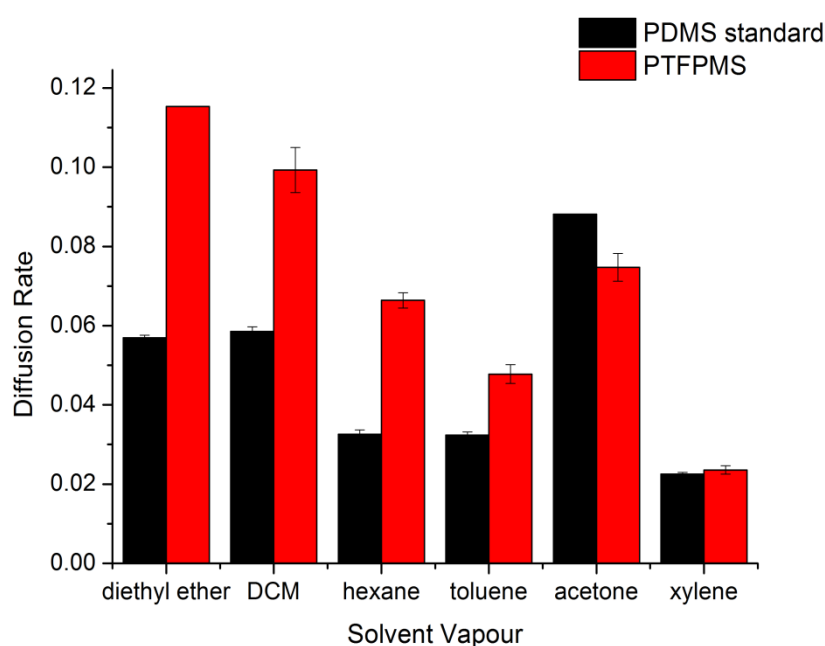


Figure 4.9: Comparison of the diffusion rate of the solvent vapours into the standard PDMS elastomers and PTFPMS elastomers.

As previously discussed the diffusion coefficient of a penetrant molecule is larger in polymers with a low  $T_g$ .<sup>9</sup> Therefore, as the  $T_g$  of PTFPMS is 55 °C higher than PDMS the diffusion of solvent vapours into the PTFPMS elastomers would be expected to be slower than into the standard PDMS elastomers.

Charati and Stern estimated the diffusion coefficients of several gases into PDMS, PPMS (propylmethylsiloxane), PTFPMS and PPhMS (polyphenylmethylsiloxane) using molecular dynamics (MD) simulations. They found the estimated diffusion coefficients decreased with the increased size of the polymer side chains and this agreed with the order shown by the experimental diffusion coefficients of CO<sub>2</sub> and CH<sub>4</sub> in the above silicone polymers.<sup>24</sup> Along with the differences in the  $T_g$  and free volume of PDMS and PTFPMS, the elastomers also had different cross-link densities. The molecular weight of the PDMS and PTFPMS chains determined using NMR spectroscopy were 24266 g mol<sup>-1</sup> and 2977 g mol<sup>-1</sup>, respectively. As the same ratio of cross-linker was used for both elastomers (ratio of SiOH groups in PDMS or PTFPMS to SiOR groups in TEOS was 1:4) it was clear that the PTFPMS elastomers have a higher cross-link density compared to the PDMS elastomers due to their much smaller chain length. In the literature it has been shown that the diffusion coefficient increases with decreasing cross-link density.<sup>26</sup> At lower cross-link densities, the individual polymer chains are not as restricted by the cross-links and therefore more mobile which facilitates diffusion. For that reason, it would be expected that the diffusion rate into PTFPMS would be slower than into PDMS. However, as shown in figure 4.9 this was not the case. One possible explanation for the very high diffusion rates into the PTFPMS elastomers is their low degree of swelling in solvent vapour compared to the standard PDMS elastomers apart from in acetone. As area growth i.e. fractional area swelling has been used to determine the diffusion rate it is clear that the extent of swelling is important.

### 4.3 Conclusions

It was concluded that the mechanism of transport into the polysiloxane networks followed mainly anomalous diffusion with  $n$  values between 0.5 and 1. The diffusion coefficient of each solvent was not calculated but it was concluded that the slope of the fractional area increase *versus* the square root of solvent vapour exposure time plot could be used to indicate the diffusion rate of the solvent vapour into the polysiloxane networks. It was found that the diffusion rates of the solvent vapours into standard PDMS were dependent on the size and shape of the penetrant solvent vapour. It was clear that the introduction of barium titanate fillers and a more polar cross-linker (TESPN) had no real effect on the solvent vapour's diffusion behaviour. However, the introduction of pores in the PDMS sponges caused the solvent vapours diffusion rate to increase. Therefore, it was concluded that PDMS sponges would be suitable to use if a decrease in response time in detecting solvent vapours was required. The diffusion rates into the PTFPMS elastomers were not comparable to the

standard PDMS elastomers as the very large difference in swelling extent of the two polysiloxane networks could not be accounted for.

## 4.4 References

- 1 C. M. Balik, *Macromolecules*, 1996, **29**, 3025-3029.
- 2 M. B. Wisnudel and J. M. Torkelson, *Macromolecules*, 1996, **29**, 6193-6207.
- 3 Y. Cheng, R. K. Prud'Homme and J. L. Thomas, *Macromolecules*, 2002, **35**, 8111-8121.
- 4 N. A. Peppas and S. L. Wright, *Eur. J. Pharm. Biopharm.*, 1998, **46**, 15-29.
- 5 B. Singh and N. Chauhan, *Acta Biomaterialia*, 2008, **4**, 1244-1254.
- 6 S. Guilbert, N. Gontard and L. G. Gorris, *LWT-Food Science and Technology*, 1996, **29**, 10-17.
- 7 T. Merkel, V. Bondar, K. Nagai, B. Freeman and I. Pinnau, *J. Polym. Sci. Part B Polym. Phys.*, 2000, **38**, 415-434.
- 8 C. McDonagh, P. Bowe, K. Mongey and B. MacCraith, *J. Non Cryst. Solids*, 2002, **306**, 138-148.
- 9 S. C. George and S. Thomas, *Prog. Polym. Sci.*, 2001, **26**, 985-1017.
- 10 J. Abraham, H. J. Maria, S. C. George, N. Kalarikkal and S. Thomas, *Phys. Chem. Chem. Phys.*, 2015, **17**, 11217-11228.
- 11 M. Seehra, M. Yalamanchi and V. Singh, *Polym. Test.*, 2012, **31**, 564-571.
- 12 A. V. Nawaby and Z. Zhang, in *Thermoplastic foam processing: principles and development*, ed. R. Gendron, CRC press, Boca Raton, 2004, ch. 1, pp. 1-36.
- 13 J. R. Royer, J. M. DeSimone and S. A. Khan, *Macromolecules*, 1999, **32**, 8965-8973.
- 14 M. Saleem, A. A. Asfour, D. De Kee and B. Harrison, *J. Appl. Polym. Sci.*, 1989, **37**, 617-625.
- 15 T. Chan, I. Lee and K. Chan, *J. Phys. Chem. B*, 2014, **118**, 10945-10955.
- 16 T. M. Aminabhavi and S. F. Harlapur, *J. Appl. Polym. Sci.*, 1998, **68**, 815-825.
- 17 M. H. Cohen and D. Turnbull, *J. Chem. Phys.*, 1959, **31**, 1164-1169.
- 18 M. Ouddane and Y. Rancourt, *J. Appl. Polym. Sci.*, 2001, **79**, 1178-1187.

- 19 S. N. Dhoot, B. D. Freeman and M. E. Stewart, in *Encyclopedia of polymer science and technology*, ed. H. F. Mark, John Wiley & Sons, Hoboken, 2007, pp. 89-98.
- 20 L. Sereda, M. M. López-González, L. L. Y. Visconte, R. C. R. Nunes, C. R. G. Furtado and E. Riande, *Polymer*, 2003, **44**, 3085-3093.
- 21 S. Jin, F. Bian, M. Liu, S. Chen and H. Liu, *Polym. Int.*, 2009, **58**, 142-148.
- 22 F. C. Campbell Jr, *Manufacturing processes for advanced composites*, Elsevier, Oxford, 2004, ch. 3, pp. 65-100.
- 23 R. O. Ebewele, *Polymer science and technology*, CRC press, Boca Raton, 2000.
- 24 S. Charati and S. Stern, *Macromolecules*, 1998, **31**, 5529-5535.
- 25 G. Lin, M. Abar and L. M. Vane, *Sep. Sci. Technol.*, 2013, **48**, 523-536.
- 26 P. Adriaensens, A. Pollaris, M. Kelchtermans and J. Gelan, *Macromolecules*, 2003, **36**, 706-711.



# Chapter 5: Passive UHF-RFID displacement solvent vapour sensor tag with a PDMS elastomer actuator

## 5.0 Introduction

There has been much interest in the fabrication of passive RFID solvent vapour sensors for applications in food package monitoring<sup>1</sup>, environmental monitoring and security.<sup>2</sup> The use of RFID technology allows for light-weight, inexpensive and energy efficient sensors. Polydimethylsiloxane (PDMS) has many desirable properties such as low chemical activity, high thermal stability, a non-toxic nature, low surface tension and high gas permeability<sup>3</sup> which has led to it being used in numerous applications including microfluidic devices<sup>4</sup>, coatings, and medical devices.<sup>5</sup> Another well-known property of PDMS is its tendency to swell in non-polar solvents.<sup>6</sup> While for some applications such as microfluidic systems the phenomenon of PDMS swelling is seen as a negative characteristic it has been exploited and utilised in several RFID solvent vapour sensor designs. To improve the sensitivity of polymer-based chemicapacitor sensors the swelling deformation of the polymer is measured as well as the change in the polymer's permittivity as a result of the absorption of the solvent vapour by the polymer.<sup>7</sup> Traditionally polymer-based chemicapacitor sensors detect organic vapours through the absorption of vapour by the polymer which results in a variation of the polymer's permittivity leading to an overall change in capacitance of the sensor.<sup>8</sup> However, the sensitivity of chemicapacitor sensors are often low as the variance in the polymer's permittivity can be extremely subtle. Fiddes and Yan demonstrated a RFID tag array which utilised carbon black/polymer composites integrated onto conventional RFID tags.<sup>9</sup> The swelling deformation of the polymer in solvent vapour caused the distance between the carbon black particles to vary resulting in a change in conductance which was detected as a change in the signal frequency transmitted from the RFID tag. The RFID tag array produces a unique pattern of signals for each solvent vapour as each of the RFID tags has a different polymer as a sensing element. Even though both of the RFID sensor designs discussed above utilise polymer swelling they are both still reliant on the variation of electrical properties of the polymer materials in response to the solvent vapour. In this chapter a RFID solvent vapour sensor tag which only utilises the physical deformation of polymer swelling as a sensing method is demonstrated, thus removing the need to measure two different responses or add expensive conductive additives to the polymer. A displacement sensor tag design was ultimately chosen where the PDMS elastomer will act as an actuator. RFID displacement sensors are very important in structural health monitoring of buildings,<sup>10,11</sup> however, the design has not been used before in a solvent vapour sensor. The RFID solvent vapour displacement sensor tag design (Figure 5.0) used in this chapter operates on the principle that as

the PDMS elastomer swells the feed loop antenna is pushed further away from the main body antenna which leads to a change in the transmitted power and read range of the RFID tag. The aim of the research described in this chapter was to fabricate and assess the performance of the prototype RFID displacement solvent vapour sensor tag. The sensor tag was tested in a range of solvent vapours using a standard PDMS elastomer as the actuator and its ability to distinguish between solvent vapours and identify solvent vapours was assessed by comparing the RFID response to both the maximum PDMS swelling extent,  $Q_V$  (measured in chapter 3) and the PDMS area swelling ratio,  $Q_A$  at a particular solvent vapour exposure time (measured in chapter 4) in each solvent vapour tested.

## 5.1 Experimental

### 5.1.1 Materials and Apparatus

Silanol terminated polydimethylsiloxane (PDMS) (cSt 1000, M. W. 26 000) was obtained from Fluorochem Ltd. Tetraethyl orthosilicate (99 %) and tin (II) 2-ethylhexanoate (95 %) were purchased from Sigma Aldrich. All the above chemicals were used as received. Homogenous mixing of the elastomer components was achieved using a DAC 150FV2-K speedmixer and elastomers were formed in PTFE square moulds (mould width = 2 cm, length = 2 cm and height = 0.2 cm). Higgs3 RFID IC was provided by Alien Technology. Acetone (lab grade), acetonitrile (HPLC grade), diethyl ether (analytical grade), methanol (analytical grade), methylene chloride (HPLC grade) and xylene (mixture of isomers with meta-xylene as the predominant isomer determined *via*  $^1\text{H}$  NMR spectroscopy) (analytical grade) were purchased from Fisher Scientific and used as received. RFID tag simulations and sensor measurements were performed using CST Microwave EM simulation software and a Voyantic Tagformance life RFID characterization system (Voyantic Ltd, Finland), respectively. Tag simulations were performed by M. A. Ziai.

### 5.1.2 Synthesis of standard PDMS elastomers

Standard PDMS elastomers were synthesised following the method described in chapter 3 section 3.1.2.1. Full characterisation of the PDMS elastomers was reported in chapter 2.

### 5.1.3 Sensor tag design

A folded dipole antenna with an inductive feed loop was designed to provide an input impedance which conjugately matched the tag transponder ASIC (Application Specific Integrated Circuit) RFID silicon chip (Higgs3 RFID chip). CST Microwave Studio EM simulation software was used to tune the sensor response to European UHF RFID frequency (865.6-867.6 MHz) for maximum power transfer between the feed loop and the ASIC. The reader power required to activate the sensor tag at distanced in the un-swollen state is given by:

$$d \leq \frac{\lambda}{4\pi} \sqrt{EIRP \times G_{tag} \times \tau / P_{th}} \quad (\text{Equation 5.0})$$

Where the transmitted power (EIRP) has a maximum of 2 W in Europe. Tag antenna gain  $G_{tag}$  and ASIC sensitivity  $P_{th}$  are fixed by the tag design and chip technology respectively and  $\lambda$  is the wavelength of the transmission signal (35 cm). The power transmission coefficient  $\tau$  between the tag antenna and transponder ASIC is variable according to:

$$\tau = \frac{4R_{ic}R_{ant}}{(Z_{ic} + Z_{ant})^2} \quad (\text{Equation 5.1})$$

Where  $Z_{ic}$  &  $Z_{ant}$  are the port impedances of the transponder ASIC and the tag antenna, respectively, while  $R_{ic}$  and  $R_{ant}$  are the real (resistive) parts. The relative position of the inductively coupled feed loop to the tag antenna affects both  $Z_{ant}$  and  $R_{ant}$ . As a consequence, if read distance  $d$  is fixed,  $\tau$  and the required transmit power are functions of the loop position. As the loop moves away from the antenna the required transmit power increases. The RFID design is shown in figure 5.0 and the tag dimensions are shown in Table 5.0. The main body of the antenna and feed loop were etched from two square pieces of 0.8 mm thick copper cladded FR4 (fibreglass reinforced epoxy laminate) circuit board. The RFID ASIC silicon chip (Higgs3 RFID chip, Alien technology) was soldered across the slot in the feed loop and the PDMS elastomer was supported by an FR4 block to restrict its movement in that direction.

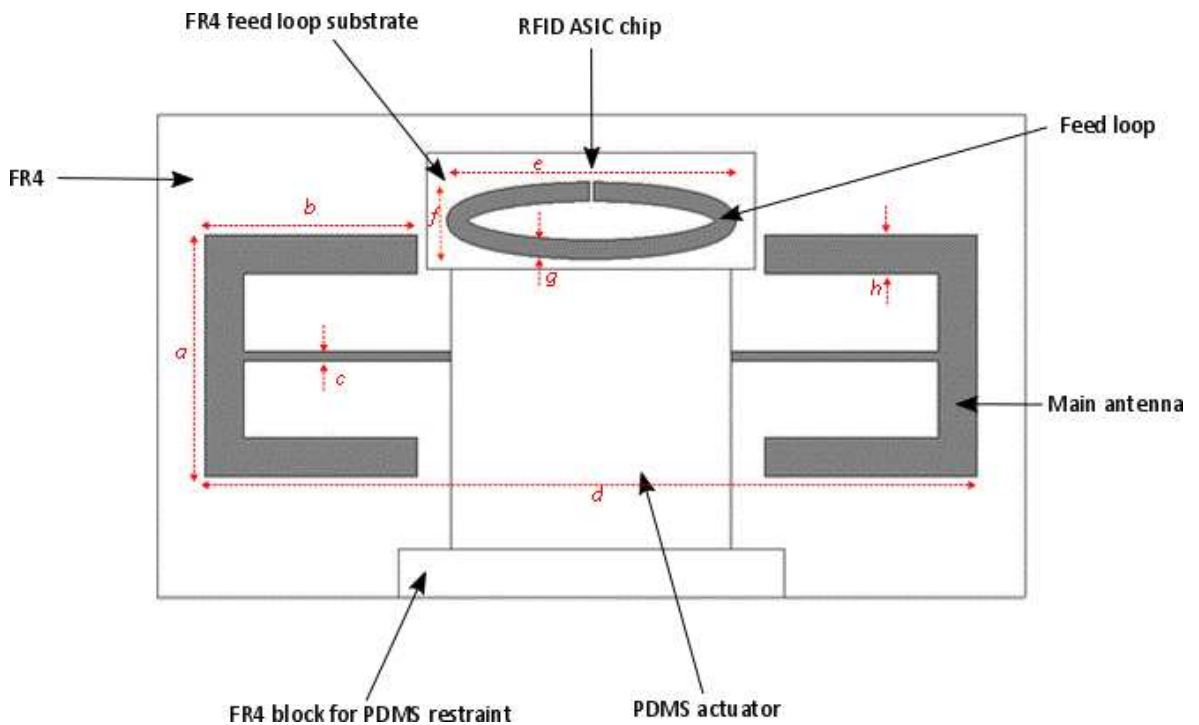


Figure 5.0: Displacement feed loop RFID tag antenna design. Dimensions in Table 5.0. Tag designed by M. A. Ziai.

Table 5.0: Dimensions of displacement feed loop RFID tag antenna

| Symbol      | a  | b  | c | d  | e  | f | g | h |
|-------------|----|----|---|----|----|---|---|---|
| Length (mm) | 25 | 25 | 1 | 80 | 14 | 3 | 2 | 4 |

#### 5.1.4 RFID sensor tag measurement

The RFID measurements were performed using the standard PDMS elastomers as the polysiloxane network actuator. An RFID tag was placed into a dessicator (internal seal diameter of 15.2 cm) with 50 cm<sup>3</sup> of a chosen solvent in an open pyrex dish. The dessicator was sealed with a flat glass lid. The dessicator was placed at a fixed distance, 30 cm above the RFID reader antenna. The tag read range was measured with a Voyantic Tagformance life RFID characterization system (Voyantic Ltd, Finland) which measures the backscattered power for the tag as a function of calibrated transmit power. Measurements were taken over a period of 24 hours solvent vapour exposure at 21 °C. For each measurement, the transmit power from the reader was ramped from 0 – 26.5 dBm over the frequency range, 800 – 1000 MHz. This transmit power value is then used to calculate tag read range for a calibrated system using a calibration tag with known parameters to determine the losses in the system. The transmitted power required to activate the tag relates directly to the coupling efficiency between the main body of the antenna and the feed loop, which decreases as the swollen PDMS standard elastomer forces the feed loop away from the main body of the antenna. To describe the RFID response the transmitted power ratio, defined as the ratio of transmitted power (at 865 MHz) for the tag at a defined solvent vapour exposure time to the transmitted power (at 865 MHz) for 0 minutes solvent vapour exposure was calculated. To fully investigate the response of the RFID tag design six solvents were used for the RFID measurements; two vapours that caused large PDMS swelling (diethyl ether and DCM), two vapours which caused mid-range PDMS swelling (acetone and xylene) and two vapours that caused small PDMS swelling (methanol and acetonitrile).

## 5.2 Results and Discussion

### 5.2.1 RFID response versus PDMS swelling

The RFID measurements were performed using six solvents: diethyl ether, DCM, acetone, xylene, methanol and acetonitrile. Figure 5.1 (a) shows the transmitted power ratio versus solvent vapour exposure time. The RFID vapour sensor was able to differentiate between solvent vapours as demonstrated by the varying magnitude of the RFID response to each solvent vapour.

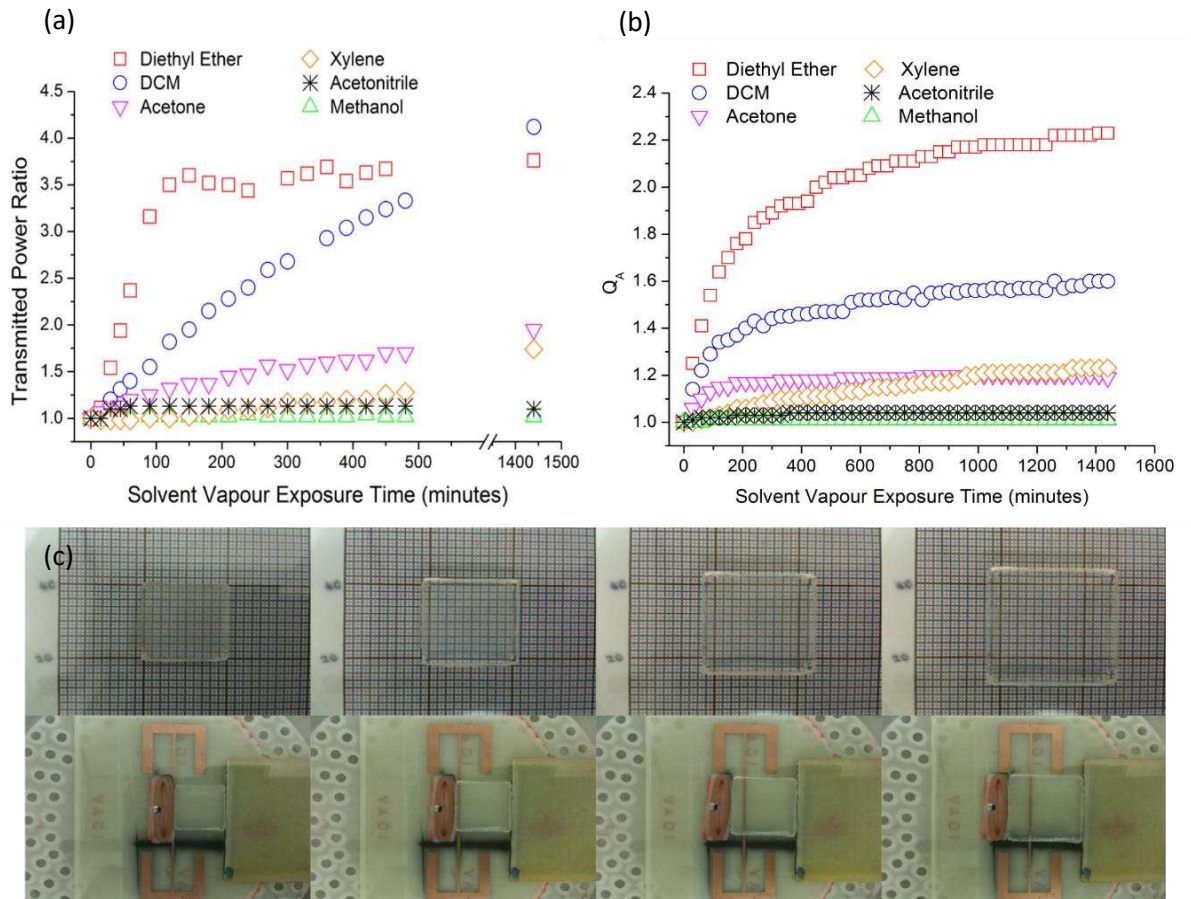


Figure 5.1: (a) Transmitted power ratio versus solvent vapour exposure time, (b) Area swelling ratio,  $Q_A$  versus solvent vapour exposure time and (c) image of a standard PDMS elastomer from left to right after 0 minutes, 30 minutes, 150 minutes and 1440 minutes diethyl ether exposure: top - images taken during absorption rate measurements and bottom - images taken during RFD measurements.

The RFID response was directly related to the displacement of the antenna loop and could therefore be related to the extent of PDMS swelling. It was observed that the shape of the RFID response curves (figure 5.1 (a)) were similar to that of the absorption rate curves shown in figure 5.1 (b). This similarity in shape suggests that the RFID response is related to the area swelling growth of the PDMS elastomers. Further repeat measurements would have to be performed to ensure the RFID responses for each solvent vapour measured in figure 5.1 (a) are accurate and reproducible. It was also observed that the RFID response plateaued at a transmitted power ratio of 3.5 at 150 minutes diethyl ether exposure even though the area swelling ratio was still increasing quite dramatically. This observation was attributed to the fact that the response of the sensor is limited by the distance of the feed loop from the main body antenna. Therefore, once the tag requires around 3.5 times more power than the minimum it requires, the tag becomes less sensitive and can no longer monitor vapour exposure.

The relationship between PDMS swelling and RFID response was investigated by comparing the transmitted power ratio at 1440 minutes solvent vapour exposure and the PDMS swelling volume ratio ( $Q_v$ ) measured in chapter 3 (Figure 5.2).

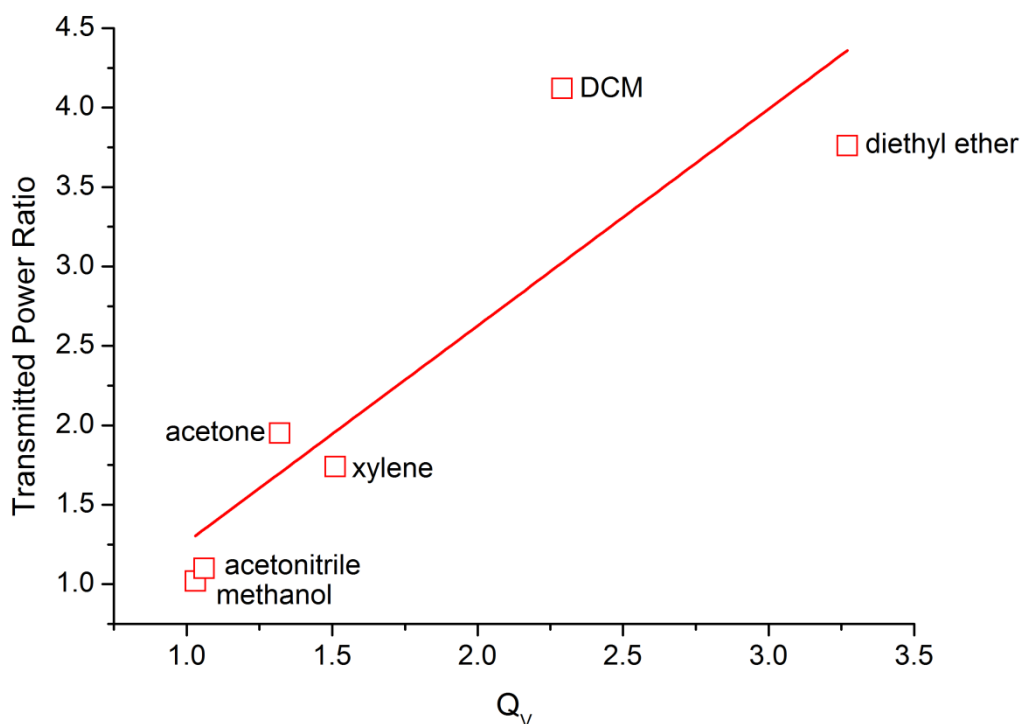


Figure 5.2: Comparison of RFID response at 1440 minutes solvent exposure time and PDMS swelling volume ratio ( $Q_v$ ).

As expected solvents that cause large PDMS swelling show the largest RFID response. Three separate groups of data were observed in figure 5.2 which relates to the three categories of how well the solvents swell PDMS: large swelling ( $Q_v > 2$ ), mid-range swelling ( $Q_v = 1.3-2.0$ ) and least swelling ( $Q_v = 1.0-1.3$ ) as previously defined in chapter 3. Diethyl ether and xylene show some divergence from the general trend that a larger  $Q_v$  will result in a larger RFID response. Whilst diethyl ether caused greater PDMS swelling than DCM its RFID response was lower. It is assumed that this is a result of the RFID responses for both DCM and diethyl ether being near to the RFID sensors upper limit. As previously discussed and shown in figure 5.1(a) the RFID sensor is limited by the distance displaced by the loop antenna which is clearly seen by the plateau at 3.5 transmitted power ratio exhibited after 150 minutes of diethyl ether solvent vapour exposure. The transmitted power ratio for both DCM and diethyl ether at 1440 minutes is above the threshold of 3.5. Xylene shows a lower RFID response than acetone even though it causes larger PDMS swelling. This observation is due to the difference in diffusion rates of xylene and acetone into the PDMS elastomers. The RFID measurements were only performed for 24 hours, however, the PDMS swelling experiments performed to obtain  $Q_v$  were performed for 72 hours. It was concluded from chapter 4 that after 72 hours solvent vapour exposure maximum PDMS swelling was achieved. However, it was also shown that maximum PDMS swelling was almost achieved after only 24 hours solvent vapour exposure with the exception of xylene and hexane. In diethyl ether, DCM, acetone, acetonitrile and methanol the standard PDMS elastomers had reached 97.6 %, 95.2 %, 95.0%, 100 % and 100 % maximum swelling, respectively, after 24 hours whereas in xylene the PDMS elastomer only reached 69.7 % maximum swelling. Therefore, the reason why the RFID response of xylene is

lower than acetone is because after 24 hours xylene exposure the PDMS elastomer has not reached its  $Q_V$  value in xylene.

A linear relationship between the transmitted power ratio at 1440 minutes solvent exposure time and  $Q_V$  was found (correlation coefficient = 0.89, R-squared value = 0.75). This linear relationship potentially will allow the  $Q_V$  and therefore the identity of the solvent vapour to be predicted from the transmitted power ratio at 1440 minutes solvent vapour exposure using the following equation:

$$Q_V = \frac{(\text{transmitted power ratio} - (-0.100))}{1.3639} \quad (\text{Equation 5.2})$$

This relationship between maximum polymer swelling ( $Q_V$ ) and RFID response allows the easy prediction of which solvent vapours would or would not be readily sensed by the RFID sensor tag described in this chapter.

### 5.2.2 RFID response time and analyte concentration

Response time is another important factor in sensors, it is the time it takes for the sensor to reach 90 % of its steady-state value.<sup>12</sup> As previously highlighted in section 5.2.1, the RFID response is related to the area swelling of the PDMS elastomers as a result of solvent vapour exposure. Therefore, it would be expected that the RFID response times would correlate with the rates of diffusion i.e. how quickly the PDMS elastomers swell in particular solvent vapours. In chapter 4, it was found that the rate of diffusion into the standard PDMS elastomers decreased in the solvent vapour order:

Acetone > DCM > diethyl ether > xylene

Therefore, it would be expected that the RFID response time in acetone should be faster than the other 3 solvent vapours. Due to the lack of sensor data between 480 and 1440 minutes solvent vapour exposure the response time to each solvent vapour could not be determined. However, to be able to preliminary investigate the RFID response times of the solvent vapour sensor tag to each solvent vapour the time taken for the RFID response to reach 55 % of its maximum value was calculated. The rate of diffusion of both methanol and acetonitrile into the standard PDMS elastomers was not calculated due to the lack of data points and therefore the response times of the sensor tag to methanol and acetonitrile absorption were also not calculated. Maximum PDMS swelling was achieved by 72 hours exposure time and therefore the RFID response at 72 hours should be used as the maximum RFID response. However, as the sensor tag measurements were only performed for 24 hours, the RFID response at 24 hours solvent vapour exposure was used as the maximum RFID response. It was shown in chapter 4 that maximum PDMS swelling was almost achieved by 24 hours with the exception of xylene where it reached 69.7 % maximum swelling. It was found that the RFID response times to the solvent vapours increased in the solvent vapour order:

Diethyl ether < Acetone < DCM < xylene

It was expected that the RFID response time to acetone would be the smallest i.e. fastest not diethyl ether. The observation that the order of RFID response times do not directly correlate with the order of the solvent vapour diffusion rates into the PDMS elastomers was attributed to the limits of the sensor tag design. In chapter 4 it was also established that the diffusion rate of the six solvent vapours tested (diethyl ether, DCM, hexane, toluene, acetone and xylene) was much faster into the PDMS sponge compared to the PDMS elastomer. Therefore, to decrease the RFID response time i.e. gain a faster RFID response time of the displacement sensor design in this chapter a PDMS sponge rather than a PDMS elastomer should be used as the actuator component.

In most cases the ability to be able to quantify analyte concentration from the sensor response is desirable. Unfortunately, as the RFID experiments were all performed in a saturated atmosphere the quantification of analyte concentration from the sensor response could not be investigated. To demonstrate if the sensor design in this chapter could be used to quantify analyte concentration the sensor would have to be exposed to a range of solvent vapour concentrations for a set period of time and then calibration curves (RFID response *versus* concentration) for each solvent vapour would need to be generated. It would be expected that the RFID response would increase with increasing solvent vapour concentration. Larger solvent vapour concentrations would lead to larger PDMS swelling which in turn would cause a larger displacement distance resulting in an increase in the transmitted power needed to power the sensor tag.

### 5.3 Conclusions

A working prototype wireless RFID passive sensor tag which exploits the swelling properties of PDMS elastomers in solvent vapours as an actuator mechanism has been demonstrated. It was found that the solvent vapour sensor tag could identify between solvent vapours and the identity of the solvent vapours could be determined from the RFID response at 1440 minutes solvent exposure using equation 5.2 if  $Q_v$  values are known. The linear relationship found between the RFID response at 1440 minutes solvent vapour exposure and  $Q_v$  enables easy prediction to which solvent vapours the RFID sensor tag described in this chapter could and could not be readily sensed. The RFID vapour sensor is limited by the distance displaced by the loop antenna as shown by the plateau in figure 5.1 (a) for diethyl ether. Further work would be to increase chemical specificity through both sensor design (via changing the distance of the actuator from the displacement component) and explore the use of the PTFPMS/PDMS double component elastomer that exhibited controlled buckling in response to solvent vapour exposure (chapter 3). Additional further work would be to investigate if the analyte concentration could be quantified from the sensor response and also investigate how the RFID sensor tag would respond to a mixture of solvent vapours.



## 5.4 References

- 1 R. A. Potyrailo, N. Nagraj, Z. Tang, F. J. Mondello, C. Surman and W. Morris, *J. Agric. Food Chem.*, 2012, **60**, 8535-8543.
- 2 R. A. Potyrailo, N. Nagraj, C. Surman, H. Boudries, H. Lai, J. M. Slocik, N. Kelley-Loughnane and R. R. Naik, *TrAC Trends Anal. Chem.*, 2012, **40**, 133-145.
- 3 J. Lötters, W. Olthuis, P. Veltink and P. Bergveld, *J. Micromech. Microeng.*, 1997, **7**, 145.
- 4 J. C. McDonald and G. M. Whitesides, *Acc. Chem. Res.*, 2002, **35**, 491-499.
- 5 A. Colas and J. Curtis, in *Biomaterials science: An Introduction to Materials in Medicine*, ed. B. D. Ratner, A. S. Hoffman, F. J. Schoen and J. E. Lemons, Academic Press, San Diego, 2004, pp. 698-708.
- 6 J. N. Lee, C. Park and G. M. Whitesides, *Anal. Chem.*, 2003, **75**, 6544-6554.
- 7 U. Altenberend, A. Oprea, N. Barsan and U. Weimar, *Anal. Bioanal. Chem.*, 2013, **405**, 6445-6452.
- 8 S. Patel, T. Mlsna, B. Fruhberger, E. Klaassen, S. Cemalovic and D. Baselt, *Sensors Actuat. B-Chem.*, 2003, **96**, 541-553.
- 9 L. K. Fiddes and N. Yan, *Sensors Actuat. B-Chem.*, 2013, **186**, 817-823.
- 10 M. J. Cazeca, J. Mead, J. Chen and R. Nagarajan, *Sensors Actuat. A-Phys.*, 2013, **190**, 197-202.
- 11 R. Bhattacharyya, C. Floerkemeier and S. Sarma, in *2009 IEEE International Conference on RFID Proceedings*, IEEE, 2009, pp. 95-102.
- 12 J. Vetelino and A. Reghu, *Introduction to Sensors*, CRC Press, Boca Raton, 2011.

# Chapter 6: Ink-jet printing of PDMS; applications for printed passive UHF-RFID wireless sensors

## 6.0 Introduction

Additive manufacturing technologies such as printing offer a reliable and economical method to produce RFID tags quickly and efficiently at low costs.<sup>1</sup> There are several additive printing techniques including screen printing, flexographic printing, gravure printing, ink jet printing and aerosol jet printing.<sup>2</sup> Many researchers have found great success in using ink jet printing to print antennas for RFID tag applications onto both paper<sup>3-5</sup> and Kapton<sup>6,7</sup> substrates. Ink jet printing is a non-contact digital printing technique with the main advantages of high printing speeds, minimal material wastage and ability to print multilayer designs.<sup>2</sup> While ink jet printing RFID antennas has been successful, to enable the realisation of fully printed RFID tags, printing of the IC component<sup>8</sup> is essential along with printing any additional components such as stimuli-responsive materials (sensing components) that the RFID tag design may have. The aim of this chapter was to explore the ink-jet printing of PDMS to work towards the use of additive manufacturing in the production of RFID tags with PDMS sensing components. Ink-jet printing of siloxanes to produce silicone resins<sup>9</sup> and PDMS<sup>10</sup> has been previously demonstrated for applications in microfluidic devices.

Ink jet printers use two main modes of operation, either 'continuous ink jet' (CIJ) or 'drop on demand' (DOD).<sup>11</sup> The difference between the two printing methods is the nature of how the ink flows through the cartridge nozzle. In CIJ printers the ink flow is continuous whereas in DOD printers the ink flow is impulsive. CIJ systems jet a continuous stream of ink which forms into droplets due to the phenomenon of the Plateau-Rayleigh instability modulated by induced vibration modulation. The droplets are then charged and pass through a set of deflector plates. The droplets used for printing are deflected onto the substrate, while the rest of the droplets are collected and returned back to the ink container.<sup>12</sup> DOD systems on the other hand only produce an ink droplet when it is needed to print. Ink droplets are generated via a pressure pulse formed in the ink cartridge which ejects ink through the nozzle. The method used to produce the required pressure pulse further classifies DOD printers into the further categories: piezoelectric, thermal, electrostatic and electrohydrodynamic. Piezoelectric and thermal DOD printers are the most commonly used. Piezoelectric materials which are used in piezoelectric DOD printers deform as a result of an applied voltage and it is this deformation that generates a pressure pulse.<sup>13</sup> Piezoelectric printers can be further classified according to the mode of deformation – the four different types are squeeze, push, bend and shear. The resistive heating element in thermal DOD printers heats the ink within the cartridge which creates a vapour bubble. As the vapour bubble expands in size it pushes the ink through the nozzle. The advantages of a continuous ink jet printer are that it can print at high

speeds and the cartridge is less likely to clog due to ink droplets being generated continuously. However, the fast printing speeds of a continuous ink jet printer can result in a loss of resolution. Further disadvantages include that the choice in ink is restricted as only ink that can be charged can be used and the cost of the printer is high due to the inclusion of the essential ink recycling system. While DOD printers cannot print as fast as continuous printers they do have the advantage of greater resolution. There are also advantages and disadvantages with the different DOD printers, for example heat sensitive inks cannot be used in thermal DOD printers as this could clog the nozzle.

The ink jet printer used in this chapter is a piezoelectric Dimatix DMP-2800 system which uses a lead zirconate titanate (PZT)/silicon bimorph as the piezoelectric material.<sup>14</sup> Sylgard® 184 was chosen as the PDMS ink as it is easy to use, its curing rate at different temperatures is well-known and has a long enough working time (up to 90 minutes). A good working time is essential to prevent the ink from curing in the ink cartridge. For optimum printing performance the surface tension of the ink needs to be 28 – 33 dynes/cm however, the main component of Sylgard® 184 - PDMS has a low surface tension of 20 mN/m. To increase the surface tension of Sylgard® 184, a solvent with a larger surface tension was required. Xylene was ultimately chosen as even though its surface tension is only 30.1 mN/m it is soluble in PDMS. In this chapter preliminary experiments to achieve ink-jet printing of Sylgard® 184 were conducted.

## 6.1 Experimental

### 6.1.1 Materials and Apparatus

Sylgard® 184 was purchased from Dow Corning and *o*-xylene was purchased from Sigma Aldrich. Both chemicals were used as received. PEL (Printed Electronics Limited) Nano P60 paper was used as received (Printed Electronics). Surface tension measurements were performed using a Kruss DSA-100 and the ink- jet printing was performed using a piezoelectric Dimatix DMP-2800 system (Dimatix-Fujifilm Inc., USA).

### 6.1.2 Fabrication of Sylgard® 184 ink

To fabricate the ink, Sylgard component A and Sylgard component B was mixed in a 10:1 ratio by mass and any trapped air bubbles were removed by applying a gentle vacuum. The resulting pre-cure Sylgard® 184 was diluted with *o*-xylene to form inks with the following pre-cure Sylgard® 184 wt% 100, 75, 50, 25, 10 and 0. The resulting pre-cure Sylgard® 184-xylene inks were placed in the fridge while not in use to prevent the ink from curing too quickly. Surface tension measurements were performed using a Kruss DSA-100 at 20°C over a period of 10.01 seconds.

### 6.1.3 Ink-Jet printing parameters

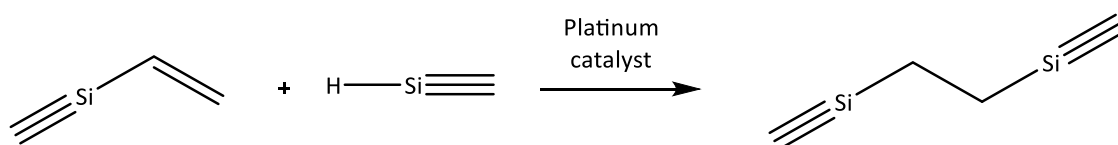
Ink-jet printing was performed using a piezoelectric Dimatix DMP-2800 system equipped with a 10 pL cartridge (DMC-11610). Various cartridge temperatures and Platen temperatures were used. Printing of the Sylgard-xylene inks were performed on a range of substrates including glass

microscope slides and PEL paper and curing of the printed Sylgard-xylene inks was performed either in situ using the platen or on a heating mantle at 60°C.

## 6.2 Results and Discussion

### 6.2.1 Characterisation of pre-cure Sylgard® 184 inks

A series of pre-cure Sylgard® 184 – xylene inks were made up by mixing the two Sylgard components (10:1 mix ratio of Sylgard component A to B) with varying weight percentages of xylene. Sylgard® 184 is a platinum catalysed addition cured (cross-linked) polydimethylsiloxane (PDMS) elastomer. Cross-linking in addition cure systems occurs via a hydrosilylation reaction between vinyl groups on the polysiloxane chains and a multifunctional silicon hydride cross-linker<sup>15</sup> as shown in scheme 6.0.



*Scheme 6.0: Addition cure cross-linking reaction.*

Sylgard® 184 is a two part addition cure system and classified as a room temperature vulcanising (RTV) system. However, the curing of Sylgard® 184 can be accelerated via heating. The typical curing times of Sylgard® 184 (fabricated using the recommended 10:1 mix ratio of component A to B) at room temperature and 150°C is 48 hours and 10 minutes, respectively. The ability to control the curing time of Sylgard® 184 via curing temperature is ideal as the ink needs to stay fluid i.e. not cure while it is in the printer cartridge and being printed. As a result the fabricated pre-cure Sylgard® 184-xylene inks were kept cool to prevent premature curing. It has been shown that ink properties such as surface tension and viscosity along with the applied piezo voltage and pulse duration have an effect on the size and velocity of an ink droplet.<sup>16</sup> The surface tension of the ink plays an important role in the droplet pinch-off process.<sup>17</sup> The stages of ideal droplet formation using a piezoelectric printer is shown in figure 6.0. When the voltage is changed the piezoelectric material deforms causing a pressure pulse within the ink cartridge. This pressure pulse causes ink to start to flow out of the nozzle. The ink gains its kinetic energy from the actuator (piezoelectric material). At this point the droplet is connected to the nozzle by the means of a thin filament. The acting force to pinch off the filament from the nozzle is surface tension. In an ideal drop formation the filament would join the main droplet forming a spherical droplet of ink. In some cases the filament will break from the main droplet and separate into several smaller droplets causing satellite droplets.

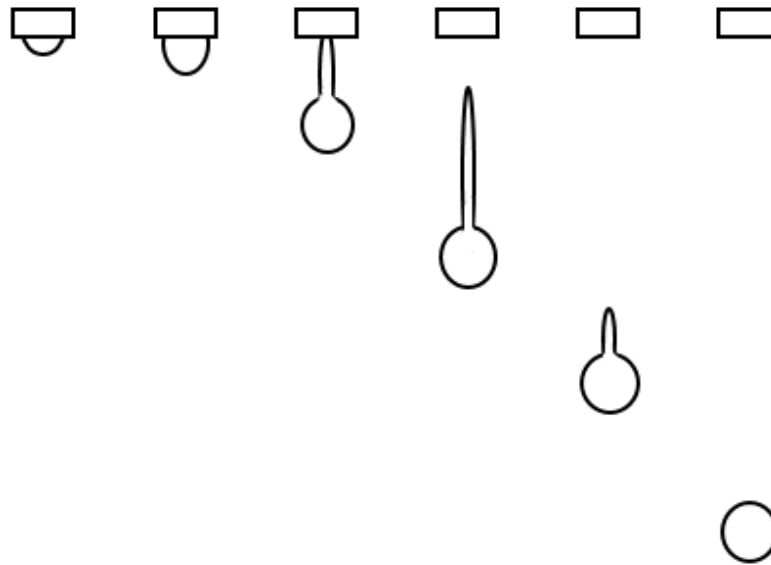


Figure 6.0: Stages of droplet formation.

Inks with a surface tension and viscosity too far away from the desired values can lead to either satellite drops or no formation of ink droplets. If the surface tension is too high ink jetting will not occur and if the surface tension is too low the ink either streams out of the nozzle or forms unstable droplets both of which lead to satellite droplets. The dimensionless Reynolds number and Weber number have previously been used to predict the ability to print an ink based on its fluid properties.<sup>18</sup> The Reynolds number,  $Re$  represents the ratio between inertial and viscous properties and is defined by:

$$Re = \frac{\rho dV}{\eta} \quad (\text{Equation 6.0})$$

Where  $\rho$  is the density of the ink,  $V$  is its velocity,  $\eta$  is the viscosity and  $d$  is a characteristic length which is normally the diameter of the jet. The Weber number,  $We$  represents the ratio between inertia and surface tension and is defined by:

$$We = \frac{\rho V^2 d}{\gamma} \quad (\text{Equation 6.1})$$

Where  $\gamma$  is the surface tension of the ink. The Ohnesorge number,  $Oh$  only reflects the physical fluid properties of the ink and removes the influence of velocity:

$$Oh = \frac{\sqrt{We}}{Re} \quad (\text{Equation 6.2})$$

The  $Oh$  number has been used to characterise the behaviour of an ink droplet being released from a cartridge.<sup>19</sup> It was found that a fluid with an  $Oh$  number between 0.1 and 1 could be a printable fluid. A fluid with  $Oh > 1$  will not form a droplet as the viscous forces will not allow the droplet to separate from the rest of the fluid in the cartridge. A fluid with  $Oh < 0.1$  will form satellite droplets.

To truly predict the printability of a fluid, the velocity needs to be taken into account which is achieved by plotting the Oh number against the Re number. The jet must have enough energy to eject a droplet corresponding to  $Re = 2/Oh$ , however, too much energy (high velocity) can cause splashing of the droplet onto the substrate corresponding to  $OhRe^{5/4} = 50$ .<sup>20</sup>

The surface tension of the ink is also an important factor in the drop impact i.e. behaviour of the ink droplet on the substrate. Inks with a surface tension much lower than the surface energy of the substrate exhibit spreading and a greater degree of wetting.<sup>21</sup> An ink's wetting behaviour on a substrate is particularly important in terms of the resolution of the printed image, for example if a very detailed image is to be printed, an ink droplet that spreads along the surface of the substrate creating a larger droplet would not be desired.

As discussed above, both the surface tension and viscosity of a fluid affects whether the fluid is printable. To achieve optimum printing performance using the Dimatix DMP-2800 system the surface tension and viscosity of the ink should be 28-33 mN/m and 10-12 cP at printing temperature, respectively. The viscosity of pre-cure Sylgard® 184 (10:1 mix ratio of Sylgard component A to B) is 3500 cP which is much higher than the desired range of 10-12 cP. The use of a 100 wt% pre-cure Sylgard® 184 ink would have most likely resulted in no ink drop formation due to clogging of the printer nozzle which is often observed for high viscous inks. There is not a literature precedent on the surface tension of pre-cure Sylgard® 184, however as Sylgard® 184 is polydimethylsiloxane based the surface tension of PDMS (20 mN/m) was used as a guideline. 20 mN/m is much lower than the desired value of 28-33 mN/m. To simultaneously increase the surface tension and decrease the viscosity of the pre-cure Sylgard® 184, o-xylene which has a surface tension and viscosity of 30.1 mN/m and 0.81 cP, respectively, was added at varying weight percentages. The surface tension of the resulting pre-cure Sylgard® 184-xylene inks (xylene wt % 100, 75, 50, 25 and 0) was measured at 20 °C and shown in figure 6.1. Unfortunately, viscosity measurements on the pre-cure Sylgard® 184-xylene inks could not be performed at the time.

Figure 6.1 shows that an increase in xylene wt% resulted in an increase in surface tension as expected and a linear relationship was found ( $R^2 = 0.96873$ ). Pure (100 wt%) o-xylene showed an average surface tension of 29.5 mN/m which was just within the desired range of 28 – 33 mN/m. Sylgard® 184 inks fabricated using solvents with a larger surface tension than xylene were attempted. 1,2-dichloroethane, cyclohexanone and dichlorobenzene with surface tensions 32.20<sup>22</sup>, 35.19<sup>23</sup> and 36.01<sup>23</sup> mN/m at 20 °C, respectively, were used to dilute the pre-cure Sylgard® 184. However, it was found that full dissolution did not occur in any of the three high surface tension solvents even at high solvent wt% even after vigorous mixing using a vortex mixer.

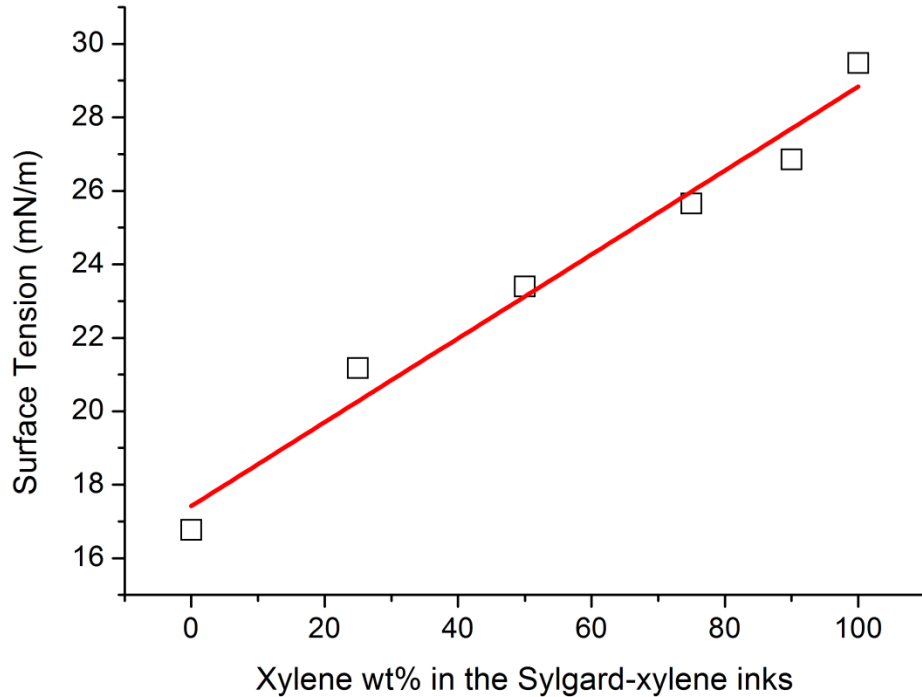


Figure 6.1: Surface tension of the Sylgard-xylene inks with varying xylene wt %.

Polymer inks such as siloxane based inks pose further problems when printing, as their viscoelastic properties affect drop formation, in particular the droplet pinch-off process. Viscoelasticity can suppress the effect of surface tension which results in a delay in the pinch-off process.<sup>24</sup> This delay in the pinch-off process results in long length filaments which often cannot reconnect with the main droplet in time causing satellite droplets. In some cases the filament does not pinch off from the nozzle causing the droplet to retreat back into the nozzle resulting in no ink jetting. Research has shown that both the polymer concentration and molecular weight has an effect on the lifetime and length of the filament.<sup>25</sup>

It was concluded that 70 wt% xylene would be the minimum amount of xylene used in the pre-cure Sylgard® 184-xylene solution inks for printing. A Sylgard® 184 (30 wt%)-xylene (70 wt%) ink would have a surface tension of 25.4 (mN/m) which while not quite the desired surface tension, it was close enough to work with. Also, the high xylene wt% in the ink should reduce both the lifetime and length of any filament formed and the viscosity of the ink.

### 6.2.2 Printing using pre-cure Sylgard® 184 (30 wt %)-xylene (70 wt %) ink

All printing was performed on a piezoelectric Dimatix materials printer (DMP) 2800 series. A schematic of a DMP 2800 printer is shown in figure 6.2. The printer has four main components:

- *Print carriage*: supports the ink cartridge.
- *Platen*: is the holder of the substrate to be printed onto. It has a vacuum system which keeps the substrate in place and flat during printing. The platen can also be set at different

temperatures (maximum 60 °C in this case) to facilitate drying of the printed ink. However, high platen temperatures can cause nozzle clogging.

- *Cleaning station*: is where cleaning cycles are performed. The cleaning station is essentially a blotting pad. Cleaning cycles can help unclog nozzles and can also be performed during printing.
- *Drop watcher*: allows direct viewing of the cartridge nozzles and the jetting of the ink.

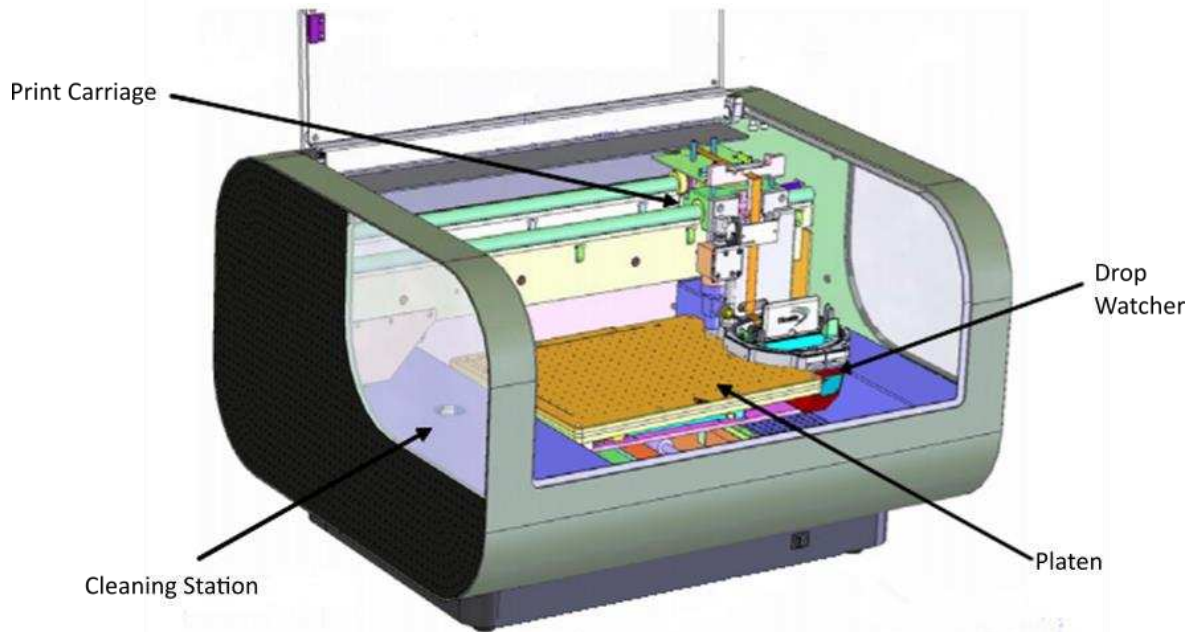


Figure 6.2: Schematic of the Dimatix materials printer 2800 series used in this chapter.

The chosen pattern to print was a 2 cm<sup>2</sup> square with a 150 micron drop spacing onto a glass microscope slide substrate. The drop spacing is measured as the distance between the centre of two subsequent ink drops in both X and Y directions. The platen was set at room temperature. Before any printing was performed the cartridge was sent to the drop watcher to observe the drop formation. It is at this point when the cartridge voltage and the waveform can be varied to ensure ideal drop formation. The waveform is divided into four different segments (1 to 4 in Figure 6.3) and each segment has three properties: duration, level (voltage) and slew rate. Each different segment is related to a different parts of the droplet formation. Segment one relates to the filling of the cartridge reservoir with ink, the voltage is decreased moving the piezoelectric material away drawing the ink in. Segment two is when the ink droplet formation is initiated via the piezoelectric material bending towards the ink reservoir as a result from an increase in voltage. Segment three relates to when the ink droplet breaks from the nozzle and segment four is a standby mode. In segment three, the voltage is reduced causing the piezoelectric material to move away from the ink cartridge back to its original standby position. The duration is how long the piezoelectric material remains in a certain position, while the slew rate is how fast the material is being deformed as a result of changing voltage.



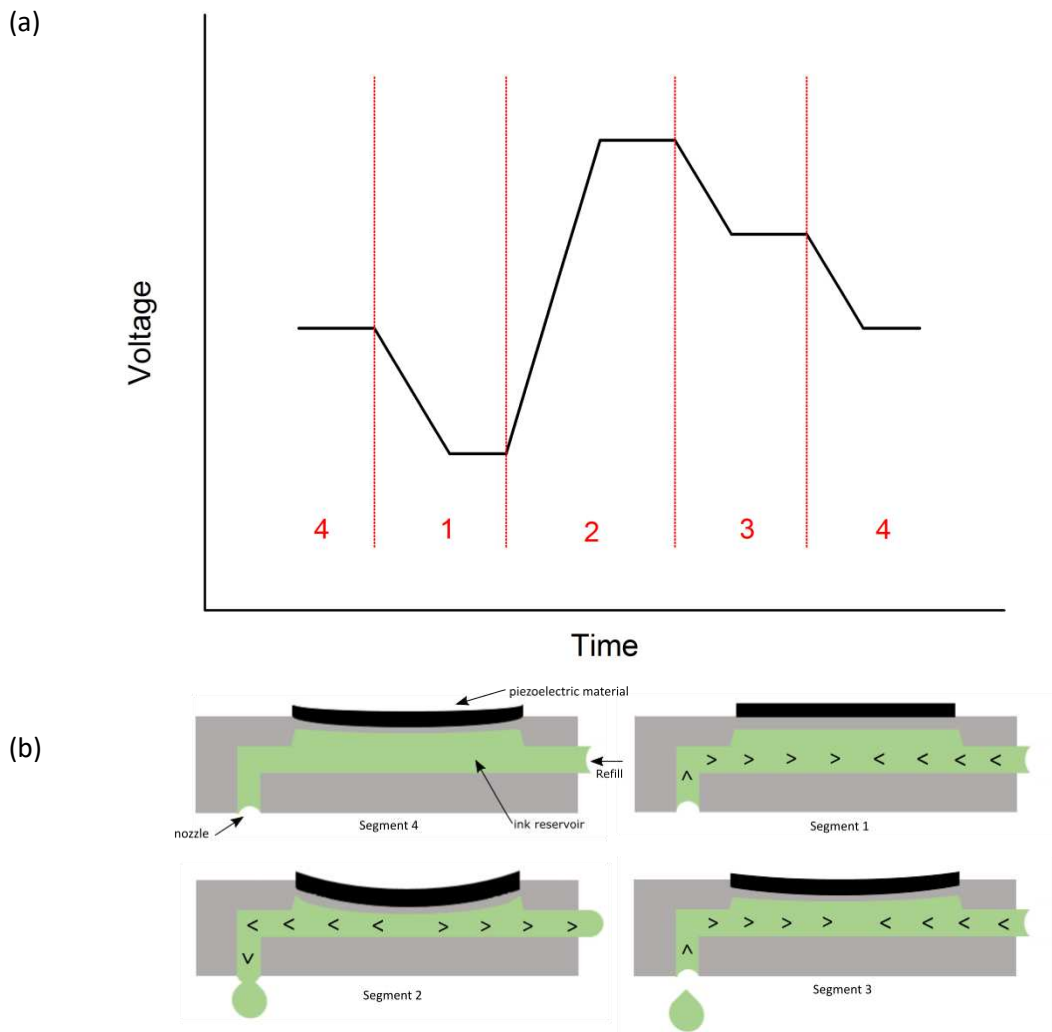


Figure 6.3: (a) Example of a printing waveform and (b) illustrations of the ink cartridge at different stages of the printing waveform. The arrowheads show the direction of the ink flow.

Initial attempts to print the ink failed due to jet clogging most likely due to the high viscosity of the ink, though increasing the voltage solved this issue initially. Increasing the cartridge temperature from room temperature up to 70 °C was also attempted, however, clogging of the jets was still occurring which was most probably due to the ink beginning to cure within the cartridge at higher temperatures. Ink jetting was achieved by lowering the cartridge temperature from 70 °C along with manipulating the waveform by varying the duration, voltage and slew rate of each segment. Further manipulation of the waveform was performed to gain the best ink droplet formation possible. An ideal droplet formation is characterised by a droplet that leaves the nozzle vertically, is a singular body, spherical in shape and has fully coalesced (i.e. the filament has fully joined the main droplet) before it has reached a distance of around 1000  $\mu\text{m}$  from the nozzle. Figure 6.4 shows the best representative images of the printed pre-cure Sylgard<sup>®</sup> 184-xylene ink on a glass slide substrate. The shapes of the majority of the ink drops were irregular as ink drop satellites were observed and no better definition was achievable even after further waveform manipulation. The

appearance of satellite droplets was attributed to both the low surface tension and high viscoelasticity of the ink.

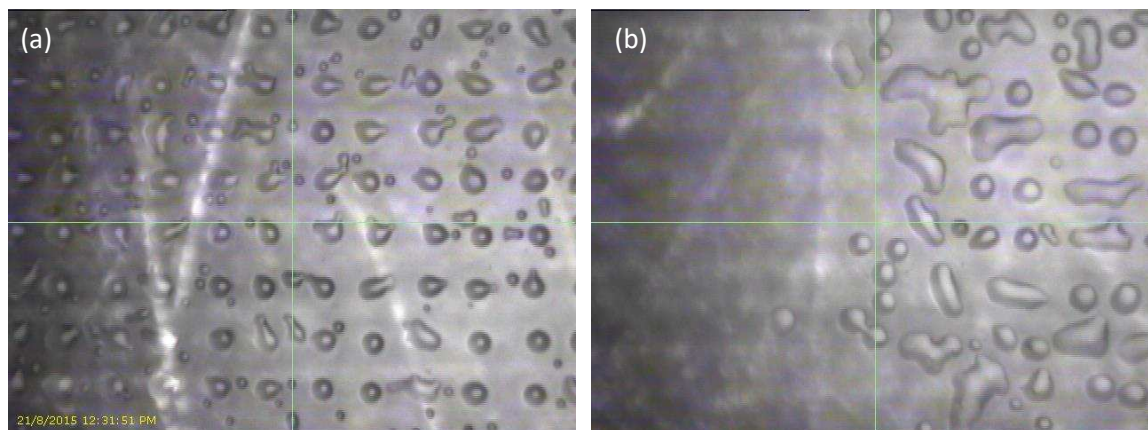


Figure 6.4: Printing of Sylgard (30 wt%)-xylene (70 wt %) ink on glass substrate with a 150 micron drop spacing (a) image taken from middle of the printed square and (b) image taken at the edge of the printed square.

However, it was noted that the satellite droplets could have also been produced by splashing which is a consequence of using high firing voltages to achieve ink jetting. To diminish the formation of satellite drops, the xylene weight percentage content of the pre-cure Sylgard® 184-xylene ink was increased. Increasing the xylene content increases the surface tension, decreases the viscosity and reduces the effect of viscoelasticity. It was decided to use a pre-cure Sylgard® 184 (5 wt %)-xylene (95 wt %) ink would be used in subsequent printing experiments.

### 6.2.3 Printing using pre-cure Sylgard® 184 (5 wt %)-xylene (95 wt %) ink

A pre-existing waveform that was optimised for printing xylene was used as a starting point due to the large xylene content of the pre-cure Sylgard® 184 (5 wt%)-xylene (95 wt %) ink. Again, the waveform settings were varied to produce the best drop formation and the resulting printed image before and after curing at 60°C was shown in Figure 6.5. A 2 cm<sup>2</sup> square pattern with a 200 micron drop spacing was printed onto a glass microscope slide substrate. Curing of the ink was performed by placing the glass slide with the printed image onto a heating mantle. Discrete circular shaped ink droplets were observed with no evidence of any satellites and it was found that the removal of xylene through curing had no effect on the shape of the printed Sylgard® 184 droplet.

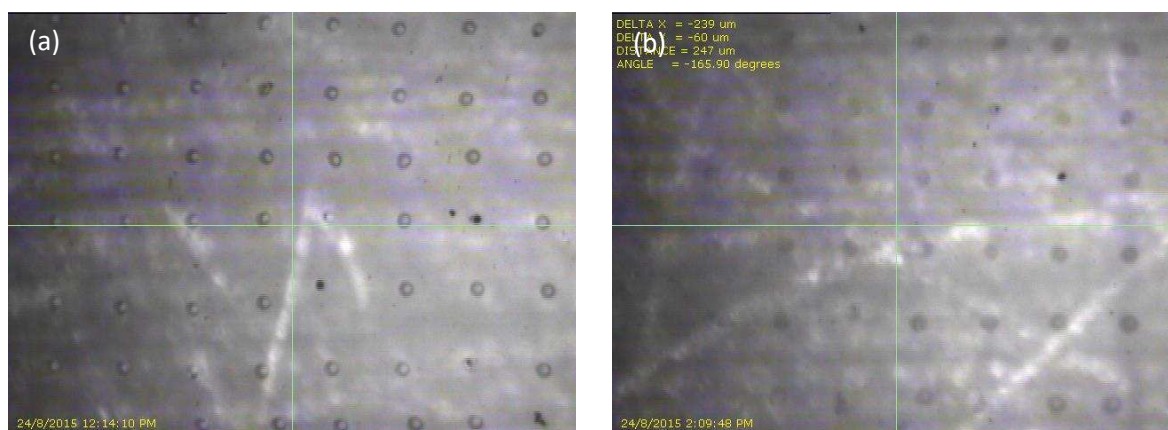


Figure 6.5: Printing of 5 wt% sylgard ink onto a glass substrate with a 200 micron drop spacing (a) before and (b) after 60 °C curing.

The minimum drop spacing required to produce distinct circular droplets was between 50 and 100  $\mu\text{m}$ . Whilst discrete ink droplets were obtained at 100 micron spacing, at 50 and 30  $\mu\text{m}$  drop spacing the droplets combined (figure 6.6). The loss of printing resolution at the smaller drop spacing was attributed to the difference between the surface energy of the ink and glass substrate. An ink with a surface energy lower than the surface energy of the substrate will spread and fully wet the surface forming large droplets. The surface energy of glass has been reported to be in the range 105 – 112  $\text{mN/m}$ .<sup>26</sup> The surface energy of the Sylgard® 184 (95 wt %)-xylene (5 wt %) ink was calculated to be 28.3  $\text{mN/m}$  using the following linear equation:

$$y (\text{surface energy}) = mx + c \quad (\text{Equation 6.3})$$

Where  $x$  is the xylene wt% content in the ink and  $m$  and  $c$  are the slope and intercept of the linear fit in figure 6.1. The values of  $m$  and  $c$  are 0.1142 and 17.4152 respectively. As the surface energy of the ink is much lower than the glass substrate the ink droplets spread and wet the substrate. At the small drop spacing of 50 and 30  $\mu\text{m}$  the ink droplets are close enough to their neighbouring droplets that when they spread they combine with one another resulting in the non-discrete droplets observed in figure 6.6. Increasing both the surface tension and the viscosity of the ink can prevent spreading and wetting leading to a better resolution.

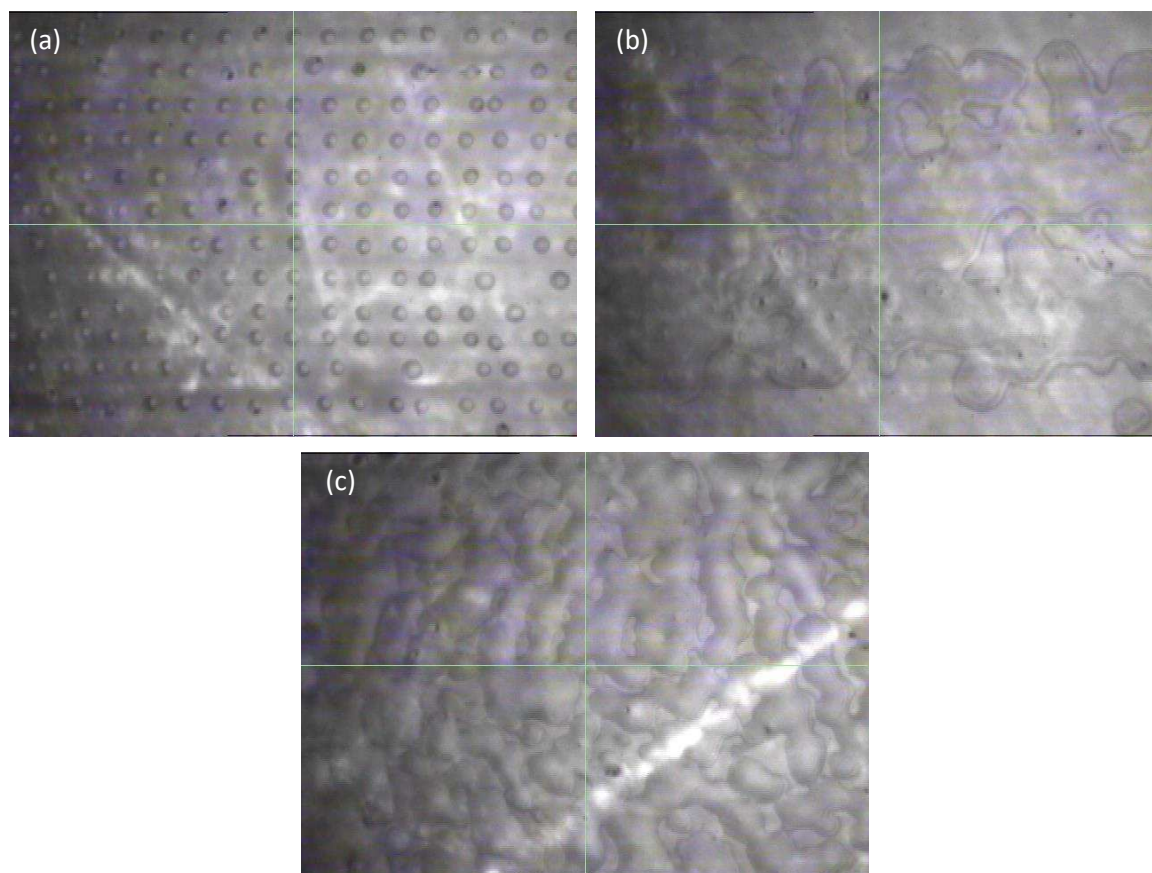


Figure 6.6: Printing of 5 wt% pre-cure Sylgard® 184 ink on glass substrate drop spacing of (a) 100 (b) 50 and (c) 30. Note figure 6.6 (b) was after 60 °C curing using a heating mantle.

Unfortunately due to the low quantity of Sylgard in the droplets, after curing there was only a small amount of PDMS left. Thus to increase PDMS deposition 2 layers of the circular drops were

sequentially printed one on top of the other. It was found that if curing of the first layer had not occurred, the second layer of drops combined with the first layer and spread which resulted in large irregular shaped printed ink droplets (figure 6.7 (a)). To prevent this, curing was performed during the printing process by setting the platen temperature to 60 °C (figure 6.7 (b)). The printing of the two layers was performed consecutively. Comparing figures 6.7 (a) and (b) it was clear that curing the ink during printing resulted in more regular shaped discrete droplets. As the first layer of ink droplets are deposited on a hot substrate, they begin to cure which increases the inks viscosity. This increase in viscosity results in less spreading and prevents splashing when the second layer of ink droplets are deposited. The first layer of semi-cured ink droplets also prevent the second layer of ink droplets from wetting their surface due to their similar surface energy. As with the first layer of ink droplets, the second layer of ink droplets would increase in viscosity as curing occurs on the hot substrate which again results in less ink spreading. Some spreading is still evident (not quite perfect circular droplets observed) which is most likely due to the fact that the first layer of ink is only semi-cured when the second layer of ink was deposited. This could be rectified by placing a pause in printing between the two layers.

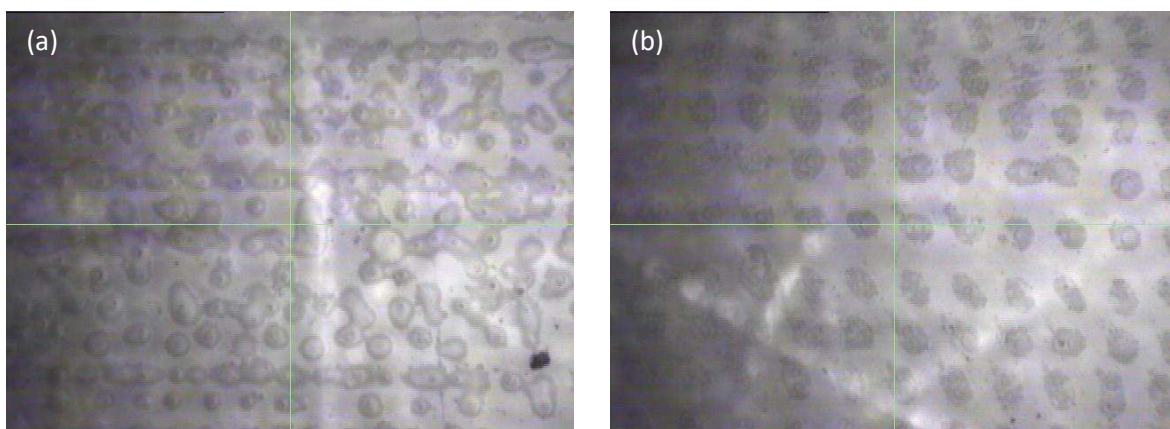
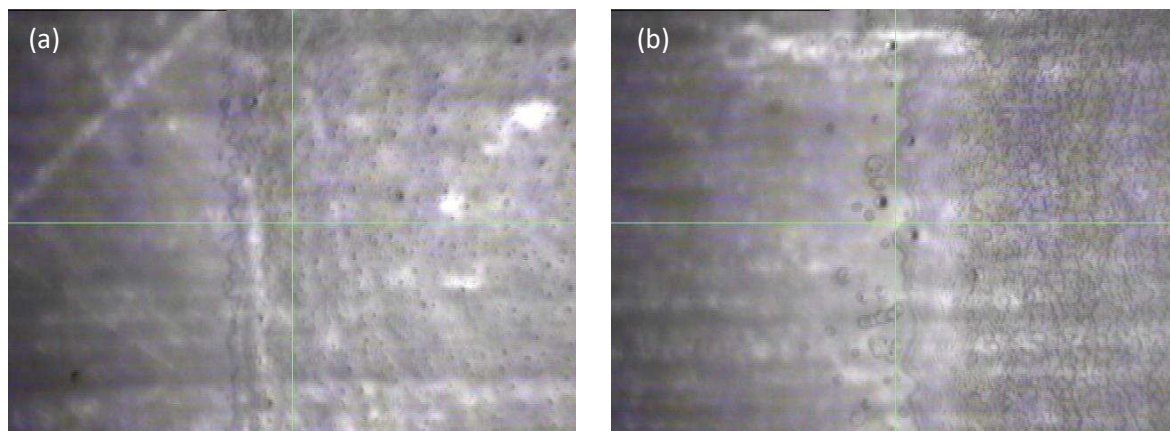


Figure 6.7: Printing of 5 wt % pre-cure Sylgard® 184 ink on glass substrate (a) 2 layers with drop spacing 100 apart and (b) 2 layers with drop spacing 150 apart with platen temperature set at 60 °C.

As well as printing patterns (in this case squares) formed of discrete Sylgard® 184 ink droplets, printing continuous films of Sylgard® 184 was also investigated. To achieve a continuous printed film of Sylgard® 184 a small drop spacing was used to ensure the ink droplets would spread and combine. A 0.5 cm<sup>2</sup> square pattern was printed onto a glass substrate and the previously modified pre-existing waveform for printing xylene was used. Continuous films of varying layers were printed, 5 layers were chosen as the minimum amount of layers and 20 layers as the maximum amount of layers attempted. A minimum of 5 layers of ink droplets was chosen to ensure that there were no gaps where the ink droplets had not been able to combine and spread within the printed film. As previously highlighted heating the substrate via raising the platen temperature to 60 °C caused the ink droplets to cure reducing the spread of the ink. While a reduction in the spread of the ink is not desired when producing a continuous film, it was thought that with the amount of layers being printed the resulting film would not have a defined shape as a result of ink splashing

and large spreading. Therefore, it was decided to have the platen temperature set at 60° C during printing. As shown in figure 6.8, continuous printed films were achieved. However, it was found that the edge of the printed continuous Sylgard® 184 film became less defined with increasing ink layers.



*Figure 6.8: Printing of 5 wt% pre-cure Sylgard® 184 ink on glass substrate with a drop space of 40 microns with platen temperature set at 60 °C (a) 5 layers using 1 nozzle and (b) 20 layers using 4 nozzles. Note that these are images of the edge of the printed continuous Sylgard® 184 film, the left hand side in both images (smoother side) is the glass substrate, while the right hand side in both images is of the Sylgard® 184 film.*

From the images in figure 6.8, it was observed that the surface of the printed Sylgard® 184 films appeared rough (bubbled). The rough appearance was attributed to the large amount of xylene evaporating off during the curing of the Sylgard® 184. The curing of the Sylgard® 184 most likely occurred too quickly preventing the even evaporation of the xylene. The thickness of the printed continuous films were not investigated. As the cured Sylgard® 184 is transparent the printed continuous films on glass were difficult to visualise using the naked eye. Continuous Sylgard® 184 films made up of 20 layers using the same printing procedure as above were also printed onto PEL Nano P60 paper. However, due to the morphology of the PEL paper and the transparent nature of Sylgard® 184 the printed films could not be observed via the naked eye or under the microscope and therefore were not further analysed.

### 6.3 Conclusions

Sylgard® 184 based inks were successfully formulated and preliminary experiments showed that the ink formulation – pre-cure Sylgard® 184 (5 wt %)-xylene (95 wt %) could be successfully printed onto glass with no evidence of satellite droplets. It was found that the minimum drop spacing to produce discrete printed droplets was between 50 and 100 microns. At 50 microns combined droplets were observed and at 100 microns discrete droplets were observed. Curing of the Sylgard® 184 via heating had no effect on the shape of the printed droplet. However, due to the low wt % of Sylgard® 184 in the ink formulation only a small amount of printed Sylgard® 184 was left on the glass substrate after curing. Increasing the amount of printed Sylgard® 184 could be achieved by printing 2 layers of droplets (droplets printed one on top of the other), however, it was found that to produce regular shaped discrete droplets from printing 2 layers, curing of the Sylgard® 184 had

to be performed during the printing process. Curing of the Sylgard® 184 during the printing process decreased both droplet spreading and subsequent splashing caused by the second layer of ink droplets hitting and combining with the first layer. Printed continuous 0.5 cm<sup>2</sup> Sylgard® 184 films made up of several printed layers (minimum 5 layers, maximum 20 layers) on glass were also achieved. Further work into improving the Sylgard ink formulation to increase the Sylgard wt% content while maintaining the desired surface tension is required. The viscoelastic effect on ink drop formation would also have to be considered. Further optimisation of the printer settings would also have to be performed before ink-jet printing of Sylgard® 184 could be used in additive manufacturing.

## 6.4 References

- 1 G. Orecchini, F. Alimenti, V. Palazzari, A. Rida, M. M. Tentzeris and L. Roselli, *IET Microwaves, Antennas & Propag.*, 2011, **5**, 993-1001.
- 2 H. Tan, T. Tran and C. Chua, *Virtual Phys. Prototyp.*, 2016, **11**, 1-18.
- 3 Y. Amin, S. Prokkola, B. Shao, J. Hallstedt, H. Tenhunen and L. Zheng, in *11<sup>th</sup> Conference on Advanced Communication Technology Proceedings*, IEEE, 2009, pp. 109-112.
- 4 A. Rida, L. Yang, R. Vyas and M. M. Tentzeris, *IEEE Antennas Propag. Mag.*, 2009, **51**, 13-23.
- 5 V. Sanchez-Romaguera, M. A. Ziai, D. Oyeka, S. Barbosa, J. S. Wheeler, J. C. Batchelor, E. A. Parker and S. G. Yeates, *J. Mater. Chem. C*, 2013, **1**, 6395-6402.
- 6 J. Virtanen, T. Bjorninen, L. Ukkonen and L. Sydanheimo, *IEEE Antennas Wireless Propag. Lett.*, 2010, **9**, 440-443.
- 7 J. Virtanen, L. Ukkonen, T. Bjorninen, A. Z. Elsherbeni and L. Sydänheimo, *IEEE Trans. Instrum. Meas.*, 2011, **60**, 2768-2777.
- 8 V. Subramanian, J. M. Fréchet, P. C. Chang, D. C. Huang, J. B. Lee, S. E. Molesa, A. R. Murphy, D. R. Redinger and S. K. Volkman, *Proc. IEEE*, 2005, **93**, 1330-1338.
- 9 V. Rajendra, C. Sicard, J. D. Brennan and M. A. Brook, *Analyst*, 2014, **139**, 6361-6365.
- 10 A. Määttänen, D. Fors, S. Wang, D. Valtakari, P. Ihalainen and J. Peltonen, *Sensors Actuat. B-Chem.*, 2011, **160**, 1404-1412.
- 11 H. P. Le, *J. Imaging Sci. Technol.*, 1998, **42**, 49-62.

- 12 J. Li, F. Rossignol and J. Macdonald, *Lab on a Chip*, 2015, **15**, 2538-2558.
- 13 O. D. Jayakumar and A. K. Tyagi, in *Functional materials: preparation, processing and applications*, ed. S. Banerjee and A. Tyagi, Elsevier, London, 2011, pp. 193-223.
- 14 I. FUJIFILM Dimatix, *Dimatix Materials Printer DMP-2800 Series User Manual*.
- 15 D. Ahn and A. Dhinojwala, in *Silicon Surface Science*, ed. M. J. Owen and P. R. Dvornic, Springer Science + Business Media, Dordrecht, 2012, pp. 23-54.
- 16 D. Cibis and K. Krüger, in IMAPS/ACerS 4th International Conference and Exhibition on *Ceramic Interconnect and Ceramic Microsystems Technologies Proceedings*, 2008, pp. 000417-000423.
- 17 P. Wang, *Master's Thesis*, University of Kentucky, 2014.
- 18 I. M. Hutchings, G. D. Martin and S. D. Hoath, in *Fundamentals of Inkjet Printing*, ed. S. D. Hoath, Wiley-VCH, Weinheim, pp. 1-12.
- 19 B. Derby, *Annu. Rev. Mater. Res.*, 2010, **40**, 395-414.
- 20 G. D. Martin and I. M. Hutchings, in *Inkjet Technology for Digital Fabrication*, ed. I. M. Hutchings and G. D. Martin, John Wiley & Sons Ltd., Chichester, 2013, pp. 21-42.
- 21 A. Kamyshny and S. Magdassi, in *Inkjet-based Micromanufacturing*, ed. J. G. Korvink, P. J. Smith and D. H. Shin, Wiley-VCH, Weinheim, 2012, pp. 173-187.
- 22 J. Lucius, G. Olheoft, P. Hill and S. Duke, *Properties and hazards of 108 selected substances*, U.S. Dept. of the Interior Geological Survey, 1990, Open-File Report 90-408.
- 23 J. J. Jasper, *J. Phys. Chem. Ref. Data*, 1972, **1**, 841-1010.
- 24 H. Huang, *NAW*, 2005, **5**, 63-68.
- 25 B. de Gans, P. C. Duineveld and U. S. Schubert, *Adv. Mater.*, 2004, **16**, 203-213.
- 26 F. Hejda, P. Solar and J. Kousal, in *WDS'10 Proceedings of Contributed Papers*, 2010, pp. 25-30.

# Chapter 7: Fabrication of silver salt-PVA composites as light sensitive components of a UHF-RFID light sensor

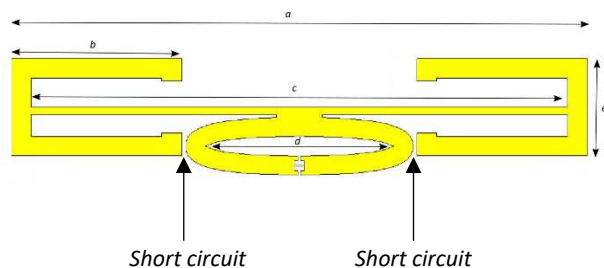
## 7.0 Introduction

Light sensors have many applications including security, indoor light intensity control and environmental monitoring. Passive RFID light sensors could provide cheaper, lighter and disposable alternatives to traditional light sensors. Amin *et al.* presented a RFID light sensor design where an off the shelf photoresistor was integrated into a multiresonator chipless RFID tag.<sup>1</sup> With light exposure, the change in resistance of the photoresistor should result in the attached resonator frequency to change. This frequency change would cause a change in the tag read range or power input which could be used to measure light intensity. Preliminary experiments showed that a frequency shift was observed for the photoresistor integrated resonator, while the frequency of the other resonators responsible for carrying the tag ID information remained unchanged as a function of light intensity. Cho *et al.* integrated a light sensor into an RFID IC chip to allow for RFID light monitoring.<sup>2</sup> While Smith *et al.* demonstrated a wireless identification and sensing platform (WISP) with the capabilities of sensing light intensity. A WISP is similar to an RFID tag as it is powered by radio frequency energy and has an antenna, however, instead of an IC chip a printed circuit board (PCB) is used instead. The authors used a similar concept to Cho *et al.* and mounted a light sensor onto the PCB.<sup>3</sup>

The aim of this chapter was to produce a photosensitive material that becomes highly conductive as a result of light exposure to act as a short circuit within the antenna of the prototype RFID light sensor tag shown in Figure 7.0. If a short circuit is formed within the antenna, an overall change in antenna impedance occurs which would cause mismatching between the chip and antenna resulting in a decreased read range. The decreased read range could then be used to monitor the amount of light exposure experienced by the RFID light sensor tag. Full antenna tag dimensions are given in Table 7.0, and the places where a short circuit would need to be achieved are labelled in Figure 7.0.



Table 7.0 : RFID antenna dimensions.



| Symbol   | Length (mm) |
|----------|-------------|
| <i>a</i> | 88.00       |
| <i>b</i> | 26.00       |
| <i>c</i> | 82.00       |
| <i>d</i> | 15.00       |
| <i>e</i> | 28.75       |

Figure 7.0: Prototype RFID light sensor tag design. Tag designed by M.A. Ziai.

Silver metal has one of the highest electrical conductivities ( $6.30 \times 10^7$  S/m) and can be formed through the photoreduction of silver salts. Previous research has shown that polymers are good matrices for the fabrication of silver nanoparticles through the reduction of silver nitrate, as the polymer can act as a surface capping agent thus controlling particle size and/or a co-reducing or reducing agent.<sup>4-6</sup> A polymer matrix also offers simplicity in processing, as it is easier to cast a silver salt/polymer composite film than directly depositing silver salts onto the prototype RFID light sensor. The polymer polyvinyl alcohol (PVA) has previously been used successfully as a matrix in the fabrication of silver nanoparticles from the reduction of silver nitrate.<sup>7-9</sup> It was shown that PVA can act both as a mild reducing agent and size reducing agent. Other advantages of PVA is its water solubility, non-toxic nature and easy film formation – no cross-linking is required as PVA films can be formed simply through drying an aqueous solution of PVA out. Silver halides, such as silver chloride and silver bromide are extremely light sensitive, however, neither are very water soluble therefore silver nitrate was chosen. Silver nitrate itself is not photosensitive, however, silver nitrate has been shown to reduce to metallic silver within polymer matrices via photochemical processes.<sup>10,11</sup>

In this chapter 40 wt%, 60 wt% and acidified 60 wt%  $\text{AgNO}_3$ -PVA films were fabricated and investigated as possible candidates for the photosensitive material required for the RFID light sensor. Formation of silver particles via light exposure was first investigated in 40 wt%, 60 wt% and acidified 60 wt%  $\text{AgNO}_3$ -PVA solutions. UV-visible spectroscopy, DLS and SEM imaging were used to detect the presence, size and shape of the formed silver particles. The formation of silver particles were then investigated in both light irradiated and non-irradiated  $\text{AgNO}_3$ -PVA films using FT-IR analysis and SEM imaging. Resistance measurements were performed on the films to investigate the relationship between the formation of silver particles via light exposure and the electrical resistance of the composite film to see if the films could be used as short circuits in the RFID tag design. The silver nitrate reduction mechanisms along with the  $\text{AgNO}_3$ -PVA film conductive mechanism was also discussed.

## 7.1 Experimental

### 7.1.1 Materials and Apparatus

PVA (M. W. 85,000 – 146,000, degree of polyvinyl acetate hydrolysis at 98-99%) (Sigma Aldrich), silver nitrate (>99.0 %), nitric acid (70 %, Fisher Chemicals), distilled water, copper cladded FR4 (fibreglass reinforced epoxy laminate) circuit board, PEL Nano 60 (Printed Electronics) and silver conductive paint (Electrolube) were used as received.

### 7.1.2 Synthesis of light sensitive PVA materials

#### 7.1.2.1 AgNO<sub>3</sub>-PVA solutions

AgNO<sub>3</sub>-PVA solutions were prepared by first dissolving 1.50 g PVA into 28.50 g of distilled water at 80 °C. The resulting 5 wt % PVA solution was cooled to room temperature before silver nitrate was added to ensure 40 wt % (1.00 g AgNO<sub>3</sub>) and 60 wt % (2.25 g AgNO<sub>3</sub>) of the AgNO<sub>3</sub>-PVA content (the water in the solution was disregarded in the calculations). The AgNO<sub>3</sub>-PVA solutions were stirred in darkness for half an hour to ensure complete dissolution of the AgNO<sub>3</sub> had occurred. The solutions were then degassed for half an hour and stored in air-tight conical flasks which were kept in the dark at room temperature and pressure until the solutions were required. The solutions were stored in the dark to prevent premature photoreduction of the silver nitrate. An acidified 60 wt% AgNO<sub>3</sub>-PVA solution was also prepared following the same method above except that prior to the addition of AgNO<sub>3</sub>, the 5 % PVA solution was acidified with 1 M HNO<sub>3</sub> solution to pH 4.

#### 7.1.2.2 AgNO<sub>3</sub>-PVA composite films

40 wt %, 60 wt % and acidified 60 wt % AgNO<sub>3</sub>-PVA composite films were prepared by pouring the respective pre-made solutions into PTFE square moulds (mould width = 2 cm, length = 2 cm and height = 0.2 cm) ensuring the solutions were flush with the top of the mould. This ensured films of similar heights were produced after water evaporation had occurred. The filled moulds were kept in the dark at room temperature and pressure to allow the solutions to dry out resulting in the formation of the AgNO<sub>3</sub>-PVA composite films. The films were dried in the dark to prevent premature photoreduction of the silver nitrate. The structure of the composite films were confirmed by FTIR spectrum.

*FTIR (cm<sup>-1</sup>) 40 wt% AgNO<sub>3</sub>-PVA film:* 3279 (hydrogen bonded O – H str); 2943, 2908 (C – H broad alkyl str); 1715, 1647 (carbonyl group) 1522 (NO<sub>2</sub> sym str); 1398 (O – H vibration); 1304 (coupling of O – H vibration with C – H wag vibration); 1142 (C – O stre); 1086, 1038 (C – O stre and O – H bend); 854, 816 (C - H out of plane vibration); 671 (absorption band associated with AgNO<sub>3</sub>); 916 (not identified).

*FTIR (cm<sup>-1</sup>) 60 wt% AgNO<sub>3</sub>-PVA film:* 3296 (hydrogen bonded O – H stre); 2943, 2911 (C – H broad alkyl stre); 1636 (carbonyl group); 1377 (O – H vibrations); 1292 (coupling of O – H vibrations with

C – H wag vibrations); 1144 (C – O stre); 1082, 1036 (C – O stre and O – H bend); 845, 814 (C – H out of plane vibration); 914 (not identified).

*FTIR ( $\text{cm}^{-1}$ ) acidified 60 wt%  $\text{AgNO}_3$ -PVA film:* 3304 (hydrogen bonded O – H stre); 2945, 2913 (C – H broad alkyl stre); 1638 (carbonyl group); 1377 (O – H vibrations); 1287 (coupling of O – H vibrations with C – H wag vibrations); 1142 (C – O stre vibration); 1082, 1036 (C – O stre and O – H bend); 847, 812 (C – H out of plane vibration); 912 (not identified).

### 7.1.3 Measurements and Instruments

The following instruments were used to characterise the  $\text{AgNO}_3$ -PVA solutions,  $\text{AgNO}_3$ -PVA films and acidified  $\text{AgNO}_3$ -PVA films before, during and after light exposure. In all measurements non-irradiated samples (films and solutions that had been kept in the dark) were also characterised. The  $\text{AgNO}_3$ -PVA solutions were kept in glass vials with lids on during light exposure. To expose the film and solution samples to light they were placed in a blacked out fume cupboard under an LED aqua light (7W, Eheim) at a distance of around 30.5 cm. Absorption spectra of the  $\text{AgNO}_3$ -PVA solutions were measured in the wavelength range of 190 – 600 nm using a Shimadzu UV1800 UV-Vis spectrophotometer. DLS analysis of the  $\text{AgNO}_3$ -PVA solutions was performed in a Malvern high performance particle sizer (Nano Zetasizer HPPS HPP5001) with a laser operating at a wavelength of 633 nm. BSE SEM (back-scattered electrons scanning electron microscope) images of both the  $\text{AgNO}_3$ -PVA films and solutions were performed using a SEM (Hitachi SE-3400)/EDX (Oxford instruments X-Max 80) integrated system. FTIR measurements were completed using a Shimadzu IRAffinity-1 spectrometer with a Specac Golden Gate™ ATR sampling accessory where each film sample was scanned 64 times at room temperature and atmospheric pressure with a resolution of  $4 \text{ cm}^{-1}$ . Resistance measurements were performed on the  $\text{AgNO}_3$ -PVA films with a probe point to point distance of approximately 2 cm using a resistance meter (ISO-TECH, IDM 201). The film resistance measurements were performed at varying internals during light exposure and three samples of each different film; 40 wt%  $\text{AgNO}_3$ -PVA, 60 wt%  $\text{AgNO}_3$ -PVA and acidified 60 wt%  $\text{AgNO}_3$ -PVA were measured and the average resistance was calculated.

## 7.2 Results and Discussion

### 7.2.1 Nature of formation of silver nanoparticles in solution

UV-visible spectroscopy, DLS and SEM micrographs was used to investigate the presence, growth and size of any silver nanoparticles formed in the light exposed  $\text{AgNO}_3$ -PVA solutions. For reproducibility and control of the light intensity, a LED aqua light (7W, Eheim) was used rather than daylight to photo reduce the  $\text{AgNO}_3$  in the  $\text{AgNO}_3$ -PVA solutions. UV-visible spectroscopy of the solutions was performed over a period of 142 hours light exposure. The non-irradiated 40 wt%, 60 wt% and acidified 60 wt%  $\text{AgNO}_3$ -PVA solutions were also measured. The solutions were not filtered or diluted before performing the UV-visible measurements. Figure 7.1 shows the UV-visible

absorption spectra for the solutions exposed to light and the non-irradiated solutions. The characteristic PVA bands at 200 – 250 nm and 300 nm attributed to the carbonyl groups<sup>12</sup> were observed for all solutions. In all cases apart from the non-irradiated 60 wt% AgNO<sub>3</sub>-PVA solution the intensity of the band at around 250 nm remained unchanged. In the spectrum of the non-irradiated 60 wt% AgNO<sub>3</sub>-PVA solution it was observed that after 124 hours darkness the intensity of the carbonyl band at 200 – 250 nm decreased and by 142 hours darkness the band had shifted to lower wavelengths. However, the carbonyl band at around 300 nm in the 40 wt% AgNO<sub>3</sub>-PVA solutions increased in intensity as a function of light exposure. All of the light irradiated solutions exhibited an absorption band around 450 nm which was attributed to silver nanoparticles.<sup>13,14</sup> The intensity of this absorption band was shown to increase as a function of light exposure time, which confirmed the reduction of silver nitrate had occurred resulting in the formation of silver particles.

The formation of silver particles as a result of light exposure was also visually confirmed (Figure 7.2). The light irradiation AgNO<sub>3</sub>-PVA solutions turned a dark grey colour which is indicative of a high silver concentration.<sup>15</sup> It is known that photoreduction of silver nitrate alone does not occur as the nitrate ions cannot be oxidised by light. However, research has shown that silver nitrate within a polymer matrix can be reduced via photochemical processes. Kutsenko and Granchak suggested that silver nitrate is reduced within the PVA matrix by the α-hydroxyl radicals –CH<sub>2</sub>-ĊOH-CH<sub>2</sub> and R<sup>1</sup>R<sup>2</sup>ĊOH which are formed through photolysis of PVA.<sup>10</sup> Photolysis of water can also occur producing a hydrogen radical which has been argued to be able to reduce silver ions to metallic silver via the following reaction:



Therefore, the reduction of the silver nitrate in the light irradiated AgNO<sub>3</sub>-PVA solutions was most likely caused by a combination of both hydroxyl radicals and hydrogen radicals produced through the photolysis of PVA and water, respectively.

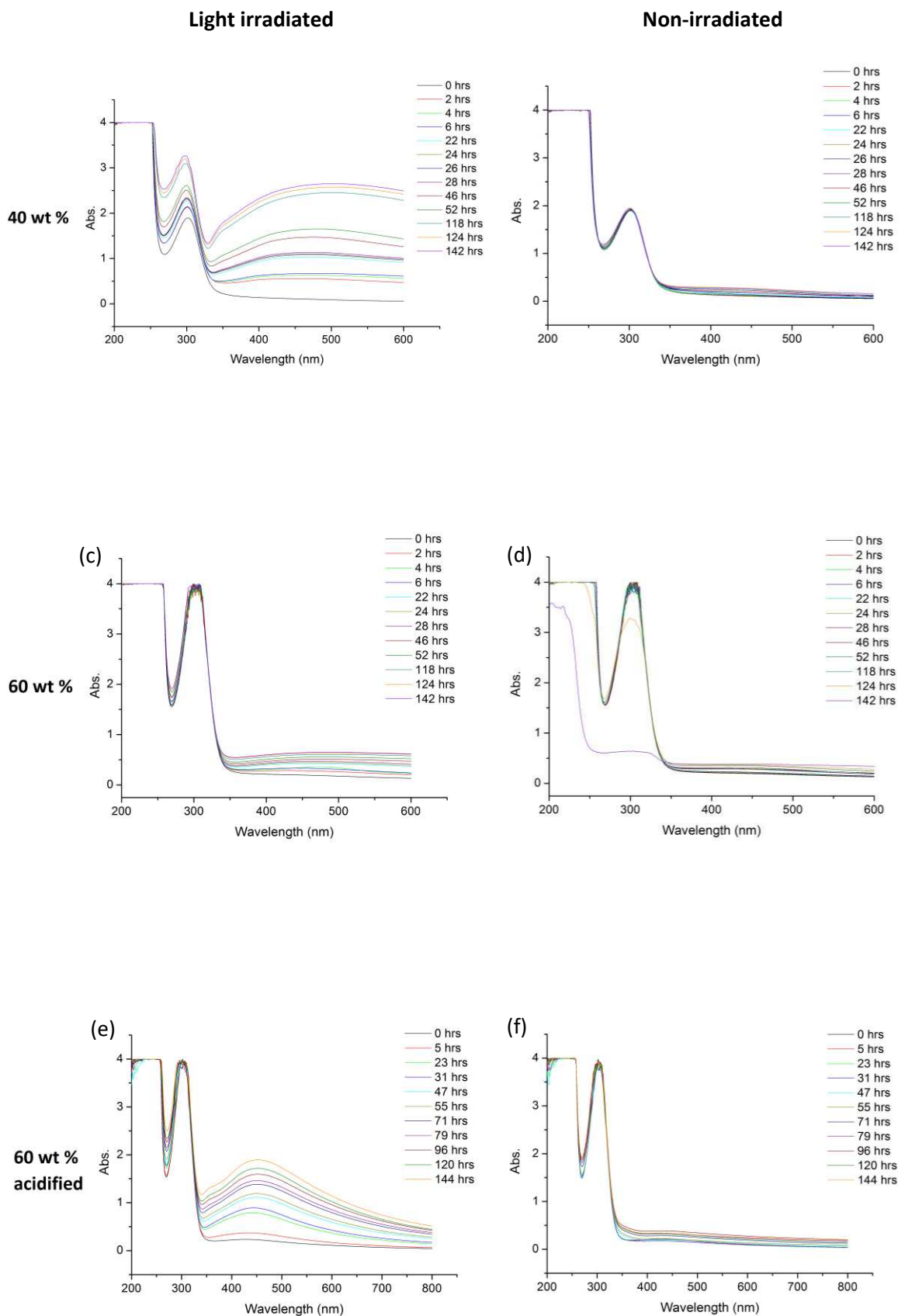


Figure 7.1: UV-Visible spectra of (a) light irradiated 40 wt%  $\text{AgNO}_3$ -PVA solution (b) non-irradiated 40 wt%  $\text{AgNO}_3$ -PVA solution (c) light irradiated 60 wt%  $\text{AgNO}_3$ -PVA solution (d) non-irradiated 60 wt%  $\text{AgNO}_3$ -PVA solution (e) light irradiated acidified 60 wt%  $\text{AgNO}_3$ -PVA and (f) non-irradiated acidified 60 wt%  $\text{AgNO}_3$ -PVA solution over time.

It was observed that the magnitude of the characteristic metallic silver band in the 60 wt% AgNO<sub>3</sub>-PVA solution was low compared to both 40 wt% and acidified 60 wt% AgNO<sub>3</sub>-PVA solutions. The low magnitude of the peak at 450 nm exhibited by the 60 wt% AgNO<sub>3</sub>-PVA solution could be due to agglomeration of the silver nanoparticles. In a UV-visible spectrum agglomeration of particles is often characterised by the broadening and intensity decrease of the absorption band. Particle agglomeration and precipitation of the 60 wt% AgNO<sub>3</sub>-PVA solution was also visually confirmed in Figure 7.2 (b). It has been shown that at high silver nitrate concentrations it is easy for the formed silver nanoparticles to aggregate.<sup>15</sup> However, PVA has shown to prevent agglomeration of silver particles<sup>16</sup> the high silver nitrate concentration used (60 wt%) has counteracted the effects of the PVA. However, the acidified 60 wt% AgNO<sub>3</sub>-PVA solution showed no signs of particle agglomeration or precipitation (Figures 7.1 (e) and 7.2, respectively) even with its high silver nitrate concentration. This observation suggested that the nitric acid used to acidify the solution acts as a particle stabiliser. Previous research has shown that in acidic conditions silver particles are less likely to agglomerate,<sup>17</sup> however, it was highlighted that at very low pH's silver particles dissolve in nitric acid forming silver nitrate.<sup>18</sup>

The absorption band attributed to silver nanoparticles was also seen to shift towards the red wavelengths as a function of time (Figure 7.1 (a),(c) and (e)) which is indicative of an increase in the size of the silver nanoparticles formed.<sup>14</sup> As shown in Figure 7.3, the lambda ( $\lambda$ ) max of the absorption band attributed to the silver nanoparticles was larger for the 40 wt% AgNO<sub>3</sub>-PVA solution when compared to the acidified 60 wt% AgNO<sub>3</sub>-PVA solution after light exposure, suggesting the photo reduced acidified 60 wt% AgNO<sub>3</sub>-PVA solution produced smaller sized silver nanoparticles.

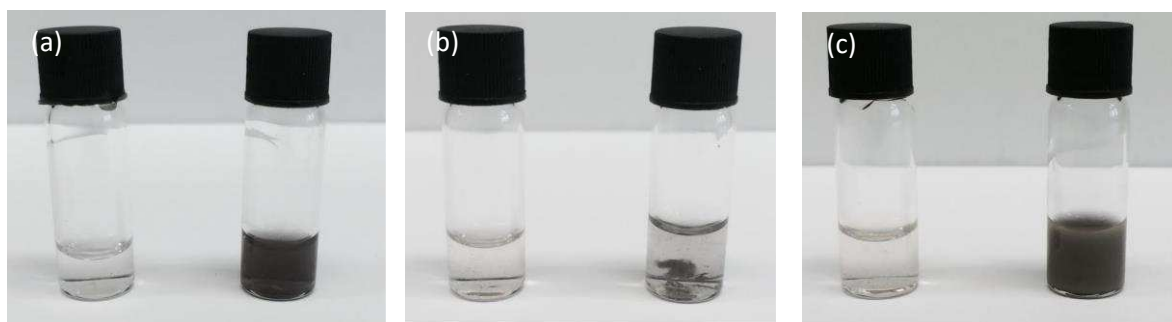


Figure 7.2: Images of (a) 40 wt% AgNO<sub>3</sub>-PVA solutions (b) 60 wt% AgNO<sub>3</sub>-PVA solutions after 142 hours and (c) acidified 60 wt% AgNO<sub>3</sub>-PVA solutions after 144 hours. In each image the solution on the left was non-irradiated and the solution on the right was light treated.

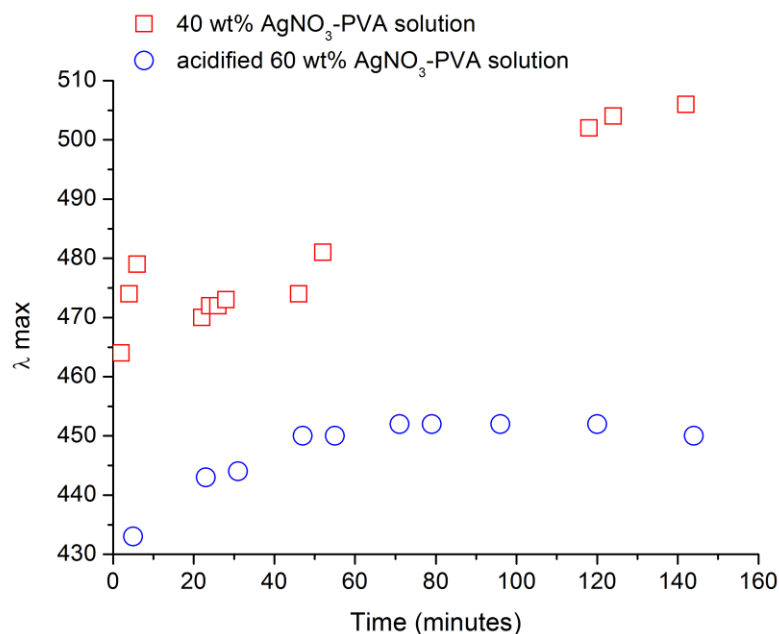


Figure 7.3: Plot of lambda max of 40 wt% and acidified 60 wt% AgNO<sub>3</sub>-PVA solutions versus light exposure time.

DLS measurements were used to confirm the size and particle size dispersity of the formed silver nanoparticles in all three photo-reduced solutions. Both the 40 wt %, 60 wt% AgNO<sub>3</sub>-PVA solutions were exposed to light for a total of 142 hours, while the acidified 60 wt% AgNO<sub>3</sub>-PVA solution was exposed to light for a total of 144 hours. Each solution was measured a total of ten times at 25 °C and was not filtered or diluted beforehand. Table 7.2 showed that the acidified 60 wt% AgNO<sub>3</sub>-PVA solution had the lowest calculated mean polydispersity index (PDI) when compared to the other two solutions.

Table 7.2: DLS results for 40 wt%, 60 wt% and acidified 60 wt% AgNO<sub>3</sub>-PVA solutions exposed to light for 142, 142 and 144 hours respectively.

| Light irradiated AgNO <sub>3</sub> -PVA solutions | Average PDI     | Mean Z-average (nm) | Mean number average (nm) | CONTIN analysis (nm)                     |
|---|-----------------|---------------------|--------------------------|--|
| 40 wt%  | 0.2907 ± 0.0154 | 7308 ± 173          | 1677 ± 372               | 2386 ± 224<br>325 ± 109<br>18.7 ± 0      |
| 60 wt%  | 0.4133 ± 0.0296 | 8903 ± 200          | 14 ± 2                   | 1137 ± 63<br>359 ± 81<br>19 ± 1<br>5 ± 2 |
| Acidified 60 wt%                                  | 0.1992 ± 0.0122 | 5540 ± 77           | 3833 ± 393               | 4924 ± 190<br>2525 ± 382                 |

PDI values range from 0 to 1; where 0 represents monodisperse samples and 1 represents highly polydispersed samples. Therefore, the silver particles formed from the acidified solution were less polydispersed and more discrete than the silver particles formed from the 40 wt% and 60 wt% AgNO<sub>3</sub>-PVA solutions. These results confirm the observations made from the UV-visible spectra. Silver particle sizes for the 40 wt% and 60 wt% AgNO<sub>3</sub>-PVA solutions could not be determined accurately using DLS. In the case of the 40 wt% AgNO<sub>3</sub>-PVA solution the count rate and size increased over the ten measurements indicating the silver particles were aggregating. In the case of the 60 wt% AgNO<sub>3</sub>-PVA solution the count rate and size decreased over the ten measurements indicating evidence of sedimentation which was visually confirmed (Figure 7.2 (b)). Sedimentation leads to inaccurate particle size distributions as the large settled particles are not measured.

The mean number particle distribution of the light irradiated acidified 60 wt% AgNO<sub>3</sub>-PVA solution was shown in Figure 7.4. The error bars displayed on the DLS distribution histogram were the standard error (standard deviation of the mean) calculated from all ten measurements. According to the DLS measurements the mean Z-average of the silver particles formed from the light irradiated acidified 60 wt% AgNO<sub>3</sub>-PVA solution was 5540 ± 77 nm. The mean number average was also calculated to ensure direct particle size comparisons could be performed between DLS measurements and measurements from SEM micrographs. The mean number average dimension of the silver particles was 3833 ± 393 nm, which was slightly lower than the calculated mean Z-average value.

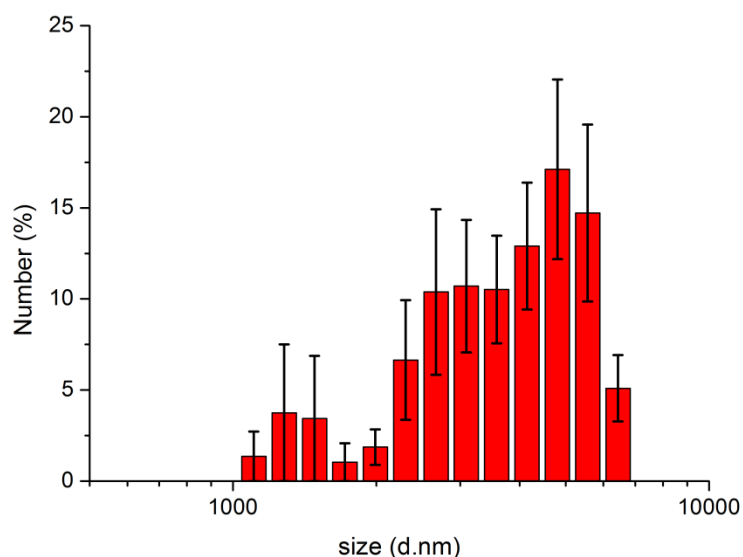


Figure 7.4: Mean number particle distribution from DLS measurements of light irradiated (144 hours) acidified 60 wt% AgNO<sub>3</sub>-PVA solution.

The Z-average ( $D_z$ ) value is an intensity weighted average, which can be defined as:

$$D_z = \frac{\sum N_i D_i^6}{\sum N_i D_i^5} \quad (\text{Equation 7.1})$$



where  $N_i$  is the number of molecules with diameter size  $D_i$ . As shown from the equation, the Z-average is dominated by the presence of large particles compared to the number mean which counts on the contribution of the number of particles at all diameter sizes. The number average ( $D_n$ ) can be defined as:

$$D_n = \frac{\sum N_i D_i}{\sum N_i} \quad (\text{Equation 7.2})$$

CONTIN analysis of the DLS measurements of the light irradiated acidified 60 wt%  $\text{AgNO}_3$ -PVA solutions showed there were two different size populations present in the sample. One size population was  $4924 \pm 190$  nm whereas the other was  $2525 \pm 382$  nm.

Images of the light irradiated  $\text{AgNO}_3$ -PVA solutions were taken using SEM to investigate the morphology and size of the formed silver particles. To prepare the solutions for SEM, they were cast onto carbon sticky tabs and left to dry in complete darkness overnight. As expected the light irradiated 40 wt%, 60 wt% and acidified 60 wt%  $\text{AgNO}_3$ -PVA solutions confirmed the presence of irregular shaped silver particles. Agglomeration was observed in the Figure 7.5 which corroborated the observed broadening of the silver plasmon peak at around  $450 \text{ cm}^{-1}$  with increasing light exposure time.

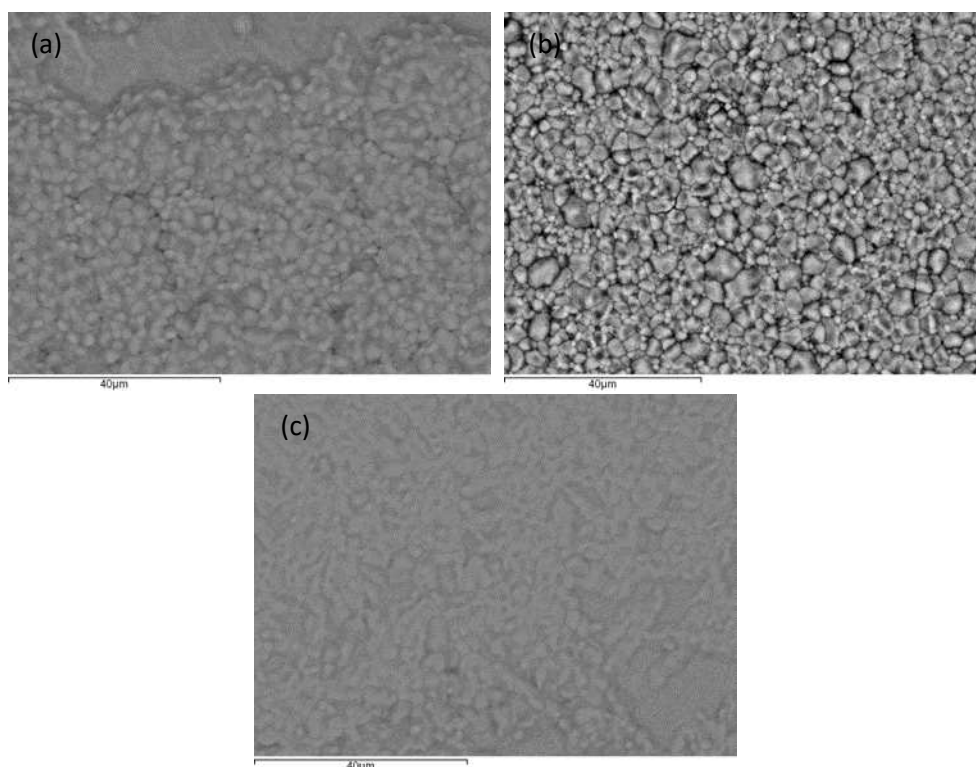


Figure 7.5: SEM micrographs of (a) 40 wt%  $\text{AgNO}_3$ -PVA solution (b) 60 wt%  $\text{AgNO}_3$  solution after 142 hours light irradiation and (c) acidified 60 wt%  $\text{AgNO}_3$ -PVA solution after 144 hours light irradiation.

Size measurements of the silver particles were attempted and performed using ImageJ software. Particles in a  $40 \mu\text{m}^2$  area were measured with any particles on the edge being eliminated from the measurements. As the particles were not perfectly spherical, the largest diameter of each particle was recorded. The particles formed in the 40 wt% and 60 wt%  $\text{AgNO}_3$ -PVA solutions had a mean

diameter of 2830 and 3250 nm, respectively after 142 hours light exposure. Size measurements could not be performed for the acidified 60 wt% AgNO<sub>3</sub>-PVA solution due to poor resolution of the SEM micrograph. The size measurements are only a rough indication of size as agglomeration of the particles introduced difficulties in measuring and as the particles were not perfectly spherical and appear to be present in layers (a possible result from the casting method) the largest diameter of each particle may not appear at the top surface.

The absorption spectra of the non-irradiated 40 wt%, 60 wt% and acidified 60 wt% AgNO<sub>3</sub>-PVA solutions (Figures 7.1 (b), (d) and (f)) did not show a definite band at around 450 nm as shown by the light irradiated solutions indicating no silver particles were formed. However, it was observed that the intensity in that area did slightly increase with time which could indicate a minimal amount of silver particles were formed. The non-irradiated solutions remained colourless which confirmed that little to no silver particles were formed. Previous research has shown that silver nitrate reduction can occur within PVA in darkness at room temperature, but this is a slow process.<sup>8</sup>

It has been shown that silver particle formation can be achieved through the light irradiation of AgNO<sub>3</sub>-PVA solutions. The reduction of the silver nitrate within the PVA solutions occurred via hydroxyl radicals and hydrogen radicals formed through the photolysis of PVA and water, respectively. Particle agglomeration combined with large particle sizes were observed for both the light irradiated 40 wt% and 60 wt% AgNO<sub>3</sub>-PVA solutions. However, the particles in the 40 wt% solution did remain dispersed as shown by both UV-visible spectroscopy and DLS. On the other hand the acidified 60 wt% AgNO<sub>3</sub>-PVA solution formed the most discrete particles sized at 5540 ± 77 nm (Z-average). The addition of acid was shown to act as a particle stabiliser which prevented agglomeration and large particles. The non-irradiated AgNO<sub>3</sub>-PVA solutions were shown to produce little to no silver particles.

### 7.2.2 Nature of formation of silver nanoparticles in films

FT-IR spectroscopy and SEM micrographs were used to characterise the structure of the AgNO<sub>3</sub>-PVA composite films and investigate formation of silver nanoparticles via light exposure. FT-IR measurements of the AgNO<sub>3</sub>-PVA films were performed at varying intervals during light and dark exposure, whereas the SEM micrographs were performed before and after light and dark exposure. FT-IR measurements were also performed on non-irradiated AgNO<sub>3</sub>-PVA composite films and neat standard PVA films. Figures 7.6, 7.8 and 7.10 showed the FT-IR spectra of 40 wt%, 60 wt% and acidified 60 wt% AgNO<sub>3</sub>-PVA films irradiated for varying lengths of time, respectively, along with the FT-IR spectrum of neat standard PVA.

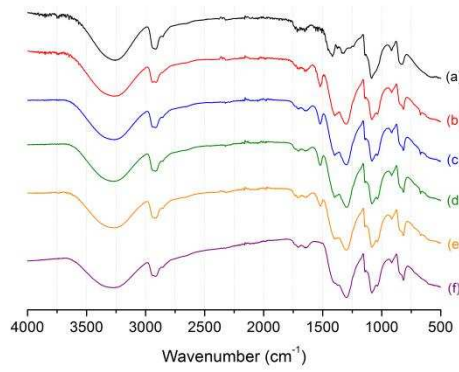


Figure 7.6: FTIR of (a) standard PVA and light irradiated 40 wt % AgNO<sub>3</sub>-PVA composites after (b) 0 hrs (c) 24 hrs (d) 48 hrs (e) 142 hrs and (f) 700.5 hrs light irradiation.

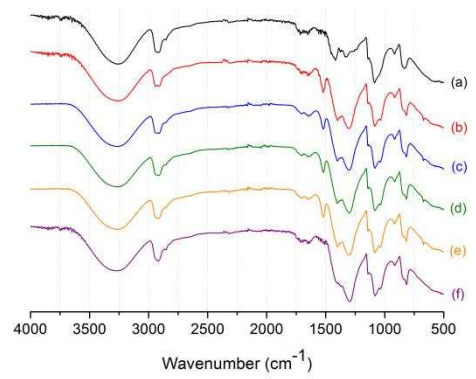


Figure 3: FTIR of (a) standard PVA and non-irradiated 40 wt % AgNO<sub>3</sub>-PVA composites after (b) 0 hrs (c) 24 hrs (d) 48 hrs (e) 142 hrs and (f) 700.5 hrs dark exposure.

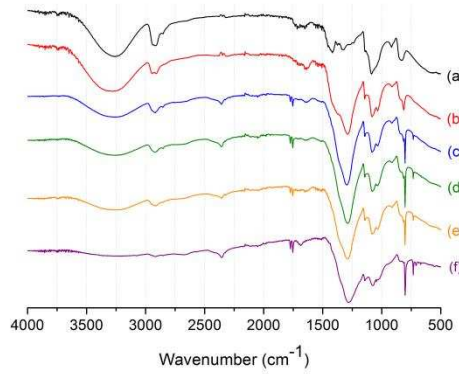


Figure 3: FTIR of (a) standard PVA and light irradiated 60 wt% AgNO<sub>3</sub>-PVA composites after (b) 0 hrs (c) 24 hrs (d) 48 hrs (e) 142 hrs and (f) 700.5 hrs light irradiation.

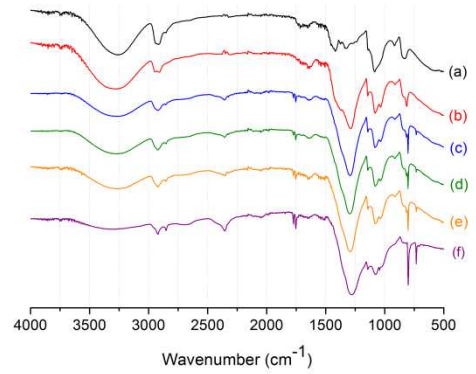


Figure 7.9: FTIR of (a) standard PVA and non-irradiated 60 wt% AgNO<sub>3</sub>-PVA composites after (b) 0 hrs (c) 24 hrs (d) 48 hrs (e) 142 hrs and (f) 700.5 hrs dark exposure.

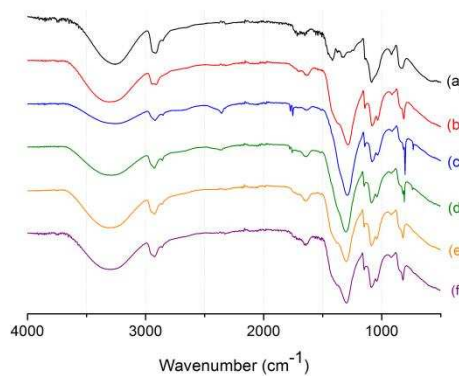


Figure 3: FTIR of (a) standard PVA and light irradiated acidified 60 wt% AgNO<sub>3</sub>-PVA composites after (b) 0 hrs (c) 23 hrs (d) 47 hrs (e) 96 hrs and (f) 144 hrs light irradiation.

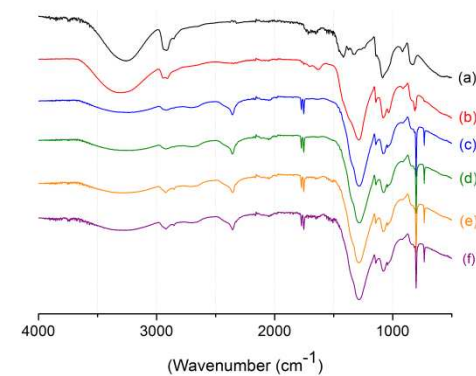


Figure 7.11: FTIR of (a) standard PVA and non-irradiated acidified 60 wt% AgNO<sub>3</sub>-PVA composites after (b) 0 hrs (c) 23 hrs (d) 47 hrs (e) 96 hrs and (f) 144 hrs dark exposure.

All the AgNO<sub>3</sub>-PVA films after 0 hours light exposure displayed the characteristic bands of neat standard PVA, however, two new peaks at 1522 and 671 cm<sup>-1</sup> were observed in the 40 wt% AgNO<sub>3</sub>-PVA film spectrum. These peaks could be attributed to silver nitrate as NO<sub>2</sub> symmetric and symmetric stretching vibrations are commonly found between 1660 – 1500 cm<sup>-1</sup> and 1390 – 1260 cm<sup>-1</sup>, respectively.<sup>19</sup> When compared to neat PVA, the peaks at 1329 and 1419 cm<sup>-1</sup> in the spectra of the AgNO<sub>3</sub>-PVA films after 0 hours light exposure had larger intensities. Previous literature has shown that a decrease in the ratio of intensities of 1329 and 1419 m<sup>-1</sup> indicates decoupling of O – H vibrations and C – H wagging vibrations due to the interaction between silver salts or silver nanoparticles and the OH groups on the polymer backbone.<sup>9,20</sup> I<sub>1329</sub> / I<sub>1419</sub> was calculated for the neat PVA and AgNO<sub>3</sub>-PVA films after 0 hours light exposure and shown in Table 7.1. It was found that the intensity ratio decreased with increasing AgNO<sub>3</sub> filler confirming an interaction between PVA and silver nitrate. A PVA-Ag<sup>+</sup> chelate structure as shown in Figure 7.12 was proposed by Huang *et al.*<sup>21</sup>

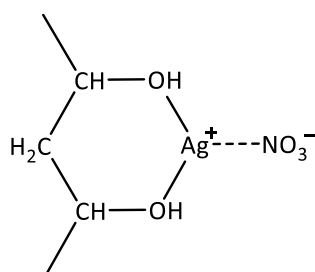


Figure 7.12: PVA-Ag<sup>+</sup> chelate structure proposed by Huang *et al.*<sup>21</sup>

Mbhele *et al.* observed the disappearance of the peak at 837 cm<sup>-1</sup> (attributed to the out of plane vibration of C – H group in PVA) in the FT-IR spectra of PVA-Ag nanocomposites.<sup>20</sup> The authors reasoned that the attachment of Ag<sup>0</sup> to PVA triggers chain restriction thus preventing the out of plane vibrations. However, as shown in Figures 7.6, 7.8, and 7.10 the peak around 837 cm<sup>-1</sup> does not disappear in the FT-IR spectra of the 0 hours light irradiated 40 wt%, 60 wt% and acidified 60 wt% AgNO<sub>3</sub>-PVA films. The lack of disappearance of the peak at 837 cm<sup>-1</sup> is most likely due to the high silver nitrate wt % used. It has been suggested that above 0.1 wt% AgNO<sub>3</sub> content, the excess Ag<sup>+</sup> ions do not co-ordinate with the OH groups in PVA but with the nitrate ion as shown in Figure 7.13.<sup>21</sup> Therefore, it is most likely that a large proportion of Ag<sup>+</sup> ions are chelated with nitrate ions over PVA. This would result in free OH groups along the PVA backbone which maintains the polymer chain mobility allowing for the out of plane vibration of C – H to occur.

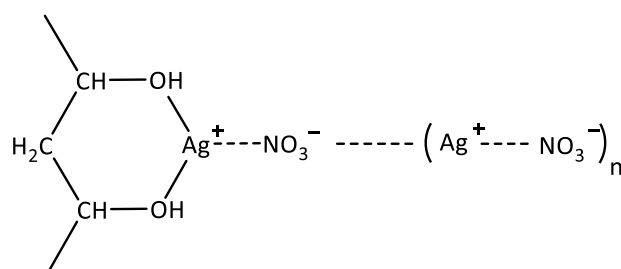


Figure 7.13: PVA-Ag<sup>+</sup> chelate structure proposed by Yen *et al.*<sup>21</sup>

Table 7.1: Intensity Ratio ( $I_{1329}/I_{1419}$ ) from the FTIR spectra of neat PVA and 40 wt%, 60 wt% and acidified 60 wt%  $\text{AgNO}_3$ -PVA films.

| Sample film                           | Intensity Ratio ( $I_{1329}/I_{1419}$ ) at 0 hours exposure |                |
|---------------------------------------|---|----------------|
|                                       | Light Irradiated  | Non-irradiated |
| Neat PVA                              | 1.03  | N / A          |
| 40 wt% $\text{AgNO}_3$ -PVA           | 0.80  | 0.81           |
| 60 wt% $\text{AgNO}_3$ -PVA           | 0.45  | 0.48           |
| Acidified 60 wt% $\text{AgNO}_3$ -PVA | 0.44  | 0.39           |

It was found that the absorption bands attributed to silver nitrate disappeared in the FT-IR spectra of both the light irradiated and non-irradiated 40 wt%  $\text{AgNO}_3$ -PVA films after 700.5 hours suggesting reduction of silver nitrate. Absorption bands attributed to a carbonyl group ( $1755$ ,  $1773$  and  $733 \text{ cm}^{-1}$ ) were shown to appear in the FT-IR spectrum of the 60 wt%  $\text{AgNO}_3$ -PVA films after 24 hours light exposure. These carbonyl absorption bands increased in magnitude and sharpened slightly as a function of light exposure time. Along with the appearance of the carbonyl peaks, the magnitude of the peaks attributed to the OH group in PVA decreased with increasing light exposure time. This suggested that the OH groups were being converted to carbonyl groups as a function of light exposure. The appearance of a carbonyl group and disappearance of the PVA OH groups was also shown in the FT-IR spectra of the non-irradiated 60 wt%  $\text{AgNO}_3$ -PVA films (Figure 7.9) suggesting the change in the structure of the  $\text{AgNO}_3$ -PVA films was not reliant on light exposure. The change in structure observed could be caused by the reduction of silver nitrate by the PVA polymer as previous literature has shown that PVA has the ability to act as both a supporting matrix and a mild reducing agent. Gautam *et al.* proposed the following reaction mechanism to describe how PVA can reduce silver ions to metallic silver:<sup>22</sup>



As shown above in equation 7.3, the hydroxyl group on the PVA backbone is oxidised to a carbonyl group while the  $\text{Ag}^+$  is reduced to metallic silver. This confirmed the observed change in the structure of the  $\text{AgNO}_3$ -PVA films was a result of the PVA reducing the silver nitrate. The appearance of a carbonyl group, along with the disappearance of the OH group as a function of light was also observed in the FT-IR spectra of the non-irradiated acidified 60 wt%  $\text{AgNO}_3$ -PVA film (Figure 7.9). However in the FT-IR spectra of the light exposed acidified 60 wt%  $\text{AgNO}_3$ -PVA film the carbonyl group (peaks at  $1755$ ,  $1773$  and  $733 \text{ cm}^{-1}$ ) appeared at 23 hours and then disappeared with further light exposure time. Also, the OH group did not disappear as a function of light exposure, suggesting that a different silver nitrate reduction mechanism was occurring.

Visual observation of the  $\text{AgNO}_3$ -PVA films further suggested that silver particles had been produced in both light and dark conditions. Previous research has shown the formation of silver particles causes a colour change – the colour changes from pale yellow to a greenish grey with increasing silver particle concentration.<sup>15</sup> After 553 hours both the light irradiated 40 wt% and 60 wt%  $\text{AgNO}_3$ -PVA films had darkened in colour and were opaque. The light irradiated 40 wt% films also exhibited a metallic sheen and had become more of a grey colour. On the other hand the non-irradiated films were not as dark in colour when compared to the corresponding light irradiated films and the non-irradiated 40 wt%  $\text{AgNO}_3$ -PVA film was still slightly translucent as shown in Figure 7.14. After 144 hours the light irradiated acidified 60 wt%  $\text{AgNO}_3$ -PVA films had darkened to a metallic grey colour, whereas the non-irradiated acidified 60 wt% films were a shiny metallic brown colour. The differences in colour between the light irradiated and non-irradiated films highlighted that with light exposure a larger concentration of silver particles are produced i.e. the reduction of the silver nitrate is faster in the light. SEM micrographs of the  $\text{AgNO}_3$ -PVA films were performed to confirm the presence of silver particles.

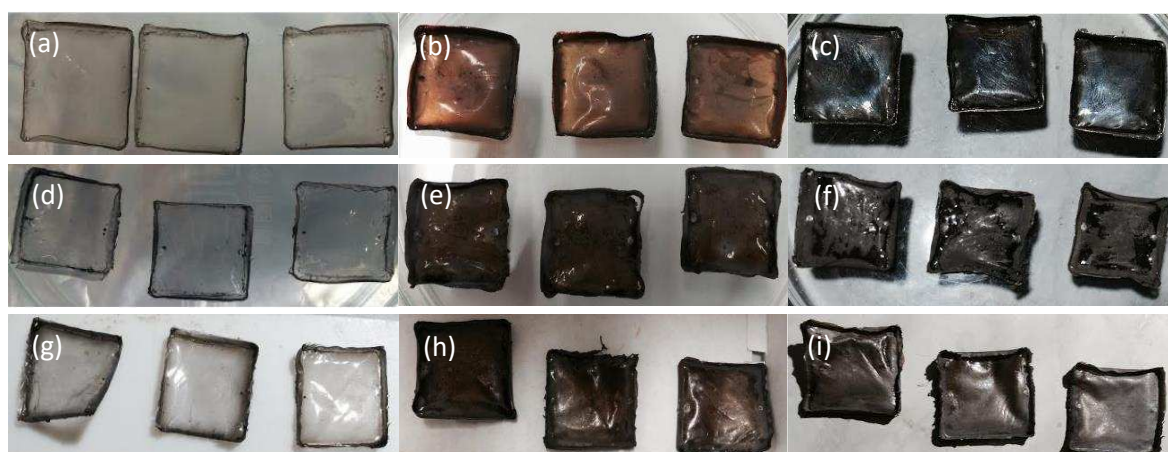


Figure 7.14: Images of 40 wt%  $\text{AgNO}_3$ -PVA films after a) 0 hrs light exposure (b) 553 hrs non-irradiated and (c) 553 hrs light exposure. Images of 60 wt%  $\text{AgNO}_3$ -PVA films after (d) 0 hrs light exposure (e) 553 hrs non-irradiated and (f) 553 hrs light exposure. Images of acidified 60 wt%  $\text{AgNO}_3$ -PVA films after (g) 0 hrs light exposure (h) 144 hrs non-irradiated and (i) 144 hrs light exposure.

Figure 7.15, 7.16 and 7.17 shows the SEM micrographs of both the light irradiated and non-irradiated 40 wt%, 60 wt% and acidified 60 wt%  $\text{AgNO}_3$ -PVA films, respectively. After 142 hours light exposure the 40 wt% film exhibited previously reported<sup>21</sup> spherulite-like morphology compared to the 60 wt% film which showed possibly formation of a silver cluster but no defined particles. Defined almost cuboidal shaped particles were observed for the 60 wt% film but not the 40 wt% film after 700.5 hours light exposure. When compared to the 60 wt% film after 142 hours light exposure where no defined particles were formed, defined non-spherical needle-like particles and a few cuboidal like particles were observed for the acidified 60 wt% film after a similar amount of light exposure time (144 hours). It was also noted that the particles formed in the acidified 60 wt%  $\text{AgNO}_3$ -PVA films did not appear aggregated like the particles in the non-acidified 60 wt% films after 700.5 hrs. Particle aggregation did not occur in the acidified films due to the stabilising effect of the nitric acid as previously discussed in the analysis of the  $\text{AgNO}_3$ -PVA solutions (section 7.2.1).

Comparing the SEM micrographs of the light irradiated and non-irradiated AgNO<sub>3</sub>-PVA films it was clear that silver particles had been formed irrespective of light exposure as suggested by both the colour change and structure change observed in the FT-IR spectra of both the irradiated and non-irradiated AgNO<sub>3</sub>-PVA films. There were slight differences in the particles formed in the light irradiated and non-irradiated 60 wt% and acidified 60 wt% AgNO<sub>3</sub>-PVA films. In the 60 wt% film the particles formed in the non-irradiated films were needle-like rather than cuboidal like particles observed in the light exposed films. In the case of the acidified 60 wt% films, less cuboidal like particles were observed in the non-irradiated film compared to the light irradiated film. These observations confirmed that the reduction of silver nitrate in the dark occurs at a slower rate than in light as suggested by the difference in colour of the light irradiated and non-irradiated films. The slow reduction of silver nitrate in darkness had been previously highlighted in literature and is due to the fact that only one reduction mechanism (equation 7.3) is predominately occurring. The possible additional mechanisms that are most likely happening in the light irradiated films are the reduction of silver nitrate by either PVA hydroxyl radicals produced through the photolysis of PVA<sup>10</sup> or excited carbonyl groups generated through the absorption of certain wavelengths of light.<sup>11</sup> Even though there is no structural evidence via FTIR spectroscopic analysis to support that the previous reduction mechanisms are occurring it is clear from the SEM images and colour of the films that silver particles were formed more quickly in light conditions and therefore a light dependant reduction must take place.

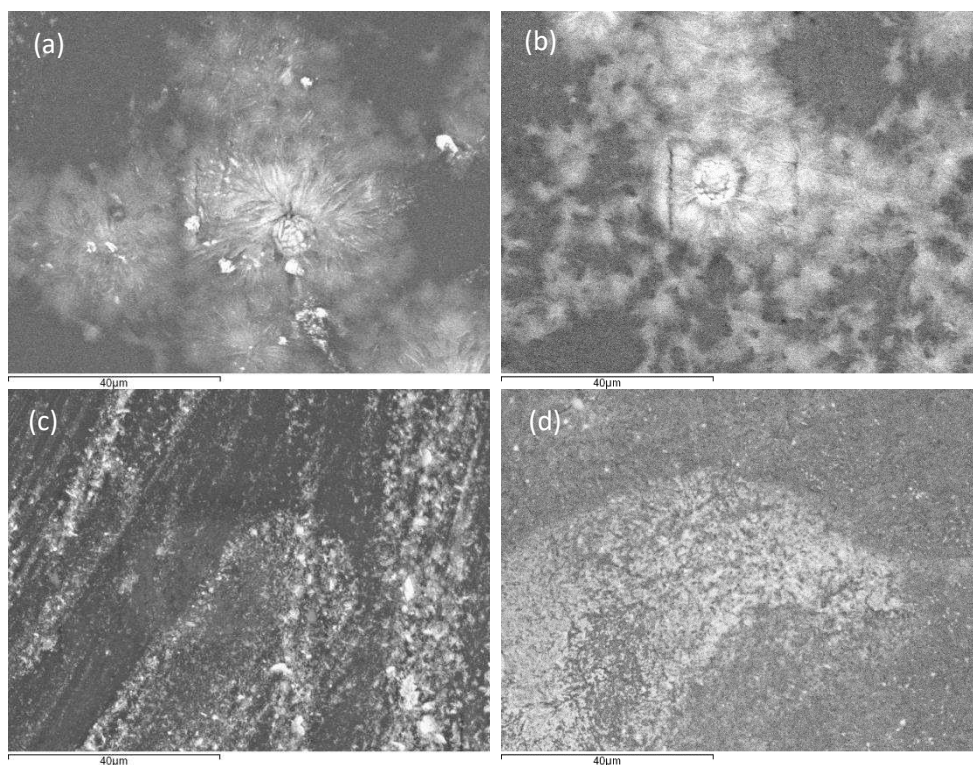


Figure 7.15: SEM micrographs of 40 wt% AgNO<sub>3</sub>-PVA film after (a) 142 hrs light exposure (b) 142 hrs non-irradiated (c) 700.5 hrs light exposure and (d) 700.5 hrs non-irradiated.

As shown through FT-IR spectroscopic analysis, visual appearance and SEM micrographs of the films silver particles were produced in the non-irradiated AgNO<sub>3</sub>-PVA films. However, in the case of the

non-irradiated  $\text{AgNO}_3$ -PVA solutions little to no silver particles were detected. The reason for this is the effect of the water content in the  $\text{AgNO}_3$ -PVA solutions on the ability of PVA to reduce the silver nitrate (equation 7.3). Equation 7.3 shows that the hydroxyl group of the PVA is responsible for the reduction of the silver nitrate. The large water content present in the non-irradiated  $\text{AgNO}_3$ -PVA solutions prevents the reduction of silver nitrate as the hydroxyl groups along the PVA polymer are involved in hydrogen bonding with the surrounding water molecules rather than coordinating with the silver nitrate. Mahanta and Valiyaveetil observed a low reduction of silver ions in PVA/dextran  $\text{AgNO}_3$  solutions and concluded it was due to the low availability of free hydroxyl groups in PVA caused by hydrogen bonding between dextran and PVA molecules.<sup>23</sup> In the case of the light irradiated  $\text{AgNO}_3$ -PVA solutions silver particles are still formed as other light dependant reduction mechanisms are occurring overriding the lack of silver nitrate reduction via the oxidation of PVA caused by the water content.

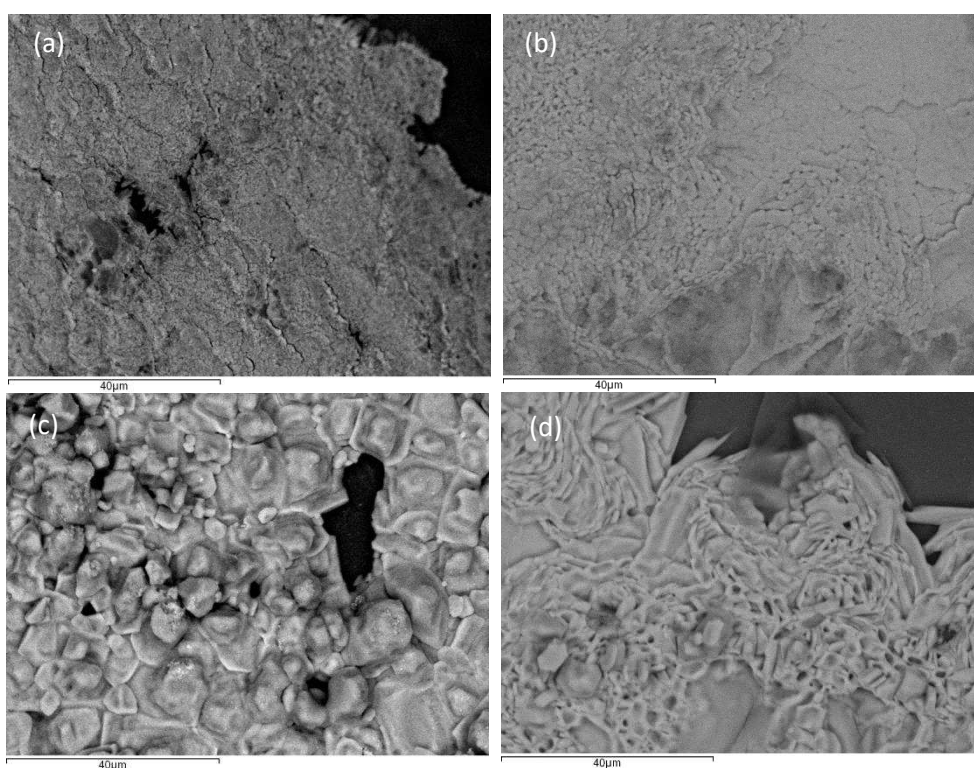


Figure 7.16: SEM micrographs of 60 wt%  $\text{AgNO}_3$ -PVA film after (a) 142 hrs light exposure (b) 142 hrs non-irradiated (c) 700.5 hrs light exposure and (d) 700.5 hrs non-irradiated.

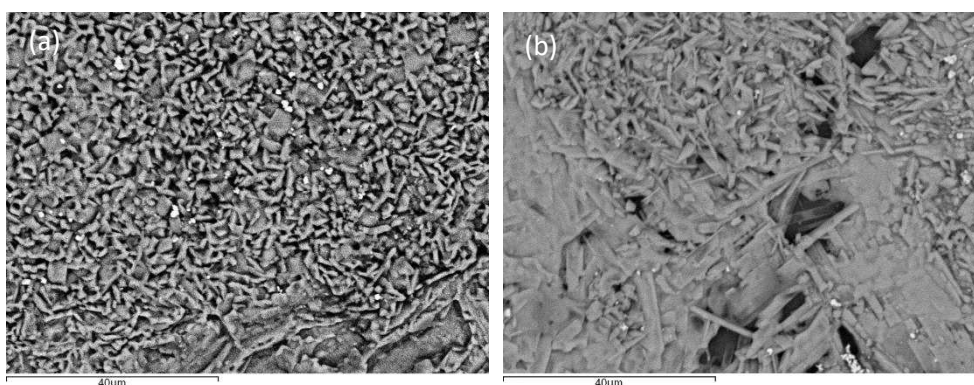


Figure 7.17: SEM micrographs of acidified 60 wt%  $\text{AgNO}_3$ -PVA film after 144 hrs (a) light exposure (b) non-irradiated.



In conclusion, silver particles are formed in both the light irradiated and non-irradiated AgNO<sub>3</sub>-PVA films via the reduction of the silver nitrate. The reduction of the silver nitrate via the oxidation of the PVA OH group occurred in both the light irradiated and non-irradiated films. However, in the light irradiated AgNO<sub>3</sub>-PVA films further light dependant reduction mechanisms occurred. Due to the additional reduction mechanisms, silver particle formation in the light exposed films occurred faster than in the non-irradiated films as shown by both SEM micrographs and visual appearance of the films.

### 7.2.3 Resistance Measurements

#### 7.2.3.1 AgNO<sub>3</sub>-PVA films

To investigate if the AgNO<sub>3</sub>-PVA films could be used in the designed RFID light sensor tag, resistance measurements of the films were performed at varying intervals during light exposure. The resistance of non-irradiated AgNO<sub>3</sub>-PVA films was also measured. For the resistance measurements the AgNO<sub>3</sub>-PVA films were placed onto glass and a probe to probe distance of approximately 2 cm (the length of the film) was used. The resistance of the 40 wt%, 60 wt% and acidified 60 wt% AgNO<sub>3</sub>-PVA films were measured over a period of 700.5 hours for both the 40 wt% and 60 wt% films and 144 hours for the acidified 60 wt% film. Three resistance measurements were performed each time and the average resistance along with the standard error of the mean was calculated. It was previously concluded that the formation of silver particles is faster in the light irradiated films when compared to their non-irradiated counterparts. Therefore, the resistance of the light irradiated films would be expected to decrease before the resistance of the non-irradiated films. Figure 7.18 shows the average resistance of the top surface of the 40 wt%, 60 wt% and acidified 60 wt% AgNO<sub>3</sub>-PVA films as a function of light exposure. The initial resistance (0 minutes) for 60 wt% AgNO<sub>3</sub>-PVA films was much lower than the initial resistance of both 40 wt% and acidified 60 wt% AgNO<sub>3</sub>-PVA films. The initial resistance of the 60 wt% AgNO<sub>3</sub>-PVA films was  $2 \times 10^4$  and  $3 \times 10^4$  ohms when compared to  $2 \times 10^5$  and  $3 \times 10^5$  ohms for the 40 wt% films and  $4 \times 10^5$  and  $8 \times 10^5$  ohms for the acidified 60 wt% films.

An initial increase in resistance for all films was observed irrespective of light exposure. The resistance of the light irradiated and non-irradiated acidified 60 wt% AgNO<sub>3</sub>-PVA films appeared to level off at around  $1 \times 10^7$  ohms after around 40 hours. This was not observed for both the light irradiated or non-irradiated 40 wt% and 60 wt% AgNO<sub>3</sub>-PVA films. For the most part both the light irradiated and non-irradiated films displayed a similar pattern as a function of time. It was clear that none of the films showed a decrease in resistance as a function time, even though silver particles are being formed. The resistance of the bottom surface of the films was also measured and the resistance of both the top and bottom surface of the 60 wt% AgNO<sub>3</sub>-PVA film was shown in Figure 7.19. It was observed that there was little to no difference between the resistance values

of the top and bottom surface for either the light or non-irradiated films. This was also observed for the other two films – 40 wt% and acidified 60 wt% AgNO<sub>3</sub>-PVA.

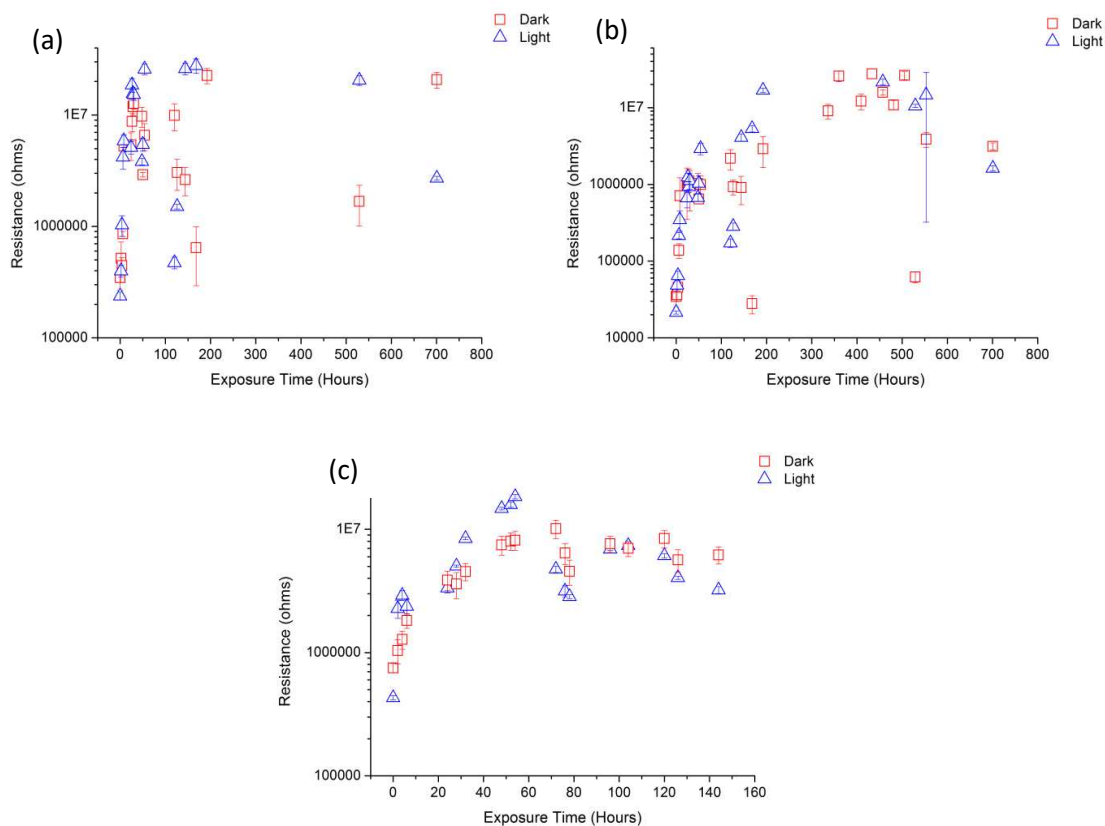


Figure 7.18: Average resistance measurements of the top surface of light irradiated and non-irradiated (a) 40 wt% AgNO<sub>3</sub>-PVA films (b) 60 wt% AgNO<sub>3</sub>-PVA films and (c) acidified 60 wt% AgNO<sub>3</sub>-PVA films. In figure 13 (a) resistance measurements were too high to record from 335 to 505 hours exposure time.

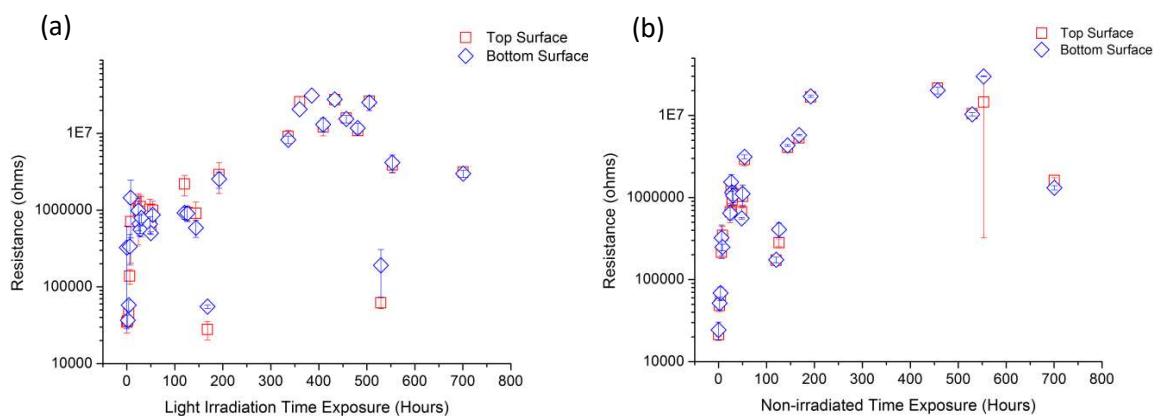


Figure 7.19: Resistance of the top and bottom surface of a 60 wt% AgNO<sub>3</sub>-PVA film (a) light irradiated and (b) non-irradiated.

To compare the conducting ability of the AgNO<sub>3</sub>-PVA films with other materials the average resistivity of the films was calculated using the following equation:

$$\rho = \frac{R \times A}{l} \quad \text{(Equation 5.4)}$$

Where  $\rho$  is resistivity ( $\Omega \text{ m}$ ),  $R$  is the average resistance ( $\Omega$ ),  $l$  is the length of the sample measured (m) and  $A$  is the average cross-sectional area of the sample measured ( $\text{m}^2$ ). The minimum resistivity of the light irradiated 40 wt%, 60 wt% and acidified 60 wt%  $\text{AgNO}_3$ -PVA films was 14.2, 1.5 and 21.5  $\Omega \text{ m}$ , respectively and the minimum resistivity of the non-irradiated 40 wt%, 60 wt% and acidified 60 wt%  $\text{AgNO}_3$ -PVA films was 13.9, 2.0 and 30.0  $\Omega \text{ m}$ , respectively. The minimum resistivity for all the films was shown at 0 hours apart from the non-irradiated 60 wt%  $\text{AgNO}_3$ -PVA films where the minimum resistivity was shown at 168 hours. The minimum resistivity of the films categorises them as semi-conductors. At room temperature, conductors exhibit a resistivity of around  $10^{-8} \Omega \text{ m}$ , semi-conductors are materials with a resistivity between  $10^{-6} - 10^3 \Omega \text{ m}$  and insulators have a resistivity higher than  $10^9 \Omega \text{ m}$ .<sup>24</sup> Even though it has been confirmed that silver particles are formed within both the light exposed and non-irradiated  $\text{AgNO}_3$ -PVA films, resistivities near to silver ( $1.59 \times 10^{-8} \Omega \text{ m}$ ) were not seen. This suggests that the conductive mechanism of the  $\text{AgNO}_3$ -PVA films was not contact conduction where the formed silver particles come into contact with each other creating a conductive pathway throughout the film. Also, if contact conduction was occurring, a sudden drop in resistance would have been observed at a particular time where enough silver particles had been formed to create a conductive pathway. As previously highlighted silver particles were produced faster in the light irradiated  $\text{AgNO}_3$ -PVA films when compared to the non-irradiated films. Therefore the drop in resistance attributed to contact conduction would have been observed at a shorter time in the light irradiated films. Combined with the fact that a large resistance drop associated with contact conduction was not observed and the resistivities of the  $\text{AgNO}_3$ -PVA films were in the semi-conductor region it was concluded that the conductive mechanism in the 40 wt%, 60 wt% and acidified 60 wt%  $\text{AgNO}_3$ -PVA films was not contact conduction.

At 0 hours the  $\text{AgNO}_3$ -PVA films did not show any structural evidence of the reduction of silver nitrate to silver by FT-IR spectroscopic analysis. However, at 0 hours the films were shown to have the electrical resistivity associated with a semi-conductor, not an insulator like neat PVA highlighting that just the addition of silver nitrate has had an effect on the electrical properties of PVA. The conductance of PVA has shown to be increased by the doping with silver nitrate and halide salts. Charge transfer complexes are formed between the silver nitrate and PVA polymer.<sup>25</sup> These charge transfer complexes assist the delocalisation of electrons and can either add electrons to the conduction band ( $\pi^*$ ) or remove electrons from the valence band ( $\pi$ ) of PVA which causes PVA to exhibit metallic properties such as increased conductance. Materials which use charge transfer complexes as the conductive mechanism exhibit resistivity values associated with semi-conductors as shown by the  $\text{AgNO}_3$ -PVA films. Charge transfer complexes have also been shown to form between silver nanoparticles and PVA.<sup>26</sup> It was concluded that the conductive mechanism in the  $\text{AgNO}_3$ -PVA films was through charge transfer complexes. The formation of charge transfer complexes would explain why the initial resistance of the 60 wt%  $\text{AgNO}_3$ -PVA films was much lower than the 40 wt%  $\text{AgNO}_3$ -PVA films. More charge transfer complexes would be formed in the film

containing the larger silver nitrate loading resulting in an increase in conductivity. It was also clear that the resistance caused by charge transfer complexes between silver nitrate and PVA could not be distinguished from the resistance caused by charge transfer complexes between silver particles and PVA as the resistance values of the irradiated and non-irradiated films were similar even though it has been shown that silver particles are formed faster in the irradiated films. The larger initial resistance exhibited by the acidified 60 wt% AgNO<sub>3</sub>-PVA film when compared to the corresponding non-acidified 60 wt% film was attributed to the effect of nitric acid on the dissociation of silver nitrate. The increased acidity from the addition of nitric acid prevents the dissociation of silver nitrate<sup>27</sup> which could have an effect on the formation of charge transfer complexes.

It was concluded that the 40 wt and 60 wt% AgNO<sub>3</sub>-PVA films could not be used in the light sensor design as the resistivity of the films was not low enough and not affected by light irradiation. To try and achieve low resistivities needed for the light sensor design, the silver nitrate percentage in the AgNO<sub>3</sub>-PVA films was increased. By increasing the AgNO<sub>3</sub> filler content, a large amount of silver particles should be formed with very close neighbouring particles allowing for a conductive pathway to be achieved.

#### 7.2.3.2 Increased AgNO<sub>3</sub> loading

The silver nitrate filler was increased up to 90 wt% to produce silver particles close together to form a conductive pathway to allow contact conduction to occur. The silver nitrate solutions were cast onto test beds rather than being poured into moulds as the test beds closely represent the antenna design of the light sensor. Also, the high wt% silver nitrate filler would form highly rigid films introducing difficulties in the resistance measurements. The test beds consisted of two linear conductive tracks separated with a small gap. The silver nitrate solutions were painted into the gap connecting the two conductive tracks and left to dry in complete darkness at room temperature. The resistance was measured using a resistance meter (ISO-TECH, IDM 201) where each probe was placed at each end of the conductive tracks.

Preliminary experiments were performed using test beds where the conductive tracks were copper etched onto FR4 and Aluminium tape on FR4. Each test bed had three sets of conductive tracks and before the test beds were used a resistance measurement was performed with a conductive wire placed over the gap connecting the tracks, to ensure a conductive pathway could be achieved. A 40 wt% silver nitrate solution was painted in the gap of the two copper etched test beds. As soon as the silver nitrate solution connected with the copper tracks, needle-like silver crystals were formed by means of the displacement reaction between the copper and silver. The formation of silver crystals was confirmed through initial resistance measurements – the average resistance was measured at 0.3 Ω. The sample was left to dry in darkness at room temperature and exposed to light for 48 hours before further resistance measurements were performed. The resistance remained low and an average resistance of 0.5 Ω was recorded after 48 hours light irradiation. The

test beds with the copper conductive tracks were not used further as the light sensor design relies on the concept of the film becoming conductive as a result of light exposure.

40 wt%, 60 wt% and 90 wt% silver nitrate solutions (synthesised following the same method as described in section 7.1.2) were used for the preliminary experiments of the aluminium tape test bed. In this case crocodile clips rather than probes were used in the resistance measurements to prevent pressure variance. Each solution was painted in the gap of the aluminium track of two test beds which were left to dry in darkness at room temperature. After drying it was observed that the 90 wt %  $\text{AgNO}_3$ -PVA film had turned white and what looked like clumps of silver crystals had formed (Figure 7.20).

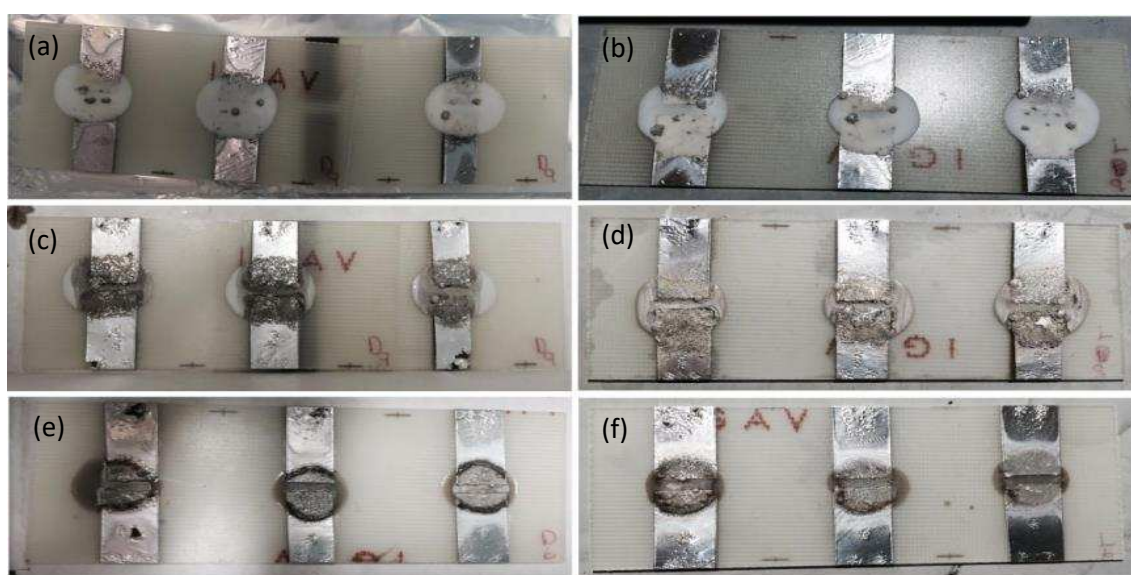


Figure 7.20: Images of 90 wt%  $\text{AgNO}_3$ -PVA aluminium test bed after (a) 0 hrs dark exposure (b) 0 hrs light irradiation (c) 144 hrs dark exposure (d) 144 hrs light irradiation. Images of 60 wt%  $\text{AgNO}_3$ -PVA aluminium test bed after (e) 144 hrs dark exposure and (f) 144 hrs light irradiation

This suggested that the aluminium had displaced the silver forming metallic silver and aluminium nitrate which is white in appearance. After 144 hours both the light irradiated and dark 90 wt% sample appeared to have formed more silver crystals. At no point did the resistance of either 90 wt% sample reach the low resistance exhibited when using the copper tracks. However, it was the sample kept in the dark and not light treated that reached the lowest average resistance of  $45 \Omega$  which was observed at 126 hours. Neither of the 40 and 60 wt% sample exhibited a white film after drying in darkness. However, after 144 hours the appearance of silver crystals were formed in both the light treated and dark standard of the 60 wt% sample. As shown in Figure 7.21 the resistance is similar for both the light exposed samples and dark samples.

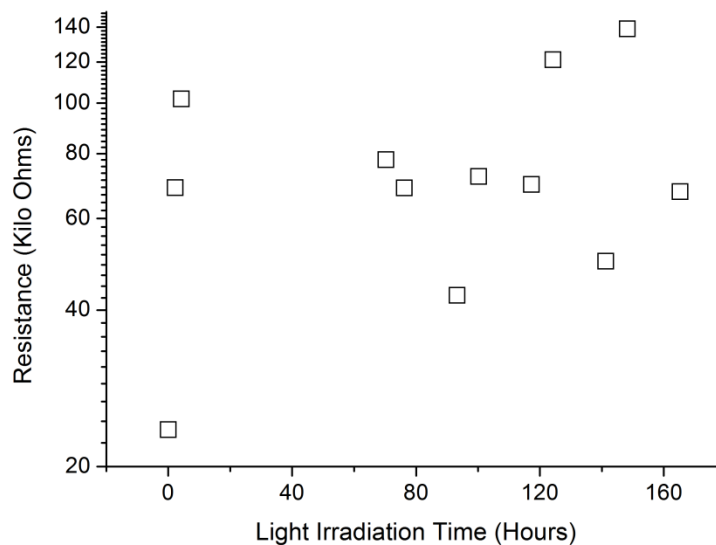


Figure 7.21: Resistance of 90 wt% AgNO<sub>3</sub>-PVA test bed over a period of 165.25 light exposure.

As previously discussed it has been shown that PVA reduces silver nitrate, however this mechanism is slow and does not explain why the resistance of the dark samples at times are lower than the light treated samples. Therefore, it was concluded a metal displacement reaction had occurred. The displacement reaction of the silver with aluminium appeared to be less reactive than with copper, this was attributed to the fact that there was most likely a small amount of aluminium oxide coating on the aluminium tape. The test beds with the aluminium conductive tracks were not further used. It was also decided that crocodile clips would not be used in further resistance measurements as they caused damage to the conductive tracks.

To prevent the issues of the metal used for the conductive tracks displacing the silver, a metal that is less reactive than silver was required which left the conductive tracks to either be silver, gold or platinum. Silver conductive paint was ultimately chosen to create the conductive tracks. PEL Nano 60 (Printed Electronics) paper was used as the test bed substrate rather than FR4. PEL paper consists of a base paper layer and an ink receiving layer. The chemical composition of the ink receiving layer is not disclosed by the manufacturer; however, it has been shown through FT-IR spectroscopic analysis that the layer is most likely silica based.<sup>28</sup> PEL test beds were made up by painting two silver conductive tracks about 0.5 cm in width separated with a gap of around 0.2 cm. The silver conductive paint was left to dry for 30 minutes at room temperature. Before any experiments occurred a resistance measurement was performed with a conductive wire placed over the gap connecting the tracks, to ensure a conductive pathway could be achieved.

A 90 wt% AgNO<sub>3</sub>-PVA solution was painted in the gap of the silver conductive tracks making sure the solution reached and covered the edges of the tracks. This was done to ensure a good

conductive pathway would be produced. The test bed was left to dry in darkness at room temperature overnight before being placed under an LED light, at a distance of around 30.5 cm. The resistance across the gap was measured over a period of 165.25 hours light irradiation time and was shown in Figure 7.21.

The lowest resistance (23.57 K $\Omega$ ) of the 90 wt % AgNO<sub>3</sub>-PVA test bed was observed at 0 minutes light irradiation time. After 2.25 hours light irradiation time the resistance began to increase. However, there was no distinct relationship observed between the resistance of the test bed and amount of light exposure it had received after 4.25 hours light irradiation time. It was to be expected that the lowest resistance measured would be the 90 wt% AgNO<sub>3</sub>-PVA film. However, a comparison between the films resistance and the test bed could not be performed. The films and test bed samples differed in size, resulting in a difference in length the resistance was measured across. Resistance values are subject to the length of the sample; the resistance increase as the length between the probes increases. Therefore, a test bed was made up with a 60 wt% AgNO<sub>3</sub>-PVA solution, left to dry in darkness at room temperature before being placed under the LED light for a total of 416 hours with resistance measurements performed periodically. The resistance of both the light irradiated 60 and 90 wt% test beds is shown in Figure 7.22. It was observed that the 90 wt % test bed did indeed exhibit the lowest resistance which was to be expected. While the increase in 90 wt% filler has shown to decrease the resistance values, a relationship between test bed resistance and light irradiation time was not observed. Also, the 90 wt% AgNO<sub>3</sub>-PVA silver test beds still did not display the very low resistance values associated with metals.

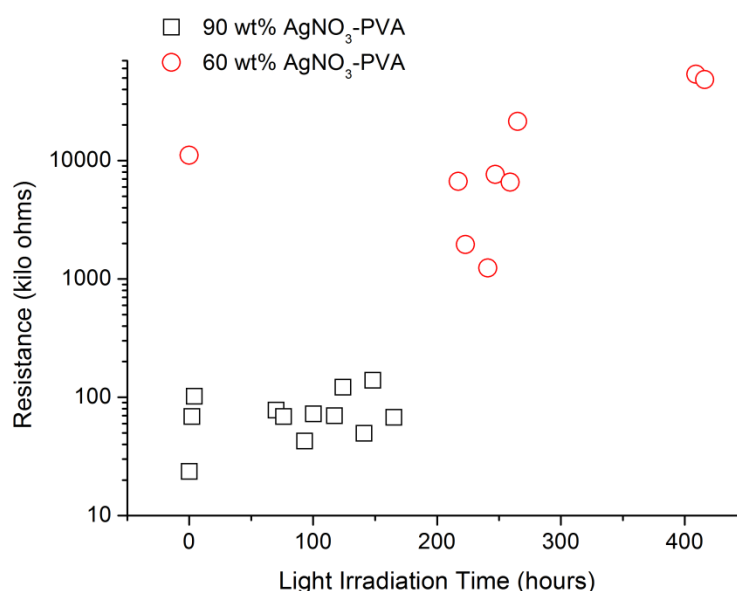


Figure 7.22: Resistance of both 90 wt% and 60 wt% AgNO<sub>3</sub>-PVA silver test beds. The lack of resistance readings between 5 – 151 and 289 – 391 hours light irradiation time for the 60 wt% test bed was due to 0.L values being measured.

### 7.2.3.3 Thermal treatment

Thermal annealing has previously been used to form silver nanoparticles within a PVA matrix through thermal reduction of AgNO<sub>3</sub>-PVA composites.<sup>7,29-31</sup> Heat treatment before light irradiation

exposure was investigated to see if thermal annealing could be used in conjunction with light irradiation to produce highly conductive films. It was thought that the heat treatment would begin the reduction of the silver nitrate and nucleation of the silver particles, while the light treatment would cause further reduction, nucleation and growth continuing the process of silver particle production. Various thermal annealing temperatures and annealing times have been used to form silver nanoparticles and it has been shown that particle size increases with annealing time as well as annealing temperature. Clemenson *et al.* found that increasing the annealing time at 110 °C only slightly increased silver particle size. Whereas, increasing the annealing temperature to 160 °C for 1 hour produced particles double the size.<sup>7</sup> At temperatures around 160 °C, a portion of the crystalline phase of PVA melts to produce amorphous lamellae where the particles develop. Porel *et al.* found low temperatures, 50 °C for 60 minutes produced either no particles for low AgNO<sub>3</sub> concentrations or few particles with varying sizes for larger AgNO<sub>3</sub> concentrations.<sup>31</sup> Therefore, to ensure reduction of the silver nitrate and nucleation of the particles began without the complete conversion of silver nitrate to silver particles the test beds were heated at 150 °C for 30 minutes. A 90 wt% AgNO<sub>3</sub>-PVA solution was painted onto two test beds; one test bed was left to dry in darkness at room temperature before being placed into an oven at 150 ° for 30 minutes and the other test bed was placed immediately into the oven with the film drying during the thermal annealing. Both test beds were removed from the oven and exposed to light. Resistance measurements were periodically taken over a period of 416 hours light irradiation time.

Figure 7.23 shows the resistance as a function of light irradiation time for both the 90 wt% test bed dried before and during heat treatment.

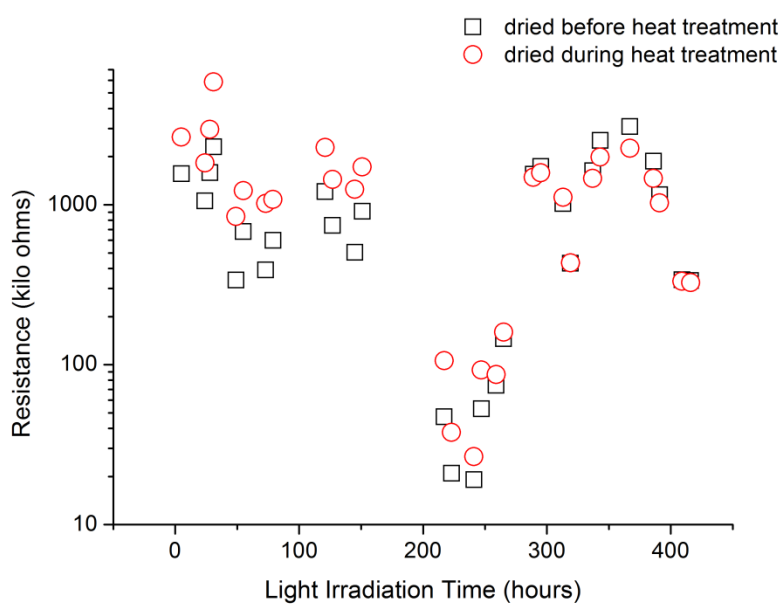


Figure 7.23: Resistance as a function of light exposure time for 90 wt% AgNO<sub>3</sub>-PVA silver test beds dried before and during heat treatment.

At 0 minutes light irradiation time both samples exhibited 0.L resistance values i.e the resistance was so high it was beyond the upper limit of the resistance meter. This was unexpected as it was



presumed a small portion of silver nanoparticles would have been produced resulting in a lower resistance. Also, it was interesting to note that the non-heat treated 90 wt% sample in section 7.2.3.2 exhibited a low resistance of 23.57 K $\Omega$  at 0 minutes. It was not clear as to why the heat treated samples showed such a large initial resistance. The resistance values of both samples decreased after 151 hours light irradiation time and the lowest resistance of the test bed dried before heat treatment was observed after 223 hours light exposure, whereas the lowest resistance of the test bed dried during heat treatment was observed after 241 hours. As shown in Figure 7.23 both samples show very similar resistance values and followed the same pattern as a function of light irradiation time. Therefore, it was concluded that no difference was made if the annealing was performed on dried films or aqueous solutions.

As discussed above increasing the silver nitrate filler loading still did not result in test beds with low resistance readings associated with metals. For the 90 wt% AgNO<sub>3</sub>-PVA test beds, it could be argued that the effect of charge transfer complexes on the conductivity of the film was negligible due to the high dopant concentration. Charge transfer complexes cause a conductive pathway through the PVA, therefore if the concentration of the PVA is low that conductive pathway is more likely to be broken. However, it was clear from the resistance values that good conductive pathways via the silver particles had not been achieved. Liang *et al.* reported conductive fern-like silver-PVA films through the *in situ* reduction of silver nitrate in PVA via heating.<sup>32</sup> The authors found that to produce an interconnected silver conductive pathway coalescence of the silver particles was essential. SEM micrographs were not performed on any of the 90 wt% test bed samples, however, it was clear from the light-irradiated 60 wt% AgNO<sub>3</sub>-PVA films that silver particles were produced and appeared to be agglomerated (Figure 7.16), but the particles did not appear to be coalesced. It is highly likely the same would be observed for the 90 wt% test bed samples except for larger silver particles. It was clear that by just increasing the silver nitrate filler therefore producing more or larger silver particles did not cause coalescence otherwise a low resistance would have been measured. Accordingly, it was concluded that to produce a highly conductive silver-polymer film via light irradiation, coalescence or a form of sintering would have to occur simultaneously with the production of silver particles.

### 7.3 Conclusions

In conclusion, it was found that silver particles were formed in the light irradiated AgNO<sub>3</sub>-PVA solutions via the reduction of silver nitrate by both hydroxyl and hydrogen radicals formed through the photolysis of PVA and water, respectively. The addition of acid was found to act as a stabilising agent resulting in discrete, least polydispersed silver particles to be formed in the light irradiated acidified 60 wt% AgNO<sub>3</sub>-PVA solution. The particles formed in the 60 wt% AgNO<sub>3</sub>-PVA solution did not remain dispersed and settled out of solution as a result of aggregation as shown by UV visible spectroscopy, DLS and visual observation. On the other hand the particles formed in the 40 wt%

AgNO<sub>3</sub>-PVA solution did not settle out of solution but were more polydispersed than the particles formed in the acidified solution. In the case of the AgNO<sub>3</sub>-PVA films, it was found that silver particles were formed in both the light irradiated and non-irradiated samples. In the non-irradiated samples the reduction of the silver nitrate was caused by the oxidation of the hydroxyl group on the PVA backbone. This reduction mechanism could not occur in the non-irradiated AgNO<sub>3</sub>-PVA solutions due to their high water content. The water molecules form hydrogen bonds with the PVA hydroxyl groups resulting in a lowered availability of the PVA hydroxyl groups for the silver nitrate. It was found that the 40 wt%, 60 wt% and acidified 60 wt% AgNO<sub>3</sub>-PVA films could not be used as the photosensitive material in the RFID light sensor tag design as the resistivity of the films was not low enough and not affected by light irradiation. The films displayed resistivity values associated with semi-conductors and it was concluded the films conductive mechanism was via charge transfer complexes. Light exposure had no effect on the film resistivity as charge transfer complexes are formed with both silver nitrate and silver nanoparticles. The silver nitrate loading was increased to 90 wt% in the attempt to produce silver particles close enough together so a conductive pathway would be formed which would result in a much lowered film resistance. It was concluded that neither increasing the silver nitrate filler content nor heat treatment before light exposure produced films with very low resistance values required for the RFID tag design. It was thought that to achieve films with low resistance values via light exposure, coalescence or a form of sintering would have to occur simultaneously with the formation of the silver particles.

### 7.3 References

- 1 E. Md Amin, R. Bhattacharyya and N. C. Karmakar, in *Antennas and Propagation Society International Symposium Proceedings*, IEEE, 2014, pp. 1308-1309.
- 2 N. Cho, S. Song, S. Kim, S. Kim and H. Yoo, in *Proceedings of the 31st European Solid-State Circuits Conference, 2005. ESSCIRC 2005*, IEEE, 2005, pp. 279-282.
- 3 J. R. Smith, A. P. Sample, P. S. Powledge, S. Roy and A. Mamishev, in *UbiComp 2006: Ubiquitous Computing*, ed. P. Dourish and A. Friday, Springer-Verlag, Heidelberg, 2006, pp. 495-506.
- 4 Z. Zhang, L. Zhang, S. Wang, W. Chen and Y. Lei, *Polymer*, 2001, **42**, 8315-8318.
- 5 C. Luo, Y. Zhang, X. Zeng, Y. Zeng and Y. Wang, *J. Colloid Interface Sci.*, 2005, **288**, 444-448.
- 6 N. Singh and P. Khanna, *Mater. Chem. Phys.*, 2007, **104**, 367-372.
- 7 S. Clemenson, L. David and E. Espuche, *J. Polym. Sci. A Polym. Chem.*, 2007, **45**, 2657-2672.

- 8 S. Clemenson, D. Léonard, D. Sage, L. David and E. Espuche, *J. Polym. Sci. A Polym. Chem.*, 2008, **46**, 2062-2071.
- 9 P. Khanna, N. Singh, S. Charan, V. Subbarao, R. Gokhale and U. Mulik, *Mater. Chem. Phys.*, 2005, **93**, 117-121.
- 10 A. Kutsenko and V. Granchak, *Theor. Exp. Chem.*, 2009, **45**, 313-318.
- 11 H. Huang, X. Ni, G. Loy, C. Chew, K. Tan, F. Loh, J. Deng and G. Xu, *Langmuir*, 1996, **12**, 909-912.
- 12 H. Zidan, *J. Appl. Polym. Sci.*, 2003, **88**, 104-111.
- 13 T. Galya, V. Sedlařík, I. Kuřitka, R. Novotný, J. Sedlaříková and P. Sába, *J. Appl. Polym. Sci.*, 2008, **110**, 3178-3185.
- 14 A. Šileikaitė, I. Prosyčevs, J. Puišo, A. Juraitis and A. Guobienė, *Mater. Sci. -Medzg*, 2006, **12**, 287-291.
- 15 A. Sobczak-Kupiec, D. Malina, Z. Wzorek and M. Zimowska, *Micro & Nano Letters*, 2011, **6**, 656-660.
- 16 K. Bogle, S. Dhole and V. Bhoraskar, *Nanotechnology*, 2006, **17**, 3204.
- 17 W. H. Eisa, Y. K. Abdel-Moneam, A. Shabaka and A. E. M. Hosam, *Spectrochim. Acta Mol. and Biomol. Spectrosc.*, 2012, **95**, 341-346.
- 18 S. Elzey and V. H. Grassian, *J. Nanopart. Res.*, 2010, **12**, 1945-1958.
- 19 R. Augustine, N. Kalarikkal and S. Thomas, *Appl. Nanosci.*, 2014, **4**, 809-818.
- 20 Z. Mbhele, M. Salemane, C. Van Sittert, J. Nedeljkovic, V. Djokovic and A. Luyt, *Chem. Mater.*, 2003, **15**, 5019-5024.
- 21 H. Zidan, *Polym. Test.*, 1999, **18**, 449-461.
- 22 A. Gautam, P. Tripathy and S. Ram, *J. Mater. Sci.*, 2006, **41**, 3007-3016.
- 23 N. Mahanta and S. Valiyaveetil, *RSC Advances*, 2012, **2**, 11389-11396.
- 24 M. Balkanski and R. F. Wallis, *Semiconductor Physics and Applications*, Oxford University Press, Oxford, 2000.
- 25 C. U. Devi, A. Sharma and V. N. Rao, *Mater. Lett.*, 2002, **56**, 167-174.

- 26 S. Mahendia, A. Tomar and S. Kumar, *J. Alloys Compounds*, 2010, **508**, 406-411.
- 27 Z. Ali, M. Helal, H. Saleh, A. Zikry and Y. Darwish, *N. Y. Sci. J.*, 2014, **7**, 84-94.
- 28 V. Sanchez-Romaguera, S. Wünscher, B. M. Turki, R. Abbel, S. Barbosa, D. J. Tate, D. Oyeka, J. C. Batchelor, E. A. Parker and U. S. Schubert, *J. Mater. Chem. C*, 2015, **3**, 2132-2140.
- 29 B. Karthikeyan, *Physica B: Condens. Matter*, 2005, **364**, 328-332.
- 30 W. Fritzsche, H. Porwol, A. Wiegand, S. Bornmann and J. Köhler, *Nanostructured Materials*, 1998, **10**, 89-97.
- 31 S. Porel, S. Singh, S. S. Harsha, D. N. Rao and T. Radhakrishnan, *Chem. Mater.*, 2005, **17**, 9-12.
- 32 K. Liang, Y. Wang, W. Lin and J. Lin, *RSC Advances*, 2014, **4**, 15098-15103.

# Chapter 8: Conclusions and further work

## 8.0 Conclusions and further work

The aim of this research was to fabricate and investigate several stimuli-responsive polymers for the use as a substrate for an UHF-RFID epidermal strain sensor tag, an actuator component of an UHF-RFID solvent vapour sensor tag and a short circuit for an UHF-RFID light sensor tag. Suitable stimuli-responsive polymers were found for both the epidermal strain sensor tag and solvent vapour sensor tag which led to prototypes of both tags to be fabricated and tested.

The epidermal strain sensor tag design required a dielectric stretchable substrate. PDMS elastomers were chosen as suitable candidates due to their elastic properties. It was concluded the addition of high dielectric filler BaTiO<sub>3</sub> was an efficient method to improve the dielectric properties of the PDMS elastomers. To prevent the reduction in flexibility associated with the addition of rigid fillers a high molecular weight PDMS was utilised. A prototype epidermal strain sensor was fabricated using a high molecular weight PDMS-BaTiO<sub>3</sub> composite with a 28.4 wt % BaTiO<sub>3</sub> loading and a silver Lycra<sup>®</sup> antenna. Antenna attachment via self-adhesion (antenna placed during composite curing) and silicone glue was explored. Self-adhesion was the preferred method and it was concluded placing the antenna 40 minutes into curing resulted in good adhesion and had no detrimental effect to the antenna's resistance. The resulting prototype strain sensor could differentiate between y and x-axis strains and monitor up to 10.4% x- axis strain. The tag also displayed no degradation in its performance over time. To be able to use the strain sensor tag as an actuator in assisted living applications, further work into reducing the size and thickness of the sensor will be performed. A suitable method of attaching the sensor to the skin requires investigation along with the performance of the sensor on the skin measuring eyebrow twitching. The fabrication of BaTiO<sub>3</sub>-PDMS films could be investigated as a means of reducing the thickness of the sensor tag.

The swelling extent of several polysiloxane networks – standard PDMS elastomers, PDMS sponges, TESPN cross-linked PDMS elastomers, 40 wt % BaTiO<sub>3</sub>-PDMS elastomers and polytrifluoropropylmethylsiloxane (PTFPMS) elastomers - in varying solvent vapours were investigated for the use as an actuator component for the UHF-RFID solvent vapour sensor tag as described in this thesis. The solvent vapour sensor tag works on the principle that as the feed loop is pushed further away from the main antenna as a result of polymer swelling the transmitted power required by the tag increases. The PDMS elastomers showed a high degree of swelling in non-polar and weakly polar solvent vapours such as diethyl ether and a low degree of swelling in polar solvent vapours such as methanol. It was concluded that the swelling extent of standard

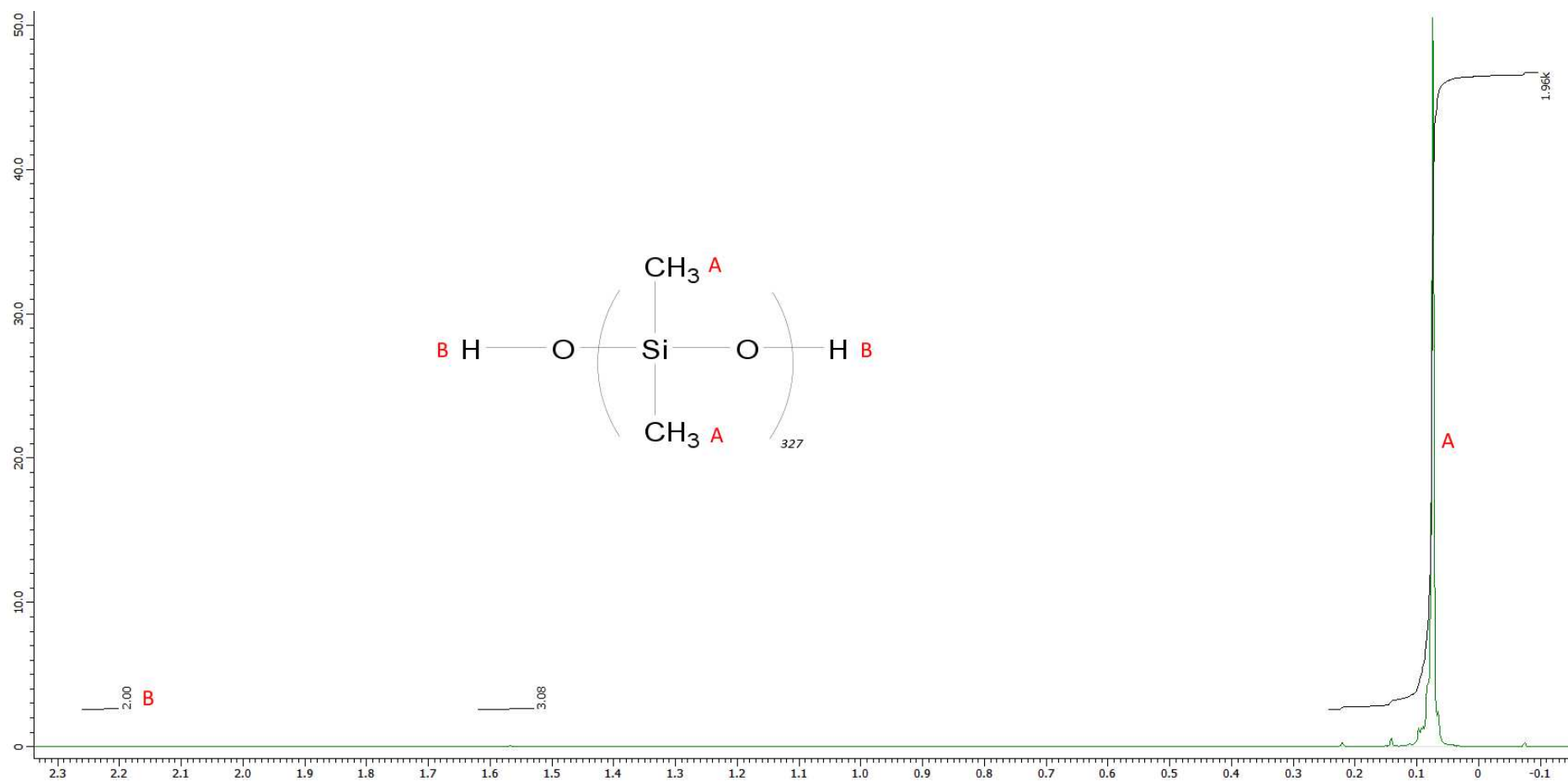
PDMS elastomers was related to both the Hansen solubility parameters and vapour pressure of the solvent vapour. The addition of pores, polar cross-links and inorganic fillers had no effect on the extent of swelling. However, the introduction of pores led to the diffusion of the solvent vapours to increase. PTFPMS elastomers on the other hand displayed dramatically different swelling extents compared to standard PDMS due to their larger cross-link density. A dual component elastomer – PTFPMS elastomer strip with a PDMS tip – showed great promise as a potential actuator. The transport of solvent vapour into the polysiloxane networks was concluded to be mainly anomalous diffusion and it was found that the diffusion rates of the solvent vapours into standard PDMS were dependent on the size and shape of the solvent vapour. The introduction of barium titanate fillers and polar cross-linker had no effect on the solvent vapour diffusion behaviour. A solvent vapour displacement tag with a standard PDMS elastomer was successfully fabricated and tested. The sensor could differentiate between solvent vapours as the RFID response was related to the extent of PDMS swelling, therefore large swelling solvent vapours showed the largest RFID response and the small swelling solvent vapours showed the smallest RFID response. However, it was shown that the sensor was limited by the distance displaced by the loop. It was also found that the RFID response times correlated to the diffusion rate of the solvent vapour into the PDMS elastomers. Repeat measurements for each solvent vapour will have to be performed to investigate the reproducibility and accuracy of the solvent vapour tag design. Further work would be to increase the chemical specificity by changing the distance of the actuator from the displacement component and investigate how the RFID sensor tag would respond to a mixture of solvent vapours. Additional further work would be to investigate if the analyte concentration could be quantified from the sensor response.

Preliminary experiments in ink-jet printing Sylgard® 184 were performed with the aim to work towards the use of additive manufacturing in the production of RFID tags with PDMS sensing components. The addition of xylene to the pre-cure Sylgard® 184 was found to be an efficient method to simultaneously increase the surface tension and decrease the viscosity of the resulting ink solution to the desired values to ensure printability. Discrete droplets were successfully printed onto glass using a pre-cure Sylgard® 184 (5 wt%)-xylene (95 wt %) ink. Curing of the printed Sylgard® 184 droplets had no effect on their shape, however, due to the small amount of Sylgard® 184 in the ink formulation only a small amount was left on the glass. It was found that printing several layers could be achieved, however, curing during the printing process was required to prevent droplet spreading and splashing which would result in satellite droplets. Continuous Sylgard® 184 films made up of a minimum of 5 layers and maximum of 10 layers were also successfully printed onto glass using a pre-cure Sylgard® 184 (5 wt%)-xylene (95 wt%) ink. Increasing the Sylgard® 184 content in the ink while maintaining the desired surface tension needs to be further investigated along with further optimisation of printer settings.

40 wt%, 60 wt% and acidified 60 wt% silver nitrate-PVA composite films were investigated as light sensitive materials that would act as a short circuit (i.e. become highly conductive) as a result of light exposure for the light sensor tag design described in this thesis. Silver particle formation was investigated in both irradiated and non-irradiated  $\text{AgNO}_3$ -PVA solutions and films. In the case of the  $\text{AgNO}_3$ -PVA solutions silver particles were only formed in the solutions that were exposed to light. It was concluded that the silver particles were formed by both hydroxyl and hydrogen radicals formed through the photolysis of PVA and water, respectively. It was also found that discrete, low polydispersed particles were formed in the acidified 60 wt%  $\text{AgNO}_3$ -PVA solution as the acid was acting as a stabilising agent. In the case of the  $\text{AgNO}_3$ -PVA films silver particles were formed in both the light irradiated and non-irradiated films. It was concluded that the reduction of the silver nitrate in the non-irradiated films was caused by the oxidation of the hydroxyl group on the PVA backbone and this reaction does not occur in solution due to the high water content. From visual inspection and the SEM images it was clear that silver particles were formed more quickly in the light irradiated films compared to the non-irradiated films. It was shown that silver particles were formed in the films, the resulting resistivity values of the films were that of semi-conductors. It was concluded that the films conductive mechanism was via charge transfer complexes rather than contact conduction between the formed silver particles. Light exposure had no effect on the film resistivity as charge transfer complexes form with both silver nitrate and silver particles. Increasing the silver nitrate content nor treating the films with heat before light exposure also did not result in resistivities associated with conductors. Due to the fact that the resistivity of the films was not very low and not effected by light the 40 wt%, 60 wt% and acidified 60 wt% silver nitrate-PVA composite films were found unsuitable to be used as the photosensitive material in the light sensor tag. New candidate materials such as poly N-vinyl carbazole trinitrofluorenone mixtures which are organic photoconductors should be further investigated.

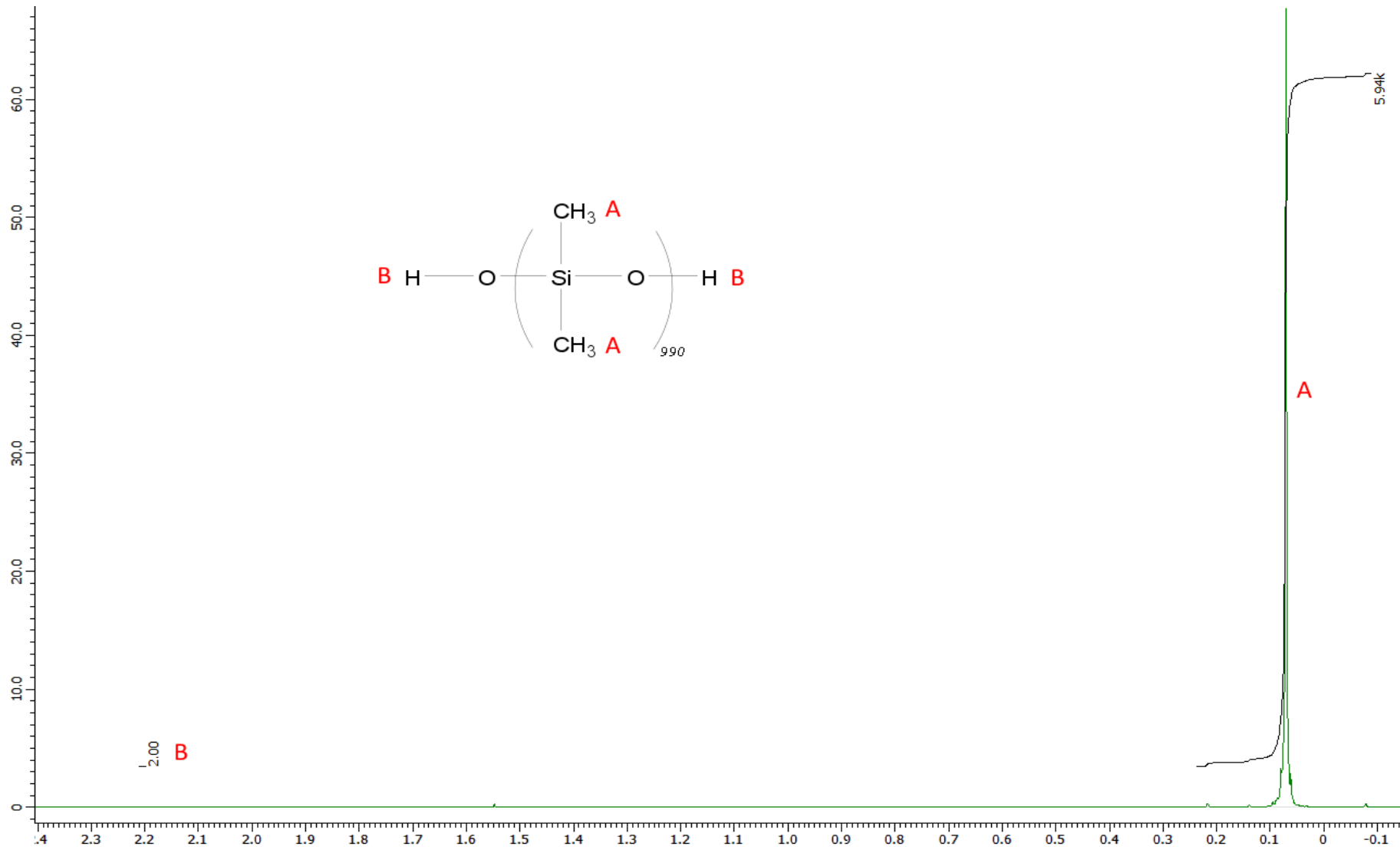
# Appendix

## A.1 NMR spectrum of silanol-terminated polydimethylsiloxane (PDMS) (cSt 1000)

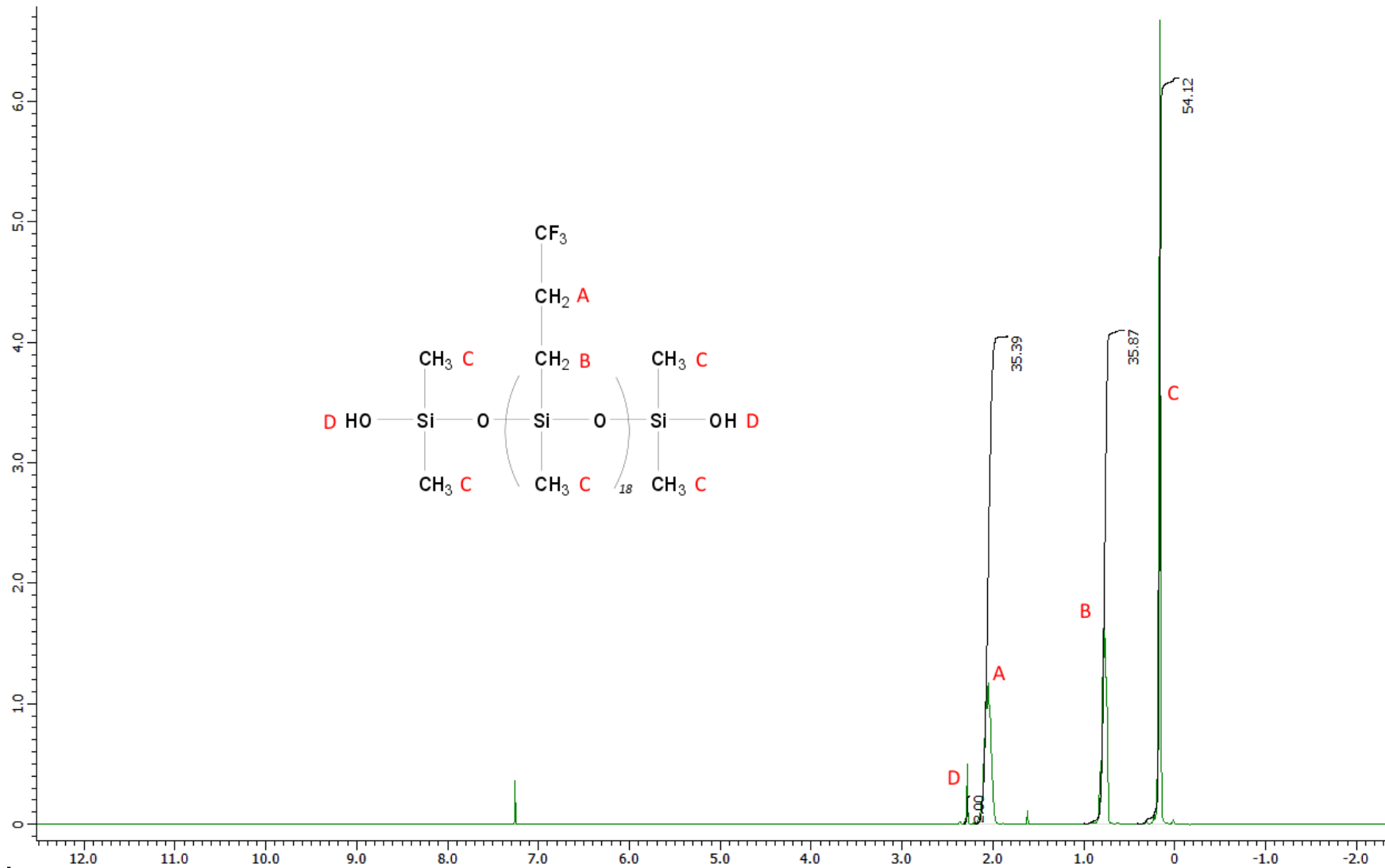




A.2 NMR spectrum of silanol-terminated polydimethylsiloxane (PDMS) (cSt 18000)



A.3 NMR spectrum of silanol-terminated polytrifluoropropylmethylsiloxane (PTFPMS) (cSt 150 – 250)



## A.4 NMR spectrum of xylene

